CRANFIELD UNIVERSITY

Arnaud Lemelle

Development of new fluorescent silica and multifunctional nanoparticles for bio-imaging and diagnostics

Cranfield Health

PhD THESIS
Academic Year 2011

Supervisor: Dr. Sarah L. Morgan
Dr. Sam E.Tothill
March 2011

CRANFIELD UNIVERSITY

Cranfield Health

Ph.D. THESIS

Academic Year 2011

Arnaud Lemelle

Development of new fluorescent silica and multifunctional nanoparticles for bio-imaging and diagnostics

Supervisor: Dr. Sarah L. Morgan
Dr. Sam E.Tothill

March 2011

This thesis is submitted in partial fulfilment of the requirements for the degree of Doctor of Philosophy

ABSTRACT

Silica nanoparticles are effective fluorophore carriers with high potential in imaging, diagnostics, and therapy. The particles are resistant to drastic change of environmental conditions (pH, temperature etc. and insulate the dyes so as to protect them from photobleaching. Silica chemistry is also versatile and affords an easy modification of the particle composition and surface to integrate targeting ligands or to integrate other nanoparticles. Regardless of their advantages, there exists a lack of dye diversity in the literature that is connected to a low affinity for

potential tools for biology and medicineThis thesis describes the development of an alternative method for the synthesis of fluorescent silica nanoparticles and their modification to incorporate iron oxide and gold.

The first part of the thesis describes the application of the amino acid route to the design of multifluorescent nanoparticles 20 nm in diameter and containing up to three fluorophores. The nanoparticles were subsequently used to label two cell lines in view of their imaging with a confocal microscope: the cancerous type took up a large concentration of nanoparticles and stored them under the form of aggregates that act as strong contrast agents whereas the normal line barely internalised the nanoparticles.

In a second time, the composition of the ceramic particles was modified and VTEOS was co-condensed with TEOS in via L-arginine catalysis to create a new hybrid structure with a size comprised ranging from 20 to 100 nm. In one embodiment, the procedure constantly yielded 40 to 50 nm nanoparticles that were employed as fluorophore carriers. Half of the selected fluorescent dyes were successfully entrapped and combined to generate distinctive spectral patterns. The second half required an alteration of the matrix to take into

account the chemical structure of the molecules and ensure that the affinity between the nanoparticles and the fluorophores is optimal. By this new approach, it becomes possible to virtually entrap and combine any fluorophores in a single pot.

Lastly, the hybrid structure was applied as a coating onto iron oxide nanoparticles for a novel class of luminescent magnetic nanoparticles taking advantage of the flexibility of the organic-inorganic composition of the silica layer. The particles were further improved by firstly decorating their surface with small gold seeds in order to impart plasmonic properties and secondly red-shifting the plasmon resonance towards longer wavelength matching conventional near-infrared laser sources by growing a gold layer. This led to an original magnetoplasmonic platform that can be altered to incorporate fluorescent dyes.

The work presented here shows the potential of the amino acid to produce very small fluorescent nanoparticles and its ability to coat other nanomaterials. Further, this report highlights the possibility of nanotechnology in medicine and how the multifunctional nanoparticles can find application in imaging, therapy, and diagnostics indistinctly.

Keywords:

Nanomedicine, imaging, sol-gel, nanoparticles, silica, iron oxide, gold

ACKNOWLEDGEMENTS

I would like to express my gratitude to my supervisor Dr. Sarah L. Morgan for her constant support and guidance throughout the time we have worked together and for having motivated me in pursuing this PhD. It is thanks to her that I have been able to learn so much and gone this far. I would also like to thank Dr. Lee Larcombe that made this project possible as well as Dr. Sam Tothill for her scientific advice.

My gratitude goes to all of the last Silsoe inhabitants, in particular to Ternura Rojas Duran, Israel Sanchez, Katherine Low, and Steve Fowler that took care of me during the first days of my coming. I would like to particularly thank Luismi Garcia Con, who started his PhD at the same time and has been my neighbour since then, for his precious help. I cannot thank enough all of the other students from Silsoe: Ewa, Megan, Neus, Manuela, Varvara, Martina as well as Henri, Sven, Giorgos, and all of the others whose paths crossed mine and made these three years an unforgivable time.

I have a particular thought to Eva, Robert, and Sarah for their perpetual good mood and for what they brought me without knowing it. The time I spent in their presence was invaluable and for that they have my sincere gratitude. A special thanks to my housemates William, Emmanuel, and Gonzalo for their support during the last months.

I cannot forget my whole family, especially my mother and my grandfather for their support and for keeping me updated on the events in France, not to mention my sister and her two boys who always found time to visit me when I went back to France, and my brother, even though we could not meet each other often.

Finally, I must thank Fiona for I keep fond memories of the moments I spent in her company, however short her stay was.

TABLE OF CONTENTS

LIST OF FIGURES

LIST OF TABLES

LIST OF EQUATIONS

ABBREVIATIONS AND NOMENCLATURE

Abbreviations

AF	Alexa fluor
AO	Acridine orange
AOT	Dioctyl sodium sulfosuccinate
APTES	aminopropyltriethoxysilane
B	Magnetic induction
CH_2OH	Formaldehyde
CT	X-ray computed tomography
DLS	Dynamic light scattering
EPR	Enhanced permeability and retention effect
ε	Dielectric constant
FITC	Fluorescein isothiocyanate
Fl	Fluorescein
FSNPs	Fluorescent silica nanoparticles
FRET	Förster resonance energy transfer
FTIR	Fourier transform infrared spectroscopy
GSH	Glutathione
H	Magnetic field

k	Wave vector
λ	Wavelength
LMWA	Low-molecular-weight-antioxidant
LY	Lucifer yellow
M	Magnetisation
MB	Methylene blue
MEF	Metal-enhanced fluorescence
MG	Malachite green
MRI	Magnetic resonance imaging
$NaBH_4$	Sodium borohydride
NH_2OH	Hydroxylamine
NH_4OH	Ammonium hydroxide
NIR	Near-infrared
NNI	National Nanotechnology Initiative
NR	Neutral red
ω	Angular frequency
OG	Oregon green
PC3	Prostate adenocarcinoma cell line
PEBBLE	Probe Encapsulated By Biologically Localised Embedding
PEG	Polyethylene glycol
PET	Positron emission tomography

PhTEOS	Triethoxyphenylsilane
PNT1A	Prostate normal epithelial cell line
PVA	Polyvinyl alcohol
PVP	Polyvinylpyrrolidone
R6G	Rhodamine 6G
RB	Rhodamine B
ROS	Reactive oxygen species
σ	Cross-section
SEM	Scanning electron microscopy
SPIO	Superparamagnetic iron oxide
Tat	Trans-activating transcriptional activator peptide
TEOS	Tetraethyl orthosilicate
TEM	Transmission electron microscopy
THPMP	3-(trihydroxysilyl)propyl methylphosphonate
TX-100	Triton X-100
USPIO	Ultrasmall superparamagnetic iron oxide
UV	Ultravisible
v	Frequency
VT-X	VTEOS-TEOS hybrid
VTEOS	Vinyltriethoxysilane

Nomenclature

- SI Prefixes for Units

k	kilo- (10^{3})
m	milli- (10^{-3})
µ	micro- (10^{-6})
n	nano- (10^{-9})
p	pico- (10^{-12})
f	femto (10^{-15})

- Units notation

°C	degrees centigrade
g	gram
L	litre
m	metre
M	molar

Chapter 1

Introduction and literature review

1 Introduction and literature review

Nanotechnology has the potential to deeply impact on society with as much strength as computing in the 1960s or biotechnology in the 1980s. The idea of controlling and using materials at the atomic and molecular scales can be traced back to Richard Feynman and his famous presentation “Plenty of Room at the Bottom” at Caltech in 1959 [*Feynman, 1960*]. The term nanotechnology – from greek nanos, dwarf - appeared and was defined by Norio Taniguchi in 1974. Although nanotechnology as a science and technology is relatively recent, men have unwittingly employed it for centuries: ancient Egyptians used gold colloids for healing whereas Romans employed silver and gold nanoparticles in craftsmanship (Lycurgus cup, 4th century AD). Later the same metallic particles were applied in stained glasses of German and French churches to display strong and bright colours. Many examples of nanotechnology applications are found throughout the millennia in all kind of craftsmanship and sciences.

The National Nanotechnology Initiative (NNI), a United States federal program established in 2001 to coordinate nanotechnology research and development, has defined nanotechnology as “*research and technology development at the atomic, molecular, or macromolecular scale, leading to the controlled creation and use of structures, devices, and systems with a length scale of 1-100 nanometres (nm)*” [*National Nanotechnology Initiave, 2011*]. Consequently, structures with a least one dimension below 100 nm and exhibiting new properties resulting from their small size, or methods to control and manipulate matter at the nanometre scale enter into the nanotechnology definition. Yet, no universal definition of nanotechnology exists and the limit at which an object is considered as a nanostructure may be larger than the 100 nm proposed by the NNI. Nanotechnology is one of the critical research endeavours of the early 21st century; for this reason, almost all countries have started their own programs. USA started its investments in 2001 through the NNI, whereas Japan prioritised nanotechnology closely after USA. In Europe, research programs in nanotechnology were embedded within national projects through the

Framework Programmes that coordinate the projects and aims of all EU members. If USA, Japan, and Europe are the strongest investors, other countries have also invested in nanotechnology. China has devoted more and more resources and has rapidly caught up with USA and Europe, while South Korea has embarked in a ten-year program [*European commission, 2002, 2007 and 2008*].

Nanotechnology is interdisciplinary in nature and gathers together various domains of science, blurring the barriers between traditionally well-defined fields such as chemistry, physics, biology, and medicine. This is both an advantage and a complication: on the one hand this approach is more likely to create synergies and to increase the pace of innovation in all other domains. On the other hand the previously well-defined domains may no longer be valid and scientists will have to gain knowledge in various fields rather than in a single one, which is a particular issue in term of education. Many applications have already been envisioned that show the multidisciplinarity of nanotechnology [*European Commission, 2006 a; Wood, 2004*]:

- **Information technologies and electronics**: new data storage media with high recording capacities, semiconductors for light-emitted diodes or lasers for optoelectronic devices and sensors, plastic electronics, spintronics, quantum computing, etc.;

- **Materials science**: new lighter and stronger alloys to reduce the amount of materials necessary to create structures or to reduce the fuel consumption of vehicles and planes, new functional surfaces such as scratch-proof, stain resistant, self-cleaning, sterile, etc.;

- **Energy production and storage**: materials for fuel cells or battery, nanostructures for hydrogen storage, low-cost photovoltaic cells, but also materials for insulation, transport, and light-efficiency;

- **Manufacturing**: development of new techniques for top-down (starting from micro-systems and reducing their size) and bottom-up (building

from the atomic and molecular level to create nanostructures) fabrication processes, for example new lithography or vapour deposition processes, etc.;

- **Instrumentation**: new tools and techniques to study the properties of materials at the nanometre scale and to control the production of nanodevices;

- **Food, water, and environment**: detection and neutralisation of micro organisms or chemicals, tracking the origin of food, reparation and clean-up of polluted soils and environments, etc.;

- **Medical applications**: bioactive and biocompatible coatings for implants, scaffold for organ growth (tissue engineering), novel systems for targeted drug delivery, contrast agents and therapies for diseases, laboratory-on-a-chip for fast and accurate diagnostics.

These are but a few applications of nanotechnology foreseen and more applications not yet envisioned ought to appear in the future. The assessment of economic implications of nanotechnology is still blurry and there is also a lack of clarity concerning products already containing nanomaterials. Certain products currently accessible to the public such as cosmetics (shampoos and sun-screens) or hard-disks already contain nanoparticles or are nanostructured. Some other products are not related to nanotechnology but employ this term as a marketing strategy to attract technophiles. However, the majority of nano-labelled products on the market apply to nanotechnology research more than public uses and viable products targeting public will be commercialised within a few years.

Figure 1-1 highlights the four phases that segment the commercialisation of nano-products timeline. The first generation of nanostructures are said to be ‘passive’, i.e. they provide specific properties and maintain them all along their use. This category encompasses nanoparticles, coatings and nanostructured materials, etc. and has more or less entered the commercialisation step. The

second generation represents ‘active structures’ or structures that modify their properties with time or with change in their environment. This category begins to emerge from laboratories and commercialisation should start within a few years. The third generation includes systems of nanostructures for complex applications such as tissues and organs growth and the fourth generation are also complex systems where each molecule has a specific function. The third category is barely starting in laboratories and may not arrive before a decade, followed later by the fourth generation [*Renn, 2006*].

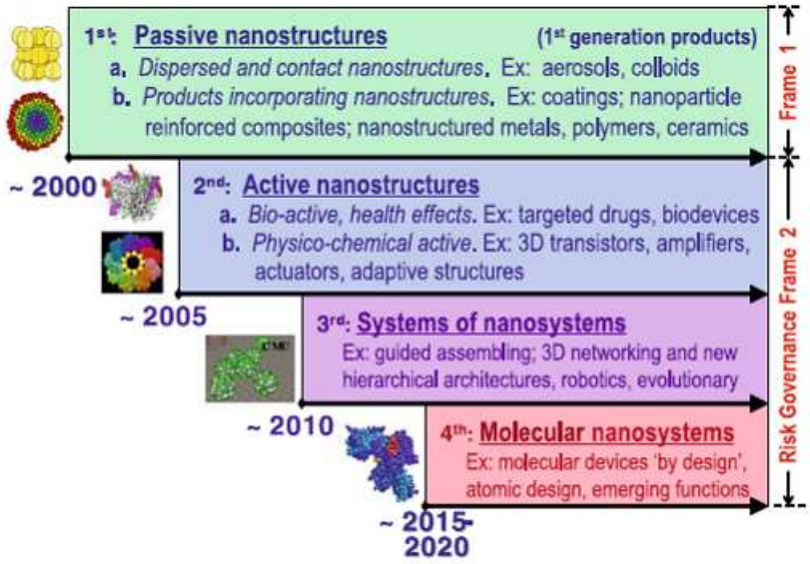

Figure 1-1: Timeline of nanotechnology development and industrialisation divided into four overlapping phases [Renn, 2006].

Nanotechnology is still in its early development but already many new systems and structures have been developed in nearly all scientific and engineering fields. In that respect, the application of nanotechnology to the biomedical field has given birth to new fields generally referred to as nanomedicine and nanobiotechnology.

1.1 Nanomedicine: applications of nanotechnology to the biomedical field

1.1.1 Overview of the nanomedicine field

By operating at the scale of biomolecules, nanotechnology brings new methods to probe or to modify biological systems [*McNeil, 2005*]. Therefore, the scope of applications as can be seen in Figure 1-2 is wide and concerns all aspects of the biomedical field, from drug and gene delivery to nanostructured coatings for implants and contrast agents for imaging, while new possibilities still not envisioned might emerge in the coming decades [*Sutter, 2006; European Commission 2006 b*]. Of all applications, imaging, cancer therapy, and diagnostics stand out as the most prioritised areas of research.

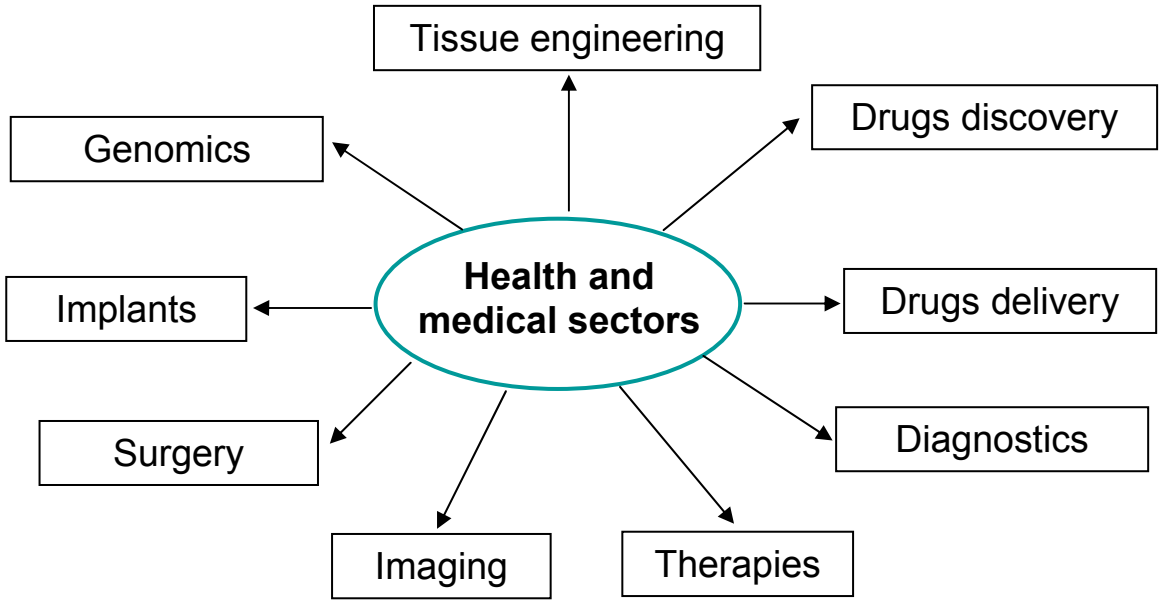

Figure 1-2: Potential applications of nanoparticles and nanostructures in medicine.

Various imaging modalities such as magnetic resonance imaging, as well as X-ray, nuclear, ultrasound or optical imaging are well-established methods to diagnose diseases or lesions, yet they are generally not sensitive enough to

detect molecular changes that are usually the first signs of evolution of healthy tissues into diseased ones. Further development of imaging involves the design of contrast agents and other nanostructures targeting specific biomarkers or biomolecules resulting from abnormal conditions in order to detect a disease in its earlier stage and treat it with as little consequences for the patients. Typical examples are quantum dots, gold nanoparticles under various shapes, or fluorescent silica nanoparticles that are progressively replacing fluorescent dyes in optical imaging, both *in vitro* and *in vivo*.

Likewise, nanotechnology offers new strategies to treat diseases and disorders such as Parkinsons and Alzeihmers or cardiovascular diseases, to improve the specificity or efficiency of existing treatments such as chemotherapy, photodynamic therapy, and other drug-based treatment. Nanoparticles have proved efficient carriers of drugs and other compounds, able to deliver their charge at precise locations due to the easy conjugation with antibodies, peptides, etc. For instance, chemotherapy generates strong side effects since the drugs are not able to distinguish between healthy and unhealthy tissues, but their entrapment within bioconjugated nanoparticles ensures that the chemotherapy drugs only target the right cells and spare the patients painful and long periods of treatment. Similarly, new possibilities such as hyperthermia or photothermal effects open new strategies to cure diseases and infections in the near future.

Lastly, nanotechnology has the potential to deeply impact on sensors, arrays, and chips technologies, offering smaller devices able to detect trace amount of proteins, antibodies, DNA/RNA and other analytes at high speed and reduced costs while requiring very small samples. New biosensors based on colorimetry, fluorescence and other physical mechanisms have born, based on the judicious employ of gold and other nanoparticles to improve the quality of *in vitro* diagnostics tools. At terms, nanotechnology offers the possibility to carry out measurements in parallel or to integrate multiple analytical tools into a single device.

1.1.2 Biocompatibility criteria and nanoparticle structures

Similarly to any medical devices, a material must not elicit deleterious or toxic effects once in contact with biological samples. This biocompatibility criterion is the key parameter for any medical devices and drastically restricts the type and number of materials suitable for *in vivo*, and potentially *in vitro* applications. For instance, titanium dioxide, stainless steel 306L, and cobalt-chromium alloys represent the majority of the prostheses replacing hard tissues such as bone (for example hip prosthesis), whereas certain glasses are bioactive or resorbable and are ideal for bone filling. Polymers such as polyethylene terephthalate have found applications as blood vessel replacement. Even though certain nanostructures exhibit outstanding optical or electrical properties suitable for photonics or electronics, their composition or their behaviour once in a biological environment may become problematic. The toxicology ambiguity of nanomaterials will be discussed later but quantum dots are the typical example of a nanomaterial with outstanding (fluorescence) properties but their heavy metal composition poses a threat in case of degradation of the particles and hampers their *in vivo* potential. On the other hand, they prove invaluable when the particles have little contact such as diagnostics or *in vitro* uses. From a general point of view, it is not possible to transpose the biocompatibility of a bulk material to its nanoscale counterpart: if gold in its bulk and particulate states is biocompatible, the same cannot be said of titanium dioxide that exhibits certain toxicity in regard to its photocatalytic effect.

Toxicology of nanomaterials remains under investigation because the organism's reaction towards the introduction of nanoparticles as well as the cellular uptake and interactions with nanostructures are not fully understood yet. To date, a limited number of nanomaterials have proved successful and have found a real application in nanomedicine as seen in Table 1-1 [*McNeil, 2005; Salata, 2004*]. With both a better understanding of cells-materials interactions and the development of - or combination into - new structures, the list is bound to expand in the coming years.

Table 1-1: Classes of nanoparticles of interest in nanomedicine and their principal applications.

Class of nanomaterials	Description	Applications
Polymeric nanoparticles	Particles made of biodegradable polymer (polylactic acid, polyglycolic acid, etc.)	Drug delivery, therapeutics, imaging
Liposomes	Vesicles made up of a lipid bilayer	Drug delivery
Dendrimers	Spherical branched polymers providing vast amounts of surface area	Drug delivery, imaging
Quantum dots	Semiconductor nanocrystals generally made of a heavy metal core surrounded by a metallic shell	Imaging
Carbon nanotubes and fullerenes	Distinct molecular forms of carbon atoms with the shape of cylinders and of sphere respectively	Drug delivery, photothermal ablation
Superparamagnetic nanoparticles	Iron oxide particles of magnetite (Fe_3O_4) or of maghemite (Fe_2O_3)	Drug delivery, imaging agent, hyperthermia
Noble metal nanoparticles	Particles typically made of gold or silver	Imaging agent, drug delivery, photothermal ablation
Gold nanoshells	Silica particles (core) coated with a thin gold shell	Imaging agent, drug delivery, photothermal ablation

Nanosystems are usually designed as a core-shell structure. The core material possesses the key characteristics that will make a particle an efficient contrast agent for imaging or a good carrier for drug. The direct delivery of core materials can be envisioned as a passive targeting where the nanoparticles travel throughout the organism to reach a particular cell type/tissue or interact with biomolecules. This is for example one way for nanostructures to accumulate into tumours via the enhanced permeability and retention effect (EPR). The incessant growth of cancerous tissues requires a vast supply of nutrients that a normal vasculature cannot provide. Then, new blood vessels are formed to provide more nutrients but these new blood vessels are irregular in shape and dilated so that the vasculature is leaky. This leaky vasculature and accompanying poor lymphatique drainage mean that particles can evade the blood stream and accumulate within the tumours without risk of clearance and

can exert their effects unhampered [*Lyer, 2006*]. However, passive targeting is an ideal case but is not a viable strategy for two reasons:

- Clearance from the organism by the action of the complement system and phagocytic cells (as discussed later);
- The necessity of EPR effect that exists principally in tumour but not in other tissues, including diseased tissues.

Hence, engineering the surface of the particles is a requirement to make the action of nanostructures more specific. For this reason, the typical architecture is based on a core-shell structure where the core is one of the materials aforementioned and the shell is designed according to the mission of the nanoparticles. Polymers and biopolymers are favoured to increase the biocompatibility of a nanomaterial as well as to increase the lifetime in blood. In that respect, coating with polyethylene glycol (PEG) is the principal strategy to obviate or at least delay the action of natural defenders because macrophages and complements proteins need more time to detect the neutral polymer. The specific recognition of cells and molecules – or active targeting – is the result of surface modification with particular ligands. Conjugation of antibodies at the surface of nanoparticles has been one of the first strategies for the recognition of antigen and directing the nanosystems towards the right target. Peptides soon followed as an answer to the large size of antibodies that increases the chance of macrophage recognition. Some peptides helps in penetrating cells such as trans-activating transcriptional activator (Tat) from Human Immunodeficiency Virus 1 whilst other help in escaping endo- and lysosomes to enter into the cytoplasm. A large range of peptides and proteins are available and proved highly effective in the detection and targeting of cancerous cells. In diagnostics, the conjugation of DNA and RNA is central and many assays rely on the conjugation of nanoparticles with oligonucleotides [*Lin, 2010; Tahnh, 2010*].

Nanomedicine relies on three major features: the new properties that the nanoscale induces, the relative size of nanostructures in comparison to biological entities, and the engineering of nanoparticles surface for active

targeting and specific recognition. Several nanomaterials have already been identified and have already made strong contribution to the biomedical field but this thesis is focused on inorganic nanoparticles exclusively. This choice is motivated by the new physical and chemical properties that are absent from polymeric nanoparticles, the higher robustness, and because the first toxicological studies of gold, silica, and iron oxide indicate that these nanomaterials are biocompatible.

1.2 Noble metal nanoparticles

1.2.1 Plasmon resonance and optical properties

Noble metal nanoparticles are an important class of materials in nanomedicine and in many other fields such as optics, solar energy, etc. Gold and silver nanoparticles have fascinated men for centuries, even though the realisation of what these particles are capable of – or simply of their existence – is more recent. For example, gold nanoparticles give the astonishing properties to the Roman Lycurgus cup dated from the 4^{th} century and displayed in the Figure 1-3. The particularity of the cup is to shine a green or red colour when the light source is outside or inside the cup. Similarly medieval glass windows of French and German gothic cathedrals contain metal colloids that give the intense red and blue hues to the windows. Faraday came up with the idea that small particles of gold and silver were responsible for the intense colours of these items but it is only in 1908 that Gustav Mie developed the theory that explain the optical properties of gold colloidal systems [*Jain, 2007*].

The exposition of noble metal nanoparticles to an electromagnetic field leads to the collective oscillation of the atoms electrons. This phenomenon known as plasmon resonance causes a considerable enhancement of the electromagnetic field around the nanoparticles. Mie applied the Maxwell's equations to an electromagnetic light wave interacting with spherical particles and applied the appropriate boundary conditions.

Figure 1-3: The Lycurgus cup appears greenwhen illuminated from outside but glows red when light source is inside the cup [*britishmuseum.org*].

The optical properties are commonly expressed in term of scattering and absorption cross-sections σ_{sca} and σ_{abs} related to the intensity loss of a beam of incident light due to elastic scattering and absorption respectively. In practice, absorption and scattering both contribute and the term of extinction, characterised by the extinction cross-section σ_{ext} is preferred:

$$\sigma_{ext} = \sigma_{abs} + \sigma_{sca}. \quad \textbf{(1-1)}$$

The extinction, scattering, and absorption cross-sections are calculated by series expansion of the electric and magnetic fields into multipole oscillations:

$$\sigma_{ext} = \frac{2\pi}{|\mathbf{k}|^2}\sum_{L=1}^{\infty}(2L+1)\,\mathrm{Re}(a_L + b_L); \quad \textbf{(1-2)}$$

$$\sigma_{sca} = \frac{2\pi}{|\mathbf{k}|^2}\sum_{L=1}^{\infty}(2L+1)(|a_L|^2 + |b_L|^2); \quad \textbf{(1-3)}$$

$$\sigma_{abs} = \sigma_{ext} - \sigma_{sca}. \quad \textbf{(1-4)}$$

with:

$$a_L = \frac{m\psi_L(mx)\psi_L^{'}(x) - \psi_L^{'}(mx)\psi_L(x)}{m\psi_L(mx)\eta_L^{'}(x) - \psi_L^{'}(mx)\eta_L(x)}; \quad \textbf{(1-5)}$$

$$b_L = \frac{\psi_L(mx)\psi_L^{'}(x) - \psi_L^{'}(mx)\psi_L(x)}{\psi_L(mx)\eta_L^{'}(x) - m\psi_L^{'}(mx)\eta_L(x)}. \quad \textbf{(1-6)}$$

Here, $m=n/n_m$ with n and n_m the refractive indices of particle and surrounding dielectric media respectively, **k** is the wavector, and $x = |k|r$, with r the radius of the nanoparticle. ψ_L and η_L are the Ricatti-Bessel cylindrical functions. The summation term index L represents the order of spherical multipole excitation in the nanoparticles. For example, L=1 corresponds to a dipole field, while L=2 corresponds to a quadrupole field, etc. [*Bohren, 1998; Maier, 2007*].

Scattering and absorption contributions of spherical nanoparticles differ with the size of the spheres. For particles with a diameter *d* larger than the wavelength *λ* of incident radiation, the extinction cross-section decomposes as a superposition of oscillating electric dipoles, quadrupoles, and higher-order multipoles. Contrariwise, particles with a diameter smaller than the wavelength of incident radiation are exclusively considered as electric dipole. The latter case has been developed by Rayleigh and is sufficient to understand the plasmon resonance mechanism. If the size of a nanoparticle is small compared to the wavelength of incident light, the light penetrates in the whole particle and grasps all of the conduction electrons. Consequently, the electrons are displaced and the nanoparticle forms an oscillating electric dipole as schematised in the Figure 1-4. This approximation is referred to as quasi-static regime or discrete-dipole approximation and results in a simplification of the cross-section expressions:

$$\sigma_{ext} = 9\frac{\omega}{c}(\varepsilon_{diel})^{3/2} V \frac{\varepsilon_{met}^{''}}{(\varepsilon_{met}^{'} + 2\varepsilon_{diel})^2 + (\varepsilon_{met}^{''})^2}; \quad \textbf{(1-7)}$$

$$\sigma_{sca} = \frac{3}{2\pi}\left(\frac{\omega}{c}\right)^4 \varepsilon_{diel}^2 V^2 \frac{(\varepsilon_{met}^{'} - \varepsilon_{diel})^2 + (\varepsilon_{met}^{''})^2}{(\varepsilon_{met}^{'} + 2\varepsilon_{diel})^2 + (\varepsilon_{met}^{''})^2}; \quad \textbf{(1-8)}$$

$$\sigma_{abs} = \sigma_{ext} - \sigma_{sca}\,. \qquad \textbf{(1-9)}$$

Here, V is the volume of particle, ω is the angular frequency of incident light, and c is the speed of light; ε_{diel} is the dielectric constant of the surrounding media and ε_{met} is the wavelength-dependent complex dielectric function of the metal nanoparticles, $\varepsilon_{met} = \varepsilon'_{met} + i\varepsilon''_{met}$. From equation (1-7), a resonance behaviour manifests whenever $|\varepsilon'_{met}(\omega) + 2\,\varepsilon_{diel}|^2 + |\,\varepsilon''_{met}(\omega)\,|^2$ reaches a minimum. Provided that $\varepsilon''_{met}(\omega)$ is small in the vicinity of the resonance ($\varepsilon''_{met} << 1$), the resonance condition is fulfilled when $\varepsilon'_{met} = -2\,\varepsilon_{diel}$ [*Yguerabide, 1998*]. For silver and gold particles, plasmon resonance falls into the visible region of the electromagnetic spectrum, respectively at ~430 nm and at ~ 520 nm, which explains the intense colours exhibited by gold and silver colloid solutions and their use in stained glass.

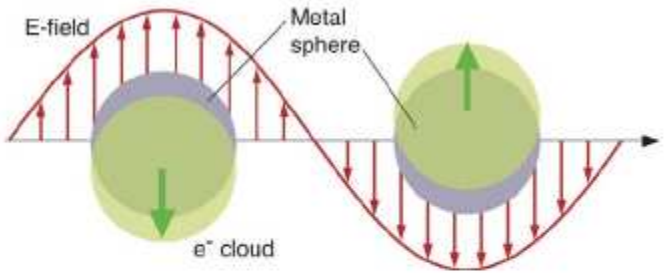

Figure 1-4: The interaction of light with a nanoparticle induces a coherent dipolar oscillation when the dimension of the particle is much smaller than the incident wavelength [Jain, 2007].

No geometric factors are present in equations (1-7) and (1-8); the volume determines the magnitude of the scattering and absorption cross-sections but not the spectral position of plasmon resonance. So, with an increase in size (still within the discrete dipole approximation) the position of the plasmon frequency is only slightly shifted as can be seen in Figure 1-5. For larger particles ($d > \lambda/20$), the quasi-static regime is no longer valid and higher multipole effects emerge. Consequently, the plasmon bandwidth broadens, additional peaks

(shoulders) emerge because of the influence of higher order multipole oscillations, and plasmon resonance red-shift. Moreover, the scattering cross-sections of equation (1-8) quadratically vary with the volume while the extinction cross-section of equation (1-7) varies linearly. Therefore, the smallest particles will mostly absorb light while relatively “larger particles” will scatter light. Moreover, extinction, absorption, and scattering cross-sections equations indicate that the resonance frequency is strongly related to the dielectric constant of the surrounding media. This effect is already employed in surface plasmon resonance to detect presence of biomolecules onto gold surfaces that translate in a slight change in plasmon resonance frequency.

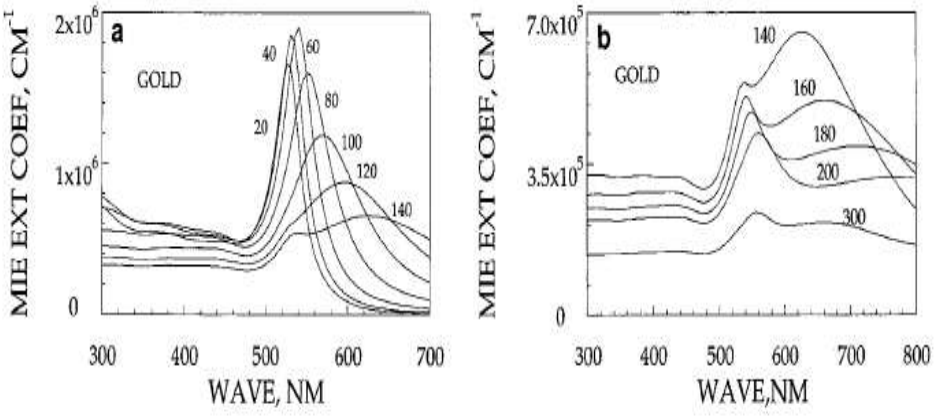

Figure 1-5: Mie extinction coefficient K ($K = C_{ext}/V_{part}$) and evolution of the plasmon feature of gold nanoparticles of different diameters [Yguerabide, 1998].

1.2.2 Red-shifting and effect of shape

It is often desirable to shift the plasmon resonance of gold towards longer wavelength, for example to match the excitation/emission of fluorescent dyes or quantum dots, matching the excitation of a laser source for optimal scattering and/or absorption, or to work in the therapeutic window that spans the near-infrared part and infrared of the electromagnetic spectrum. Increasing the size of noble metal nanoparticles red-shift their plasmon resonance but in a limited

range and the change has detrimental effects on the final scattering/absorption efficiency due to the multipolar interactions arising. Other strategies have been devised to red-shift the plasmon resonance via a modification of the particles composition and/or shape.

In the 90s, Halas and co-workers have. devised and controlled the synthesis of noble nanoshells, layered, spherical nanoparticles consisting of a dielectric core - typically silica- surrounded by a thin metallic shell (gold or silver) [*Oldenburg, 1998*]. The presence of silica near the gold layer modifies the environment of the noble metal and deeply affects the plasmon resonance frequency. Varying the size of the silica core or the thickness of the metal layers shifts the plasmon wavelength to the near-infrared without inducing a dramatic increase of size of the final nanoparticles as can be seen in Figure 1-6 [*Hirsch, 2006*].

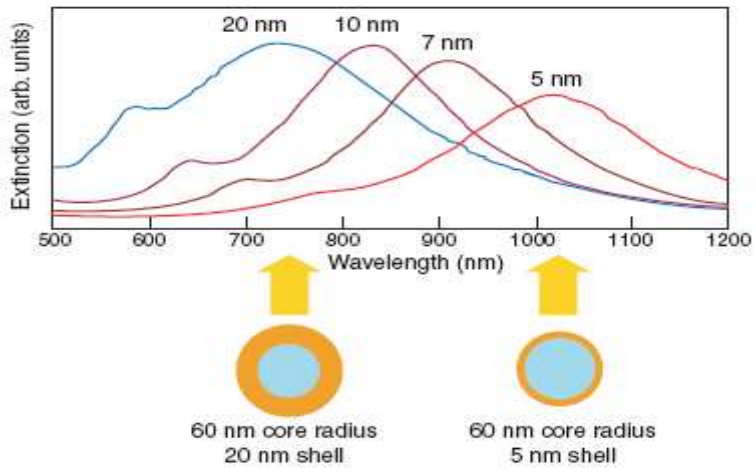

Figure 1-6: Extinction spectra of gold nanoshells as function of the shell thickness ([Jain, 2007]).

Changing the composition of gold nanoparticles is not the only way to tune their optical properties and a change of shape elicits analogous effects. Typically, rod-shaped nanoparticles best exemplify the effect of shape on the plasmon resonance of gold and silver nanoparticles. Nanorods display two plasmon resonance bands: one plasmon band around 530 nm that corresponds to the transverse plasmon excitation - perpendicular to the major (long) axis - and a

stronger band at longer wavelengths related to plasmon oscillations of electrons along the long axis of the particle as depicted in the Figure 1-7. The longitudinal absorption mode strongly depends on the aspect ratio of nanorods, i.e. the value of the long axis divided by the short axis of the rod-shaped particles. It is the variation of this ratio that allows the tunability of nanorods and the possibility of designing particles with a plasmon band in the near-infrared. In comparison, the transverse oscillation of electrons is independent on the nanorod dimensions and fluctuates between 520 and 530 nm [*Jain, 2006*]. Variation of the aspect radio enables to tune the plasmon resonance of the longitudinal axis. In the same vein, other shapes exhibit unusual optical behaviour such as gold nanostars that possess multiple plasmon resonances according to their number of points, or gold nanocages with long range plasmon resonance frequencies [*Chen, 2005 b; Nehl, 2006*].

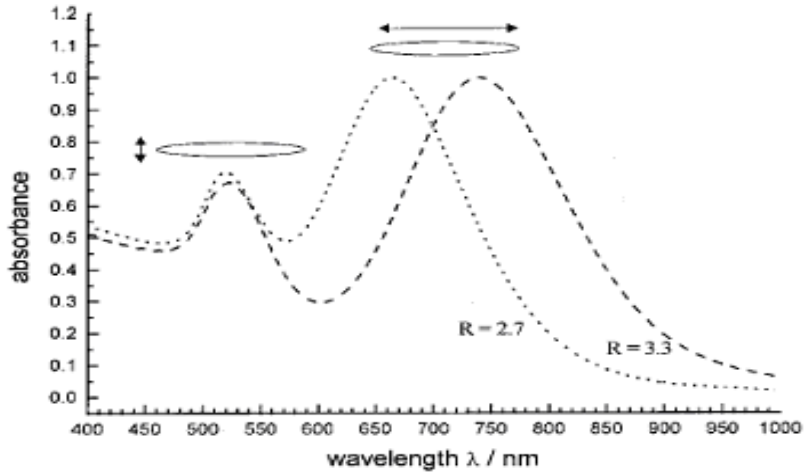

Figure 1-7: Absorption spectra of gold nanorods with different aspect ratios R (value of the long axis divided by the short axis) (Jain, 2006]).

Finally, aggregation is one way to alter the properties of noble metal nanoparticles: in an array or an aggregate of noble metal nanoparticles additional shifts appear because the respective plasmon resonance of each particle interact one with another. Incidentally, the plasmon frequency red-shift and the plasmon bandwidth broadens whilst the electric field is far more

amplified than with single particles. The effect is valid for nanospheres and for other shapes as long as the nanoparticles are sufficiently close, typically less than 2.5 times the particles radius, for the plasmon resonance coupling to occur [*Maier, 2007; Rechberger, 2003; Chien, 2008*]. Light polarization is another factor intervening in the enhancement of the electric field: considering a chain of nanoparticles regularly spaced, a polarization direction of the incident light parallel to the particle chain red-shifts the plasmon resonance frequency and contrariwise slightly blue-shift it when the light is polarized orthogonally. This phenomenon is more easily understandable when considering nanoparticles as dipoles. When light is polarized in parallel to the particle chain, the positive charge of a particle faces the negative charge of the particle at its left as schematised in the Figure 1-8. As a result, the repulsive forces are weakened and the plasmon resonance is lowered. On the other hand, when the electric field is orthogonal to the particle chain the charge distribution of both particles acts cooperatively to enhance the repulsion between the particles and the resonance frequency is increased. Predicting the optical properties of clusters is complicated because aggregates usually form randomly. Inducing in situ aggregation remains nevertheless of high interest in various biomedical fields, such as bio-imaging and therapy because of the red-shift and the enhancement of plasmon resonance.

Throughout the history of humanity: Ancient Egypt, China, medieval time, civilisations used the bulk and colloidal forms of gold to treat various ailments. With a better understanding of the physical properties of gold nanoparticles, new possibilities emerged in fields such as bio-imaging, treatment, or detection of biomolecules.

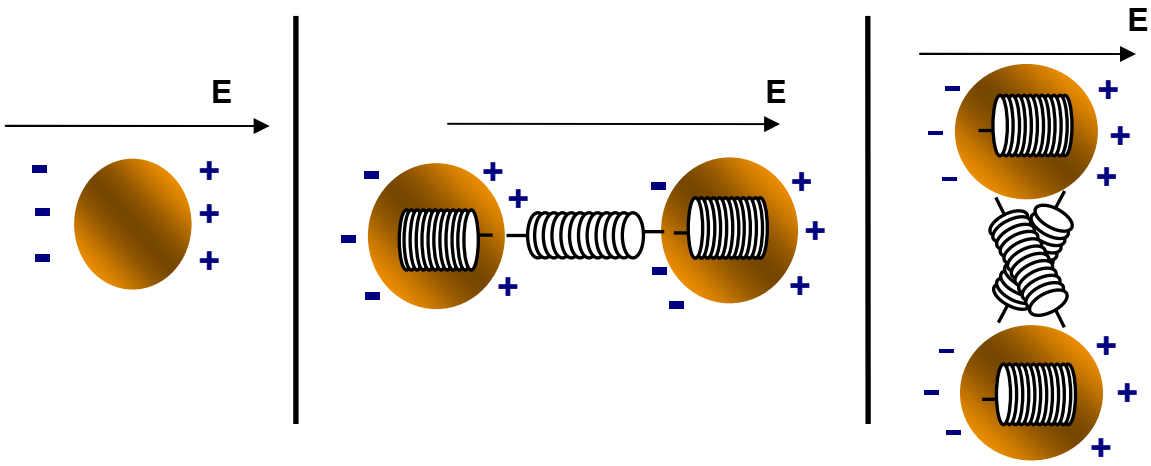

Figure 1-8: Schematic representation of an isolated and of a pair of closely spaced gold nanoparticles, with polarisation of light parallel and orthogonal to the long particle pair axis.

1.2.3 Contrast agent for bio-imaging

Gold nanoparticles are versatile contrast agents suitable for multiple imaging modalities. Their high electron density makes of noble metal particles particularly apparent under x-ray, be it computed tomography or any other electron microscopy, including scanning and transmission electron microscopy that are more dedicated to materials analyses. Gold is likewise very effective with acoustic imaging and has been show to enhance the quality of such modality [*Cai, 2008; Labhasetwar, 2007; Li, 2007*]. Yet, optical modalities remain where gold has made a serious breakthrough: in comparison to fluorescent dyes that are traditionally employed as stain and contrast agents, the metallic nanoparticles are not prone to photobleaching – a loss of fluorescence resulting from photodegradation – and may be detected over prolonged period of time. Moreover, the optical cross-section under plasmon resonance is in no comparison to that of fluorophores and the important light scattering generates a signal that is easily detected. Last but not least, the possibility of tuning the plasmon resonance towards the near-infrared, i.e. in the therapeutic windows that span between 650 and 900 nm, where little

endogenous fluorophores and other species are susceptible to absorb or scatter light or to fluoresce is invaluable for *in vivo* imaging [*Jain, 2007*].

Gold nanoparticles have been detected using various optical modalities. For instance, darfield imaging is a traditional optical modality equipped with a dark field condenser so that only allows the collection of highly diffracted rays after illumination of a sample with white-light source. The light source covers a large wavelengths range, including that matching the plasmon resonance of gold nanoparticles. At such wavelengths, light is strongly scattered and is collected by the dark-field condenser and display on images. When a heterogeneous sample of gold nanoparticles is imaged, each population of particles can be discriminated by a different colour bound to their respective plasmon resonance wavelength. The effect is limited with nanospheres, but dark field imaging is particularly suited to the imaging of gold nanorods and nanoshells as exemplified in Figure 1-9 [*Sonnichsen, 2002*]. Confocal imaging – a variation of fluorescence microscopy able to reduce the autofluorescence background and to provide three-dimensional pictures of a sample – has also frequently obtained good results in the detection of gold nanoparticles. The lack of intrinsic fluorescence is compensated by the possibility to collecting imaging in reflectance mode, where the light scattered by the metallic contrast agents is detected. Two-photon microscopy is another optical imaging modality that is less common than the former two but is a very powerful apparatus: instead of illuminating the sample with white-light source or a UV/visible laser, two-photon and multiphoton microscope employs pulsed laser emitting in the near-infrared, which is of high interest for gold nanoshells and nanorods [*Wang, 2005 a*].

The procedure to conjugate gold surface with antibodies, peptides, and other ligands is well documented due to the frequent employ of gold (thin films, etc.) in biomedical applications. The same procedure are transposable to the nanoparticle form and has allowed the conjugation with epidermal growth factor receptor (EGFR) and other ligand able to recognise the biomarkers overexpressed on cancer cells: oral, cervical, skin and other cancers have successfully been detected after appropriate surface design of gold

nanospheres and nanorods under all of the optical modalities mentioned previously [*Durr, 2007; El-Sayed, 2003; Oyelere, 2007, Sokolov, 2003 a*].

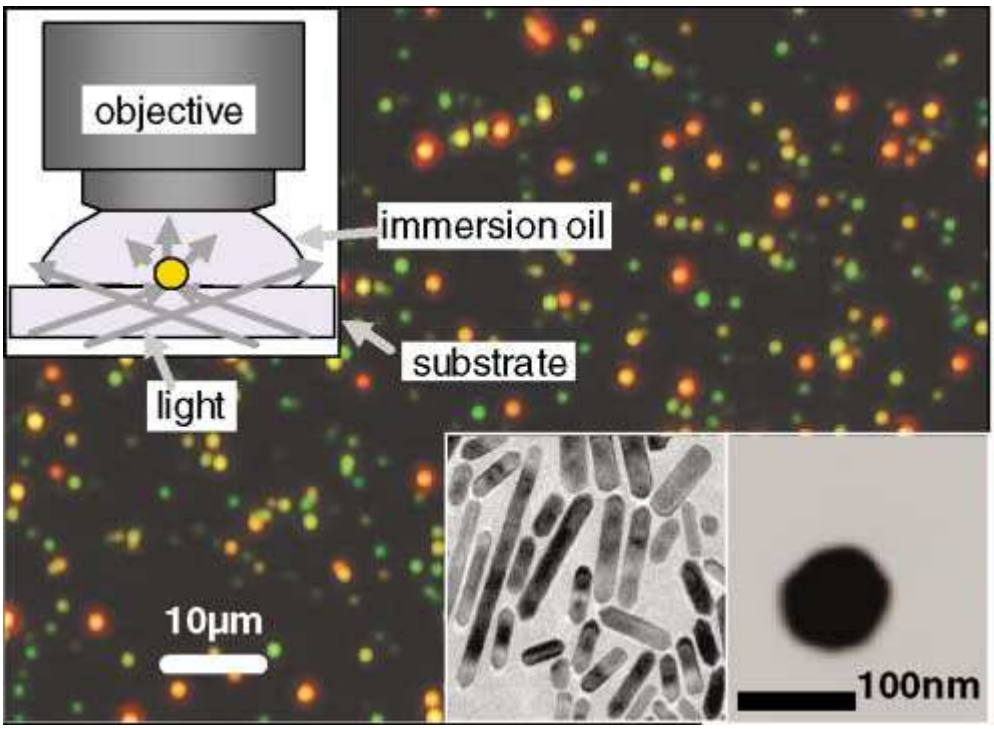

Figure 1-9: Dark-field microscopy picture of gold nanorods with various aspect ratios [Sonnichsen, 2002].

1.2.4 Photothermal therapy

A distinctive capacity of gold and silver nanoparticles is their ability to rechannel light energy into the form of heat provided that the particles are strong absorbers [*Govorov, 2007*]. This photothermal effect is principally achieved through the use of pulsed lasers at the plasmon resonance frequency and the raise of temperature is restricted to the direct vicinity of the nanoparticles. Practically, the absorption of light creates a heated electron gas that cools down by exchanging its energy with the particles lattice through electron-phonon interactions. Subsequently, the lattice cools rapidly by exchanging its energy with the particles environment. The laser parameters, i.e. power, pulse duration, time of exposure, etc. induces various effects on the particles vicinity and on the

particles themselves as schematised in the Figure 1-10 [*Pustovalov, 2008*]. At a first level, the raise of temperature is limited, without consequences for the particles but sufficient to affects cells or proteins (hyperthermia). At higher temperature, the heat front diffuses away from the particles and affects a larger space around the particles. At a second level, the heat front diffuses further away and the conditions may be sufficient to induce cavitation phenomena, with the formation of bubbles that expand and collapse, reaching very high temperature and pressure. In the next step, the photothermal conversion crosses the melting point of noble metals and the particles start degrading, firstly melting, then evaporating up to the point where the particles fragment. Each of these phenomena provokes interesting effects on biological media and has found potential therapeutic applications, principally in cancer therapy. For example, cancerous cells are more sensitive to changes of temperature than normal cells and a slight increase of temperature may elicit deleterious effect for abnormal tissues while sparing the healthy one [*Pissuwan, 2006*]. As often in nanomedicine, the objective is to firstly target the cancerous cells via bioconjugation to bring as many gold nanoparticles in contact with the tumours and therefore induce plasmonic amplification phenomenon to promote hyperthermia or to give birth to cavitation and bubbles generation [*Zharov, 2005 and 2006*]. Even fragmentation of the nanoparticles offer therapeutical perspective as the diffusion of the fragments is limited in space, but sufficient to pierce the membrane of cells. Treatment is not the sole purpose of the photothermal conversion and the generation and propagation of bubble or the expansion of heated liquid are precisely the physical features that photothermal and photoaccoustic imaging modalities detect.

A certain number of studies have proved the effectiveness of photothermal treatment towards cancer. For instance, El-Sayed et al. used anti EGFR antibodies-conjugated nanoparticles to target human oral squamous cell and illuminated the particles with a normal argon laser at various laser intensities, using dark-field microscopy to observe the effects on cells [*El-Sayed, 2006*]. Yet, such therapy would be more effective with near-infrared or infrared sources: Halas' group has demonstrated at several occasions that gold

nanoshells are suitable contrast agents as well as photothermal agents, proving suitable to resect tumors in mice [*Gobin, 2007*]. El-Sayed's groups took advantage of the near-infrared longitudinal plasmon resonance of gold nanorods to achieve similar results on two malignant oral epithelial cell lines [*Huang, El-Sayed, 2006*].

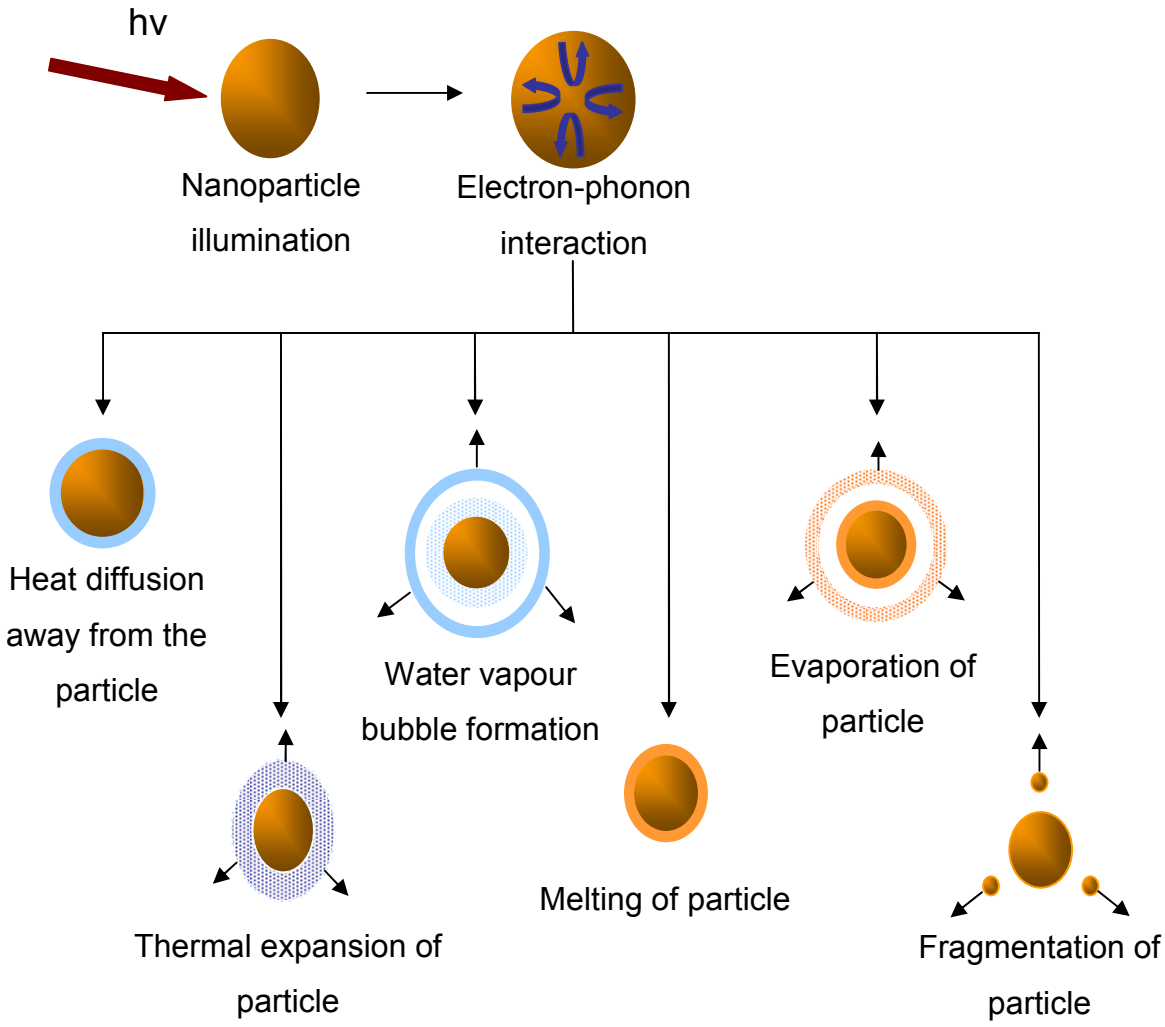

Figure 1-10: Excitation of gold nanoparticles with short pulses laser leads to various photophysical reactions such as diffusion of heat away from the particle, generation of pressure waves and bubbles formation, melting of the particle, evaporation or fragmentation.

1.2.6 Diagnostics

Gold has a long history in diagnostics and sensing of proteins, not only as nanoparticles but as thin films. Gold nanoparticles have been traditionally employed in immunostaining, where the gold particles are conjugated to an antibody against specific biomolecules or cellular compartment. The high atomic weight of gold generates a high contrast when imaged by transmission electron microscopy. Yet, it is the peculiar interactions between gold and silver surface with organic molecules that have drawn the attention for sensing and diagnostics [*Chen, 2010*]. In sensors, the noble metal particles are highly sensitive to the presence of analyte molecules in their vicinity as it affects their plasmon resonance and may be detected by dark-field microscopy. Similarly, plasmon resonance is modified after aggregation of nanoparticles which is interesting to design colorimetric assays. The original work of Mirkin et *al.* involved the conjugation of gold nanoparticles with single strands of DNA. When particles conjugated with complementary strands were added to the same solution, particles bound one to the other due to the hybridisation of DNA strands. As a consequence, the originally red suspensions turned violet/blue once gold aggregates formed [*Mirkin, 1996*]. Similar results were obtained with gold nanoshells for the detection of antibodies in blood samples and with aptamer-modified gold nanospheres for the detection of cancerous cells and can be extended to any process where aggregation at small or large scale occurs [*Hirsch, 2003; Medley, 2008*]

Noble metal surfaces quench the fluorescence of dyes when the distance metal-fluorophore is very close and this effect is used in several sensors to quantitatively measure the concentration of analytes. The strategy proceeds in two steps: first of all, the nanoparticles are conjugated with a ligand that binds specifically to the analyte of interest. The particle suspension is afterwards saturated with analyte molecules conjugated with a fluorescent dye: due to the close proximity between the gold surface and the fluorophore, the signal of the dye is quenched. In a second time, the particles are added to the sample to analyse: if no analyte is present, no fluorescence is detected because of the

quenching. On the contrary, the analyte molecules compete with the fluorophore-tagged molecules present on the particles to have access to the ligands and progressively replace the tagged-biomolecules. As a result, the fluorescence in solution increases with time, even more that the concentration of analyte originally present in the sample is high [*Sperling, 2008*].

Noble metal surfaces induce a strong increase of the Raman scattering signal of molecules in their vicinity. When molecules scatter light, the scattered photons carry the same energy/frequency and same wavelength than the excitation photons (elastic or Rayleigh scattering). However, the frequency of a small fraction of the scattered photons is different from that of the excitation photons (inelastic or Raman scattering). The Raman signal is intrinsically weak and requires a consequent analyte concentration for being detected, but when a gold or silver surface is present near the molecules of interest, the Raman scattering is strongly enhanced. This surface enhanced Raman scattering is linked to the plasmon resonance of noble metal nanoparticles and its electric field enhancement so the probability to scatter light is much higher and the Raman scattered signal is several order of magnitude higher than without nanoparticles [*Sperling, 2008; Li, 2008*].

Similarly to Raman spectroscopy, the strong light scattering under plasmon resonance elicits an enhancement of fluorescence excitation and/or emission of dyes nearby under strict conditions. This phenomenon, exhibited by films and colloids, is referred to as metal enhanced fluorescence (MEF) or radiative decay engineering and it offers the possibility to improve the technologies based on fluorescence, for instance DNA analysis, sensors and probes, imaging, etc. MEF occurs when the absorption and/or the emission of a fluorophore overlap with the plasmon resonance frequency of the metal nearby as schematised in the Figure 1-11. On the one hand, the incident light interacts with the metallic surface to generate the plasmon resonance and the enhanced electric field subsequently excite a fluorophore in the vicinity of the gold or silver. In that case, plasmon resonance is used to enhance the excitation of the fluorophore. On the other hand, the effect may be opposite and it is the emitted light from the

fluorophore that induces the oscillation of electrons responsible for the electric field light enhancement, in which case the dye molecule acts as a source for the metallic object [*Lakowicz, 2005*]. The MEF has a potential application in surface assays based on fluorescence where silver and gold nanoparticles can increase the signal of fluorophores and quantum dots to achieve higher sensitivity [*Aslan, 2004*].

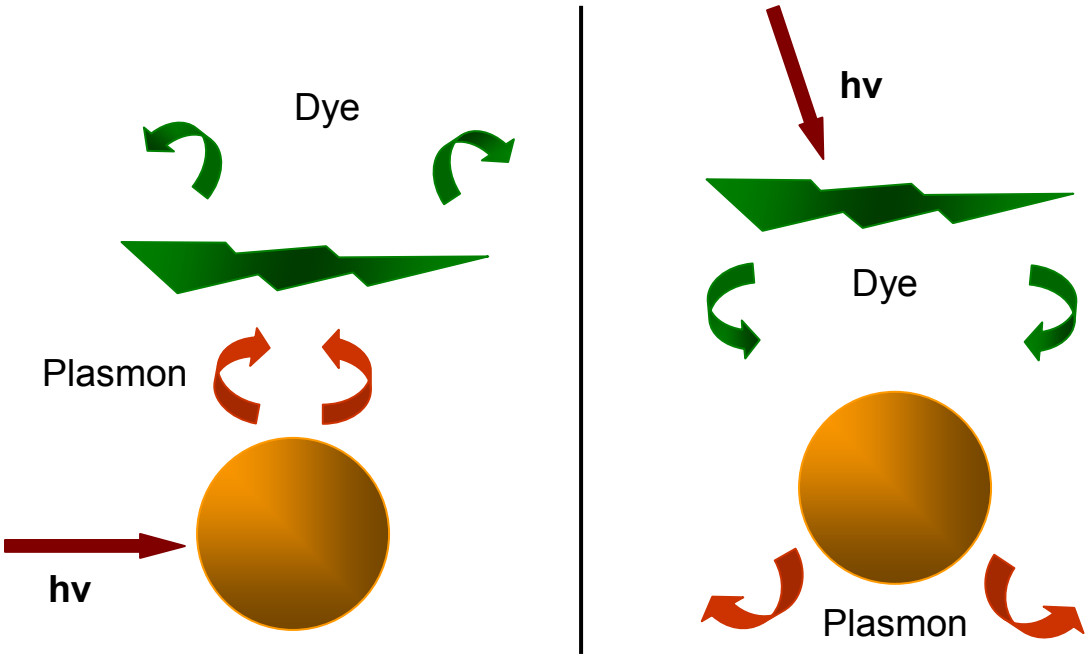

Figure 1-11: Metal enhanced fluorescence occurs either when fluorescence excitation or emission matches the plasmon resonance of a noble metal nanoparticle nearby.

In summary, gold nanoparticles are highly versatile and play or will play a fundamental role in many applications and in particular in imaging, diagnostics, and potentially therapy. The possibility to carefully tune the plasmon resonance coupled to the ease of surface modification enables to match the commercially available laser sources and to precisely target the right species. There already exists report of tumour treatments and *in vivo* imaging in mice but the limited depth penetration of light in tissue - a few centimetres with NIR light – is at present the principal limitation to gold nanostructures and limits the detection to

superficial area in skin and regions accessible to endoscopy exclusively. However, advanced in photonics and plasmonics may be able to circumvent this setback and make it possible to detect and treat deep tissue targets.

1.3 Magnetic nanoparticles

1.3.1 Magnetic nanomaterials and iron oxide

Magnetic nanoparticles are a fundamental class of nanomaterials with high potential in medicine and other applications in relation with the health sector. Similarly to other nanomaterials encountered so far, magnetic nanoparticles are potential drug and gene carriers, contrast agents for magnetic resonance imaging, and even therapeutic mediators in hyperthermia treatment [*Gould, 2006*]. The obvious feature of this class of nanomaterials is its specific reaction towards magnetic field and the small dimension of magnetic nanocrystals give birth to a brand new magnetic behaviour named superparamagnetism. Various alloys have been engineered throughout the last decades, made of chromium, cobalt, neodymium, and other rare earth and transition metals, but only a few are or may be biocompatible. Of all nanomaterials alloys developed so far, iron oxide is the most widespread, although a few iron and cobalt alloys have occasionally proved viable biomedical products. Iron oxide exists naturally under various crystalline forms that exhibit specific magnetic behaviours, but magnetite Fe_3O_4 and maghemite γ-Fe_2O_3 are preferred due to their biocompatibility, chemical stability in biological and physiological conditions and because their synthesis is easy and inexpensive compared to other magnetic nanocrystals [*Figuerola, 2010; McBain, 2008*]. They are in principle gradually recycled by the organism and therefore more tolerated than other magnetic materials so long as the dosage remains controlled [*Park, 2006 a*]. Iron oxide crystals are generally categorised into superparamagnetic iron oxide (SPIO) for particles with a hydrated diameter superior to 50 nm and ultrasmall superparamagnetic iron oxide (USPIO) for smaller structures.

The oldest and most common method – which is also the simplest and fastest – is the wet precipitation (also called co-precipitation) of iron salts in alkaline conditions. In the case of iron oxide nanoparticles, Massart developed a method that has since then become a standard [*Massart, 1981*]. The method consists in mixing ferrous chloride ($FeCl_3.6H_2O$) and ferric chloride ($FeCl_2.4H_2O$) in water at a molar ratio 1:2 in presence of a base, either potassium hydroxide or ammonium hydroxide:

$$Fe_{aq}^{3+} + Fe_{aq}^{2+} + 8OH_{aq}^{-} \longrightarrow Fe_3O_4 + 4H_2O. \quad \textbf{(1-10)}$$

Massart's method yield nanoparticles 8 to 15 nm in size. Depending on the type of iron salts (nitrates, sulphates, etc.), as well as on the Fe^{3+}/Fe^{2+} molar ratio or the pH, the size and shape of the particles can be tailored. Maghemite is obtained from magnetite when a Fe_3O_4 suspension is washed with nitric acid, not only to neutralise the remaining base in solution, but also to convert the Fe_3O_4 structure into maghemite Fe_2O_3:

$$(Fe_8^{3+})_{tet}(Fe_8^{3+}Fe_8^{2+})_{oct}O_{32} \xrightarrow{H^+} \frac{3}{4}(Fe_8^{3+})_{tet}(Fe_{\frac{40}{3}}^{3+}V_{\frac{8}{3}})_{oct}O_{32} + 8H_2O + 8Fe^{2+}. \quad \textbf{(1-11)}$$

The principal limitation of the co-precipitation procedure is the low degree of crystallinity as well as a relatively important size dispersity of the nanoparticles due to the limited reaction temperature of the reaction. An alternative route is, as often with nanomaterials, the water-in-oil microemulsion to produce monodisperse samples, but once again the presence of water as media limit the reaction temperature and consequently the crystallinity of the crystals is not optimal. However, crystallinity is directly connected to the performance of the magnetic nanomaterial and a high crystallinity is desirable for optimal performance.

Proceeding at high temperature (hydrothermal synthesis) is the common route to obtain highly crystalline particles. After the iron salts are dissolved in water, the temperature is increased well above the boiling point of water: the synergetic combination of high temperature and high pressure resulting from

water vaporisation improve the crystallinity of the particles at the cost of size and shape control. Other techniques include decomposition of organometallic reagents in high-boiling point organic solvents and chemical vapor deposition to produce small crystalline nanoparticles but both are non-environmentally friendly and chemical vapor deposition requires specific and expensive equipment [*McBain, 2008*].

Because of the tendency of iron oxide nanoparticles to agglomerate, an additional step is engaged where complexes agents such as citric or oleic acids, dextran, silica and other hydrophilic polymers are added to stabilise the crystals. This step is usually processed after the formation of nanoparticles, but some groups coupled particles growth and stabilisation with polyvinylpyrrolidone or other stabilisers [*Mornet, 2004*].

1.3.2 Magnetism behaviours

The magnetic properties of iron oxide nanoparticles and of magnetic materials in general are the consequence of the response of their electrons magnetic moments to an external magnetic field. The magnetic moment of electrons has two origins: their rotation around their respective nucleus (orbital component) and their spinning in “up” and “down” directions. In other terms, electrons are like small magnets with orbital and spinning moments.

The net magnetic moment of a substance is the sum of its electrons magnetic moments and the large numbers of atoms in materials is such that the electrons are arranged to cancel out their magnetic moments. In particular, electrons are paired with opposite magnetic moments, (Pauli Exclusion Principle) or combined into filled electron shells (subshells) with zero net orbital motion. Yet, in certain case the subshell of material is not entirely filled and its atoms possess unpaired electron that induce the magnetic properties of the material. When an external magnetic field ***H*** is applied to a material, its atomic magnetic moments respond to the external source in the form of magnetic induction **B**

that represents the internal field strength within a material (the magnitude of the field strength within the material) and is defined by [*Andrä, 1998*]:

$$\boldsymbol{B} = \mu_0 (\boldsymbol{H}+\boldsymbol{M}); \quad \textbf{(1-12)}$$

where μ_0 is the permeability in a vacuum and **M** is the material magnetisation, that is the magnetic moment per unit volume that results from the tendency of atomic magnetic dipole to align with an external field.

Magnetisms falls into three categories: diamagnetism, paramagnetism, and ferromagnetism to which two subclasses of ferromagnetism are added: ferrimagnetism and antiferromagnetism [*Callister, 2001*]. Diamagnetism is the tendency for a material to oppose any magnetic field it is subjected too. The electrons of a diamagnetic material are all paired so that the net magnetic moment is null, which translates macroscopically by an absence of any intrinsic magnetic effect schematised in the Figure 1-12. In presence of an external field, a magnetic moment is generated in a direction opposite so that diamagnetic materials tend to be repelled by any external magnetic sources. Aluminium oxide, gold and silver, silicon, and zinc are some examples of diamagnetic substance.

In contrast, paramagnetic materials possess unpaired electrons, for example because of unfilled electron shells where atomic or molecular orbitals contain a single electron. The unpaired electrons are free to align in any direction and electron magnetic moments naturally get a random orientation that result in a null net magnetic moment. The second difference with diamagnetism is that instead of opposing to an external magnetic field the magnetic moments of unpaired electrons align with it and contribute to reinforcing the total magnetic field. Common paramagnetic materials include aluminium, chromium, titanium, or zirconium.

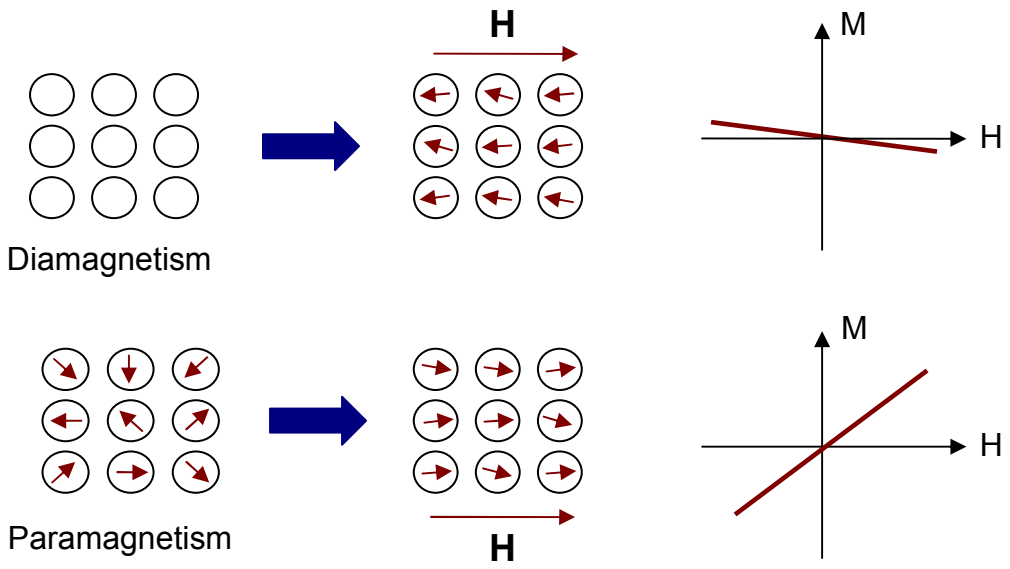

Figure 1-12: Schema of the electron magnetic moment alignment in absence and in presence of external magnetic field in diamagnetic and paramagnetic materials and respective M-versus-H behaviour curves.

Likewise, ferromagnetic materials possess unpaired electrons, but do not exhibit a random orientation. Hence, the magnetic moments naturally orient parallel one to the other to maintain a low energy state. Microscopically, the order existing in ferromagnet translates into magnetic domains where all magnetic moments are parallel as exemplified in the Figure 1-13. However, the order is maintained until a certain temperature called Curie temperature, above which the thermal disorder that installs into the materials is strong enough to overwhelm the ferromagnetic order and make the magnetic lose its magnetic properties.

In their natural state, each domain is magnetised to its saturation magnetisation (the maximum value of magnetisation a material reach under sufficiently high magnetic field) and neighbouring domains have a slightly different magnetisation orientation. The magnetisation ***M*** in absence of external field is then the sum of the magnetisation of all domains and is equal to zero when the

material is unmagnetised. When a ***H*** field is applied, the magnetic induction **B** increases with H until it reaches a threshold value: the saturation magnetisation of the ferromagnetic material. Microscopically, the external magnetic field influences the domains and as ***H*** increases, more and more domains change their shape and size to align to the external field via the movement of boundaries. In fact, the domains oriented favourably will grow at the expense of those that or not favourably aligned. At the saturation magnetisation, the specimen is composed of a single domain nearly aligned to ***H***.

When the external field is suppressed, the domains do not regain their original orientation. Instead, they conserve the saturation value or their magnetisation decreases at a slow rate. Even when the source is entirely suppressed, a residual magnetic field – or remanent magnetisation - resides in the ferromagnetic substance. This phenomenon of magnetisation lagging behind the magnetic field is called hysteresis and plays a fundamental role in most of the magnetic events encountered in our everyday life. The number of ferromagnetic elements is limited to rare earth gadolinium and dysprosium, metals iron (ferrite, magnetite), cobalt, nickel, and some of their alloys such as FePt and FeCo likewise display a ferromagnetic behaviour.

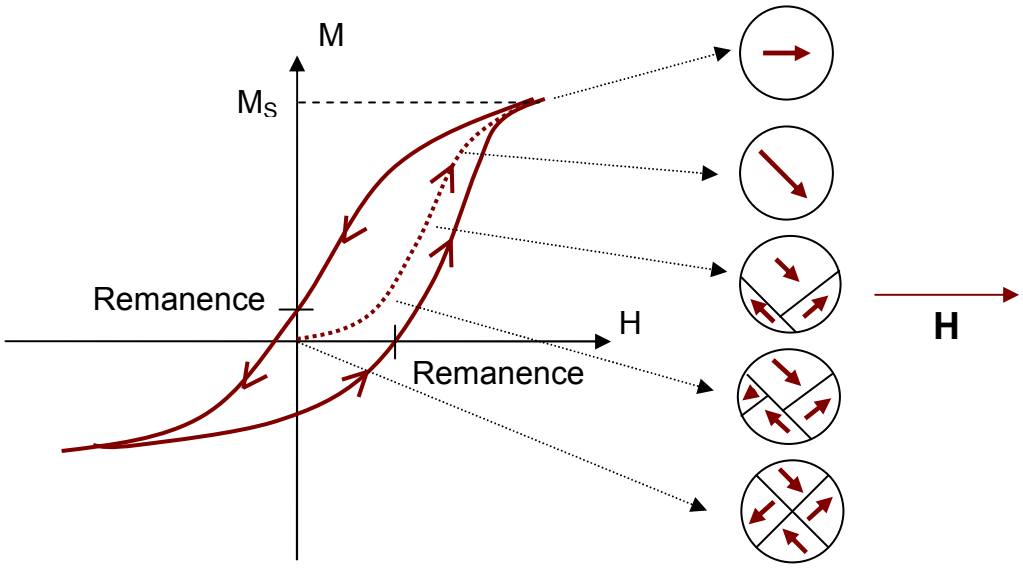

Figure 1-13: M-versus-H behaviour of a ferromagnetic and evolution of its magnetic domains at different stage of the magnetisation process.

The organised orientation of magnetic moments into their respective domains may lead to two sub-categories of ferromagnetism. Antiferromagnetism differs from ferromagnetism in that the magnetic moments of neighbour electrons are in opposite directions as can be seen in the Figure 1-14. As a result, the net magnetic moment of a ferromagnetic material is equal to zero since all electrons magnetic moments cancel. The case of ferrimagnetic lays somewhere in-between ferromagnetism and antiferromagnetism: the magnetic moments of neighbour electrons are in opposite directions similarly to antiferromagnetic substances. However, the magnetic moment of one of the sublattice thus created (i.e. electrons pointing in one direction) is higher than the other so that the net magnetic of a ferrimagnetic material is not null and the material retain its magnetisation even in absence of an external magnetic field.

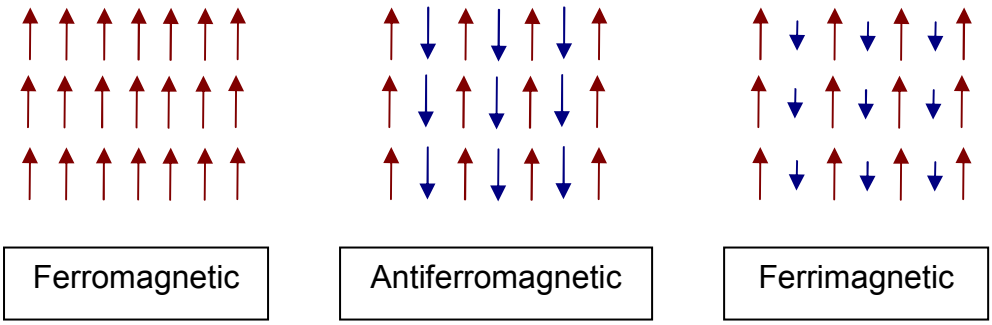

Figure 1-14: Orientation of magnetic moments in a ferromagnetic, antiferromagnetic, and ferromagnetic substances.

When the size of a crystal is smaller than the dimensions of ferri- or ferromagnetic domains (typically 30 nm), the whole crystal behaves as a single magnetic domain. This is the case for nanoparticles that can be envisioned as single magnetic monodomains where all magnetic moments are parallel. The consequences are first the alignment of all particles with an external magnetic field, and secondly the absence of remanent field after magnetisation of the particles since all monodomains regains a random orientation. This new behaviour is called superparamagnetism as the saturation magnetisation reached by superparamagnetic nanoparticles is far superior to that of

paramagnetic substances as highlighted in the Figure 1-15 [*Jun, 2008; Leslie-Pelecky, 1996*]. Yet, the saturation magnetisation of nanoparticles may decrease as the crystals dimensions diminish. In particular, iron oxide nanoparticles suffer from a dramatic drop of their magnetic properties when their dimensions become too small, although parameters such as crystallinity, presence of impurities, or stabilisers or surfactants play a role on the magnetic properties as well.

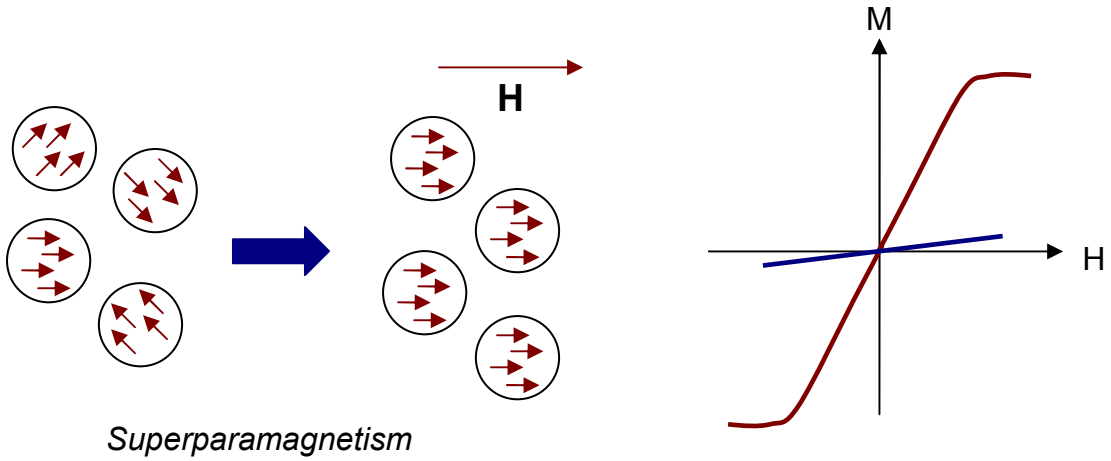

Figure 1-15: Effect of an external field on superparamagnetic nanoparticles and comparison of M-H curves of superparamagnetic (red) and paramagnetic substances (blue).

1.3.3 Applications in bio-imaging

Superparamagnetism is the core of some of the newest applications of magnetic nanoparticles as it affords a strong saturation magnetisation without retaining any remanent field that would induce the nanoparticles to clump one to the other. There is a wide range of applications of iron oxide and other magnetic nanomaterials, from separation to drug delivery [*Figuerola, 2010; Pankhurst, 2002*]. The primary application of superparamagnetic nanoparticles is undoubtedly as contrast agent for magnetic resonance imaging (MRI). Several SPIO and USPI are commercially available or in the latest phase of clinical trial

[*Qiao, 2009 a*]. The MRI signal is correlated to the magnetic relaxation of water proton after application of a magnetic field. The role of contrast agent is to create inhomogeneities in the magnetic field than translate in a change of protons relaxation. Practically, a first snapshot is taken prior to injecting the particles or other contrast agent. A second picture is acquire afterward and compared to the pre-contrast picture. SPIO and USPIO typically create a hyposignal, i.e. produce a very strong negative contrast on post-contrast MRI picture [*Nam, 2009*]. Gadolinium ions, a paramagnetic substance has be the principal contrast agent for MRI but raises some question about toxicity, but SPIO and USPIO offer the double advantage of a lower toxicity and higher saturation value that generates a stronger contrast on images.

The natural reaction to the injection or intrusion of particles is the recognition and clearance by macrophages that subsequently transport the foreign agents to the organs of the reticuloendothelial system (spleen, liver, bone marrow, nodes). Larger particles are quickly detected and cleared from the circulation to get mainly stocked in liver and spleen. Smaller are able to escape – temporarily – and remain for longer period in the organism, translocating and travelling into deeper tissues prior to being cleared up and gathered up in bone marrow and nodes. Through surface engineering and proper choice of particles size, iron oxides are able to target –actively or passively - specific tissues for MRI imaging. A common practice is to inject SPIO and larger particles that will accumulate in the liver and spleen preferentially. When the SPIO-loaded macrophages arrive in the reticuloendothelial system organs, they appear as dark areas due to the crystals effect, but tumours and other unhealthy areas are devoid of macrophage and are not subject to the particles effects. In consequence, a strong contrast establishes between the healthy and diseased tissues on MRI images. The same strategy was followed with USPIO to differentiate healthy nodes from tumoral ones [*Bellin, 2000; Semelka, 2001*]. Polymer coating and stabilisers have an impact on the potential tissues and organs that SPIO and USPIO are able to reach. For instance, silicon-coated particles have been employed to differentiate the gastrointestinal tract from its surrounding organs. Likewise, macrophage, stroke, atherosclerosis and a

certain other ailments-related changes have been imaged using SPIO and USPIO at several occasion [*Corrot, 2006*]. For more precise location, however, particles surface has to be modified for specific antigen recognition and hereby to prove more specific in their targeting. Active targeting originally involved engineering of the crystals to express antibodies at their surface; later on, peptides and small ligands have started to replace antibodies because of the large size of the latter, bringing iron oxide nanoparticles on the path of molecular imaging, enlarging the potential target not only to organs but to smaller, less attainable regions [*Corrot, 2006; Figuerola, 2010*]. This may be extended to the tracking of stem and transplanted cells to follow their evolution through time [*Elias, 2009*].

Active targeting is still prone to certain barriers, such as the necessity for the targeting ligand not to hamper the bioactivity of the magnetic crystals. Furthermore, size remains an important criterion for *in vivo* imaging since it not only the fate of the particles – although coating modulates the final reaction of the organism – but also the entry in smaller vessels or translocation through natural barrier such as the blood-brain barrier. Another challenge is to find nanomaterials with higher intrinsic magnetisation than SPIO or USPIO. With better magnetic properties, the dose of particles necessary to obtain similar – or better – contrast is lessened. Certain alloys start making their way as MRI agents but the question of their biocompatibility remained to be entirely solved. For example, Lee et *al*. doped the spinel structure of iron oxide with metals such as manganese, iron, cobalt, or chromium. Manganese-doped iron oxide had superior magnetic properties than all of their counterparts and the first cytotoxicity studies did not reveal toxicological effects [*Lee, 2007; Maenosono, 2008*].

1.3.4 Magnetic guidance and separation

A second important feature of iron oxide nanoparticles is magnetic guidance, i.e. the capacity to drag the particles directly to the sites of interests using an

external field or to separate species. The direct application of magnetic guidance is the delivery of drugs, gene (transfection), or other therapeutic agents right to the proper location. When current treatments such as chemotherapy rely on large dose of drugs delivered through the systemic circulation, affecting all cells on their track, magnetic guidance afford a more precise and sensitive approach and avoid the side-effects of drugs. A more specific delivery of drugs also means lesser doses since the majority of therapeutic molecules reach their dedicated target. The therapeutic is usually embedded into a polymer corona to be slowly released by change of temperature or pH, enzymatic clivage of the polymer chain or other biodegradation, or magnetically trigger. In principle, drugs-loaded particles are firstly injected to a patient, then dragged either throughout the whole process or via a magnet surgically implanted at the site of interest. The magnetic force that exerts on the particles will attract and concentrate them right into the proper location as schematised in the Figure 1-16 [*Dobson, 2006*].

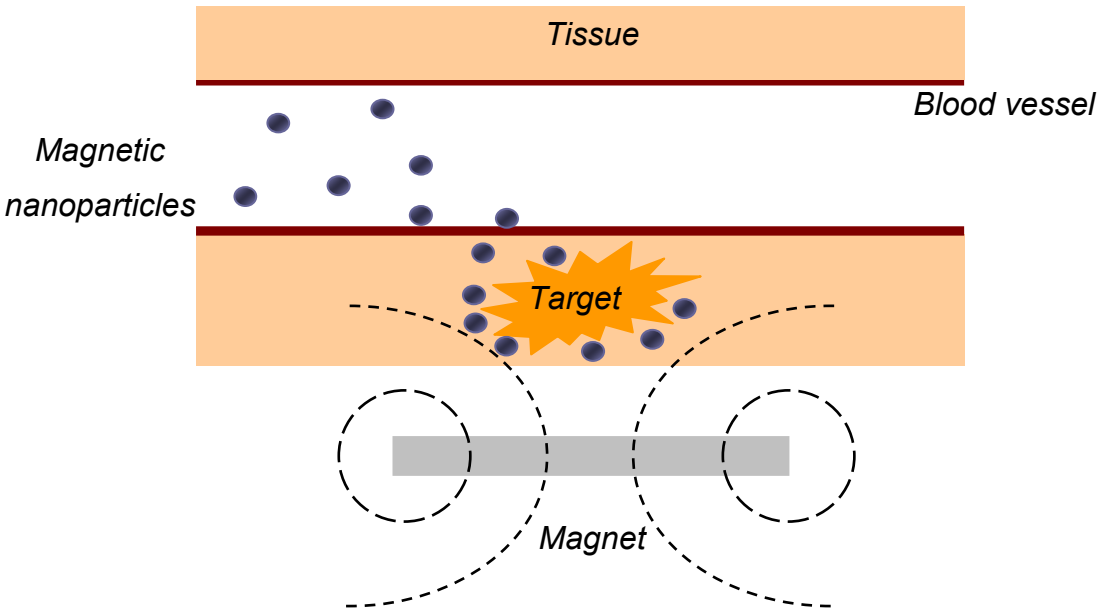

Figure 1-16: Schema of magnetic guidance of magnetic nanoparticles in blodd vessel as a mean to drag and concentrate the particles to a defined target.

In vivo application of magnetic guidance still faces obstacles. First of all, the magnetic field strength decreases quickly with distance. Penetration depth of the magnetic field of typical magnets is of few millimetres, although the distance has been augmented to 15 cm with neodymium iron boron magnets as well as via alteration of the geometry and duration of the external field. Yet, treatments may be more effective close to the surface or in areas with slow blood flow with average permanent magnet or low level of external magnetic field values. Alternatively, a magnet can be surgically placed in the tumours to treat deeper located lesions. Secondly, particles distribution is not focused in a small area and may accumulate in nearby tissues as well. In other terms, the field geometry is an important factor but its control is not as easy as with a laser. Thirdly, the accumulation of particles due to the close proximity of the external source may lead to embolisms as the particles agglomerates block the blood vessels, unless the blood flow is slow [*Arruebo, 2007; Neuberger, 2005*].

In spite of the apparent difficulties that magnetic guidance may be facing, drug-delivery via magnetic carrier is comparatively not new. In fact, microspheres made of albumin or biodegradable polymer such as poly (lactic acid), as well as liposomes may be loaded with magnetic particles to deliver. Attempts with nanoparticles are more recent and the first clinical trial dates from 1996, and although unsuccessful, revealed than more of 50% of the nanoparticles ended up in the liver. More recent attempts have been more promising and even successful, whilst at the same time drugs for other diseases or for inflammatory sites destination showed that cancer is not the only ailment that is treated, even though it is the focus of most studies. Rather than delivering biomolecules, magnetic nanoparticles may be used as a mean of separating species or cells, possibly in view of concentrating samples prior to analyses, in immunoassays and in other sensing tools [*Arruebo, 2007*]. The principle is that the magnetic nanoparticles label a particular biological entity and the complex is separated from its media by application of a magnet or any other external source. The strategy implies that the magnetic are bound to the proper markers beforehand similarly to an active targeting. Since *in vitro* conditions do not poise the same requirement in term of size, larger particles can be employed, although

superparamagnetic nanoparticles remain as valuable as ferro- or ferrimagnetic crystals and other magnetic microspheres. Similarly, the requirements on the external magnetic field are not as restrictive as in *in vivo* applications. In some case, a permanent magnet is placed along the wall of glassware and the supernatant is discarded. In some other cases, the media passes through a flow column to speed up the accumulation of magnetically retrieved species, in which case the magnetic gradient must prove stronger than the hydrodynamic force that the flow exerts on the particles.

1.3.5 Hyperthermia

Lastly, magnetic nanoparticles are also suitable thermal agents for hyperthermia treatment consisting in raising the temperature up to 42°C and maintaining it for 30 minutes or more. The specificity of hyperthermia lies in the higher sensitivity of cancerous cells compared to healthy one that are unaffected at the 42°C threshold. Although procedures exist to induce hyperthermia such as radiofrequency capacitance hyperthermia, whole body hyperthermia or injection of hot water *in situ*, none proved satisfactory and some even proved risky due to the damage of all tissues indistinctively. Yet, magnetic hyperthermia involves nanocrystals to target the right areas and to convert the energy of an alternative field into heat. In itself, magnetic hyperthermia is analogous to photothermal conversion of gold nanoparticles except for the physical mechanism responsible for the heat generation. The main difference with the previous applications of magnetic nanocrystals is the strength and frequency of the external field as it is necessary to send an alternative field to obtain the expected raise of temperature. The principal challenge is to define the proper magnetic fields conditions – in term of strength and frequency – that are clinically acceptable. Alternating magnetic field may end up in deleterious physiological effects such as muscles or cardiac stimulation or unwanted heating due to Eddy currents.

The mechanisms behind heat generation depend on the magnetic behaviours of the materials. In ferromagnetic materials, heat release occurs through hysteresis losses or losses during magnetisation reversal: part of the magnetic energy is lost during the hysteresis loop as the magnetic domains grow and re-orientate. The losses are proportional to the field frequency and the area of the hysteresis loop and take the form of heat. In monodomain crystals the losses proceed via rotational motion: the rotation may be of the particles themselves (Brownian rotation) or of the atomic magnetic moments within each particle (Néel relaxation) because of the torque exerted by the external field. The heat generation during Brownian rotation is due to the friction that creates between the particles and the surrounding media. Néel relaxation implies that the alternative field is able to overcome the magnetic anisotropy energy barrier in order to reverse the crystals magnetisation as can be seen in Figure 1-17. Typically, both Brown and Néel mechanisms are responsible for the raise of temperature that superparamagnetic nanoparticles generate [*Levy, 2008*].

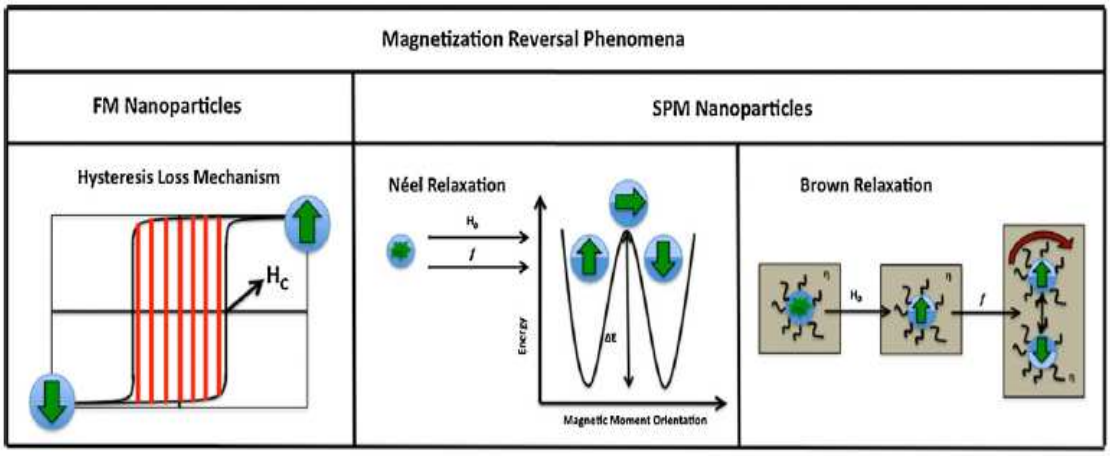

Figure 1-17: Origins of hyperthermia in ferromagnetic substance and in superparamagnetic nanoparticles [*Levy, 2008*].

For a long time, finding the proper parameters to the magnetic field hampered the clinical applications of magnetic hyperthermia since the conditions were not safe for patients. Nowadays, the treatment is underway as the first systems are

being clinically evaluated: Thiesen and Jordan have reported the feasibility of magnetic hyperthermia on prostate cancer in rats and later on used superparamagnetic iron oxide fluid to treat human patients suffering from glioblastoma multiforme and patients with recurrent prostate cancer [*Thiesen, 2008*]. Besides, an increasing number of studies suggest that the particles can be tracked by MRI before applying the alternative field so that the nanocrystals act as both a contrast and a thermal agent. The major drawback associated to magnetic hyperthermia is the potential overheating of tumours and heat propagation to the neighbouring tissues. Ferromagnetic particles may be made so that their Curie temperature, i.e. the temperature above which the particles become paramagnetic, equals 42°C or slightly above so self-regulating the maximal temperature attainable and avoid the risks of overheating. Yet, this strategy is not applicable to all materials and ferromagnetism is not entirely desirable for in vivo application due to the potential magnetically-induced aggregation of the particles.

1.4 Silica nanoparticles

1.4.1 Sol-gel process

Silica differs from other nanomaterials: where quantum dots are subject – as discussed later - to quantum confinement, gold nanoparticles possess plasmon resonance, and iron oxide reacts to magnetic field, silica nanoparticles do not exhibit any intrinsic property. Instead, silica is a highly robust matrix able to carry and protect various biomolecules, from drugs to fluorescence dyes and even other nanoparticles. The synthesis of silica nanoparticles is based on a sol-gel process, a versatile solution for the processing of ceramics and glasses at low temperature that produces a large variety of forms such as ultra-fine powders, coating, fibres, membranes, monolithic ceramics and glasses, extremely porous materials, or particles as represented in the Figure 1-18. Ceramics processed by sol-gel find applications in various fields such as photonics and electronics (laser elements, capacitor, transparent

semiconductors), energy (solar cells, electrolyte for fuel cell), materials (refractory ceramics, fibres, scratch-resistant coatings) or biomedical (implant coating, entrapment of enzyme) [*Dimitriev, 2008*].

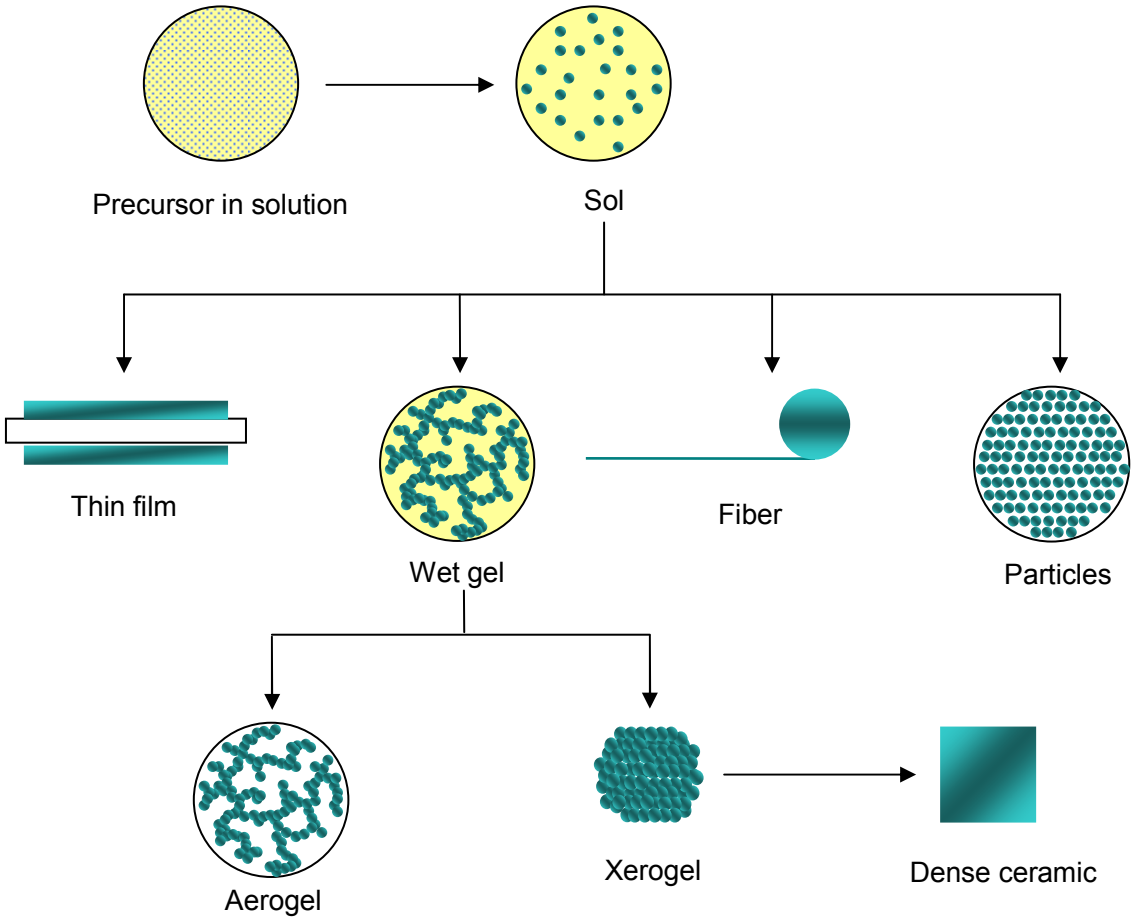

Figure 1-18: The sol-gel process allows the elaboration of material under various shape and form.

A sol-gel process requires precursors in solution that react with water and yield an oxide network through inorganic polymerisation. In a first time, precursors are hydrolysed and condense into oligomers of various degree of polymerisation to eventually evolve into a colloidal system (particles in suspension in a liquid) or “sol”. During the next step, particles coalesce and assemble into a single oxide network where some liquid is still present inside the pores or “gel” as schematised in the Figure 1-19 [*Celzard, 2002*]. Further

treatments include aging and drying to stabilise the structure as well as heating treatment and sintering to obtain more or less porous materials. Gelation, i.e. passage from precursors/sol to gel is not an absolute step and the sol may be stabilised to produce nano- or microparticles.

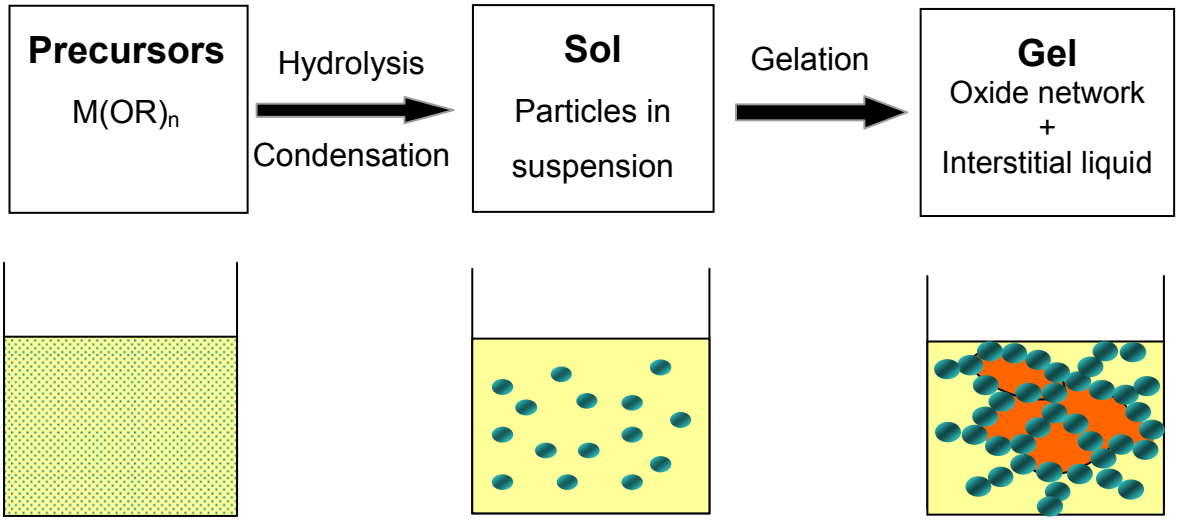

Figure 1-19: Schematic representation of a sol-gel process, with the transition from precursors in solution to particles (sol) and to an inorganic network (gel).

Typical precursors are metallo-organic compounds such as metallic alkoxides $M(OR)_n$, where M is a metal or metalloid (titanium, zirconium, aluminium, silicon, etc.) and R is an alkyl group (methyl CH_3, ethyl C_2H_5, etc.). Silica is one of the most studied metals of the sol-gel process, historically because it was the first system reported, but also because of the lower costs of its precursors and the greater flexibility of silica chemistry. Tetramethoxysilane (TMOS) $Si–(CH_3)_4$ and tetraethoxysilane (TEOS) $Si–(C_2H_5)_4$ are the most common silicon precursors. Besides, the introduction of organosilanes $Si(OR)_{4-x}R'_x$ (with x = 1 or 2 and R' is an organic group) has become more and more popular since organosilanes allow the formation of hybrid organic-inorganic systems, more flexible than pure silica network. Vinyltriethoxysilane, phenyltriethoxysilane or aminopropyltriethoxysilane are some examples of the precursors commonly employed that impart organic character to silica gels [*Schubert, 1995*].

Generally silicon alkoxides are not miscible in water and therefore require a co-solvent, mainly an alcohol, for the reactions to proceed.

Addition of water to the the precursor initiates the hydrolysis during which alkoxide groups are converted into hydroxyl:

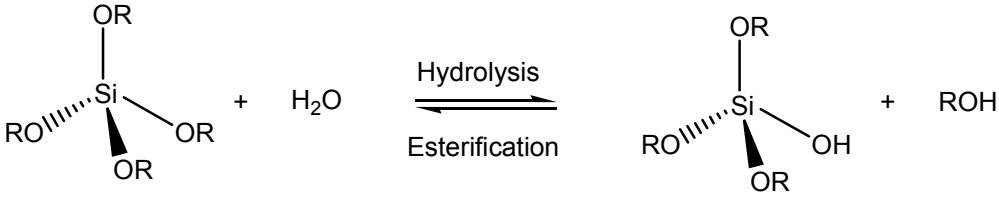

(1-13)

Then two partially hydrolysed molecules link together in a condensation reaction (polymerisation) by creating an oxo bridge M-O-M, or siloxane Si-O-Si for silica systems. The link occurs either through oxolation where two hydroxyl groups –OH react together and release water:

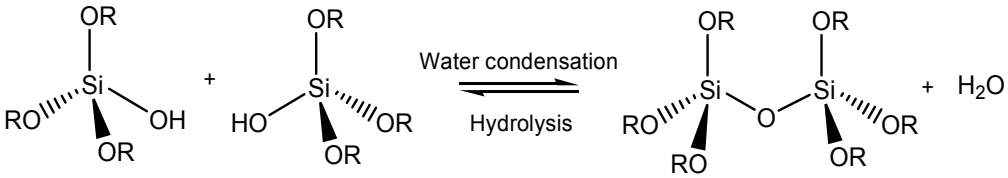

(1-14)

or through alcoxolation where a hydroxyl group –OH react with an alkoxide –OR and results in the release of alcohol:

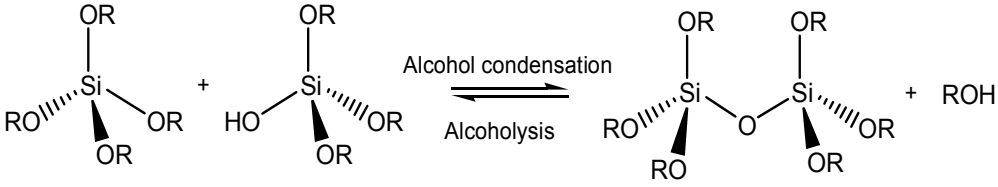

(1-15)

The presence of a catalyst is indispensable to initiate the process since silicon precursors react very slowly (if at all) with water under neutral conditions. Hydrochloric acid and ammonia are the typical catalysts, although fluorhydric and acetic acid and amines are sometimes employed. The choice of catalyst has a deep impact on the final morphology of sol and gel as highlighted in the Figure 1-20:

- In acid-catalysed conditions, particles aggregate before their growth so that the final network is mostly build from low density polymers and are poorly connected;

- In basic-catalysed conditions, precursors form either highly branched clusters that link one to the other or a colloidal system where particles coalesce and evolve towards a colloidal gel.

The difference of morphologies lies in the competition of hydrolysis and condensation as the two reactions are strongly affected by pH. Other parameters such as water-to-precursor molar ratio, temperature, and concentration of reagents influence the final structure although catalyst nature and concentration provides the most significant effects.

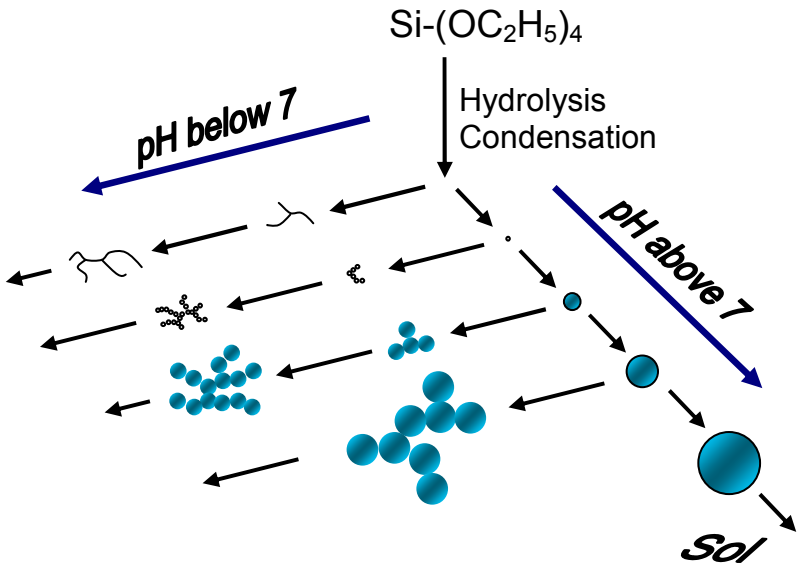

Figure 1-20: Influence of pH on the final structure of gels [Brinker, 1990].

Hydrolysis is acid- or base-catalysed and it is generally admitted that it proceeds by bimolecular nucleophilic substitution (S_N2 reaction) where the electron-rich oxygen of water (nucleophilic) attacks the electron-poor silicon atom (electrophilic) and replaces an alkoxide group (leaving group). Under acidic conditions an alkoxide group is protonated in a rapid first step. The

protonated alkoxide withdraws electron density from silicon and therefore renders it more electrophilic. As a result a water molecule attacks silicon whereas the protonated alkoxide group leaves the coordinate:

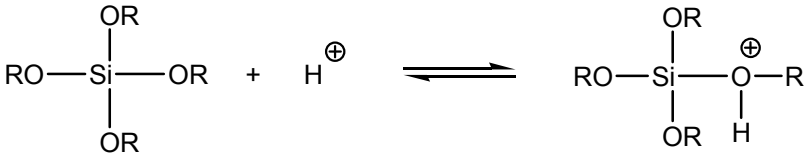

(1-16)

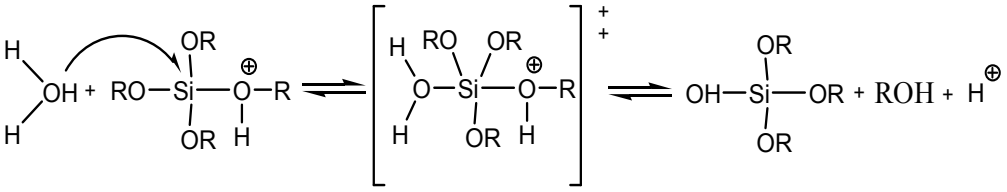

(1-17)

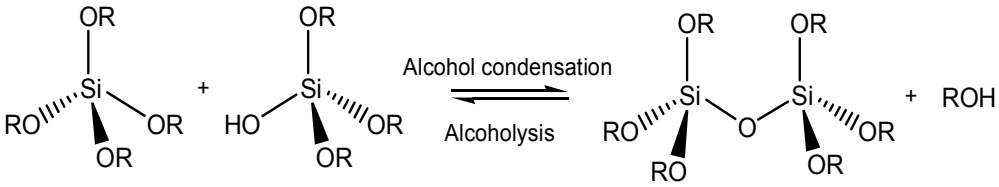

(1-18)

Under basic conditions, however, a hydroxyl anion directly attacks the silicon atom and induces the departure of an alkoxide group:

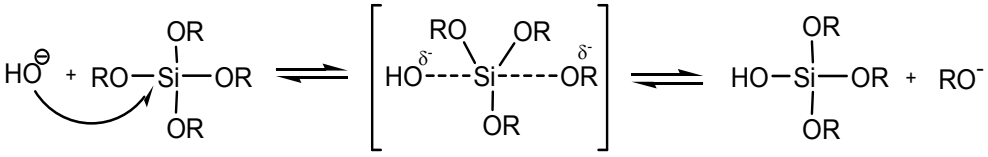

(1-19)

Condensation leads to the formation of siloxane bonds Si–O–Si. The reaction occurs through attack of a silanol group on a silicon atom with expulsion of water or of alcohol. Under acidic conditions, mechanism involves the formation of protonated silanols similarly to acid-catalysed hydrolysis. Consequently the silicon atom becomes more electrophilic and more prone to nucleophilic attack. Protonated species react and connect with neutral ones, either through siloxane bonds with either formation of water or alcohol:

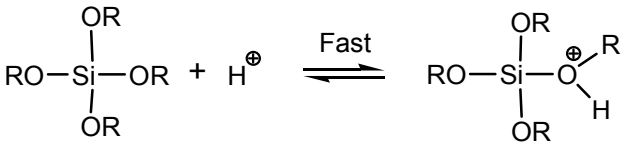

(1-20)

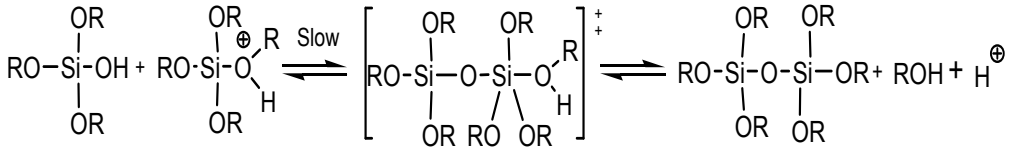

(1-21)

Above pH 2-4.5, an alkoxide is deprotonated and the resulting silanol (nucleophilic) attacks a neutral species following a nucleophilic substitution reaction:

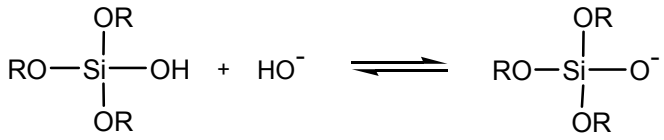

(1-22)

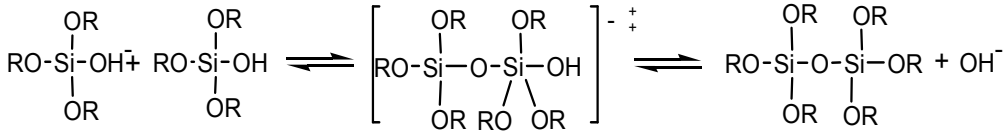

(1-23)

Hydrolysis and condensation are concomitant. Furthermore the rate of the two reactions is very sensitive to pH and to the steric and electronic environments that result from each step of hydrolysis and condensation. The substitution of alkoxide groups with hydroxyl and siloxane modifies the electronic environment of the silicon atom and creates steric hindrance. Hydroxyl, silanol and siloxane change the acidity of silicon and consequently influence the nucleophilic attack on silicon as can be seen in Figure 1-21.

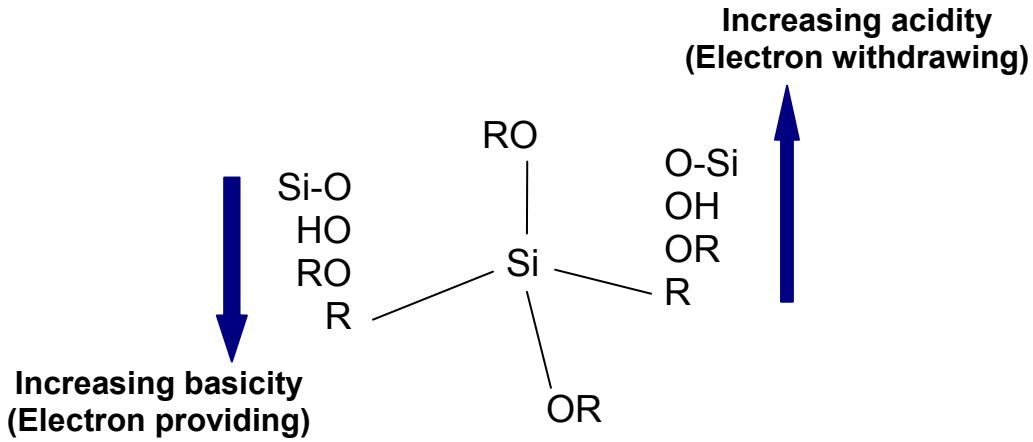

Figure 1-21: Inductive effects of substituents attached to silicon [Brinker, 1990].

In acid conditions, transition states positively charged are favoured by electrodonnor substituents such as alkoxides. However the hydroxyl groups that form during hydrolysis are less electrodonnor than the alkoxide –OR groups so that the hydrolysis rate decreases with each new hydrolysis step. Similarly siloxane groups O–Si are electron withdrawing and cause more steric hindrance than hydroxyls so that condensation rate is even slower. Consequently, in acid conditions, hydrolysis usually ends up before condensation starts and the polymers are mainly long extended chains weakly branched.

Inversely, in basic conditions, hydroxyl anions attack on the silicon atom: Electron withdrawing groups such as –OH and –O–Si favour the nucleophilic attack. As hydrolysis proceeds, more hydroxyl groups replace the initial alkoxide so that hydrolysis rate increases with each subsequent step. Similarly formation of siloxane bonds increases the condensation rate and proceeds at the same speed than hydrolysis. The resulting polymers are compact and highly reticulated.

1.4.2 Stöber method and particle synthesis

The gelation process is blocked under certain environmental conditions to produce spherical particles of various dimensions. The principal method of production of silica nano- and microparticles was developed in 1968 by Stöber and Fink [*Stöber, 1968*]. Their method involves the hydrolysis and condensation of TEOS in a water-alcohol mixture under basic conditions, typically catalysed by ammonium hydroxide NH_4OH:

$$Si(OC_2H_5)_4 + 4\ H_2O \rightarrow Si(OH)_4 + 4\ C_2H_5OH \quad \textbf{(1-24)}$$

$$Si(OH)_4 \rightarrow SiO_2 + 2\ H_2O \quad \textbf{(1-25)}$$

According to the two reactions, 4 moles of water are necessary to hydrolyse TEOS or 2 moles when condensation goes to completion. Practically, however, the water content in Stöber method ranges from 7 to 53 whereas pH is kept

high by the employ of ammonium hydroxide. These conditions promote the TEOS condensation and the formation of dense spherical nanoparticles over polymeric networks and gels. Gelation does not occur because of the negative charges at the surface of the particles that repulse the spheres. The size of submicroparticles depends principally on the water content and catalyst type and concentration but Stöber method covers sizes ranging from few tens of nanometres up to a micrometer as can be seen in the Figure 1-22.

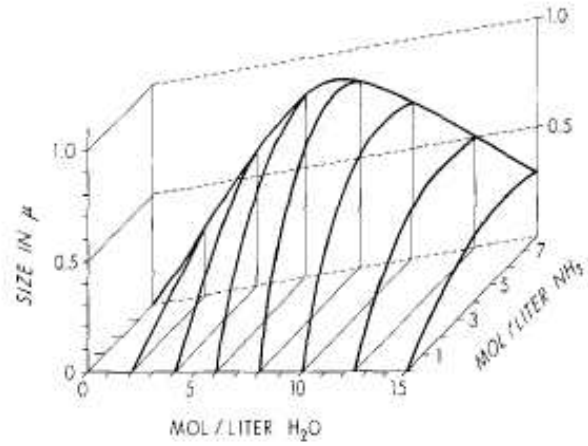

Figure 1-22: Variation of water on TEOS ratio and catalyst concentration control the final size of nanoparticles [Stöber, 1968].

The Stöber method was further developed and the influence of various parameters, including reagents concentration, temperature, solvent, or addition rate, was investigated. However, effects of these parameters are difficult to isolate and are usually interdependent, albeit certain trends emerge [*Park, 2002; Rao, 2005*]:

- Nature of precursor: the change of alkoxide group modifies the hydrolysis and condensation rate of the silane. For example rates of tetramethoxysilane are ten times faster than that of TEOS. More generally increasing the alkyl chain length of the alkoxide groups increases the reactions rates;

- Concentration of precursor: studies on the silane concentration effect indicate an increase of the particles size with increased concentration. Nevertheless, the effect is strongly related to the water content and invert effect may also occur according to the domains of reagent concentration;

- Nature of solvent: generally solvent is of the same nature than the alkoxide so that no transesterification occurs. The effect remains obscure although reactions rates seem faster in the most polar solvent;

- Effect of catalyst: ammonia and ammonium hydroxide are typical catalysts in the Stöber method. They promote the condensation reaction and the formation of spherical, regular particles. Similarly to the precursor concentration, results on the effect of catalyst concentration are often contradictory from one study to the other and depend on the range of reagent concentration. Other catalysts such as rginine and lysine have been investigated and yield smaller and more uniform particles than ammonia-catalysed particles;

- Effect of temperature: studies tally on a reduction of particles size with increase of temperature. Authors suggest that higher temperature yields more nuclei and lead to the formation of more numerous but smaller particles than in room temperature;

- Effect of water to Si ratio *(r)*: results are contradictory with some studies observing a decrease of the size as *r* increases whereas other found the opposite.

Although the Stöber method has been refined since its report, the principal drawback lies in the relative polydispersity of particles below 100 nm. Besides, the negative charge of silica particles is generally not sufficient to totally prevent aggregation or is not reactive enough so that an additional layer of organosilane is necessary to satisfactorily disperse the spheres or allow bio-conjugation. Nevertheless the procedure is an easy, flexible, and inexpensive way to

produce silica particles. A new solution referred to as amino acid catalysis and consisting in replacing ammonium hydroxide by amino acid to catalyse hydrolysis and condensation reaction has recently been proposed [*Yokoi, 2006*]. Among other advantages, this method offers the possibility to dramatically decrease the particle diameter to a few tens of nanometer and make the whole process cleaner by operating in milder conditions.

Reverse microemulsion is the second route to produce silica nanoparticles and circumvent the problem of size and size dispersity [*Yamauchi, 1989*]. Micelles encapsulate water and ammonium hydroxide so that hydrolysis and condensation proceed inside the nanodroplets as TEOS molecules become progressively soluble in the water pools. Through micelles collision, the micelles exchange their content and allow the sol-gel reaction to occur. Furthermore, the cavity of the micelles confine the particles grow and therefore a high monodispersity is achieved [*Bagwe, 2004*]. The size and shape of micelles, and by extension of particles, are controlled by varying the parameters of the microemulsion: molar ratio of water to surfactant, nature of surfactant, and concentration of reactants.

In order for hydrolysis to take place, TEOS molecules have to diffuse from the surrounding organic phase into the micelles and the water pools. After addition of TEOS to the system, the molecules get partitioned between droplets and organic phase by formation of monomers with one silanol group ($Si(OR)_3OH$). Further, hydrolysis renders monomers more hydrophilic, and they eventually solubilise entirely inside the water nanodroplets. Since ammonium hydroxide is already present inside the micelle, nucleation proceeds [*Arriagada, 1999 a and b*]. The rate of hydrolysis and nucleation strongly depend on the water on surfactant ratio (R): at low R value, many small micelles are present in the oil phase. The water molecules are mostly bound to the surfactant and cannot react with the few TEOS molecules around the micelles. Since the water concentration is very small, hydrolysis and condensation are not favoured. On the contrary, at high R values many TEOS are present in the micelles while the water pool is big enough to favour the hydrolysis of silane molecules and initiate

the nucleation. In consequence, reverse microemulsion requires relatively high water on surfactant ratio and high concentration of reagents to promote small nanoparticles. The employ of surfactant is also the mean by which mesoporous nanoparticles are produced. This role is principally attributed to hexadecyltrimethylammonium bromide (CTAB), the same surfactant required in the synthesis of gold nanorods and some other nanoparticles with specific shape or porosity [*Qiao, 2009 b*].

1.4.3 Fluorescent silica nanoparticles (FSNPs)

The principal interest of silica nanoparticles is their insensitivity to environmental changes: high variations of temperature or pH do not degrade the silica matrix, a property that makes of silica particles a carrier of choice for many biomolecules and occasionally to transport drugs. More precisely, drug delivery is mostly devoid to mesoporous structures, which controlled porosity is more favourable to the slow release of compounds. Denser architectures are more suited to biomolecules that need to be sequestered. Although quantum dots are highly promising fluorescent probes, fluorescent dyes remain the principal agent for most fluorescent-based technology. Fluorescent dyes – or fluorophores – are molecules able to absorb light at specific wavelengths and reemit it at longer wavelengths under a process called fluorescence. They have a long history – dating from the late 1800s – and were initially introduced in fluorescent microscopy, although their extensive use is more recent [*Prasad, 2003*]. Typical dyes emit in the UV or visible, but new fluorophores emitting in the near-infrared or in the infrared have been elaborated since then. In parallel, contrast agents for multiphoton microscopy have attracted attention and provide new possibilities for the bio-imaging science [*Frangioni, 2003; Wu, 1999*]. Other dyes exhibiting new physico-chemical properties were later discovered, generating heat, reacting to other stimuli than light (temperature, pH, etc.) or inducing chemical reaction with their environment. For instance, photosensitisers employed in photodynamic therapy generate singlet oxygen when illuminated

with the proper light wavelength and are potential therapeutic agents for the treatment of cancer, skin diseases and some other ailments [*Pervaiz, 2006; Unger, 2004*]. Fluorophores suffer from photobleaching, i.e. a loss of fluorescence with time principally because of photo-oxidation. Photobleaching is a fast process that binds fluorophores to a few minutes illumination at best. Although this side-effect has not hampered the development of fluorescent dyes, the possibility of circumventing this problem and proceeding for longer period of time is desirable. Furthermore, many dyes such as near-infrared and multiphoton dyes are hydrophobic and aggregate in many physiological media, losing their optical properties. Encapsulating dyes within a carrier offers a solution to insulate and then to protect the dyes from their environment while gathering thousands of molecules into a single sphere for more intense signal. Contrary to polystyrene and latex microparticles are generally polydisperse, and swell or dissolve in certain solvent, silica is more robust and entirely shields the dye from their environment. Moreover, the large variety of organosilane is ideal to express functional groups necessary to the surface engineering of nanoparticles.

Dyes can be covalently or physically entrapped within the silica particles depending on the synthesis route and nature of the fluorophores. The major contribution to dye-doped nanoparticles is undoubtedly that of van Blaaderen that is a variation of the Stöber method where fluorescein isothiocyanate (FITC) was conjugated to an organosilane so that the sylilated dye was able to be covalently bound to the silica network of the particles [*van Blaaderen, 1992 c*]. The advantage of this approach is the covalent link between the dye and the silica matrix that prevents any leakage whilst the high number of fluorescent molecules per particle considerably increases the signal of each particle and considerably reduces the photobleaching issue [*Santra, 2006*]. Similar results were obtained few years later with rhodamine isothiocyanate and were later extended to maleimide-derivative rhodamines and even to near-infrared dyes; the common point is the necessity to firstly conjugate the fluorophores with an organosilane in order for the complex to co-condense with TEOS as schematised in the Figure 1-23 [*Verhaegh, 1994*].

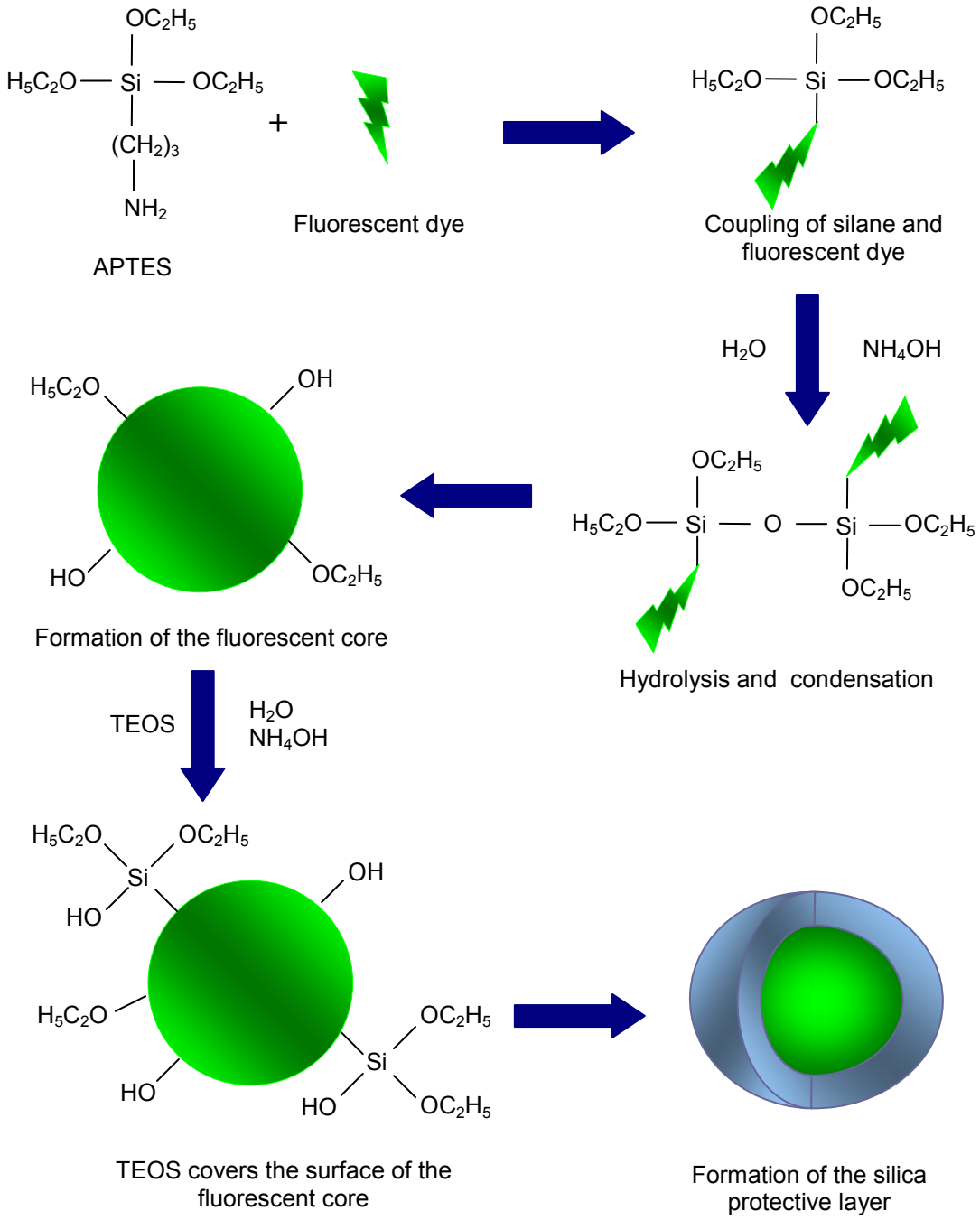

Figure 1-23: Preparation of fluorescent dye-doped silica nanoparticle via van Blaaderen's procedure where a fluorophore is covalently bound to an organosilane and get integrated to the silica nanoparticle.

Physical entrapment consists in simply introducing the fluorophore during the growth of the particles. The network retains fluorophores through electrostatic

interactions and affinity with the hydrophilic silica matrix, although the weak interactions between dyes and matrix may result in leaking out of the nanoparticles and a loss of fluorescence with time. The method is sometimes found with the Stöber method but is mostly involved with reverse microemulsion. To entrap lanthanide chelates. The main limitation is the preference of organic dyes for the oil phase rather than the water pools and reverse microemulsion usually fails in entrapping organic fluorophores. The solution consists in either proceeding with a normal oil-in-water emulsion or choosing inorganic dyes, typically lanthanide chelates such as Tris(2,2'-bipyridyl) dichlororuthenium (II) hexahydrate (RuBpy) and Tris (2,2'-bipyridyl) osmium (II) bis (hexafluorophosphate) (OsBpy) or europium complexes, that are highly hydrophilic and penetrate within the micelles [*Bagwe, 2004; Jiang, 2010; Wang, 2005 b*].

1.4.4 Applications

In respect to the traditional application of fluorescent dyes, fluorescent silica nanoparticles (FSNPs) have proved their worth as contrast agents in optical imaging. Rhodamine-loaded FSNPs have been employed to label many type of cancer types including oral, lung, cervix, liver or breast using proper ligand such as folic acid to recognise overexpressed antigen specific to each cell line [*Santra, 2005 a; Shi, 2010*]. Silica particles were also employed as a substitute to quantum dots and magnetic particles to image sentinel lymph node *in vivo* in mice [*Jeon, 2010*]. Yet, most common fluorescent dyes emit in the visible range and their signal is hampered by the autofluorescence of tissues and the low depth penetration of visible light (a few millimetres at best). Progressively, near-infrared and two-photon dyes were loaded into the silica matrix and the particles become more suited for scattering and thicker samples [*Ohulchanskyy, 2010, Yao, 2006*]. In particular, the C-dots are an improvement to van Blaaderen's FITC-doped particles with a considerably reduced size of 20 to 30 nm that have been engineered to contain various near-infrared dyes and obtained promising

results as contrast agent for live imaging in mice [*Burns, 2009*]. Likewise, the same strategy has been followed with photosensitisers in order to impart more specificity to photodynamic treatment. The specific targeting that silica nanoparticles obviate the risks of systemic distribution of the drug into the whole organism and the retention time during which patients are light-sensitive (including daylight) and that is source of severe burning due to the improper activation of the photosensitisers [*Ohulchanskyy , 2007; Roy, 2003*].

Organosilanes are able to condense onto silica surface by reaction with free silanol and is a very versatile way to modify the surface of FSNPs with a great variety of chemical functions that can in turn be used as an anchor for targeting ligands. Coupled to their high brightness, silica nanoparticles are especially powerful as a replacement to fluorescent dyes in assays and methods relying on fluorescence. Using FSNPs in immunoassays has become a standard procedure, for example in the detection of hepatitis B surface antigens with an ELISA assay but also in the detection of bacteria and other pathogens [*Yan, 2007, Yang, 2004, Zhao, 2004 a*]. The use of FSNPs entrapping different dyes engineered to recognise a specific analyte is one way to achieve multiplexed system, although they lag behind quantum dots and their narrower emission peaks [*Knopp, 2009*]. Similarly, FSNPs are used in the detection of DNA or RNA for gene expression or profiling and for procedure requiring the hybridisation of nucleic acid [*Tan, 2004*]. For instance, Zhao et *al*. designed an assay where a first DNA strand was immobilised onto a glass surface and a second sequence was conjugated to FSNPs in order to capture a third target sequence complementary to the first two strands as can be seen in the Figure 1-24 [*Piao, 2008; Zhao, 2003*]. Therefore, FSNPs have a high potential in sensing and diagnostics and provide a solution to the photobleaching of dyes and to the low sensitivity of certain assays relying on fluorophores.

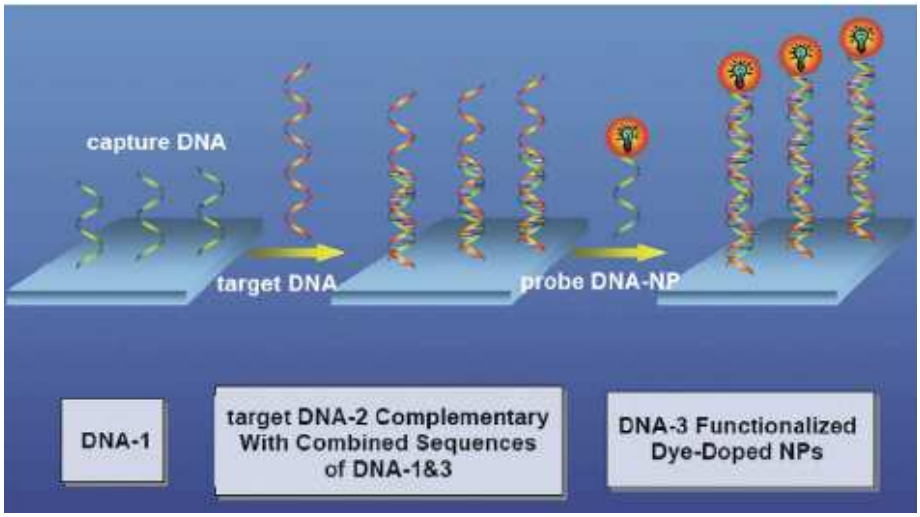

Figure 1-24: Schema of a DNA assays where DNA-conjugated FSNPs are used for the recognition of DNA [Yan, 2007].

1.4.5 Multifunctional nanoparticles

Taken separately, all of these particles belong to the "first generation" of particles, structures exhibiting one or two characteristics but with restricted possibilities. With better control over the synthesis and physico-chemical properties of nanomaterials, particles have evolved to the "second generation" where nanostructures are – ideally – able to react accordingly to the environmental conditions. In a first time, the objective behind combining nanomaterials was to solve certain issues that individual nanoparticles face. An example is the coating of quantum dots with silica in order to improve the stability of the semiconductor nanocrystals and confine them within a resistant shell to limit the risk of degradation and resulting leakage of heavy metal leakage [*Koole, 2008*]. Similarly, depositing a first silica layer onto gold or silver particles completed by a second layer entrapping fluorescent dye is theoretically the best way to benefit from the metal enhanced fluorescence effect. In fact, the first attempts saw the creation of nanocomposites where the nanoparticles made of iron oxide, noble metal and other materials were integrated within a silica matrix for protection, stabilisation, and/or functionalisation purpose. In

parallel, bi- or multimodal architectures that fulfil multiple tasks have elicited more and more interest. For example combining the fluorescence or plasmonic imaging of quantum dots and other gold nanoparticles with the effect of iron oxide nanocrystals on magnetic resonance imaging has become popular. Step by step, the idea of combining nanomaterials into theragnostics agents, i.e. structures similar to the Figure 1-25 with dual imaging and therapeutic applications, has progressed. In a sense, multifunctional platforms are closer to the ideas lying behind the concept of second generation of nano-objects, being more flexible than the first nanocomposites developed. A typical multifunctional system is able:

- To detect a specific target via surface modification;
- To be magnetically or optically driven by an external source;
- To reveal its location by fluorescence, photothermal, magnetic or any other imaging mean;
- To deliver drugs, gene or to elicit therapeutic effects such as hyperthermia or photothermal ablation;
- To follow in real-time the changes occurring during the therapeutic phase;
- To be cleared without harmful effect for the organism.

Silica is the most popular matrix to link all components altogether due to the uniform size and versatility of its chemistry, low cost, ease of bio-functionalisation, and low toxicity. As reviewed, silica is a host of choice for fluorescent dyes but also to other nanoparticles, assembled into a core-shells structure [*Klichko, 2009; Piao, 2008*]. Iron oxide nanoparticles play a key role in the multifunctional architectures and have been including within the silica matrix at length. The choice other components depends on the modalities and purpose of the nanoplatform, with a large preference for gold - frequently under the form

of a final shell – and at lesser extent of quantum dots for optical imaging. Gene and drug delivery are generally entrusted to mesoporous particles but the change of porosity is not an issue and other nanoparticles have been integrated to this slightly different matrix. For instance, Liong et al. engineered a multifunctional mesoporous silica nanoparticle to confine iron oxide nanoparticles for magnetic guidance and MRI imaging, incorporating FITC covalently bound to the silica network for optical imaging, and loaded with Paclitaxel (anticancer drug), the whole targeting cancer cells via folic acid conjugation [*Liong, 2008*].

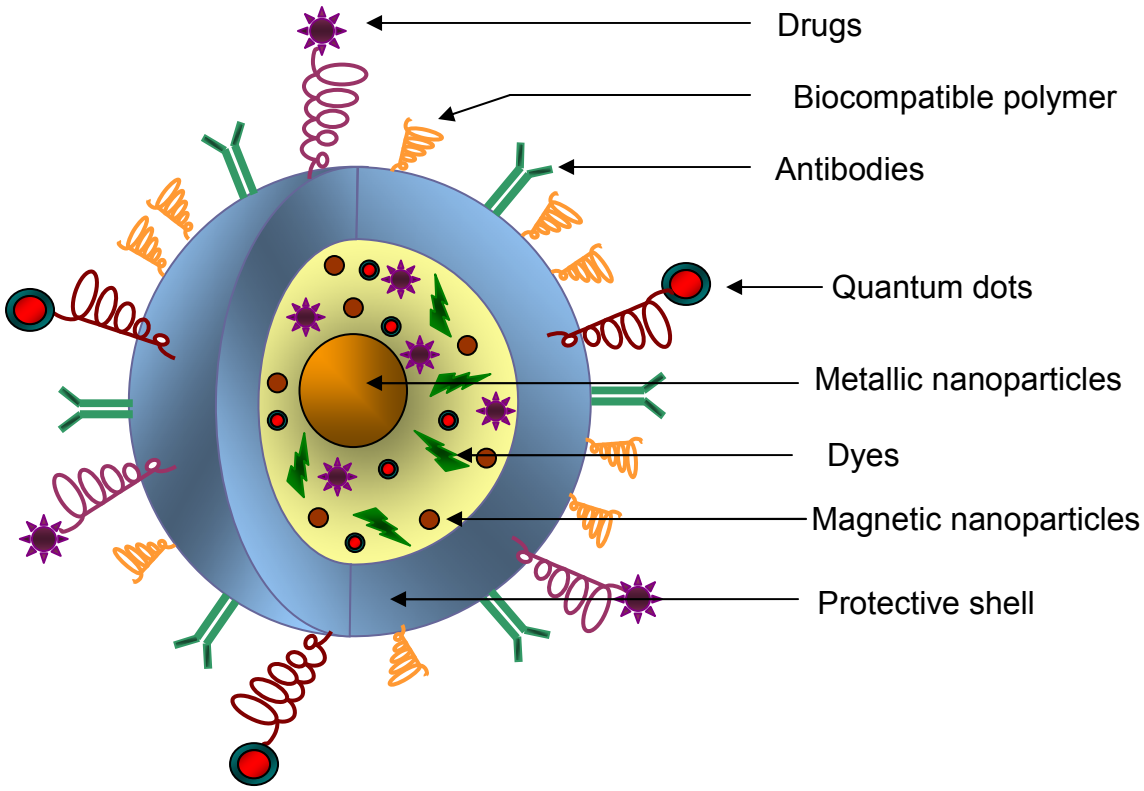

Figure 1-25: Representation of a multifunctional platform made of the combination of several nanomaterials and biomolecules.

1.5 Quantum dots

1.5.1 Composition and origin of fluorescence

Quantum dots are newer that the other nanomaterials introduced so far. They consist in semiconductor nanocrystals 1 to 10 nm in size possessing unique optical and electrical properties and are potential candidates for solar cells, electronics, as well as in certain biomedical applications. The distinctive feature of quantum dots lies in their size-dependent emission, i.e. the light the particles emit is directly related to the size (and composition) of the crystals, and range approximately from 400 nm to 2 µm [*Seydel, 2003; Walling, 2009*]. Quantum dots usually have core-shell architecture: the core is made of semiconductors from groups II-VI, IV-VI, or III-V, in particular cadmium selenide CdSe, cadmium sulphide CdS, indium arsenide InAs, and indium phosphide InP are the most widespread materials. The shell is also composed of semiconductor with higher bandgap energy such as zinc sulphide ZnS or zinc selenide ZnSe.

The quantum dots properties stem from their core: it is the bandgap energy, i.e. the difference of energy between the lowest level of the conduction band and the highest level of the valence band that controls the emission of the nanoparticles. The material must firstly absorb a photon with sufficient energy to promote an electron from the valence band to the conduction band, with creation of an exciton (electron-hole pair) during the process as represented in the Figure 1-26. The electron stays momentarily in the conduction band and falls back to its origin, firstly falling down to the bottom of the conduction band then relaxing to the valence band. During the transition, a photon with energy equivalent to the bandgap energy is emitted and the electron recombines with its corresponding hole.

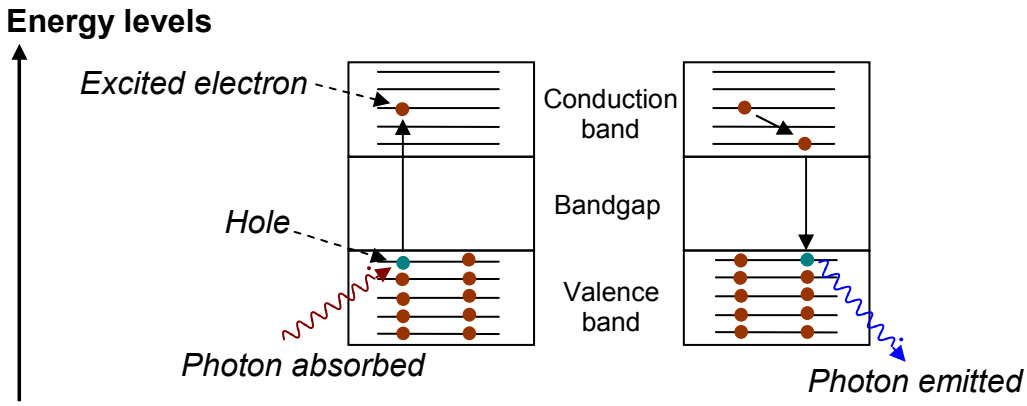

Figure 1-26: Mechanisms of absorption and emission of a photon in a semiconductor

The bandgap energy of quantum dots is directly correlated to the size and composition of the material with the consequence that the semiconductor emission is totally tunable. The bandgap tunability is linked to the quantum confinement effects –confinement of electrons and holes in semiconductors by a potential well - occurring in semiconductor nanoparticles. This effect occurs when the size of particles becomes smaller than the electron-hole distance in an exciton (Bohr's radius) that might be formed in a bulk semiconductor. Under the Bohr's radius, the energy levels of nanoparticles cannot be treated as continuous anymore but must be treated as discrete levels instead as schematised in the Figure 1-27. Because the energy levels are discrete, a change of atoms in the structure has deeper repercussions, for instance altering the bandgap energy [*Alivisatos, 1996*]. Typically, smaller particles generally exhibit higher bandgap energy and are blue-shifted compared to bigger particles or to bulk materials. The shell role is to passivate the core: the bandgap energy of ZnSe and ZnS is chosen very high to ensure that the excitation and emission originate from the core exclusively. The role of the shell is also to increase the photoluminescence of the nanoparticles and to limit or suppress the phenomenon of "blinking" - intermittent switching off and on of the particles - quantum dots suffer from and is an important issue for real-time processes.

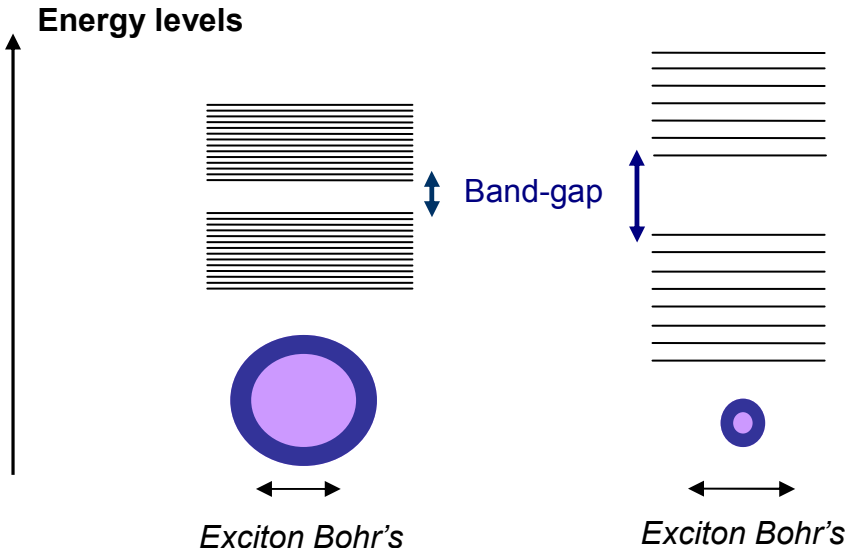

Figure 1-27: At the difference of bulk material, the energy level of semiconductor quantum dots must be considered as discrete when their size falls below the Bohr's radius.

The fluorescence properties of quantum dots are superior to that of fluorescent dyes on several points. First of all, semiconductor nanocrystals are not prone to photobleaching or photodegradation and can be imaged over extended period of time without loss of fluorescence. In addition, the luminescence of quantum dots is more intense and the emission profile is narrower and entirely tunable. Finally, a single UV source is sufficient to excite a quantum dots solution and even an array of quantum dots.

1.5.2 Reverse microemulsion

A common synthetic route of quantum dots involves the mixing of heavy metal salts in high temperature solvents that act as both reacting media and capping agents for limiting the growth of particles. However, reverse microemulsion is the preferred approach [*Foglia, 2001; Pileni, 1993*]: a reverse micellar system is composed of water and oil (organic solvent) that are naturally immiscible.

Surfactant is added to the system at a concentration where it assembles into aggregate - or micelles - at the water/oil interface. In an oil-in-water microemulsion, the hydrophobic tail forms a core where oil is encapsulated, whereas the hydrophilic head stretch outside to remain in contact with water. Structure is inverted in a water-in-oil microemulsion, with hydrophilic heads forming the core of micelles and tails in contact with the exterior oil phase as exemplified in the Figure 1-28.

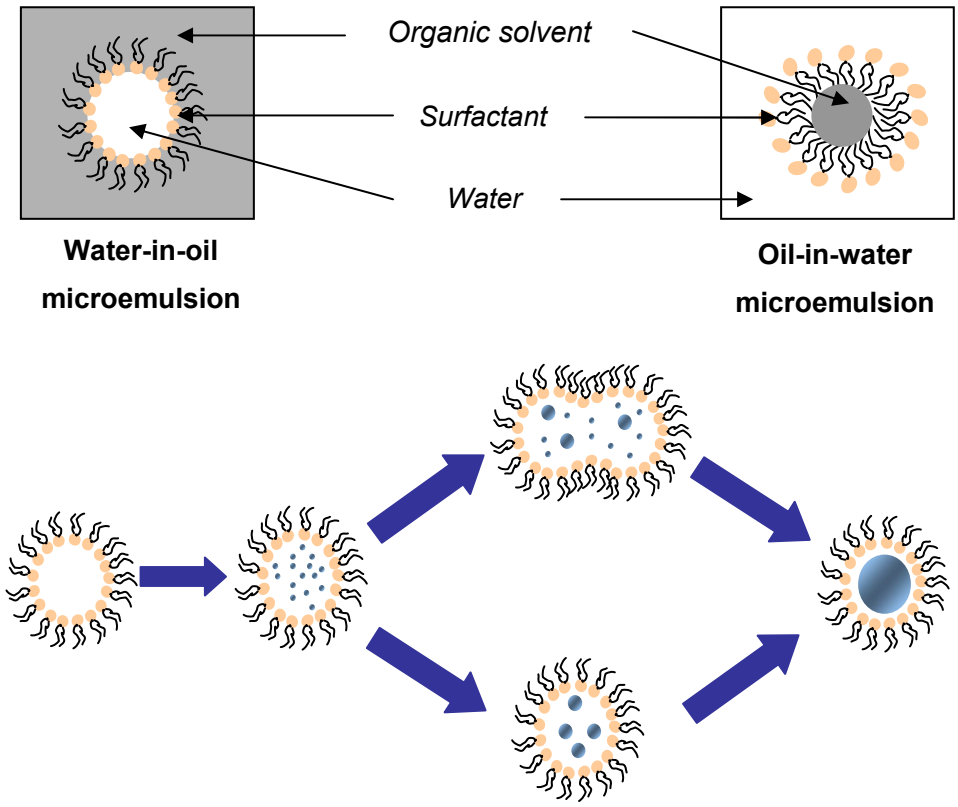

Figure 1-28: Water-in-oil and oil-in-water emulsions and schematisation of the micelle collision resulting in the growth of nanoparticles.

The preparation of nanoparticles requires that the salts used as precursors solubilise within the micelles. The reactions proceed during the collisions between the droplets, where the micelles exchange their content and progressively form the nanoparticles. Additionally, microemulsions confine the synthesis within the cavity of the micelles so that the growth of the particles is mechanically limited by the dimension of the cavity. The reverse microemulsion

approach is common to many nanomaterials and may be modified into an oil-in-water emulsion when the precursors and reagents are hydrophobic. Surface modification with capping ligand and polymer coatings render the particles soluble in water and polar solvents whilst conjugation with aptamers, antibodies, or peptides provides a mean for more specific targeting and help in increasing the biocompatibility of the quantum dots.

1.5.3 Imaging

The strong fluorescence of quantum dots is an undeniable advantage in bio-imaging, in particular because the nanocrystals are able to emit light in the near-infrared [*Gao, 2004*]. Since UV lamps are the best sources of excitation, quantum dots are interesting contrast agents for normal epifluorescence microscopy. Usual laser sources of confocal microscope - 488, 514, 543, and 633 nm - are less optimal, although confocal microscope can be upgraded with blue diode and UV laser sources. On the other hand, multiphoton excitation microscopy, whose features are discussed below, benefits more from the employ of quantum dots due to the high 2-photon absorption cross-section of the semiconductor nanoparticles [*Deerinck, 2003; Larson, 2003*]. Therefore, several studies focused on the labelling of cells and their subsequent imaging and an important in vivo study already show the potential for imaging in small animals. For instance, Maysinger et al. injected quantum dots in mice and observed a peak of fluorescence after three days and the signal persisted up to seven days [*Maysinger, 2007*]. In particular, the article demonstrated that QD 705 (emission 705 nm) injected in the brain cortex were visualised through the skull that otherwise screened the signal of fluorescent agents emitting in the ultraviolet and visible range. The long wavelength emission of quantum dots is particularly helpful for the tracking of nanoparticles in blood and to determine their fate after injection [*Jiang, 2008; Tada, 2007 a*]. However, the limited penetration of depth mark quantum dots out for skin or superficial targets that can be accessed by enodscopy [*Jiang, 2008*]. In fact, quantum are slowly

getting their way in surgery where surgeon use quantum dots to better visualise lesions and not letting damaged tissues non-operated [*te Velde, 2010*].

The capacity of imaging multiple populations of quantum dots with a single source has often been point up: for instance, Kobayashi and co-workers used multicolour imaging - five quantum dots types with distinct emission profiles –to study the lymphatic drainage in the neck and upper trunk after injection of the quantum dots in various sites as can be seen in the Figure 1-29 [*Chan, 2002; Kobayashi, 2007*]. The study is a good example of the advantage of colour-coding to detect multiple targets simultaneously. Such example of imaging of multiple location in one go have multiplied and are not limited to organs but also to the imaging of organelles within single cells so long as the surface of the nanoparticles is designed to bind to the proper markers [*Chan, 2002; Yezhelyev, 2007*].

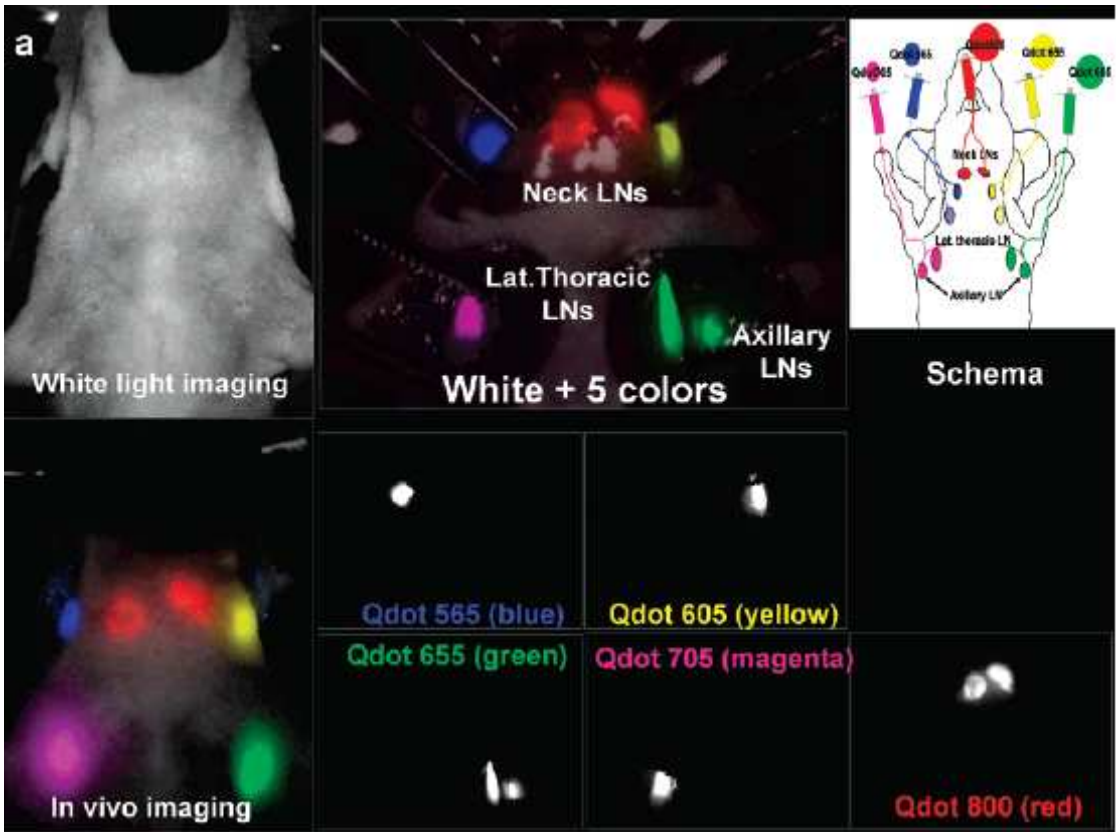

Figure 1-29: *In vivo* imaging distinctive lymphatic drainages injected with five carboxyl-modified quantum dots colours [Kobayashi, 2007].

1.5.4 Diagnostics and microbeads

Quantum dots are likewise powerful assets for the sensing of very small concentrations – picomolar to attomolar range – of proteins and other analytes [*Wagner, 2007*]. Quantum dots have been employed in fluorescence-based assays to detect changes in biomarker expression that may translate a differentiation into diseased cells. Yet, such markers are generally present at very low concentration in saliva, urine, or other fluids tested and require very sensitive assays to be detected. Quantum dots have been used as substitutes to the fluorescent dyes of ELISA assays and, although they did not demonstrate higher sensitivity than conventional ELISA, easily detected multiple analytes simultaneously [*Goldman, 2004; Smith, 2006*]. Nucleic acid biomarkers are another target for bioconjugated quantum dots to detect early mutations or hereditary predisposition towards cancer. New biosensors based on fluorescence resonance energy transfer (FRET) may use quantum dots as donors to detect proteins and nucleic assays and were found superior to sensors relying on conventional fluorophores [*Gerion, 2003*].

The real potential of quantum dots lies in their multiplexing potential: rather than employing a single particle population to target one specific analyte, the nanoparticles can be gathered into a larger structure such as a microsphere. Even though detection of five or more targets is easily achievable with a five colour assay, basing the detection on the sole emission wavelength aspect become quickly limited when the number of targets increases. In comparison, loading microparticles with well-defined set of quantum dots appear as a more flexible alternative. Technologies exist that afford a precise control of the particles fluorescent pattern and intensity profile so that the spectral signature - or barcode - of the microsphere is precisely tuned both in terms of emission profile and in term of intensity level [*Han, 2001*]. For instance, six quantum dots colours with ten level of intensity lead theoretically to one million potential combinations. Consequently, simultaneous detection of multiple analytes from the same sample volume is possible if the microspheres are conjugated with

proper ligands and considerably reduce the time for analyses and costs of the procedure [*Algar, 2010*].

Thus, quantum dots are powerful fluorescent nanoparticles with the potenttial to replace certain fluorescent dyes to gain more sensitivity and to allow multiplexed detection. However, the composition of quantum dots is a major barrier to their application *in viv*o but is less of an issue for *in vitro* and diagnostics applications. Originally, many studies highlighted that quantum dots progressively exert toxic effects on cells. Release of cadmium ions – one of the principal components of quantum dots - after endocytosis caused damages to mitochondria and other subcellular components, and at certain occasion causes cellular death [*Walling, 2009*]. In comparison, iron oxide, gold and at some extent silica do not pose the same threat that the semiconductor particles. This is precisely the major downside of nanomedicine: the lack of paradigm in assessing nanoparticles toxicology impedes the full development of nanomedicine. As long as clear regulation is not declared and that nanotoxicology does not provide the fist clear evidence of the toxicity or lack of toxicity of nanomaterials, the decelopment of nanotechnology will be slowed down.

1.6 Toxicology and biological responses of the organism

1.6.1 Historical perspective of particles toxicology

The environmental and health impact of nanomaterials is of great importance in the development of nanotechnology. The reduction of materials to the nanometre scale goes in par with the apparition of new, unique properties. At the same time, the small size and large specific area of nanostructures elicit their own specific biological responses that cannot be predicted based on the reaction of biological systems to bulk materials of similar composition. Therefore, all of the uncertainties about the response of an organism towards

nanomaterials raise questions about the possible toxicologic effects on humans and ecosystems.

The recognition and the categorisation of nanoparticles toxicology as a distinctive branch of toxicology are relatively recent: the real emergence of “nanotoxicology” as a full discipline is strongly bound to the work of Oberdöster on fine (< 1µm) and ultrafine particles (< 0.1 µm) [*Oberdörster, 2007*]. Paradoxically, interactions of nanoparticles with biological entities and their unusual behaviour were already observed twenty to thirty years ago. It has been long known that fine and ultrafine particles are naturally present in the environment or generated through natural events (volcanoe eruption, forest fires, etc.) in substantial amount. These natural nanoparticles are generally considered as harmless, except in certain specific cases. Since the industrial revolution, the society has developed at a frenetic pace and new sources of particles appeared. These “anthropogenic” particles are often the results of combustion and other industrial processes (cars, power plants, etc.) and more broadly of pollution and toxicological studies established that anthropogenic particles are responsible for several cardiac and pulmonary diseases. More recently, the development of nanotechnology initiated the manufacture of new materials reduced to the nanoscale - or engineered nanoparticles - and thereby have become a new source of particles. The necessity to assess nanotechnology risks where additionally urged by stormy debates between nanotechnology promoters and opponents regarding hazard and social impacts, and the will of industrial to start commercialisation as soon as possible. Actually, the uncertainty about toxicology of nanoparticles represents the principal brake to the development and industrialisation of nanotechnology: if carbon nanotubes and some other nanoparticles (gold and silver colloids, silica Ludox ©, quantum dots, etc.) are now commercially available, their safety or toxicity is not proved and the studies often contradictory. Yet, a few products already include nanomaterials: sporting goods, tires, clothing, cosmetics (in particular sunscreens), electronics, etc. but their number is still limited (about 1020 products referenced in 2010 [*The Project on Emerging Nanotechnologies*] and

the distrust of consumers is certainly what prevents more goods to enter onto the market.

At the beginning, nanoparticles were loosely studied alongside ultrafine particles, principally because respiratory toxicologists were the first to fully recognise that very small particles may behave differently than bigger structures when they studied the inhalation of ultrafine particles and their effect on the lower respiratory tract. Oberdörster et *al*. compared 20 nm TiO_2 and Al_2O_3 particles to their 500 and 250 nm respective counterparts and observed a more acute pulmonary inflammation when nanoparticles were employed [*Oberdörster, 2007*]. Additional studies of carbon and TiO_2 correlated the increased toxicity of ultrafine particles with the higher specific area of these very small structures. Poland's comparison of carbon nanotubes to asbestos fibres triggered strong negative reactions from the scientific community as well as from the media and the public. Poland found that both materials induced strong inflammatory response of lung tissues and at some extent carcinogenicity resulting from the inhalation of nanoparticles [*Poland, 2008*]. A striking result was the detection of macrophages attempting to phagocyte fibres: the cells struggled to incorporate the long tubes into phagosomes and the tubes ended up protruding beyond the cell membrane limits (frustrated phagocytosis), with high oxidative stress immediately afterwards and induction of chronic inflammation. The only solution was for the macrophages to fuse together into a foreign body giant cell to attempt to clear the particles. Incidentally, Poland's work indirectly fuelled an amalgam that nanoparticles necessarily behave like asbestos. Yet, a direct comparison of fine or ultrafine particles with engineered particles is too hasty.

However, the initial toxicological assessment of engineered particles was based on similar criteria to that of anthropogenic particles, but steadily the toxicology of engineered nanoparticles diverged from their fine and ultrafine counterparts and called for a different approach.

1.6.2 Nanotoxicology: a distinctive branch of toxicology

Oberdörster's work on TiO_2 nanoparticles did not take into account the higher reactivity of nano-objects. Therefore, at similar weight dosage, the toxicological assessment necessarily detected a more acute and deleterious response towards the smaller particles. In comparison, the toxicity of nano- and submicrometric particles were found similar when the dosage was brought back to a specific surface dosage [*Oberdörster, 2007*]. In the same vein, inhalation of nanoparticles was the principal way of assessing their toxicity since fine particles are mainly air-borne. If this is true for carbon nanotubes, which production method poses risks of air dispersion, most of the other nanoparticles for biomedical preparation are synthesised in liquid phase. Although not exempt from potential inhalation risks, it is more probable that the particles will be employed under the form of hydrocolloids, i.e. dispersed in water or dispersed in another liquid medium and injected, swallowed, or taken by other route that inhalation. Another important difference between anthropogenic and engineered particles lies in the size dispersity: fine and ultrafine particles are often heterogeneous when engineered particles are designed with a narrower size to ensure that the particles exhibit identical properties and the biological response they elicit should be more uniform. This difference of characteristics has its importance in the reaction of organisms to nanoparticles and in the end engineered nanoparticles and ultrafine particles behave differently and must be screened separately.

With these differences in mind, nanotoxicology started to be considered as a separate branch of particle toxicology. The number of reports and studies of engineered nanoparticles progressively grew in number but still faced an important barrier. Small alterations of the structure are sufficient to induce totally different physico-chemical properties. Furthermore, biological activities of nanoparticles depend on more numerous, more complex, and more interrelated parameters than usually encountered in bulkier material, and if size and dosage remain important factors, other parameters must be taken into account. Oberdörster defined up to 16 factors that ought to be screened when

considering a nanoparticles sample: size, size distribution, concentration, shape, surface area, composition, surface chemistry, surface contamination, surface charge, crystalline structure, agglomeration state, porosity, method of production, preparation process, heterogeneity, and storage of material [*Oberdörster, 2005*]. To make the assessment more arduous, all these factors are inter-related and their importance occurs at different stage of the toxicology assessment (long material storage increase the change of aggregation but do not affect directly cells behaviour for example). In spite of the growing number of studies, teams eventually did not compare the exact same nanomaterials and systems and a direct comparison between these studies is consequently impossible. Yet, a few trends have already started to emerge and give a better understanding of the effect of many of Oberdöster's parameters.

The size of nanoparticles remains of primary importance as it is the small scale of nanostructures that enables them to cross natural barriers (translocation from the lung to blood or from the nose to the brain, blood brain barrier, etc.) or to enter within cells. At some extent, reducing size helps in escaping the macrophages recognition and reduces the chance of clearance from the organism. Nevertheless, it is often considered that smaller size of particles goes in par with higher toxicity. An example is the high toxicity of Au_{55}, a gold nanoparticle composed of exactly 55 atoms (1.4 nm) and has been found cytotoxic whereas larger gold nanoparticles are considered as biocompatible and do not elicit toxicity [*Tsoli, 2005*]. It is important to keep in mind that this finding is valid for unmodified gold and may not be transposable to other nanomaterials because of a change of size or may be invalidated were a proper coating found.

Strongly related to the particles size is the specific surface of nanoparticles: even though the particles dimension becomes smaller, a greater number of their atoms are displayed at the surface and are therefore susceptible to react with the molecules in their vicinity. For instance, metal oxide nanoparticles are famous for their pro-oxidative effects depicted in the Figure 1-30: some such as

titanium oxide are photo-activated by UV, other are electron acceptor or donor or are responsible for redox reaction that lead to the generation of radical species, or degrade and have high chances to induce cell injuries via oxidative stress [*Nel, 2006*].

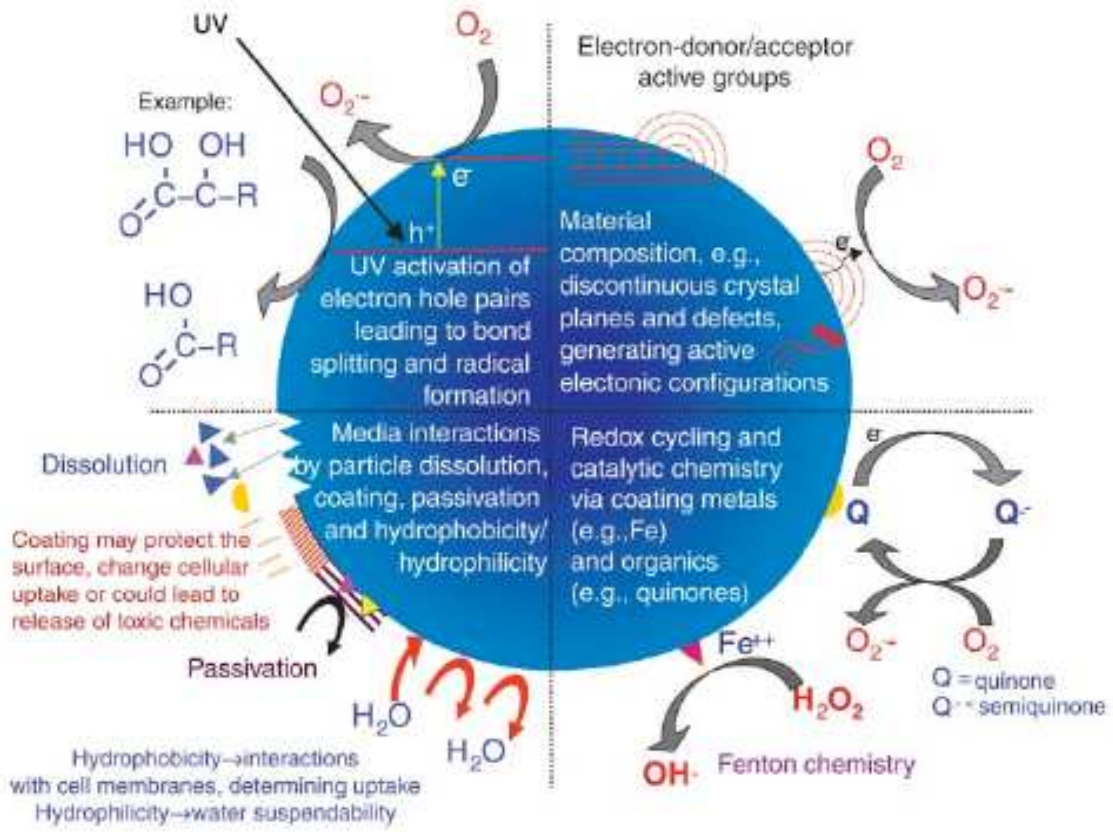

Figure 1-30: Possible mechanism behind the interaction between nanomaterials and biological media and example of particles reactivity – induced phenomena that lead to increased oxidative stress in cells [Nel, 2006].

Crystallinity and composition of nanoparticles also enter into consideration. Titanium dioxide nanoparticles are frequently found in sunscreen, solar cells, or self-cleaning surfaces. TiO_2 exists under various crystalline forms – principally rutile, anatase, and brookite – and is known for its capacity to generate radical species under UV illumination. It has been shown that the toxicity of TiO_2

particles is linked to the phase of the nanomaterial and that anatase phase is 100 times more toxic than the rutile phase [*Sayes, 2006*]. Crystallinity has less to do with the most common inorganic particles of interest in biology than with nanoparticles found in other application where the crystalline structure is often related to particular properties.

The chemical composition of nanoparticles is another parameter of paramount importance, not only the nature of the material, but also the presence of contaminant or of doping elements within the nanomaterial or the degradation products. Contaminants may issue from the chemical or physical process that gave birth to the nanostructures. For example, single-walled carbon nanotubes were reported to induce oxidative stress in several cell lines, but the main reason was later identified as residual metals, necessary to catalyse the synthesis of nanotubes but improperly removed. Likewise, the toxicity of gold nanorods was identified and attributed to remaining CTAB surfactant that were still stuck on the surface of the nanorods; after proper purification, the gold nanoparticles proved non toxic. On the other hand, doping a nanomaterial with another element has sometimes led to a diminution of the toxicity. George et al. detected an important decrease of toxicity of ZnO nanoparticles once doped with iron. They hypothesised that the presence of iron modifies the dissolution characteristics of the metal oxide, which is the reason of the high cytotoxicity of pure ZnO while other teams recorded similar effect on single-walled carbon nanotubes [*Connor, 2005; Fadeel, 2010*].

In the same vein, surface chemistry has an overall impact on the particles stability and on the interactions between nanoparticles and their environment. The surface modification of a particle acts as a way to prevent aggregation or to render the particles soluble in aqueous media. Aggregation is a major source of concern as it modifies the chemical and physical properties of primary particles and their larger sizes augment the chance of macrophages recognition and following clearance although some studies suggest that small clusters of particles are sometimes desirable and necessary to enter cells [*Lévy, 2010 b*].

The fate of nanoparticles after achieving their aim must be taken into consideration. Many inorganic nanoparticles will not be degraded by enzymes, pH, or other parameters and their clearance is more likely to be driven by urine and faeces [*Choi, 2007*]. There is a time period between the moment nanoparticles are taken up and the moment they are cleared from the system, but the longest this period the more chance they elicit detrimental effects on the cells. For this reason, the degradation products resulting from the action of pH and enzyme have to be carefully assessed. For instance, quantum dots pose the threat of leaking heavy metals when corrode, whereas polymeric nanoparticles are highly sensitive to solvents and pH and the effects oligomers and monomers resulting from the degradation of a polymer are impossible to predict, even if the starting polymer chains are relatively biocompatible.

Considering all nanomaterials existing so far, the variety of size, synthesis procedure, surface modification and coatings reported in the literature, a consensus about how assessing the safety of nanostructures is dramatically missing. For all of the alterations that groups bring, the *in vitro* testing is not automatically taken into account and even when toxicity assessment is carried out, groups test different cell lines and different conditions that further blur the prediction of nanomaterials safety. In addition, *in vitro* studies provided the first information of potential cellular responses, but many important effects such as inter-cellular communication, transportation in blood, bile, or lymph and so forth cannot be incorporated in such models, but at the same time, it is absolutely impossible to tests all of the nanoparticles and their characteristics on animals [*Oberdörster, 2005*]. The fact that nanotoxicology is unregulated is the primary reason of the absence of clear evidence regarding the safety or dangerousness of the most common nanosystems and the most urgent challenge is to define and develop a paradigm to standardise assessment of nanomaterials. Gradually, radical oxygen species measurement has made its way and appears nowadays as a paradigm to assess nanoparticles toxicity [*Meng, 2009*]. This choice is strongly bound to the effects of fine and ultrafine particles inhalation

on lungs reported by atmospheric toxicologists and was adopted based on the evidence of strong oxidative stress that some nowadays current nanoparticles elicit on cells.

1.6.3 Oxidative stress paradigm

The viability of cells is tighly bound to the highly regulated equilibrium between pro-oxidants and antioxidants [*Kohen, 2002; Li, 2003*]. Pro-oxidants, also called reactive oxygen species (ROS), are able to damage the cell membrane, DNA, and proteins as represented in the Figure 1-31. They are classified into:

- "Radical" group that includes nitric oxide ($NO^{\bullet}$), superoxide and hydroxyl radicals ($O_2^{\bullet}$ and $HO^{\bullet}$), singlet oxygen ($^1O_2$)and other species containing at least one unpaired electron that make the species highly reactive;

- "Nonradical" group that are highly reactive – though not as much as radicals - such as hydrogen peroxide (H_2O_2), aldehydes, ozone, or dioxygen.

Radicals must be produced at the same site as a biological target to induce damage, for example close to DNA strands, mitochondria membrane, or close to proteins. However, transition metals such as copper and iron are generally bound to such sensitive targets but are also involved in the chemistry of radicals via the Fenton and Haver-Weiss reactions [*Kohen, 2002*]. Consequently, the transition metals convert nonradical species into radical species *in situ* and cause oxidative damages. The source of radicals generation are exogenous (ionising and nonionising radiations, food, drugs, pollutants, etc.) and endogenous (mitochondria actions, by-products of enzyme activity, action of NADPH-oxidase produced by white blood cells, etc.) and the production of oxidants is a continuous flux..

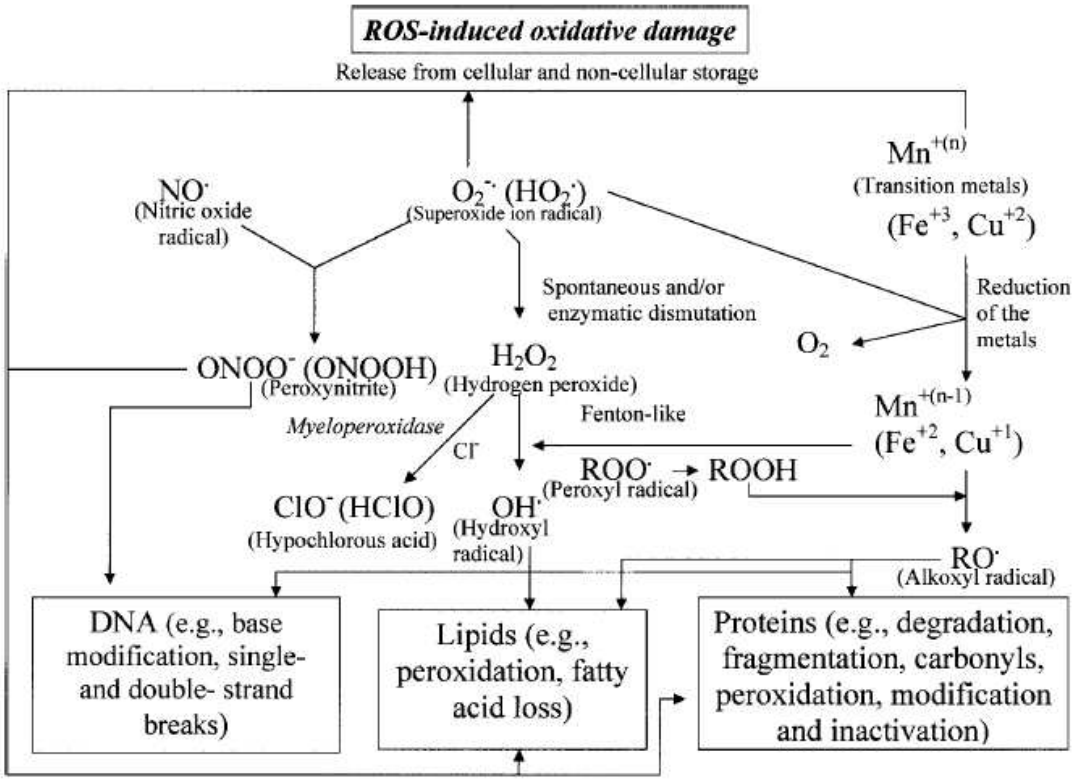

Figure 1-31: Radical and nonradical species thought to be involved in cellular oxidative stress [Kohen, 2002].

The organism erects defensive mechanisms against the constant exposure to ROS, for example through the tight regulation of the enzymes activity responsible for the (direct or indirect) production of radicals, or through the action of enzymes and small molecules dedicated to repairing the oxidative damages (DNA repair system, molecules donating hydrogen atoms, etc.). The key mechanism involves antioxidant molecules, typically low-molecular-weight-antioxidant (LMWA) and antioxidant enzymes that directly interact with ROS or sources of pro-oxidants to neutralise them as can be seen in the Figure 1-32. The mechanisms of action of LMWA may indirectly suppress ROS, for example by chelating transition metals to prevent their involvement in reaction yielding oxidants, or directly scavenge the radicals. Glutathione (GSH) is a primordial LMWA present at high concentration in humans, animal, and plants and works in conjunction with peroxidase in the decomposition of H_2O_2 but also in ascorbic

acid metabolism, communication between cells, and many other processes. It also directly scavenges $HO^{\bullet}$, RO, ROO and a few other radicals and becomes in its turn a radical that is regenerated in the oxidised form glutathione disulfide (GSSG) that results from the binding of two GSH [*Kohen, 2002, Dikcinson, 2002*].

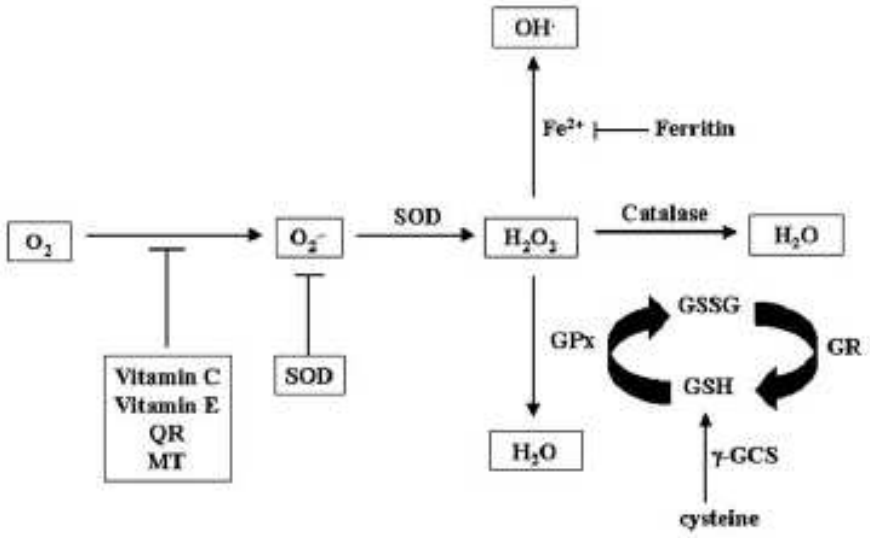

Figure 1-32: Action of antioxidant as a defence mechanism towards radical species [Kohen, 2002].

Oxidative stress arises when the cell redox equilibrium between antioxidants and pro-oxidants is unbalanced and the ROS overwhelmed the natural defences of the cells [*Meng, 2009; Xia, 2006; Chang, 2010*]. The oxidative stress model posits that the cellular response is organised into three phases. In Tier 1 – the normal protection against pro-oxidants - the transcription factor nuclear factor erythroid 2-related factor 2 (Nrf2) induces the production of more antioxidant and detoxification enzymes and LMWA such as GSH. When the response is not sufficient to curb the oxidative stress level and fails in re-establishing the redox equilibrium, the responses become more damaging and evolves to inflammation (tier 2) or to cell death (tier 3). In tier 2, the action of antioxidants is insufficient to restore the hemostatic balance and the increase of intracellular calcium concentration activates the mitogen-activated protein

kinase (MAP kinase): the kinases of the MAPK family are intimately integrated to the signal transduction via their ability to phosphorylate transcription factors and proteins. They also remodel the chromatin to express genes involved in inflammation, apoptosis, proliferation, differentiation, etc. [*Seger, 1995*]. Among the kinases, C-Jun N-terminal kinase (JNK) and p38 kinase play a role in the protein 1 (AP-1) and nuclear factor κβ (NF- κβ) pathways [*Chen, 1999; Karin, 1997*]. NF- κβ and AP-1 are two transcription pathways that upregulate the expression of chemokine and cytokine that mediate the inflammation of tier 2 as summarised in the Figure 1-33 [*Mazzoli-Rocha, 2010; Donaldson, 2003*].

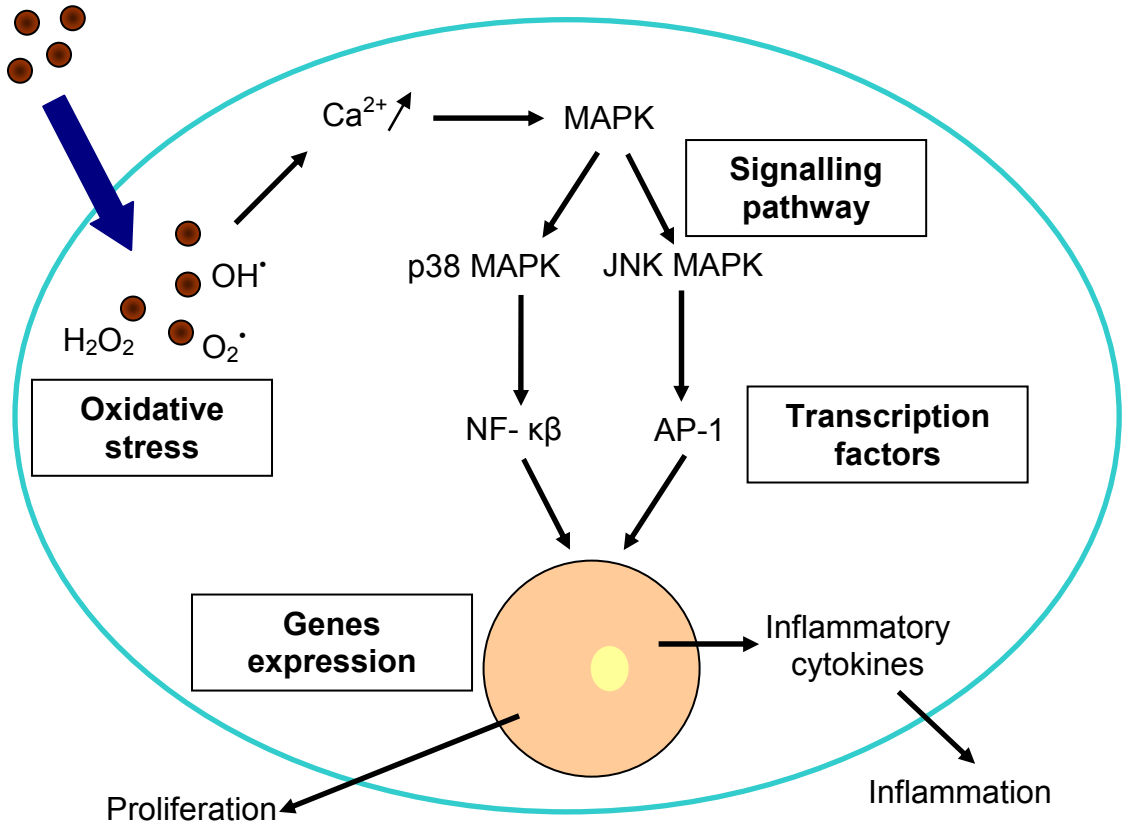

Figure 1-33: Oxidative stress pathways resulting from the internalisation of nanoparticles.

In Tier 3, the mitochondria membrane is disrupted and the consecutive cascade of reactions brings the cells to its death. The mitochondrial membrane is highly

sensitive to many physiological parameters including ROS and may trigger the mitochondrial membrane permeabilisation (MMP) that is a major event in apoptosis. Mitochondria release the pro-apoptotic cytochrome c in the cytoplasm that binds to apoptotic protease and activate factors that initiate the apoptosis of cells. Furthermore, the release of cytochrome c in turn activates caspase 9, triggering the caspase cascade that likewise plays an essential role in apoptosis and necrosis [*Kroemer, 2003*].

A number of assays can be used to assess viability and/or toxicologic signs such as DNA damage or oxidative stress. For instance, 2',7'-dichlorofluorescein diacetate, and dihydrorhodamine123 directly react with ROS; thiobarbituric acid assay to malondialdehyde detects signs of lipid peroxidation; and 5,50-dithio-bis(2-nitrobenzoic acid) combined with glutathione reductase measures the GSH/GSSG ratio that is a direct sign of potential depletion of the antioxidant and therefore an indicator of oxidative stress [*Marquis, 2009*]. With a appropriate choice of dyes, Georges and Xia were able to detect simultaneously signs of oxidative stress. The later probed the mitochondrial membrane potential to detect a loss of MMP (5,5',6,6'-tetrachloro-1,1',3,3'-tetraethylbenzimidazolylcarbocyanine iodide), the intracellular calcium concentration (Fluo-4) and cell integrity (propidium iodide) using a confocal microscope. The later probed DNA cleavage (DyeCycleOrange), caspase activation (D2R trifluoroacetate), lysosomal integrity (acridine orange), and cytoplasmic and mitochondrial free calcium (Fluo-3 and Rhod-2 respectively) [*George, 2010; Xia, 2008*] Additionally, proteomics brings elements that display protein modification or expression of new proteins that are as many clues of oxidative stress, for example expression of JNK and p38-MAPK, release of cytochrome c after mitochondrial disruption, or the phosphorylation of transcription factors NF- κβ or Nrf2 [*Xiao, 2003*].

The physicochemical features of nanomaterials, however well characterised they may be, represent only one aspect. It is however the interactions between nanoparticles and biological entities that ultimately define the fate of

nanoparticles and their potential safety or toxicity. At present, several barriers need to be overcome such as reducing or obviating the surface fouling with proteins, escaping the macrophages recognition and the retention of particles into the organs of the reticuloendothelial system, and ensuring that the particles do not pose any threat on the long term and are ultimately cleared from the organisms. The first step to overcome these challenges is to firstly understand what is the organism overall reaction towards the introduction of nanoparticles and then to understand how the particles interact with the cells and what factors promote their internalisation.

1.6.4 Complement and reticuloendothelial systems

The active and passive targeting envisioned through the use of nanoparticles and nanocarriers is an ideal case. In practice, the organism is in constant vigilance to the apparition of new and foreign bodies that may pose a threat to the general systems and promptly deals with them. Nanoparticles are no exception and have to face the traditional defence mechanisms personified by the complement system and the cells of the reticuloendothelial system. Biological media are complex fluids containing among others a large variety of nonspecific proteins that cover foreign bodies (opsonisation) and help phagocytic cells in recognising these alien elements. Only a few minutes in blood are sufficient to form a full protein corona, which composition is dictated by the particles surface properties such as hydrophilicity/hydrophobicity, charge, curvature radius, etc. It is believed that the fate of nanoparticles and their recognition is directly connected to the nature of the opsonin proteins [*Vonarbourg, 2006*]. The complement system proteins are in the front line of the defence mechanisms and the principal actors in the recognition of foreign bodies that will lead to immune reaction. About 30 proteins compose the complement system, some travelling in the plasma, other on the membrane of cells were they act as receptors and in particular on the surface of cells of the

immune system. Activation of the complement systems follows three pathways that can be seen in the Figure 1-34:

- Fixation of the C1q protein to an antibody or on C1q receptors
- Spontaneous binding of C3 fragments to the surface of the foreign bodies
- Binding of lectin on certain carbohydrates found in viruses and bacteria

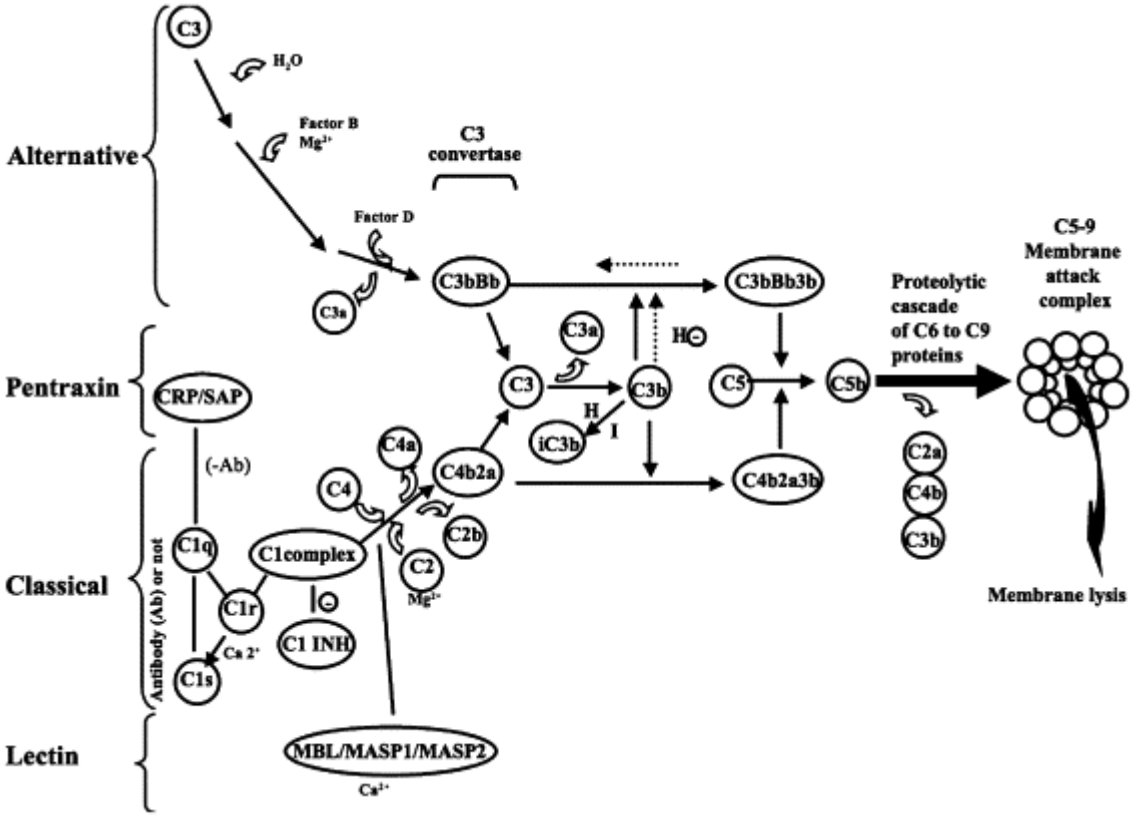

Figure 1-34: Schematisation of the cascade reaction resulting from the complement system activation [Vonarbourg, 2006].

All three pathways lead to an enzymatic cascade that ends up in the formation of the C3 convertase enzyme that cleaves the abundant C3 protein. The C3b fragment initiates the cleavage of C5 to C9 proteins that assemble into a

membrane attack complex but C3b is equally recognised by phagocytic cells receptors. In parallel, C3a as well as C4a and C5a that results from the cleavage of C4 and C5 are strong inflammatory agents which role is to recruit cells able to initiate the inflammatory such as eosinophils and basophils.

It is unlikely that the membrane attack complex is able to pierce or destroy nanoparticles - especially inorganic nanomaterials - then the complement system eventually mediates the interactions between nanostructures and the second line of defenders that are the cells of the reticuloendothelial system (RES). These cells are mostly phagocytic cells such as monocytes and macrophages, dendritic cells, or neutrophils. By themselves, phagocytes are not – or hardly – able to recognise and clear the nanoparticles and need to bind to opsonins first. The specialised receptors present at the surface of the RES cells recognise some of the opsonin proteins naturally or after they underwent a conformational change after adsorption onto the nanoparticles. The second option is the nonspecific adhesion of opsonised particles onto the cells without receptors as intermediate. In both case, the same fate await the particles since the RES cells phagocyte them and get activated [*Nie, 2010; Vonarbourg, 2006*]. After phagocytosis, the cleared particles are brought to the organs of the reticuloendothelial systems, principally in the liver and spleen, followed by the lungs, lymph nodes, and bone marrow. After a period of time that depends on the surface properties of the nanoparticles and the protein corona, the particles accumulate in the RES but the fate afterwards is not well understood. It has been reported that the particle either induce deleterious effects on the macrophages of the liver and spleen if they remain for extended periods of time in these organs, but in vivo studies suggest that the organism get rid of the nanoparticles by urine and faeces excretions.

1.6.5 Internalisation of nanoparticles

Although the action of some nanoparticles such as photocatalytic activity, dissolution of material, or redox potential may affect the cells from the exterior,

notably through membrane degradation, it is more likely that nanoparticles will be taken up and exert their effects intracellularly. Not only the particles must not elicit adverse effects when inside the cells, but some are engineered to purposefully carry and release therapeutic compounds directly within the cytoplasm or the nucleus. The mechanisms that underlie nanoparticles internalisation are still unclear apart from the fact that the uptake depends on the physicochemical properties, cell type, and nanomaterials microenvironment such as the type of proteins that adsorb onto the particles once in biological media.

The cell membrane is a dynamic structure that coordinates and regulates the exchanges of molecules between the extracellular media and the cytoplasm: small molecules such as ions and sugars are able to diffuse through via pumps and channels, but larger molecules must be captured and enclosed within a membrane to finally enter within the cells in a process called endocytosis. Endocytosis follows multiple pathways that differ in their mode of uptake but each of them has been shown to be equiprevalent in the internalisation of nanoparticles. The first pathway is the clathrin-mediated endocytosis, an essential route for most cells for the internalisation of nutrients that has the specificity of relying on receptor-ligand recognition. Clathrin is a protein with a three-legged structure (triskelion) that creates patches onto the plasma membrane: it complexes with AP2 to assemble into polyhedral lattices that gradually curves the membrane and form a pit (clathrin-coated pit) where cargo molecules and nanoparticles accumulate. The budding structure evolves and becomes more and more invaginated and the neck narrows to the point of creating a constricted pit. Dynamin forms a spiral around the neck to form a full vesicle roughly 100 nm that pinches off the membrane and moves into the intracellular domain, where the clathrin coating is disassembled to free the vesicle to fuse with other vesicles (endosomes) as represented in the Figure 1-35 [*Doherty, 2009; Conner, 2003; Lodish, 2003*].

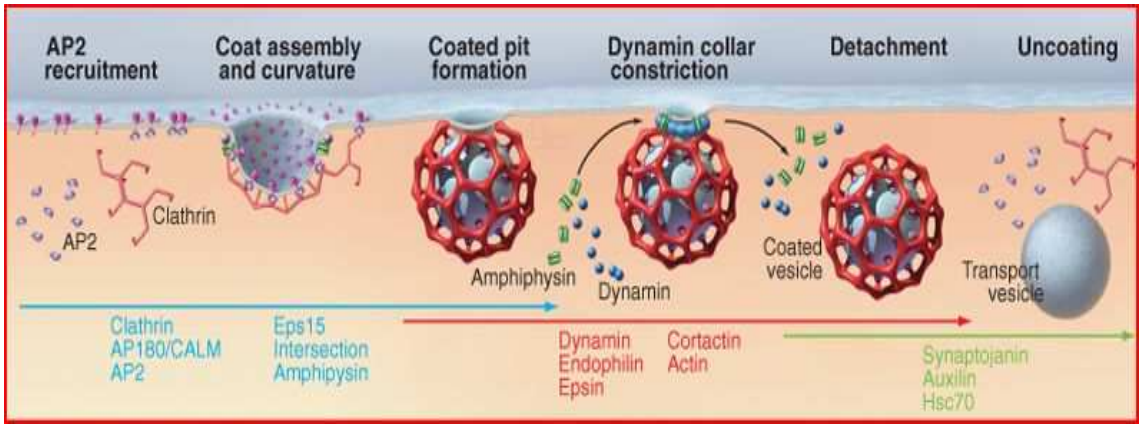

Figure 1-35: Schematisation of the clathrin-mediated endocytosis pathway [Pollard, 2007].

Phagocytosis is another pathway triggered by receptor-antigen binding but is mostly found in specialised cells such as macrophages/monocytes, neutrophils, and dendritic cells in order to clear large debris and pathogens including remnant of dead cells, foreign bodies, or bacteria. Phagocytosis enables to internalise large objects (larger than 750 nm) by creating a protrusion of the cell membrane that surrounds the foreign body. More precisely, the recognition of the targets ligands triggers the assembly of actin filaments adjacent to the pathogen. The growth of the actin filament supports the membrane extension from both side of the target (phagocytic cup). The phagocytic cup finally closes and zippers tightly around the foreign body into a phagosome that is directed through the membrane and to the cytoplasm. At the same time, all membrane components are removed and replaced by other component that will induce the fusion with lysosomes - that contain hydrolytic enzyme- to result into a phagolysosome as schematised in the Figure 1-36 [*Lodish, 2003*].

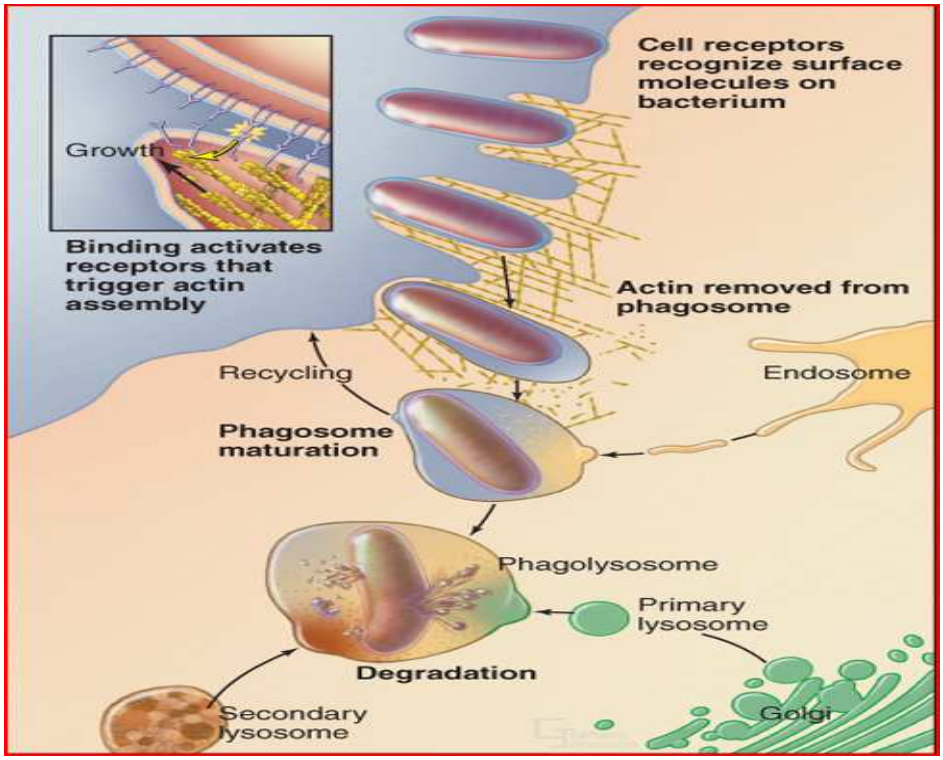

Figure 1-36: Schematisation of the phagocytosis of bacteria [Pollard, 2007].

In the same vein, macropinocytosis is a non-specific pathway where the membrane protrudes and engulfs large volume of surrounding extracellular fluid. Then it collapses and fuses with the membrane, creating a pocket up to several micrometers large - or macropinosome - containing cargo, particles, and fluid. The resulting vesicle further travels into the cytosol where it fuses with lysosomes, endosomes, and other vesicles.

Lastly, caveolae-mediated endocytosis is another non-specific pathway where cargo and particles accumulate in flask-shapes pits 60-80 nm diameter in the membrane coated with cholesterol and the cholesterol-binding caveolin protein. After closure of the caveolae, the vesicle transports its content through the membrane and into the intracellular domain where its fate is similar to the other pathways seen in the Figure 1-37. There exists clathrin- and caveolae-

independent pathways as well but the mechanisms that sustain them are not elucidated.

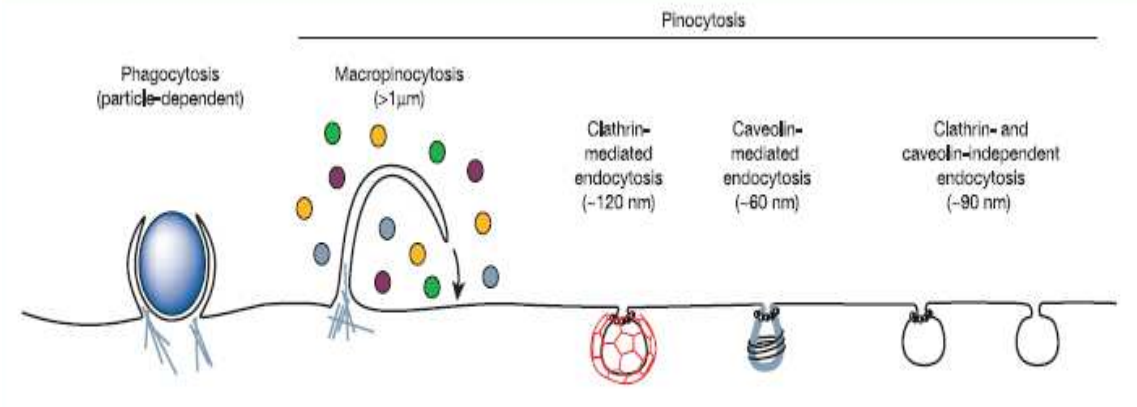

Figure 1-37: Summary of the different endocytosis pathways that can be involved in the uptake of nanoparticles [Conner, 2003].

Reports of nanoparticles uptake are contrasted and there exists no general rule to predict the fate of nanoparticles once in biological systems. For instance, some studies reveal that macrophages take up SPIO by receptor-mediated pathways but pinocytosisis the major way of access with gold nanoparticles and scavenger-receptors for carboxylate-modified polymeric nanoparticles. In some cases, particles diffuse within the cells without going through any membrane-dependent pathway and have a direct access to the cytoplasm and by extension to the nucleus and cellular compartments [*Unfried, 2007*]. It is generally admitted that the nanoparticles surface characteristics, particles microenvironment, and cell types are the key parameters in the interaction between nanomaterials and cells.

Smaller dimensions are not a guarantee of facilitated access to the cytoplasm. Instead, an optimal size, correlated to the radius curvature, accelerates the membrane wrapping that is at the core of some endocytosis pathways. Nanosphere optimal size appears to be 50 nm and explain the tendency of smaller particles to form some clusters to undergo internalisation. It has long been believed that the wrapping time of nanorods was longer than that of

nanospheres, but some new evidences tend to indicate that the tendency may be inverted with proper coating [*Chithrani, 2006*]. Furthermore, modelling suggest that certain shape such as cylinders and hemispheres are more promising to escape the RES detection and circulate in the blood unhampered for longer time.

Findings on the surface charge are contrasted: for example positively charged albumin nanoparticles were internalised in high quantity but the same effect was not detected with cationic polystyrene particles. From a general point of view, the uptake of negatively charged particles is limited on account of the negative charges of the plasma membrane. However, this uptake is not inexistent and it is believed that anionic particles cluster and accumulate on the scarce positively charged regions of the membrane. In contrast, cationic nanoparticles do not face this problem and bind to some of the numerous negatively charged groups onto the cells membrane and are easily internalised. Neutral particles present the lowest affinity for cells and are little or not taken up [*Verma, 2010*]. However, the intrinsic surface features are usually modified by coating with polymers and other ligand that introduce steric hindrance as well as charge changes. The well-known PEG coating is a popular strategy to impart stealthiness to nanoparticles as the polymer chains are neutrally charged and readily escape the RES system, if only for a certain period of time, but this coating although affect the endocytosis by other less specific cell lines. Hydrophobic interactions with cell membranes are complex, but some groups suggest that hydrophobic particles are quickly engulfed possibly because of the highly hydrophobic conditions that exist in the interior of the membrane, but their lifetime is also generally shorter due to their propensity to aggregate in aqueous media, which facilitate the macrophages recognition and phagocytic actions [*Nel, 2009*].

The other complicating factor is the non-specific adsorption of proteins onto the nanoparticles as soon as they are suspended in a biological medium. This is a parameter of utmost importance considering that it is not the surface of the nanoparticles that enters into contact with the cells but instead all interactions occur through the protein corona that covers the nanomaterials. Even PEG

coating usually said to be insensitive is still subject to non-specific adsorption but the first, effective strategies to control or totally prevent the protein corona formation start to appear [*Park, 2010*]. Lastly, the cell types that may be in contact with nanomaterials are not limited to macrophages/monocytes or to endothelial cells in the lung in relation to the potential inhalation of particles. Instead, the particles will be in contact with multiple types of cells ranging from endothelial cells to fibroblasts, without mentioning cancerous tissues, and focusing on the single macrophage uptake is not adequate. The interactions with non-phagocytic cells results from a specific design of the particles surface where a ligand is tasks to target a specific cell line and where PEG and other neutral polymers decrease the opsonisation and the recognition by the RES agents. Since cells metabolisms are different, their reactions towards nanoparticles and the way they internalise them ought to be different as well [*Napierska, 2010*].

To put it simply the numerous *in vitro* studies involving a large range of nanoparticles interacts with different cell lines and the few *in vivo* highlight that there is not a single pathway defining the uptake of nanoparticles. Many points remain obscure such as the exact effect of surface aspect or the fate of the nanoparticles once in the intracellular domain. All of these unknowns reflect the difficulty to assess nanomaterial toxicology and the impossibility to apply the traditional assessment methods.

1.6.6 Overview of the toxicology of key nanomaterials

Gold in its bulk form is inert and biocompatible and it is assumed that nanoparticles do not exert cytotoxicity for the same reasons. Many studies agree on the lack of toxicity of gold nanoparticles: for instance, Chithrani and *al*. assessed the toxicity of gold nanospheres with sizes ranging from 14 to 100 nm but did not detect any deleterious effects on cells [*Chithrani, 2006*]. Gold

nanorods produced analogous results but require a perfect purification and removal of CTAB contaminant that has been found to be the principal source of toxicity of the rod-shape particles [*Connor, 2005*]. The surface modification and capping ligands may be responsible for a slight toxicity: this was the case with cationic gold nanospheres that induced a slight toxicity at very high dose whilst the anionic version was not found cytotoxic at all [*Goodman, 2004*]. From a general point of view, most of the usual ligands, including citrate, cystein, biotin, etc., were not found to elicit any response from cells over time and the results tend to indicate the high biocompatibility of gold nanoparticles under their spherical and rod shaped [*Connor, 2005*], although the toxicity of the new shapes has not yet been investigated.

There is however one exception with the Au_{55} cluster, a particle composed of exactly 55 atoms of gold for a diameter of 1.4 nm. This particle was found highly toxic in certain cells, although the toxicity differed from one cell line to the other. It is suspected that the particular geometry of the cluster that ay interacts with in a unique manner with the DNA strands by fitting perfectly in the DNA grooves [*Pan, 2009; Tsoli, 2005*]. Small clusters were likewise found to induce some toxic effects, although not acute than that of Au55 but capping with proper ligand may help in suppressing the cytotoxic effects [*Pan, 2007*].

Investigation of the cellular uptake of gold nanoparticles highlighted the existence of an optimal size of 50 nm for the endocytosis (clathrin-mediated pathway) of nanospheres. Smaller 14 nm spheres create clusters of 5 or 6 particles to favour their internalisation whilst larger particles uptake kinetics was slower [*Chithrani, 2007*]. After their endocytosis, nanoparticles accumulate in endosomes where they aggregate and are further exocytosed. In contrast, a PEG contrast renders the particles totally invisible and prevented the uptake of gold whereas a small number of TAT peptide-conjugated nanoparticles were localised in the cytosol. Gold nanoparticles were rarely found in the nucleus and remain principally in vesicles unless their surface are engineered with ligands such as TAT or peptides helping in the evasion from the endosomes and/or in the entrance into the nuclear domain [*Nativo, 2008, Shukla, 2005*]

The few *in vivo* studies demonstrate a certain discrepancy with *in vitro* models. In one occasion, particles with a diameter comprised between 8 and 37 nm were found toxic in mice but not smaller and larger size. The findings contradict most of the *in vitro* studies however the particles were not modified, apart from the citrate molecules that resulted from the synthesis process [*Chen, 2009 a*]. Most other *in vivo* studies agree on the fact the biodistribution of gold nanospheres is size dependent and that most of the particles accumulate in the spleen and kidneys whereas the smallest are able to diffuse to more organs and even in the brain [*Alkilany, 2010*]. To date, there is no evidence of the long-term fate of the particles and their potential degradation or renal excretion: the particles are eliminated from the blood stream and retargeted toward the organs of the RES, but their accumulation in such organs may be problematic (splenic and hepatic toxicity, etc.).

Iron oxide nanoparticles position differently from other nanomaterials since magnetite and maghemite are naturally found in the organism, and it is supposed that SPIO and USPIO can be degraded by endogenous iron metabolism pathways, for example metabolised in the liver and recycled for blood cells formation or secreted via the kidneys. Iron is both a requirement for the maintenance of human life, but also a potentially toxic compound. This element is found in oxygen and proteins transport, oxygen sensing, and is involved in many biochemical reactions including metabolic purposes. Eighty percent of the total iron is incorporated into haemoglobin essential for erythrocytes and most of the remaining iron is found in macrophages and hepatocytes. Conversely, iron also catalyses the Fenton reaction that sees the conversion of hydrogen peroxide into hydroxyl radicals that causes important oxidative stress and damage organic molecules including lipids, DNA, proteins, but also disrupt the mitochondria membrane potential and induce apoptosis, or break the DNA strands and may initiate carcinogenesis or cell death [*Singh, 2010*]. Under normal conditions, iron ions in the plasma are harnessed and complexed with transferrin that binds to transferrin receptors and get endocytosed. Then, iron is chelated, and stored in ferritin, a molecule that sequester vast quantity of iron and maintain it in a non-toxic form.

Consequently, there is a labile iron pool onto the cells that store or release iron in accordance with the cell needs.

Cells lysosomes contain enzyme and other biomolecules intervening in the iron homeostasis pathways and able to degrade iron [*Ohkuma, 1978*]. It was established that iron oxide nanoparticles are indeed degraded in acidic condition equivalent to that existing in lysosomes - even in absence of enzymes – and that the degradation kinetics depends on the particles coating and may range between 3 to more than 30 days [*Lévy, 2010 a*]. Moreover, the degradation within the endosome was not found homogeneous and some particles dissolve within the endosomes whereas some kept their integrity and more importantly, the particles magnetic properties were still preserved [*Arbab, 2005*].The degradation of SPIO and UPIO poses the threat of iron overload that would result inthe iron homeostasis unbalance that in turn would induce toxic effects. Yet, a coating affording long dissolution kinetics may help reducing the toxicity of the iron overload by sequestering the iron and letting time for the cells to process the excess of iron and regulating avoiding at the same time the formation of high ROS in excess that would induce toxicity [*Arbab, 2003*].

In vitro studies compared USPIO and SPIO with different coating and capping ligands and make their comparison arduous. For instance, PEG coated nanoparticles did not elicit harmful effects unless short chains polymers are employed [*Häfeli, 2009*]. In some reports, polyvinyl alcohol was shown to reduce the cytotoxicity of SPIO compared to their uncoated version but other works found that cells did not internalise PVA-coated iron oxide particles [*Mahmoudi, 2009; Petri-Fink, 2006*]. Instead, vinyl alcohol/vinyl amine copolymer was necessary do get uptake – modulated by the number of amine per chain – and help reducing the toxicity [*Petri-Fink, 2007*]. Dextran-coated USPIO and SPIO are the standard iron oxide nanoparticles but their internalisation is not ideal at the difference of some other anionic capping ligands [*Wilhelm, 2003 and 2008*]. Carboxydextran reduced the cell viability in a concentration-dependent manner unless the particles concentration fell below a 100 µg/mL threshold [*Lunov, 2010*]. As a comparison, Buyukhatipoglu et *al*.

investigated the effect of uncoated USPIO and observed that ROS formation increased in a time- and dose-dependent manner. More peculiar, they noted morphological changes in the endothelial cells incubated with USPIO such as formation of actin stress fibres and increase of the Young Modulus (cells stiffer) related to the ROS increase, the phenomenon was suppressed when the cells were cultured in presence of ROS scavengers [*Buyukhatipoglu, 2011*].

In vivo injection of dextran-coated iron oxide nanoparticles has already proved safe enough to be clinically approved. The small size of USPIO helps in crossing natural barrier such as the blood-brain barrier, a feat rarely reported with other nanomaterials. Occasionally, iron oxide particles (silica-coated) were found to cross the blood-testicle barrier in parallel to the organs of the RES without inducing lesions, toxicity, or mutagenecity [*Kim, 2006 a; Kwon, 2008*]. Vinyl alcohol/vinyl amine copolymer and PVA-coated USPIO showed an opposite trend after injection in sheep that in *in vitr*o study: the former elicited a strong inflammation whilst the latter induced a milder inflammation that was quickly attenuated as a higher proportion of PVA-modified particles accumulated in the tissue. However, the inflammation observed with the first polymer may be caused by the conjugation of fluorescent dye rather than because of the polymer itself [*Schulze, 2005*].

First toxicological data of silica focused on the crystalline form of micro and submicrometric, where chronic inhalation is known to induce silicosis - a progressive fibrotic lung disease where silica particles are surrounded by concentric layers of collagen, macrophages, lymphocytes, and fibroblasts – and are also involved in lung cancer and other pulmonary diseases. Amorphous silica is generally as less hazardous than crystalline silica and the toxicity of the former is less documented, but with the shift of toxicology researched towards nanoparticles, the trends has done a turn-about [*Napierska, 2010*]. Comparison of amorphous silica nanoparticles with submicrometric crystalline silica revealed a higher toxicity in the nanoparticles, both time- and dose-dependent and the tendency of larger particles to induce lower toxicity has been reported at several

occasions [*Lin, 2006; Napierska, 2009*]. Amorphous nanoparticles appear to increase the ROS generation compared to crystalline structure, and the activation of Nrf-2 but studies do not tally on the activation of the transcription factors and the other kinase signalling pathways [*Eom, 2009; Liu, 2010; Tao, 2008*].

Nevertheless, a single parameter is not responsible for the toxicity or lacks thereof of silica nanoparticles but it rather the combinations of parameters such as porosity, specific surface, cell line, etc. [*Rabolli, 2010*]. For instance, Trewyn et al. observed that cancerous cells eagerly endocytose nanoparticles whereas cells such as fibroblasts internalise particles in much smaller quantities and more rapidly with spherical particles than with tube-shaped one [*Trewyn, 2008*]. The shape of mesoporous particles were found to affect the internalisation as well as the viability of cells: spheres uptake is slower than short and long rod-shaped particles but the toxicity found in spherical silica particles was also found lower [*Huang, 2010*]. Moreover, surface modification may help in reducing the toxicity of silica nanoparticles, although the effect is cell-dependent. Hence, aminated-mesoporous showed reduced toxicity than unmodified one [*Tao, 2002*]. In another study, He et *al*. demonstrated that phosphor-modified silica particles were less toxic than their aminate- and unmodified counterparts, although the effect must be correlated to the lower uptake of negatively charged phosphor-expressing structures in comparison to positively charged-aminated one [*He, 2006*].

The possibility to impart fluorescent to the ceramic matrix helped in the tracking of silica within the cells and the particles quickly gather into lysosome, although the extent of internalisation depends on the post-treatment (calcinations, etc.). Sun et al. were able to follow the fate of a single mesoporous silica particles using differential interference contrast microscopy and clearly distinguished the membrane crossing and the surrounding by an endosome [*He, 2009 a; Sun, 2008*]. Only one occurrence of FSNPs translocated into the nucleus was reported, where the particles inhibit the replication, transcription and cell

proliferation but no other group found similar evidence, even with smaller particles [*Chen, 2005 b*].

Few *in vivo* studies have been carried out and often deal with the inhalation fine and ultrafine silica particles. For engineered particles, intravenously injected particles accumulate preferentially in the liver, spleen, and lung but rarely in other organs such as heart or brain. Although their concentration in such organs decreases over time, they were still detected 30 days after injection. No pathological changes are usually noted, with the exception of liver inflammation response but coating with PEG was able to obviate the toxic effect of the nanoparticles. A maximal secretion was detected at a period ranging from 24 h for urine to72 hours for faeces and the rate decreased afterwards [*Cho, 2009; Kumar, 2010; Xie, 2010 a*].

Quantum dots are not a homogeneous class of nanomaterial: instead of a single element such as gold or silica, the semiconductor core (and shell) is made of a combination of heavy metals and metalloids, as well as a great diversity in their coating and capping ligand present to increase the biocompatibility of the nanostructures and impart hydrophilicity. The composition of quantum dots is the principal barrier to their employ *in vivo*: rupture or degradation of the coating could reveal the core or enables its dissolution and the release of ions that are known to be toxic even at very low concentration. Nevertheless, new quantum dots made of silicon have attracted interest due to the potentially higher biocompatibility [*Erogbogbo, 2008*].

In vitro studies are often contradictory: many showed a dose- and size-dependent toxicity of quantum dots at dose often inferior to that tested with other nanomaterials, may the effect is also strongly correlated to the capping ligands and coatings that may be responsible for the harmful effects of the particles. Some studies suggest that the toxicity of quantum dots is the result of their degradation, either because of photolytic and oxidative degradation of the quantum dots suspensions or because of intracellular processes in a dose-

dependent manner. Exposition to air and/or UV degrades the coating and exposes the metallic core, favouring toxic effects. In cells, the nanocrystals may be retains for periods exceeding 10 days and the low pH and enzymes actions may causes degradation of the nanomaterials but such studies are still rare [*Derfus, 2004; Hardman, 2006*].

The variation of composition, size, coating bioactivity, and storage may be in turn responsible for variable systemic distribution after injection in organism, for example accumulation in lymph node preferentially or on the contrary in spleen and liver. However, an increasing number of in vivo studies in rat have concluded that injection of quantum dots do not cause appreciable toxicity even on the long-term [*Hauck, 2010*]. At present, it is impossible to get a precise idea of the conditions where quantum dots elicit toxic effects, especially considering the divergence between in vitro and in vivo experiments, although the first applications of nanocrystals in surgery have already arisen as a tool to better visualise lesions in tissue.

Although the control over nanostructure accelerates, the use of nanoparticles for therapeutic applications still faces some major barriers. Probably the most important criterion is the lack of guidance of toxicology assessment and of regulation policy. In spite of the oxidative stress paradigm that have arisen as strong candidate to determine the potentially deleterious effects of nanomaterials, the divergence of systems, conditions, cell tested and applications totally throw confusion and makes it impossible - or hardly possible – to predict the safety of a nanoparticles. Moreover, even though standard characterisation methods provide information on the composition, surface aspect, shape, crystallinity and other physicochemical characteristics, the dispersion of nanoparticles into biological fluids further complicate the matter by generating changes in the properties of the materials, from aggregation to dissolution or opsonisation that may dramatically alter the properties of the original particles.

Beyond the toxicological aspect, the proper targeting of nanostructures remains a technological challenge: organism responses towards the presence of foreign bodies reduce the half-time of nanoparticles in blood and lead to their accumulation in specific organs in view of their excretion. Even though the surface engineering of particles surface provide a solution for the active targeting of cells or biomolecules, the intracellular fate of nanoparticles, in particular the evasion from endosomes and lysosomes into the cytoplasm and potentially into the nucleus is still a complicated matter.

1.6.7 Aims and objectives

The research presented in this thesis is an exploratory project investigating different routes to fulfil two aims:

- The development of hybrid organic-silica nanoparticles to carry a larger variety of fluorophore than conventional silica nanoparticles and enabling the simultaneous encapsulation of multiple dyes into a single structure;
- The development of modular nanoparticles based on a core-shell architecture and allowing the combination of gold, iron oxide, and (fluorescent) silica indistinctly.

The objectives to fulfil these aims were defined as follow:

1. To synthesise fluorescent silica nanoparticles following the traditional Stöber and reverse microemulsion synthesis methods in order to identify the limitations responsible for the lack of fluorophore diversity in the literature;
2. To test the amino acid catalysis route as an alternative to the conventional methods to produce small particles (< 100 nm diameter) and to further explore its potential in the design of fluorescent and multifluorescent nanoparticles;

3. To develop a new type of hybrid organic-inorganic nanoparticles with tunable composition based on the amino acid catalysis;

4. To demonstrate the potential of the hybrid nanoparticles as innovative fluorophore carrier by: testing a large number of fluorophores not reported in the literature and by creating multifluorescent systems with controlled spectral signature;

5. To design multifunctional nanostructures by coating gold or iron oxide with silica and then by combining all three nanomaterials into a single structure.

Chapter 2

Synthesis of silica nanoparticles by the Stöber method and reverse microemulsion approach

2 Synthesis of silica nanoparticles by the Stöber method and reverse microemulsion approach

2.1 Introduction

The first major contribution to the production of silica particles dates back to the work of Stöber and Fink (1968), who obtained particles from a simple sol-gel process in alkaline conditions and thoroughly studied the influence of parameters such as water content as well as the type and concentration of solvent and silicon precursors on the final dimensions of particles [*Stöber, 1968*]. The advantage of what has since then been known as the Stöber method lies in its simplicity: the protocol consists in mixing silicon precursors and water in an alcoholic solution containing ammonium hydroxide to catalyse the hydrolysis and condensation of the silanes. The highly basic conditions that ammonium hydroxide imposes on the system favours the condensation of the species over their hydrolysis, which results in the formation of spherical objects. Furthermore, the negative charges at the surface of the particles promote the repulsion between the spheres and the system stabilises in the sol phase (no gelation) whilst maintaining narrow size dispersity. Later on, other teams refined the initial Stöber method to produce smaller particles, studying at length the effects and interactions of the parameters involved [*Rao, 2005; Rahman, 2007*].

Alongside the development and refinement of the synthesis of silica and some other oxide colloids by the sol-gel process, various models have emerged to explain the mechanisms underlying the particle growth. The most famous model is LaMer's model, which predicts that growth of particles crosses two consecutive steps: a nucleation step where the precursors are consumed to create nuclei, and a growth step where the remaining precursors add to surface and enlarge the nuclei [*LaMer, 1950*]. Alternatively, Bogush and Zukoski reached the conclusion that large particles are the results of aggregation of smaller particles - or seeds - that stop their growth once they reach a certain

colloidal stability. Other studies advocate that the two mechanisms are responsible for particle growth, but from a general point of view, the actual mechanism has not been entirely elucidated [*van Blaaderen, 1992 a and b*].

While the Stöber method is an easy procedure, it is generally considered that its major drawback is the relatively large diameter of particles it produces (typically in the submicrometric range). Variation of silane or water concentration is one way to decrease the particle dimensions, but reverse microemulsion is generally preferred for producing smaller objects. Osseo-Asare and Arriagada paved the way to a new method to engineer nanoparticles – not exclusively silica – by confining the particle growth within micelles [*Osseo-Asare, 1990*]. Reverse microemulsion yields highly monodisperse of the colloids since the particle growth is mechanically restricted by the micelle dimensions. However, the presence of surfactant molecules at the surface of the particles requires extensive washing and thermal post-treatment for a total removal. The choice of surfactant has an influence on the structure of the nanoparticles: silica nanowires and silica nanorods or mesoporous structures are examples of shapes it is possible to obtain by varying the surfactant nature and synthesis conditions [*Slowing, 2005*].

Silica in itself lacks of intrinsic physical or chemical properties but are excellent carriers when compared to other polymeric carriers:

- Silica is usually considered as a biocompatible material and is consequently suitable for biomedical applications;
- The silica matrix is insensitive to changes of pH, temperature, salinity, and other harsh conditions;
- The mild synthesis conditions enables the addition and encapsulation of biomolecules within the particles;

- A large number of organosilanes are commercially available for surface modification and subsequent bio-conjugation with antibodies, polymers, etc.;

- The inorganic network is optically transparent and does not affect magnetic fields.

The last point is of importance for the carriage of fluorescent dyes, the principal application of silica nanoparticles. Organic fluorescent dyes are sensitive and can easily photobleach, but silica nanoparticles offer a nearly complete insulation from the environment which considerably reduces photobleaching. Furthermore, each sphere contains thousands of fluorophores and is brighter than free fluorophores in solution [*Larson, 2008; Nooney, 2009*].

The first major contribution to the design of fluorescent silica nanoparticles (FSNPs) is attributed to van Blaaderen and Vrij [*van Blaaderen, 1992 c*]. Their procedure was based on a modification of the Stöber method where fluorescein isothiocyanate (FITC) was conjugated to the aminosilane (APTES) and subsequently co-condensed with TEOS. The major consequence is the covalent binding of the sylilated dye to the silica matrix and the impossibility of leaking without degradation of the particles. Furthermore, a small quantity of APTES-FITC conjugate was sufficient to yield very bright particles able to fluorescence for prolonged period of time. Van Blaaderen took advantage of the silica chemistry flexibility to design various architectures based on the alternation of blank and fluorescent layers. Later, FITC was replaced by rhodamine isothiocyanate and proved that van Blaaderen's approach works so long as a dye is capable of covalently binding to an organosilane [*Verhaegh,* 1994]. In the end, isothiocyanate, maleimide and succimidyl esters derivatives of dyes are the principal fluorophores used with the van Blaaderen's method. In spite of its advantages, this method typically yields submicrometric particles, with the exception of the C-dots (Cornell dots), core-shell silica structures 20-30 nm in diameter with high brightness comparable to that of quantum dots [*Ow,*

2005]. C-dots are also based on FITC-APTES conjugates but alexa dyes and texas red have also been integrated into silica nanoparticles [*Larson, 2008*].

More commonly, the reverse microemulsion approach is preferred for smaller particles, although the nature of the fluorophores and the encapsulation mechanisms are different since the fluorophores are mostly retain within the particles by electrostatic interactions, but van Blaaderen's method is nonetheless compatible with the reverse microemulsion strategy. Yet, it is more frequent to find rare earth – and in particular lanthanide chelates – than organic fluorescent dyes. Lanthanide chelates such as Tris-(2,2'-bipyridyl) dichlororuthenium (II) hexahydrate (RuBpy) and Tris(2,2'-bipyridyl) osmium(II) bis (hexafluorophosphate) (OsBpy) or europium complexes are interesting in that they possess a very large Stoke's shift and their brightness is comparable to their organic counterparts [*Bagwe, 2004; Wang, 2005b; Yao, 2006*].

The aim of this chapter is to show the limit of the Stöber method and reverse microemulsions in terms of fluorophore compatibility and particle diameter. To tackle this aim, the first objective consists in estimating the effects of some synthesis parameters (catalyst and water concentrations) on the final particle diameter. Production of dye-doped particles was also attempted following van Blaaderen's modification of the Stöber method. The second objective was to assess the capacity of the reverse microemulsion to synthesise fluorescent silica nanoparticles. Since very few studies have reported the encapsulation of organic fluorophores, 3 dyes (acridine orange, and rhodamine 6G and B) were chosen to test the electrostatic encapsulation of fluorophores.

2.2 Materials and methods

2.2.1 Materials

Chemicals were purchased from commercial sources and used as received without any treatment. Tetraethyl silicate (TEOS) and acridine orange were purchased from BDH. Heptane, anhydrous ethanol (>99.5 %), ammonium hydroxide, docusate sodium salt (AOT, >99 %), cyclohexane (>99 %), 1-hexanol (98 %), 3 aminopropyltriethoxysilane (APTES, >98 %), and fluorescein isothiocyanate (FITC, Isomer I) were obtained from Sigma Aldrich. Rhodamine B (RB) and rhodamine 6G were purchased from Fluka. Triton X-100 was acquired from Promega. Highly purified water (Milli-Q) was obtained from a Millipore "Direct-Q 3" water purification system.

2.2.2 Synthesis procedures

- **Preparation of blank and FITC-doped nanoparticles following the Stöber method**

APTES-FITC conjugate with a molar ratio of 1:20 was prepared by dissolution of 5.25 mg of FITC ($1.35*10^{-5}$ mol) in 5 mL of anhydrous ethanol, followed by addition of 60 µL of APTES ($2.56*10^{-4}$ mol). The glass vial was covered with aluminium foil and kept under magnetic stirring during 24 hours. The conjugate was later used without purification.

Blank nanoparticles were obtained following Stöber's protocol [*Stöber, 1968*]. Typically, 2.8 mL of ammonium hydroxide was added to 35 mL of anhydrous ethanol, followed 5 minutes later by appropriate amounts of TEOS (1.5 or 2.5 mL) and magnetically stirred for 24 hours. The synthesis of FITC-loaded particles followed the same protocol, where ammonium hydroxide (50 or 100 µL), TEOS (250 or 500 µL) and APTES-FITC conjugate (100 or 250 µL) were mixed in 10 mL anhydrous ethanol (**Appendix A**). In one experiment, the temperature was raised to 60°C. The glassware was covered with aluminium

foil to protect the dye from light. All samples were recovered by centrifugation, three times 15 minutes at 1200 g or until the supernatant remained clear. Between each step, the samples were washed with distilled water and vortexed. Finally, the pellets were weighed and the particles were suspended in Milli-Q water.

- **Dye-doped nanoparticles via the reverse microemulsion route**

Microemulsions were initially obtained by mixing 1.77g of triton X-100, 7.5 mL of cyclohexane, 1.6 mL hexanol, and appropriate amount of Milli-Q (0.5 or 1 mL) and ammonium hydroxide (150 or 300 µL) (**Appendix A**). Once the solution became transparent, 50 µL of rhodamine B (RB), rhodamine 6G (R6G), or acridine orange (AO) solution (1mg/mL in water) was added followed five minutes later by 500 µL of TEOS. At the end of the procedure, the colloidal suspensions were washed with acetone to break the micelles and favour the recovery of the nanoparticles. All samples were thereafter collected by centrifugation by three cycles of 15 minutes at 1200 g or until the supernatant remained clear, with washing in distilled water between each step. Finally, the pellets were weighed and the particles were suspended in Milli-Q.

2.2.3 Characterisation

- **Scanning electron microscopy (SEM)**

The particle size and morphology were examined using scanning electron microscopy (SEM). The nanoparticle suspensions were firstly diluted: the samples were sonicated and subsequently 25 µL of suspension was poured in an eppendorf and the total volume was increased to 500 µL with Milli-Q water so that the SEM samples were totally transparent. One drop of suspension was deposited into a silicon grid and let to dry in a desiccator for at least 24 hours.

Finally, the particles were imaged using a high resolution FEI XL30 SFEG analytical SEM (Philips, Netherland).

- **Dynamic light scattering (DLS)**

The size and size distribution of the particles were measured by dynamic light scattering (**Appendix B**) using a Zetasizer nano series S with an He/Ne laser of 633 nm wavelength (Malvern Instruments, UK). The particle suspensions were firstly diluted: 10 µL of the sample was poured in a quartz cuvette and completed with 1 mL Milli-Q. The refractive index and absorption of silica nanoparticles were fixed at 1.25 and 0.01 respectively. For each sample, four measurements of 20 runs (15 seconds each) were carried out, with the temperature maintained at 25°C.

- **Fourier transform infrared spectroscopy (FTIR)**

The particle composition was analysed by infrared spectroscopy: a volume of nanoparticle suspension was taken, centrifuged, and dried in the oven for 1 day. The resulting powders were subsequently analysed in KBr powders using a Thermo Nicolet Avatar 370 spectrometer (Thermo Scientific). Infrared spectra were recorded over the wavenumber region 4000 to 400 cm^{-1} with a resolution of 4 cm^{-1}.

- **Fluorescence measurement**

Absorbance and fluorescence of FITC-doped nanoparticles were recorded in 96-well plates with a Varioskan Flash Spectral Scanning Multimode Reader (Thermo Fisher Scientific) equipped with a xenon flash lamp. All measurements were performed on 200 µL of 1 mg/mL suspensions of particles diluted in Milli-Q and at room temperature. Excitation and emission spectra of FITC/AO, R6G,

and RB were acquired with fixed wavelength set at 450/530, 490/580, and 500/600 nm respectively.

- **Confocal microscopy**

Fluorescent properties of FNSPs were additionally assessed using a confocal microscope. A drop of particle suspension was deposited onto a glass slide alongside a few drop of glycerol, covered by a cover slip, and kept at 4°C to let the water evaporate and to stabilise the particles. The FSNPs were imaged using a LSM 510 Meta Invert Laser Scan Microscope (Zeiss). Images were obtained using a Plan-neofluar 40X/1.4 oil immersion objective and the 488 nm laser source was use to excite FITC. All images were the average of sixteen scans and were obtained with the same optical aperture, lens, and scan speed and colour-coded in green. The software (Zeiss LSM confocal software) was also configured to subject a specific region of interest to a laser power of 15% in order to bleach the sample and images were taken every 30 seconds.

2.3 Results

2.3.1 Production of particles by the Stöber method

The first particles were synthesised following the Stöber method of pure silica without any fluorescent dye. The process proved very simple: all reagents were solubilised in ethanol and left under vigorous magnetic stirring for 24 hours, and the particles were easily collected by centrifugation (white pellet). After a few hours of reaction, the initially transparent solution transformed into a white, milky suspension due to the formation of silicic acids $Si(OC_2H_5)_{4-x}(OH)_x$ and then of particles. The morphology of the particles was characterised by SEM and the images displayed closely packed, highly spherical objects with diameter over 550 nm in three of four experiments (Blank 1, 2, and 4) and decreased to 450 nm in the last sample (**Figure 2-1**). Water was added to the reacting medium because it affects the sol-gel reaction kinetics and because Stöber identified it to be one of the parameters influencing the final particle diameter [*Brinker, 1990, Stöber, 1968*].

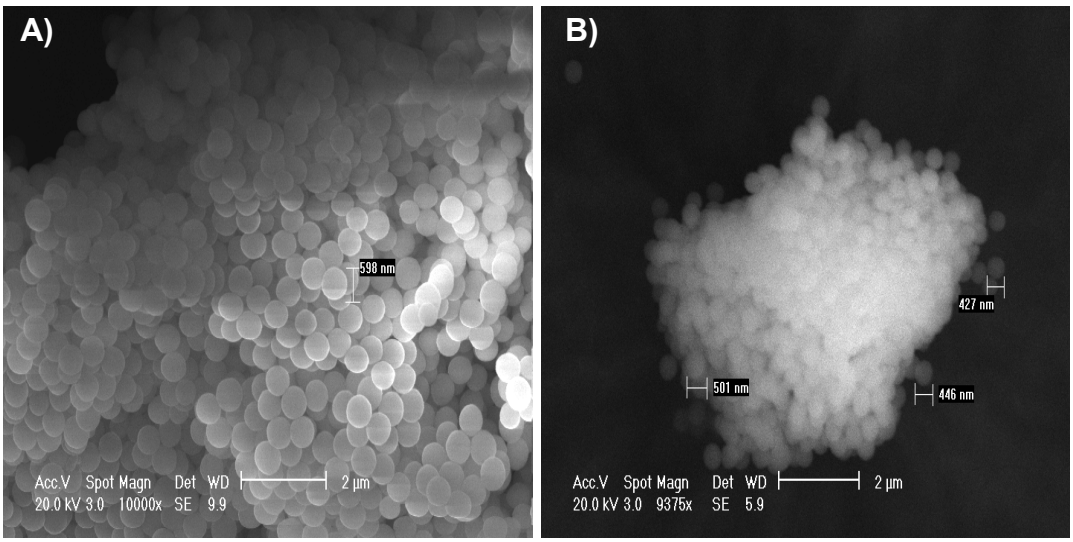

Figure 2-1: SEM pictures of nanoparticles produced from 1.5 mL TEOS (A), and 1.5 mL of TEOS and 5 mL of H_2O (B).

The protocol was modified to impart fluorescence to the particles. FITC was first conjugated to APTES via a covalent thiourea bond between the isothiocyanate group of the dye and the amine moiety of APTES (**Figure 2-2**). The new silylated fluorophores were consequently able to co-condense with TEOS molecules and covalently integrated into the final inorganic network. The strong orange colour that is characteristic of FITC upon binding to APTES (in comparison, free FITC exhibit a yellow colour) was a first proof of the dye presence. An interesting result was the decrease of particle diameter when the reaction temperature was raised to 60°C and where the particles were 125 nm in diameter.

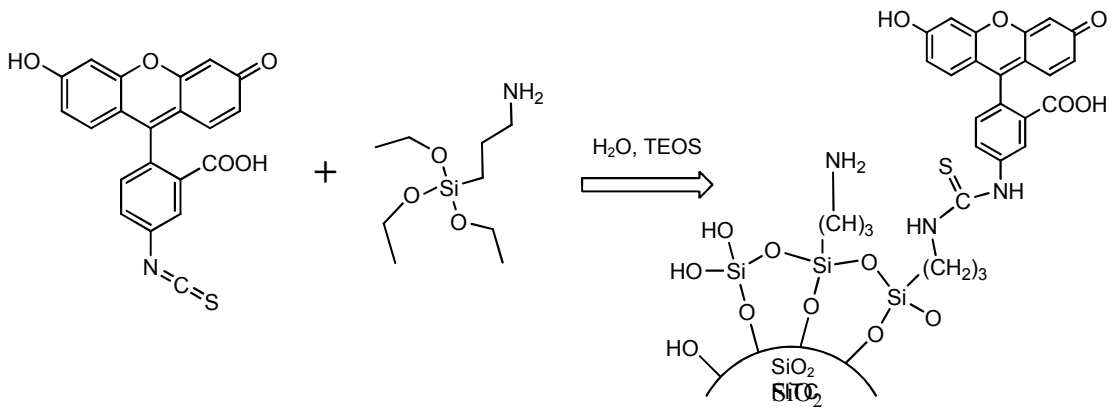

Figure 2-2: Reaction of FITC with APTES for the covalent binding of dyes within silica nanoparticles.

The particles composition was then analysed by infrared spectroscopy. The infrared spectrum of blank nanoparticles, i.e. pure silica particles without FITC, displayed the characteristic peaks of silica-based materials: a strong band centred on 1092 cm^{-1} accompanied by a smaller peak at 797 cm^{-1} from siloxane bonds Si-O-Si and another intense peak at 955 cm^{-1} characteristic of silanol groups Si-OH (**Figure 2-3**). The coupling of FITC and APTES replaces the isothiocyanate group by a thiourea group N-CS-N. This change translates by the disappearance of the 2030 cm^{-1} of the isothiocyanate N=C=S of FITC and the appearance of a new peak at 1350 cm^{-1} [*Gök, 2004*]. The peak centred on 1100 cm^{-1} of the APTES-FITC spectrum is attributed to a partial condensation

of the APTES, although there should not have been any trace of water in the solution to induce any polymerisation. The final FITC-doped particle spectrum looks like that of blank particles with a strong siloxane band at 1100 cm^{-1} and a smaller silanol around 950 cm^{-1}. The presence of a large band in the 3500-300 cm-1 region indicates that some free amine groups are still present and that the reaction between APTES and FITC was not complete.

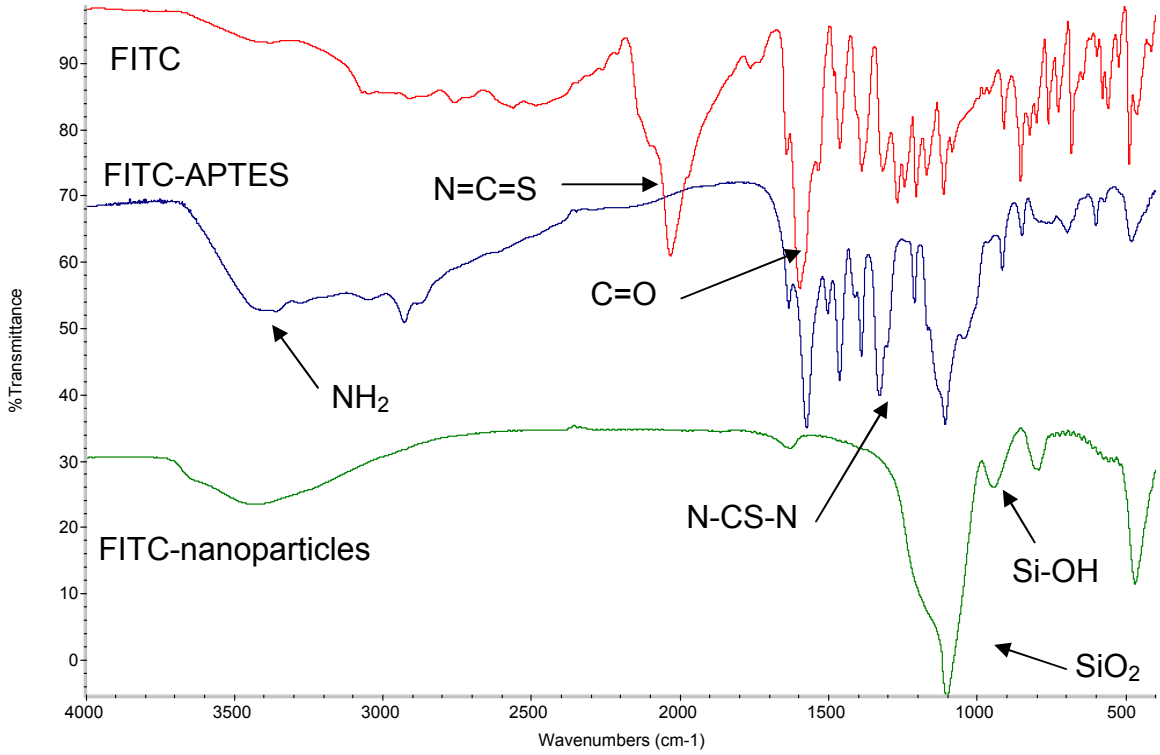

Figure 2-3: Infrared spectra of FITC (red), FITC-APTES (blue), and FITC-doped particles (green).

Blank silica nanoparticles are naturally white, but the strong orange colour that came birthed from the incorporation of the APTES-FITC complex gave a first hint of the actual entrapment of the fluorescent dye. The optical properties of each sample were measured and compared to that of free FITC and of FITC-APTES. All batches of particles exhibited identical excitation and emission profiles, with a strong absorption at 495 nm and emission at 515 nm (**Figure 2-4**). There was a slight shift in the excitation maximum of APTES-FITC and

FITC-doped particle compared to that of free FITC (490 nm) that may be attributed to a change of the dye local environment.

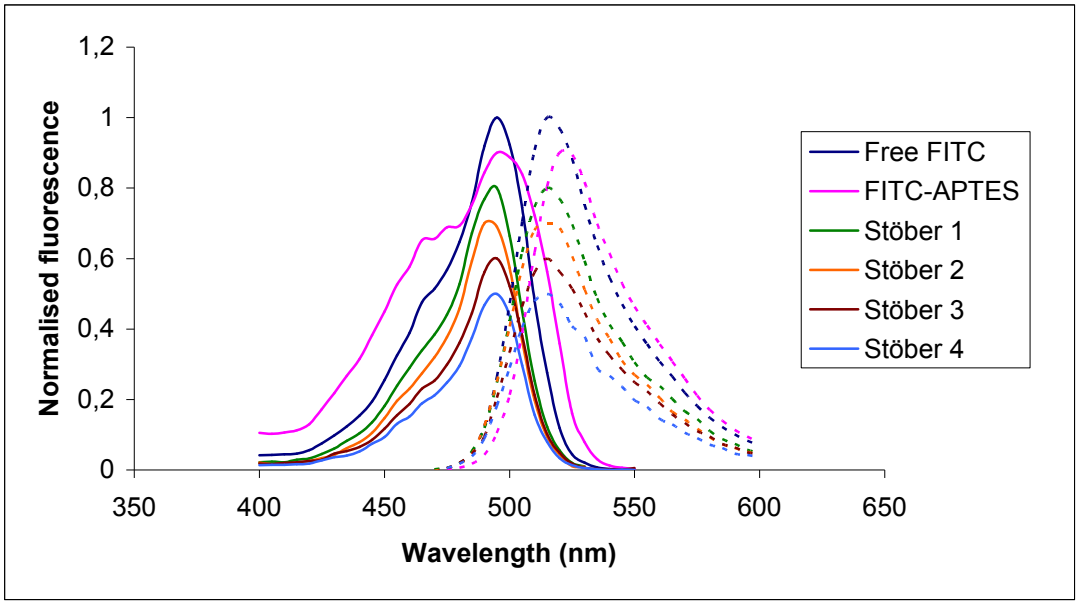

Figure 2-4: Excitation (plain) and emission (doted) spectra of free FITC, FITC-APTES and particles produced via the Stöber procedure.

Next, about 15 µL of the FITC-doped particle suspensions were deposited onto glass slides and imaged using a confocal microscope. Immediately, the particles strongly fluoresced under the green channel (488 nm-laser source excitation, bandpass 505-530 nm) and required some attenuation via modifications of the microscope setup (**Figure 2-5 A**). The images confirmed the aggregated state of some of the samples, although the exact size of the objects could not be measured with precision. A bleaching sequence was initiated to test the resistance of the particles to photobleaching. An area of the sample was subjected to a more intense illumination over a pre-defined period to bleach the fluorophores more quickly and pictures were taken at regular time (every 30 seconds) to follow the changes. While many conventional dyes bleach after a few minutes illumination at normal laser power, the particles retained their activity for more than 10 minutes at high light dose, although some bleaching was observed (**Figure 2-5 B to D**). Considering that the light

dose during the bleaching sequence was 3 times that of the normal setup and the illumination was kept constant, the silica particles are very robust contrast agents able to be imaged over extended periods of time.

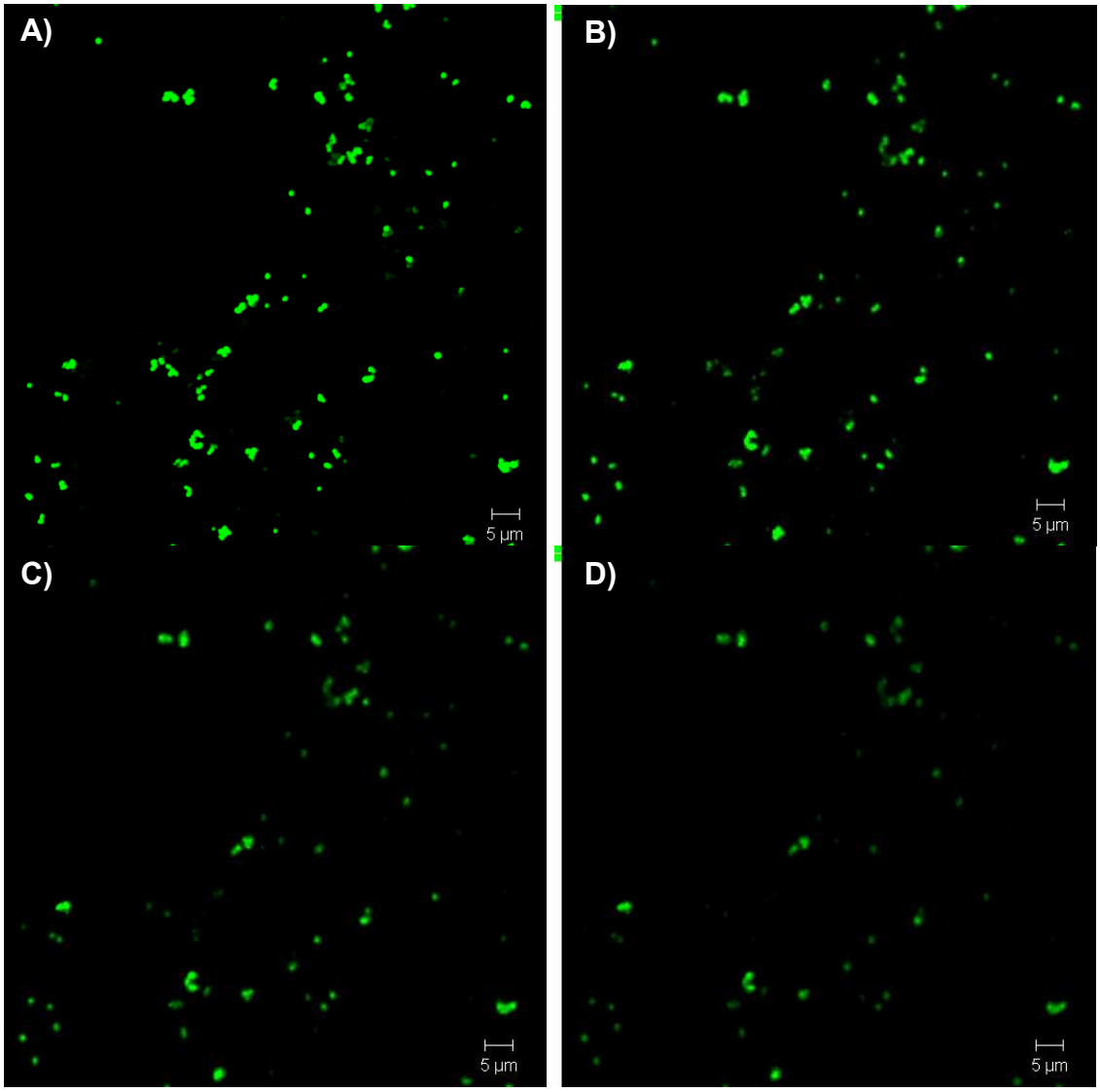

Figure 2-5: FITC-loaded nanoparticles obtained under a confocal microscope (A) and after 5, 10, and 15 minutes of the bleaching sequence (C, and D respectively).

2.3.2 Reverse microemulsion

The reverse microemulsion approach was tested to produce smaller nanoparticles than with the Stöber method. The ammonium hydroxide and the

silicon precursor and water concentrations were varied in view of detecting their effects on the particle diameter. SEM images showed that the first experiment (Mic-1) yielded 50 nm particles, although some particles were connected by necks that may be the sign of aggregation (**Figure 2-6**). The particles in the second experiment (Mic-2) were much smaller but the diameter could not be measured by SEM with precision and the particle dimensions were estimated between 10 and 20 nm. However, the sample appeared aggregated and displayed chains of linked particles visible throughout the whole sample. Finally, Mic-3 and Mic-4 yielded 60 and 70 nm-diameter nanoparticles respectively and are visually similar to Mic-1.

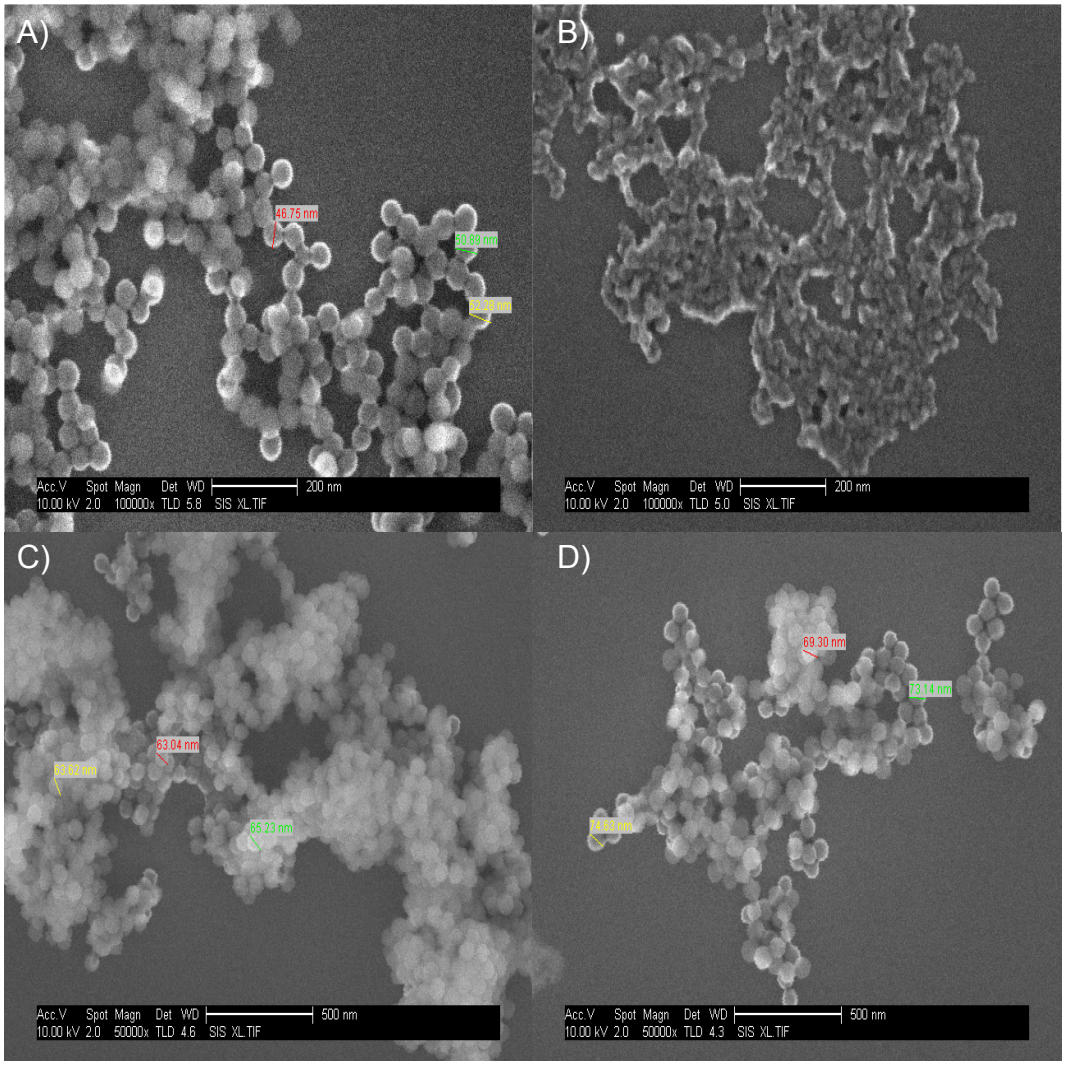

Figure 2-6: SEM images of RB-doped Mic-1 and Mic- (A and B), R6G-encapsulating Mic-3 (C), and AO-loaded Mic-4 (D).

The samples were also characterised by dynamic light scattering (DLS) to get information related to the hydrodynamic radius as well as the potential aggregated or non-aggregated state of colloids. In the case of Mic-1, the hydrodynamic diameter ranged between 185 and 380 nm, although very small particles with a diameter of circa 12 nm were detected (**Figure 2-7 and Table 2.1**). The large diameter is most likely due to the aggregated structure observed on the SEM images. In fact, the zetasier determined a polydispersity index (PdI) of 0.618 for Mic-1: this high value is generally the sign of an aggregated state, which tallies with the electron microscopy results. In contrast, well dispersed suspension should have a PdI of 0.1 or below, but Mic2, Mic-3, and Mic-4 had for value 0.334, 0.207, and 0.164 respectively, which suggests a possible aggregated state of the samples.

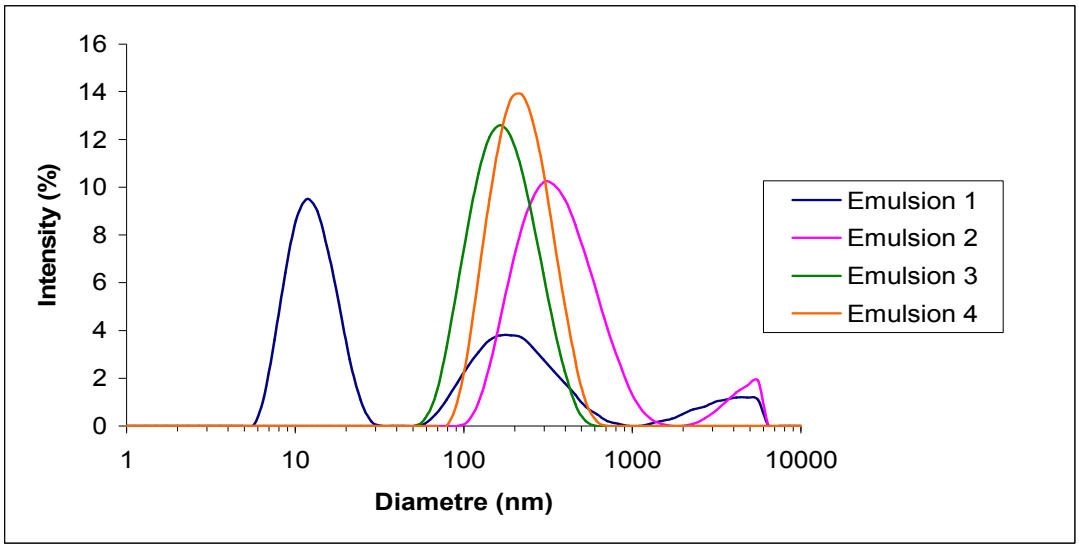

Figure 2-7: Hydrodynamic diameter of the microemulsion-based experiments.

The composition of the four experiments determined by FTIR is typical of silica material with the prominent siloxane peak at 1100 cm^{-1} and the additional peak at 870 cm^{-1} that derives from free silanol groups within the particles (**Figure 2-8**). The only exception appears at 1612 and 1513 cm^{-1} of Mic-2 spectrum; which originates from the C-C bonds of the surfactant molecules' benzene ring

Table 2-1: Average diameter and polydiserpsity index of nanoparticles synthesised by the reverse microemulsion method.

Experiment	SEM average diameter	DLS average diameter	Polydispersity index
Mic-1	50 nm	224 nm	0.618
Mic-2	15 nm	388 nm	0.334
Mic-3	63 nm	185 nm	0.207
Mic-4	70 nm	231 nm	0.164

[*Kimura, 1996*]. This contamination exemplifies one of the major weaknesses of the reverse microemulsion, which requires a very long purification process to get rid of the surfactant molecules.

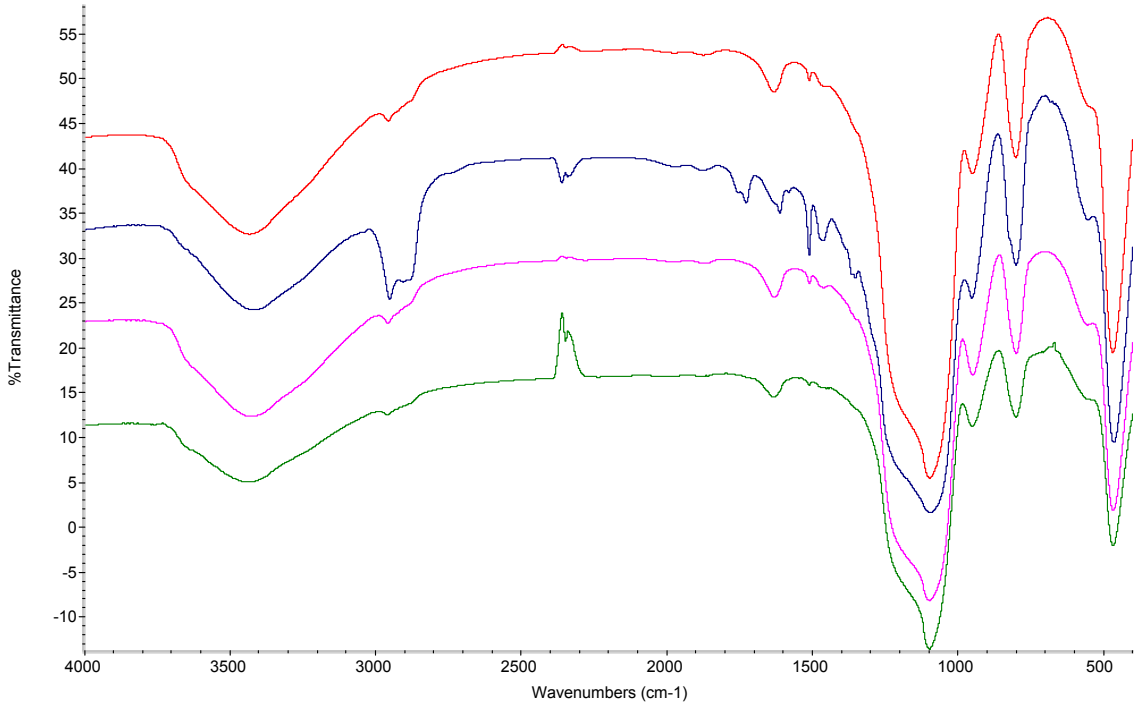

Figure 2-8: Infrared spectra of Mic-1 (red), Mic-2 (blue), Mic-3 (pink), and Mic-4 (green).

Preliminary tests with APTES-FITC conjugates were successful and produced yellow nanoparticles identical to that yielded by van Blaaderen's method. To assess the capacity to encapsulate other organic fluorophore, FITC was replaced by rhodamine B (RB), rhodamine 6G (R6G), and acridine orange (AO), three dyes that were available in the laboratory and of interest for fluorescence imaging (**Table 2.2**). Mic-1 and Mic-2 were synthesised in presence of RB but only Mic-2 exhibited a very weak pink colour whereas Mic-1 remained blank. Mic-3 (R6G) and Mic-4 (AO) had a slightly stronger pinkish and orange colour respectively but none of the samples exhibited the same strong coloration than FITC-doped particles synthesised by the Stöber method. These results indicate that a small number of fluorescent molecules have penetrated and remained trapped inside the silica matrix during the particle growth, although additional characterisation are required to fully determine this number.

Table 2- 2: Excitation/emission wavelengths and colour of the nanoparticles obtained by reverse microemulsion.

Experiment	Fluorophore	Excitation/Emission	Particle colour
Mic-1	Rhodamine B	555/580 nm	Blank
Mic-2	Rhodamine B	555/580 nm	Faint pink
Mic-3	Rhodamine 6G	525/555 nm	Faint pink
Mic-4	Acridine orange	502/526 nm	White-orange

In contrast, the supernatant of all samples were highly coloured and translates a higher affinity of the dyes for the organic phase than for the aqueous phase where the particles are formed. The fluorescence measurement of all samples showed traces of RB at 550 and 580 nm (excitation/emission), of R6G at 525/555 nm, or of AO 495/520 nm but the intensity was in no comparison with the bright fluorescence recorded with the FITC-doped particles at equivalent particle concentration (100 µg/mL) (**Figure 2-9**).

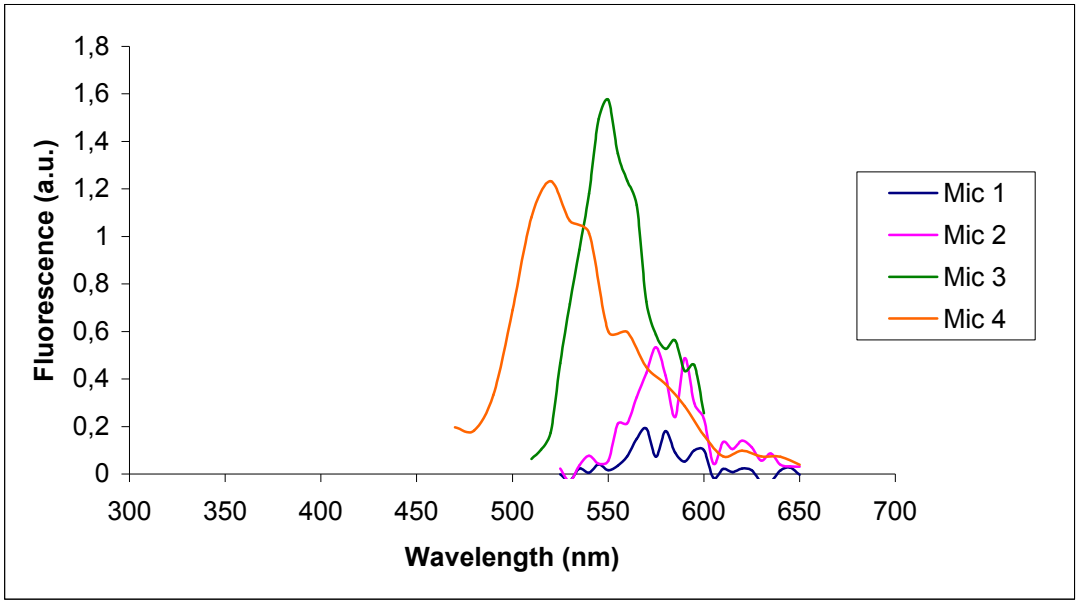

Figure 2-9: Fluorescence spectra of Mic 1 and 2 loaded with RB, Mic 3 containing R6G, and Mic 4 encapsulating AO.

2.4 Discussion

The results presented in this chapter are preliminary results following the protocols developed by other teams. The aim was to acquire a first experience of the synthesis of silica and fluorescent silica nanoparticles using the Stöber method and the reverse microemulsion, but not to conduct a complete characterisation of the particles or optimisation of the process.

The Stöber method naturally yielded well-defined spherical particles with diameter over 500 nm. Water was added to the precursors as well because its presence may influence the final particle dimensions: Stöber and Fink were able to tune the particle size by varying the alcohol/silicon precursor/water molar ratio and to some extent by changing the nature of alcoholic and precursors. In most cases, they obtained submicrometric (over 100 nm) and micrometric particles. Here, it was difficult to obtain small particles, even in the presence of water but proceeding at higher temperature succeeded in reducing the particle diameter to circa 125 nm. This strategy is known to promote the formation of more nuclei over their growth [*Sugimoto, 2007*]. A more in-depth study of each parameter influence ought to be undertaken to synthesise nanoparticles, yet the experiments carried out here to highlight the advantages and potential setbacks of the Stöber method. The experiments showed that this method is simple and solely involves the mixing of reagents and ammonium hydroxide in an alcoholic solvent, but it will not produce nanoparticles unless the precursor and catalyst concentrations are strictly controlled [*Park, 2002*].

Conversely, the reverse microemulsion technique is favoured for the synthesis of small and monodisperse nanoparticles of all compositions (silica, iron oxide, quantum dots, etc.). The method is a two phase system where an organic and an aqueous phase are separated by micelles, therefore this strategy is not as straightforward as the Stöber method. The four emulsions tested produced particle between 30 and 70 nm in diameter because the micelles mechanically restrict the size of the final nanoparticles. More experiments would be necessary to clearly asses how water and surfactant concentrations affect the

micelle/particle size, but these experiments are beyond the scope of this thesis. The main setbacks are the presence of organic solvent (harmful and potential toxic) and the long purification process. The purification of the particles was complicated and required several washing step, including washing in acetone to break the micelles. After centrifugation, the particle suspensions got a “soaping” texture signalling that some surfactant and in one case (Mic-2) it was not possible to entirely remove the surfactant. FTIR analyses detected TX-100 traces in Mic-2, but the fact that no signal was detected in the other samples is not a certainty that the particles are free from the surfactant but may be instead caused by a low concentration that falls below the detection threshold of FTIR. Dialysis and/or thermal treatments are potential alternative but are more time-consuming that centrifugation. Getting ride of the surfactant is important for cell-related application because it may be a source of toxicity. In summary the reverse microemulsion technique appears as the opposite of the Stöber method: it easily produces nanoparticles, potentially with a high monodispersity, but the presence of organic solvent and extensive washing and long purification process make of the emulsion strategy a less attractive approach than the Stöber method.

The entrapment of fluorescent dyes is one of the main interests of silica nanoparticles and the natural next phase was to incorporate fluorophores into the particles. Van Blaaderen’s modification of the Stöber method was used to synthesise FITC-doped nanoparticles. FITC has been the first dye incorporated by this method and has since then become a standard. It easily reacts with APTES via reaction between the isothiocyanate of the former and the amine group of the latter. The bright orange material, the same colour as the FITC-APTES conjugate, was a first indicator of the presence of fluorophore within the particles and fluorescence emissions of free FITC and nanoparticles perfectly matched. Van Blaaderen’s modification not only avoids leakage of fluorophore owing to the covalent binding of the fluorophore to the silica matrix but allows exert a good control over the optical properties of the dyes and is suitable for

the design of structures made of multiple layers, potentially containing different fluorophores. Nevertheless, the covalent binding is also a weakness by restricting the number of fluorophores suitable for the sylilation: few dyes possess a reactive organic groups to bind to a fluorophore so that a time-consuming and often difficult chemical reaction is required to make the fluorophore reactive. Few studies explore the possibility to retain the fluorophores by electrostatic interactions, even though using commercial version of dyes rather than their isothiocyanate or maleimide-derivatives is cheaper.

It is possible to estimate the number of fluorophore molecules per particle by measuring the fluorescence of a suspension of known particle concentration and size and to report the value to the calibration curve of free fluorophore. By this mean, the fluorescence of the sample can be related to the equivalent number of fluorophore molecules and to quantify the number of dye molecule per particle. The same strategy can be employed to determine the fluorophore losses by measuring the fluorescence of supernatant [*Traver, 2010*]. Because of the large number of fluorophore present in individual particles, the samples appeared very bright under the confocal microscope. More importantly, the signal barely weakened under strong and constant illumination whereas many stains and dyes are known to photobleach quickly under similar conditions. It is not sure, though, that the effect is due to an actual protection of the fluorophore or to the great number of molecule per particle. Part of the signal was however lost but growing an additional, protective layer of silica may help circumventing the photobleaching issue. Measuring the FSNPs lifetime is one way to quantify the fluorescence stability of the particles and to compare to free dyes in solution. The strong fluorescence and limited bleaching are fundamental assets for contrast agents and explain the high interest in silica carriers.

The optical properties of silica nanoparticles synthesised by reverse microemulsion were likewise tested. There exist very few studies of the encapsulation of organic fluorophore by microemulsion contrary to lanthanide

chelates that are systematically used. Therefore, the experiments carried out in this chapter aimed partially at finding a reason for this gap. Here, RB, R6G, and AO were selected because they are cheap dyes, matche the bandpass filters of the confocal microscope (green and red channel), and because of their availability in the laboratory. Both rhodamines have very high quantum yields (0.75 for RB and 0.95 for R6G) and close chemical structures but different emission/excitation profiles (555/580 for RB and 525/555 for R6G) [*Kubin, 1982*]. Their direct encapsulation, i.e. without any chemical modification or sylilation, was rarely attempted. Acridine orange is a cheap dye commonly employed for cellular staining and with excitation and emission analogous to that of FITC. However, its quantum yield is far lower (0.2) than the other fluorophores which may explain why it has never been tested with silica nanoparticles.

The initial tests ended in blank particles but eventually the reverse microemulsion yielded slightly coloured particles. More precisely, the fluorophores molecules barely penetrated within the micelles and remain in the organic phase so that most of the dyes were lost after centrifugation. Lanthanide chelates are the most frequent fluorophores encountered when it comes to reverse microemulsion precisely because these species are highly hydrophilic and naturally solubilise into the micelles where the particles form. Strategies have been elaborated in order to increase the hydrophilicity of organic fluorophores: the molecules can be conjugated to molecules such as dextran that will help in localising the dyes in the aqueous phase [*Zhao, 2004 b*]. Alternatively, an oil-in-water emulsion may be created instead of reverse microemulsion, where the growth of particles proceeds in the organic phase. In that case, organic molecules solubilise within the micelles and are entrapped during the particle formation. In all cases, the procedure becomes considerably more complex and explains why inorganic fluorophores are preferred.

2.5 Conclusion

In summary, this chapter was principally a test of the two principal synthesis methods of fluorescent silica nanoparticles. The aim was to determine their practicability and their advantages rather than provide an in-depth characterisation of the particle and particle fluorescence. On the one hand, the Stöber method and the related van Blaaderen's modification have multiple advantages: simplicity, flexibility, design of layered architectures, control of the fluorescence properties etc. The major setbacks are the naturally large dimensions of the spheres and the fact that van Blaaderen's method relies on covalent bonding of fluorophores, which can restrict the number of fluorophores suitable for this method. On the other hand, the reverse microemulsion approach yields smaller and potentially more monodisperse particles in the nanometre range, but it suffers from the complexity to prepare emulsions (use of surfactant and organic solvents), long purification, and difficulty to solubilise the fluorophores in the micelles.

More time could have been devoted to the characterisation of the particles (determination of the size dispersity and of the particle stability, quantification of the number of fluorophore per particle, etc.) or to study with greater care the influence of various parameters over the particle dimension. However, none of these methods appeared to provide a satisfactory solution to the synthesis of small nanoparticles able to carry a large diversity of dyes. In fact, a novel method based on the use of amino acid to catalyse the sol-gel reaction was found to produce very small particles in aqueous environment and therefore appeared as a promising alternative to reverse microemulsion. Yet, the potential of the amino acid route to produce fluorescent silica nanoparticles had not yet been explored and consequently the Stöber and the reverse microemulsion methods were discarded and the amino acid route was explored instead.

Chapter 3

Development of multifluorescent nanoparticles for cell labelling and confocal microscopy

3 Development of multifluorescent nanoparticles for cell labelling and confocal microscopy

3.1 Introduction

The European Union has identified bio-imaging as one of the key research areas where nanotechnology can impact. Numerous imaging modalities are available, including MRI, computed tomography, optical microscopy, etc. The current trend sees the combination of two or more modalities to provide more sensitive, specific, and fast analyses. The principal example is the combination of positron emission tomography (PET) with x-ray computed tomography (CT). CT creates very sensitive three-dimensional images of tissues through the reconstruction of two-dimensional x-ray pictures and allows the acquisition of large data volume whilst PET detects the signal of radioactive probes and provides information about functional processes that occur within the body. The duality of PET/CT enables precise localisation of the biological processes of interest and is advantageous for the detection of cancer stage or for the planning of surgical operations. New dual diagnostic modalities progressively appear on the market such as combined MRI/PET that suppresses the radiation burden of x-ray and more can be envisioned such as MRI and ultrasound or ultrasound and optical imaging [*Schiepers, 2011*]. Nanotechnology can improve the hardware of conventional imaging modalities to gain sensitivity, speed of signal acquisition, etc., to miniaturise the equipment, or to facilitate the combination of modalities into a single apparatus. Nevertheless, the main focus of attention lies in the development of contrast agents and other beacons. Traditionally, certain modalities already rely on beacons such as radioactive ^{11}C, ^{18}F or ^{124}I for PET and gadolinium ions for MRI which are either necessary to generate a signal or to create a strong contrast on the images that helps in the diagnosis [*Anderson, 2010*]. With the exception of PET, the sensitivity of most imaging modalities is limited to the organ/tissue level but rarely to the molecular level, yet early detection of diseases requires the recognition of

molecular events. Loci of inflammation, aberrant vascular structures, differentiation of healthy cells into cancerous ones are some examples of events where “molecular imaging” would prove invaluable.

Nanoparticles present two potential advantages for molecular imaging: they can elicit their own optical/magnetic/radioactive signal that the imaging modalities record and they can be modified to bind and interact with specific targets via bio-conjugation or surface modification. Therefore, the aim of nanotechnology in the imaging domain is to devise contrast agents that localise with more precision and more specificity certain tissues and favour the detection at a more sensitive level than what is currently achieved [*European Technology Platform on NanoMedicine, 2006*]. Over the last decades, new probes have been developed: quantum dots, gold or iron oxide nanoparticles are the prime examples of nanoparticles with high potential in molecular imaging and some iron oxide nanoparticles are even clinically approved for MRI application. New contrast agents will emerge with the appearance of multifunctional structures suitable for dual imaging or matching the requirement for several modalities simultaneously. Progress in genomics and proteomics shed light on the mechanisms underlying diseases and identified the potential culprit of change such as proteins, enzymes, DNA/RNA that are potential targets of molecular imaging. The tools exist but the main challenge remains to modify the probes in order to bind to the correct antigen or cellular target to ensure that the particles reach their destination unhampered.

MRI and optical modalities are the principal imaging techniques on which nanotechnology focuses. Briefly, iron oxide nanoparticles are the principal contrast agents for MRI and create a strong disturbance of the local magnetic field. They are preferentially used for the detection of tumours or the tracking of dendritic cells/macrophages or stem cells and other transplanted cells. Gold nanoparticles under their various shapes rely on plasmon resonance to create a strong signal for optical imaging, including confocal microscopy or optical computed tomography. In contrast, fluorescence-based optical imaging

modalities are able to identify quantum dots and fluorescent silica nanoparticles (FSNPs) [*Sharma, 2006*].

Nanoparticulate systems for the other modalities remain rarer, although strong candidates, in particular gold nanoparticles, have emerged. Probes for PET are based upon the conjugation of radionuclides into or onto nanoparticles since the nanomaterials of interest in medicine lack radioactive features [*Nahrendorf, 201*0]. The development of x-ray probes is more recent: high atomic number elements are usually ideal for x-ray imaging but they are rarely biocompatible. The most widespread probes are iodinated compounds that possess high X-ray energy specific mass attenuation coefficient, and mass energy absorption coefficient that are critical parameters for CT.

Lately, small gold nanoparticles have proved to be powerful x-ray contrast agents, even surpassing iodine whilst iron oxide has shown promises in a few studies as well [*Kim, 2007*]. Likewise, gold is an excellent probe for photoaccoustic imaging as this modality relies on the acoustic response of tissue after pulsed laser irradiation. Thus, the tunability of plasmon resonance to the NIR infrared where most of the pulsed laser sources emit is ideal. Gold nanoshells are the most frequent, but gold nanorods have already obtained excellent results and gold nanocages that possess a higher extinction cross-section are attracting attention. Silica nanoparticles are potential probes when combined to indocyanine green, the sole fluorophore approved by the FDA as a photoaccoustic agent [*Hahn, 2011*]. Multimodal probes usually combine the described materials to be detected by multiple modalities simultaneously [*Cho, 2010 a*]. The advantage of combining modalities is that the probes need a single injection instead of one injection per modality, which is time saving, cheaper, and avoids the repetitive use of potentially dangerous agents such as radionuclides. Gold and/or iron oxide are almost always integrated because they are suitable for several modalities or function, including the most clinically relevant ones [*van Schooneveld, 2010*].

PET, MRI, and CT are commonly found in clinics and hospitals but less in laboratories. On the contrary, optical modalities are more suited to cell culture and thin tissue samples for *in vitro* experiments. They have the advantages of being non-invasive, enable real-time acquisition, possess a high resolution, and are cost-effective [*Sokolov, 2003 b*]. The most widespread techniques are based on fluorescence and take advantage of the large number of fluorophores commercially available. The principal limitation of optical imaging is the high turbidity of tissues, i.e. they are composed of many absorbers, scatterer, and other endogenous fluorophores responsible for autofluorescence - in particular haemoglobin and melanin - that absorb and scatter light, hampering the detection of the fluorophores [*Tromberg, 2000*]. Consequently, it is difficult to uncouple the effects of scattering, absorption and autofluorescence and the depth of penetration of visible light usually employed is of a few millimetres (even less with UV excitation sources).

Infrared and near-infrared (NIR) light penetrates deeper in tissue than visible light. The region of the electromagnetic spectrum between 700 and 1000 nm is known as the “optical window” precisely because few biomolecules in tissues are able to interfere at these wavelengths and the depth penetration reaches the centimetre range [*Frangioni, 2003; Taroni, 2003*]. New modalities based on nonlinear processes, principally two-photon excitation (TPE), become popular because they are powerful tools surpassing the usual fluorescent imaging modalities [*Helmchen, 2005*]. NIR and multiphoton dyes are the best candidates for *in vivo* imaging but traditional dyes emitting in the UV and visible remain perfectly suited for *in vitro* applications.

The previous chapter showed that silica nanoparticles were bright contrast agent but are still restricted by their large size or by a limited variety of fluorophore. However, the traditional methods are unable to synthesise at the same time small particles and particles able to contain a large variety of fluorophores. For this reason, another approach based on the catalysis of sol-gel reactions by amino acid was explored as an alternative to the Stöber

method and reverse microemulsion. This strategy is a biomimetic approach based on the observation that in certain organisms, proteins containing specific sequences of amino acid are able to catalyse the polymerization of silicon precursors to precipitate silica and further mould it into complex structures. It has been found that these sequences are generally rich in aminated amino acid (lysine and arginine). The amino acid route that resulted from this observation possesses interesting features:

- Proceeding in water or aqueous environments;
- Production of very small nuclei 1 to 20 nm in diameter;
- Possibility to enlarge the particles and control their final dimension by incremented addition of silicon precursors (seed regrowth).

Overall, the amino acid route combines the simplicity of the Stöber method with the small size of reverse microemulsion whilst in milder conditions. Because of its novelty, the potential of the amino acid route to produce fluorescent nanoparticles has not yet been investigated but the possibility to create multilayered structures via seed regrowth opens new possibility to design multifluorescent nanoparticles where each layer of the particle can contain one type of fluorophore.

The aim of this chapter is to investigate the potential of the amino acid route to produce fluorescent nanoparticles that can be used as contrast agents in confocal microscopy. The objectives are then divided into:

- The design of core-shell nanoparticles by taking advantage of the seed regrowth strategy
- The encapsulation of up to three fluorophore in separate layers and the assessment of the “multifluorescent” nanoparticles (MFSNPs)

The direct labelling of cancerous cells with MFSNPs for confocal microscopy imaging to detect the particle localisation and their capacity to fluoresce in multiple canals simultaneously.

3.2 Materials and methods

3.2.1 Materials

Chemicals were purchased from commercial sources and used as received without any treatment. Tetraethyl silicate (TEOS) and acridine orange (AO) were purchased from BDH. Anhydrous ethanol (>99.5 %), L-arginine (>98 %), 3-(trihydroxysilyl)propyl methylphosphonate monosodium salt solution (42 wt.%, THPMP), 3-aminopropyltriethoxysilane (APTES, >98 %), and fluorescein isothiocyanate (FITC, Isomer I) were obtained from Sigma Aldrich. Rhodamine 6G (R6G), methylene blue (MB), and tween 20 were acquired from Fluka, Fisher Scientific, and Acros Organics respectively. Finally, sytox green (SG) and streptavidin, Alexa Fluor 555 conjugate (AF, 2 mg-mL) were obtained from Invitrogen. Highly purified water (Milli-Q) was obtained from a Millipore “Direct-Q 3” water purification system.

Prostate cell line were PC3 (derived from a human prostate adenocarcinoma of a 62 years old Caucasian male – ECACC: 90112714) and PNT1A (derived from a human post pubertal prostate normal, from a 35 years old male at post mortem, immortalised with SV40). All cells were grown from seed culture stored under liquid nitrogen and cultured in Dulbeccos modified eagles medium (DMEM) containing HAM’s F12 (1:1) 1x nutrient mix plus 15 mM HEPES & L-glutamine (GIBCO, Invitrogen). The media was supplemented with 10% heat inactivated foetal calf serum (FCS), 200 mM L-glutamine (Invitrogen), 1000 units of penicillin and 1 mg streptomycin (GIBCO, Invitrogen) per bottle. Cultures were grown at 37°C in a 5 % CO_2 atmosphere and were maintained by passage when they had grown to 80-90 %.

3.2.2 Methods

- **Synthesis of multifluorescent nanoparticles following an amino acid route**

The synthesis of blank and dye-loaded nanoparticles proceeded in five steps and all combinations of the three dyes were attempted (**Figure 3-1**):

- Silica seeds were initially formed by mixing 330 mg of L-arginine with 6.9 mL Milli-Q water. Afterwards, 555 µL TEOS was added five minutes later and the solution was magnetically stirred for 24 hours;

- The first layer was to contain MB: 1 mL of seed solution was mixed with 3.6 mL of Milli-Q and in some cases with 32 µL of a 15 mM MB solution. Then, 255 µL of TEOS was added and the reaction was left to proceed for 12 hours under magnetic stirring;

- The second layer was designed to encapsulate R6G: the former suspension was mixed with 250 µL of MilliQ, 211 µL of TEOS, and 63 µL of a 7.9 mM R6G solution if the particles were to contain the dye. This step lasted 12 hours under magnetic stirring;

- The third layer was obtained by addition of 62 µL of an APTES-FITC conjugate solution (see preparation in Chapter II) to the particle suspension or 1.2 mL of TEOS for a blank layer. The solution was magnetically stirred for 12 hours.

- 1 mL of TEOS was introduced to the suspension, followed 30 minutes later by 30 µL of THPMP and 5 µL of APTES and left for 12 hours under magnetic stirring.

The samples were centrifuged 3 times at 1200 g for 15 minutes or until supernatant remained clear, with washing first with acetone and then with distilled water.

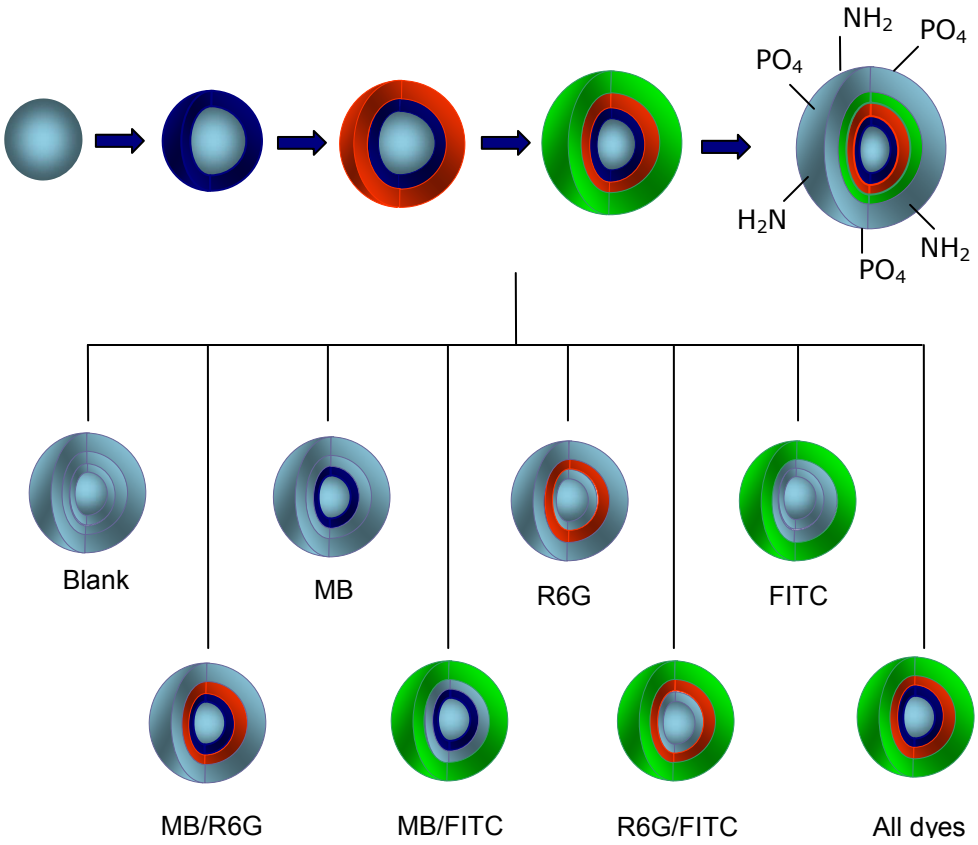

Figure 3-1: Representation of the synthesis steps of the multifluorescent nanoparticles and the dye combinations.

- **Cell culture**

Once PC3 and PNT1A lines adhered, passaging required the use of trypsin/EDTA to detach the cells from the surface of the culture flasks. Cultures were first washed in 10 ml of sterile PBS followed by the addition of 5 mL of 1x 0.5 % trypsin/EDTA solution (GIBCO, Invitrogen, UK) to each flask. This was incubated at 37ºC for approximately one minute, or until detachment could be detected, upon which the cells were removed from the flask and placed into a centrifuge tube containing 5 mL of media to inactivate the trypsin. The suspension was then centrifuged at 307 g at 4ºC for 5 minutes. The supernatant was discarded and the cells resuspended in 3 mL of media. Finally, 1 mL of the cell suspension was subcultured into each fresh flask.

- **Incunbation with NPs**

Cells were grown in a T75 flask until 80% confluence was reached (~800*10^4 cells/mL) and then trypsinised and resuspended in 1 mL of DMEM media. Cells were seeded in a 8-well plate (1 µL-Slide 8 well, ibidi Integrated BioDiagnostics) at a concentration of 15000 cells/well completed with 300 µL DMEM and incubated overnight. At the end of the period, media was discarded, the plate was washed with PBS and the wells were filled with nanoparticles suspended in DMEM (100 µg/mL). The cells were incubated for a period ranging from 1 to 3 days. Finally, the particle suspensions were discarded, the plate washed with PBS and fixed by dipping the plate 15 minutes in cold PBS and then 15 minutes in cold methanol.

After fixing, the nucleus of cells labelled with FITC-doped nanoparticles were stained with sytox green (500 nM) and their cytoplasm was counter-stained with AlexaFluor 555 (5 µg/mL). Sytox green was later replaced by acridine orange (20 µL/mL) in the multifluorescent nanoparticles experiments.

3.2.3 Characterisation

- **Scanning electron microscopy (SEM)**

The particle size and morphology were examined using scanning electron microscopy (SEM). The nanoparticle suspensions were firstly diluted: the samples were sonicated and subsequently 25 µL of suspension was poured in an eppendorf and the total volume was increased to 500 µL with Milli-Q water so that the SEM samples were totally transparent. One drop of suspension was deposited into a silicon grid and let to dry in a desiccator for at least 24 hours. Finally, the particles were imaged using a high resolution FEI XL30 SFEG analytical SEM (Philips, Netherland).

- **Dynamic light scattering (DLS)**

The size and size distribution of the particles were measured by dynamic light scattering using a Zetasizer nano series S with an He/Ne laser of 633 nm wavelength (Malvern Instrument, UK). The particle suspensions were firstly diluted: 10 µL of the sample was poured in a quartz cuvette and completed with 1 mL Milli-Q. The refractive index and absorption of silica nanoparticles were fixed at 1.25 and 0.01 respectively. For each sample, four measurements of 20 runs (15 seconds each) were carried out, with temperature maintained at 25°C.

- **Fourier transform infrared spectroscopy (FTIR)**

The particle composition was analysed by infrared spectroscopy: a volume of nanoparticle suspension was taken, centrifuged, and dried in the oven for 1 day. The resulting powders were subsequently analysed in KBr powders using a Thermo Nicolet Avatar 370 spectrometer (Thermo Scientific). Infrared spectra were recorded over the wavenumber region 4000 to 400 cm^{-1} with a resolution of 4 cm^{-1}.

- **Fluorescence measurement**

Absorbance and fluorescence of FSNP were recorded in 96-well plates with a Varioskan Flash Spectral Scanning Multimode Reader (Thermo Fisher Scientific) equipped with a xenon flash lamp. All measurements were performed on 200 µL of 1 mg/mL suspensions of particles diluted in Milli-Q and at room temperature. Excitation/emission spectra of FITC and R6G were acquired with fixed wavelength set at 450/530 and 490/580 nm respectively.

.

- **Confocal microscopy**

FSNP and cells were imaged using a LSM 510 META Inverted Laser Scan Microscope (Zeiss). The system is equipped with three laser lines that were used separately to excite the samples. Images were obtained using a Plan-neofluar 40X/1.4 oil immersion objective and the resulting images were colour-coded in green, red, and blue for excitation at 488, 543, and 633 nm respectively. Furthermore, the software (Zeiss LSM confocal software) enables overlaying pictures to produce dual-coloured images. All images were the average of sixteen scans and were obtained with the same optical aperture, lens, and scan speed.

3.3 Results

3.3.1 Synthesis of multifluorescent nanoparticles

The multifluorescent nanoparticles were based on small seeds obtained by the amino acid route and onto which three silica layers were grown. Additionally, the surface was modified to express amine and phosphonate groups, a procedure usually employed to improve the stability of the particles. Each new layer aimed at containing methylene blue (MB), rhodamine 6G (R6G), and fluorescein isothiocyanate (FITC) in that order, and all combinations from blank particles to structures containing all three dyes were tested. DLS measurements were conducted to follow the change of dimensions throughout the whole process. The initial seeds were found to be 5 nm in diameter but the protocol only yielded trace amounts of nanomaterial. The diameter grew to 6, 8, 11, and 20 nm respectively (**Figure 3-2**) but the high polydispersity index of the samples indicates that the particles potentially clustered and even aggregated after the reaction with APTES and THPMP. SEM pictures confirmed the DLS findings as the images displayed very small particles 20 to 30 nm in diameter that formed large aggregates despite of the surface modification with the two organosilanes (**Figure 3-3**).

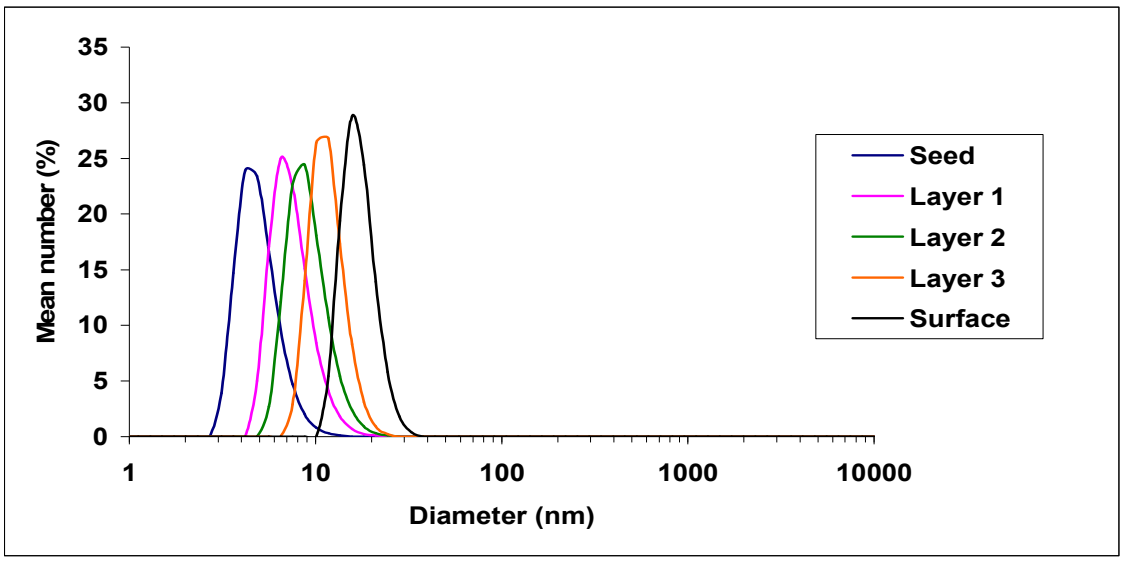

Figure 3-2: DLS spectra of R6G-FITC-containing silica nanoparticles.

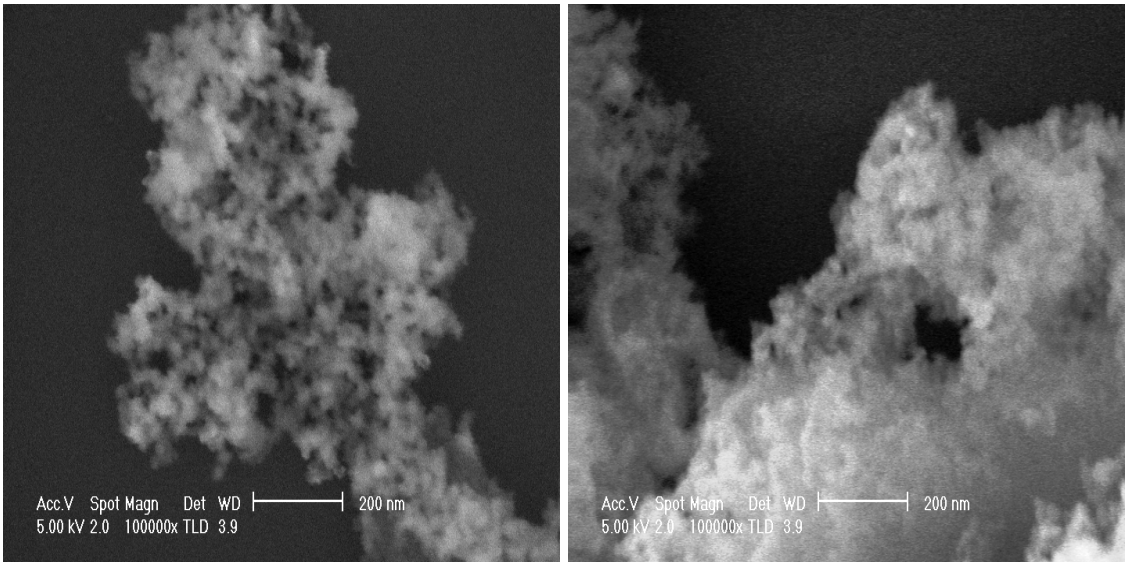

Figure 3-3: SEM picture of R6G-doped nanoparticles (left) and particles containing all three dyes (right).

FTIR spectra taken at different steps of the procedure all displayed the siloxane and silanol peaks which confirm that the silica matrix formed (**Figure 3-4**). The addition of APTES and THPMP slightly modified the spectrum with a broadening of the 3500-3000 cm^{-1} region as an effect of the amine groups as well as of the 1300-1100 cm^{-1} region. Phosphonate is supposed to create peaks at 1244, 1050, and 1026 cm^{-1}, but the large band characterising Si-O-Si screens the phosphonate signal. The other possibility is that THPMP did not react with the particles in the first place but FTIR is not able to detect it. Zeta potential measurement would be the best way to follow the changes of the particle surface by detecting the alteration of the particle charge when amine and phosphonate are expressed. It can only be said, from the FTIR spectra, that APTES has reacted with the particles and amine groups are present but the phosphonate groups have yet to be identified.

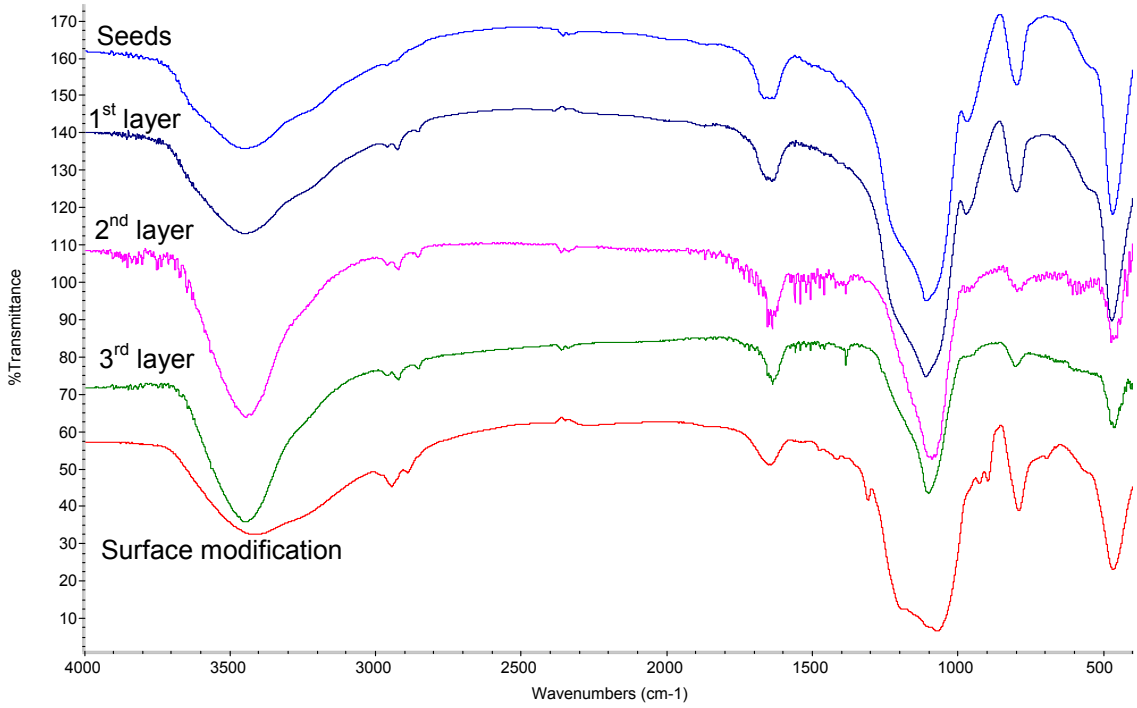

Figure 3-4: Infrared spectra of MFSNP of the different stages of synthesis of the particles from the silica seeds to the surface-functionalised final particles.

The nanoparticles suspensions exhibited bright colours directly related to their dye composition. Hence, blank particles were white, whereas FITC-, R6G-, and MB-doped particles were respectively yellow, red, and blue. The colour of the nanospheres containing two fluorophores was that of the corresponding mixture of colour: orange for FITC-R6G particles, green for MB-FITC, and violet for MB-R6G. Likewise, the solution containing all three dyes displayed a violet colour (**Figure 3-5**).

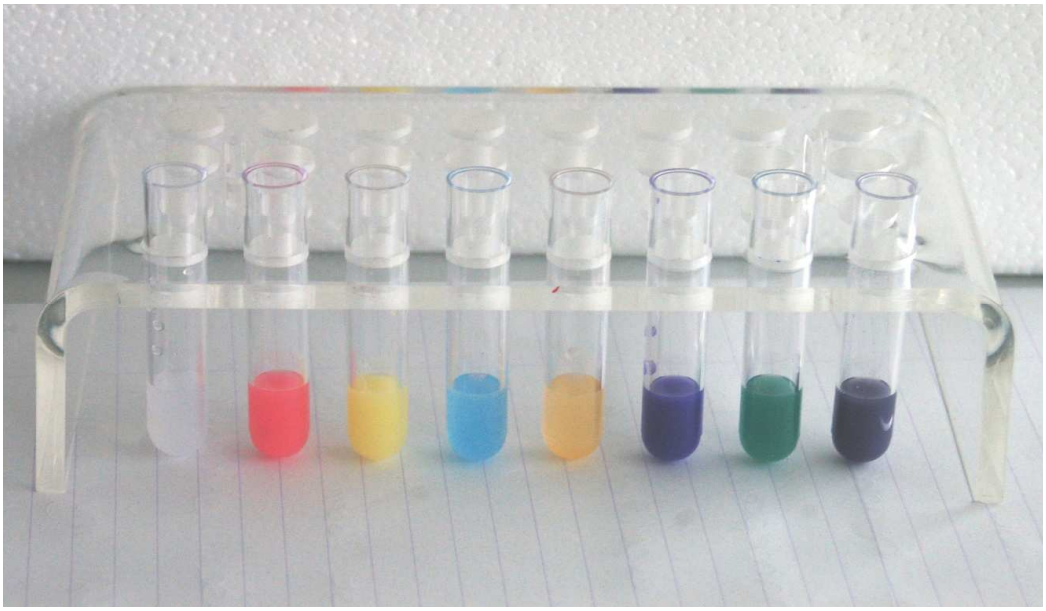

Figure 3-5: (From left to right) blank, R6G-, FITC-, MB-, R6G-FITC-, MB-R6G-, MB-FITC-, R6G-FITC-MB-doped nanoparticles.

Absorbance spectra of solution containing FITC presented a peak at 490 nm while particles containing MB exhibited a peak at 610 nm with a broad shoulder in the 650-670 nm range (**Figure 3-6**). R6G-doped nanoparticle solutions exhibited a peak at 525 nm as well as a shoulder at 500 nm. The latter occurs when dyes are in close proximity or because of the formation of dimers during the dye encapsulation. The spectra of samples containing two dyes displayed multiple peaks, for instance at 495 and 525 nm for the FITC-R6G sample or the FITC peak and MB band for the FITC MB-loaded nanoparticles. The same effects were visible on the sample containing all three dyes. However, there is no certainty that each particle effectively carry all the fluorophores. In fact, the suspensions may be composed of mixed particle populations containing one, two, or three fluorophores.

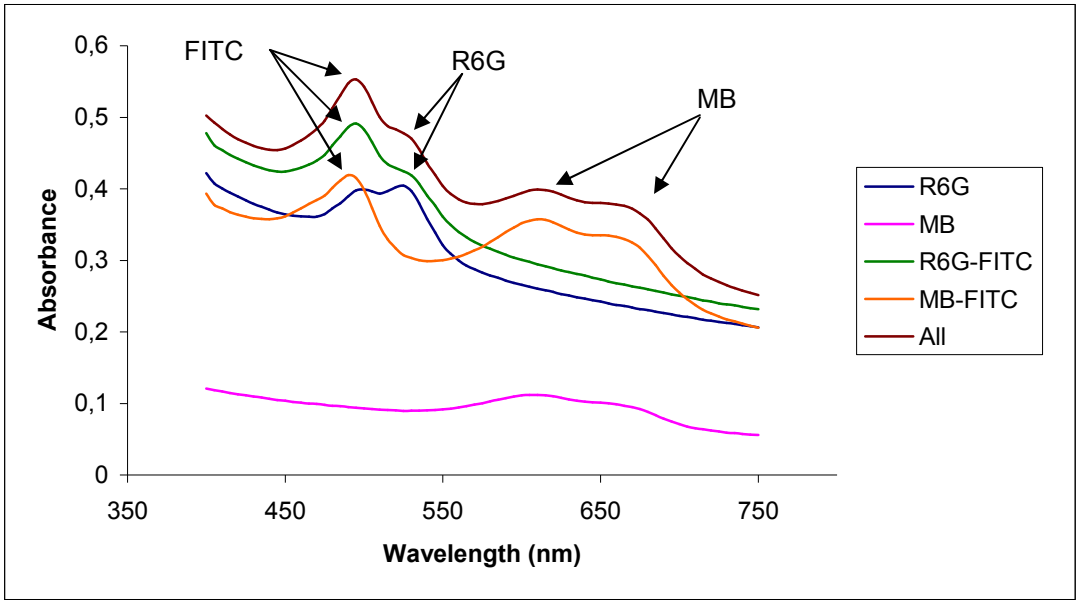

Figure 3-6: Absorbance spectra of MFSNPs containing R6G, MB as well as thei dyes combined to FITC.

Fluorescence measurements confirmed the dye composition of the nanoparticles, with excitation/emission at 525/555 nm and 495/515 nm whenever R6G and FITC were present respectively. Both dyes signals were clearly distinguishable with a single excitation wavelength, although the overlapping of FITC and R6G means that part of the FITC signal is used to excite R6G (**Figure 3-7**). In contrast, MB did not display any fluorescence at all and the excited light may have been converted into another form that photoluminescence. However, additional analyses are required to confirm that a single particle effectively contain all of the fluorophores were trapped during the particle growth and not that the suspension is composed of different populations of particles with random optical signatures. To do so, single fluorescence spectroscopy could be sensitive enough to measure the optical properties of a single object. In the same vein, the new generation of confocal microscope has a sensitivity of a few nm and may be able to distinguish the signal of single particles and to subsequently determine their spectral signature.

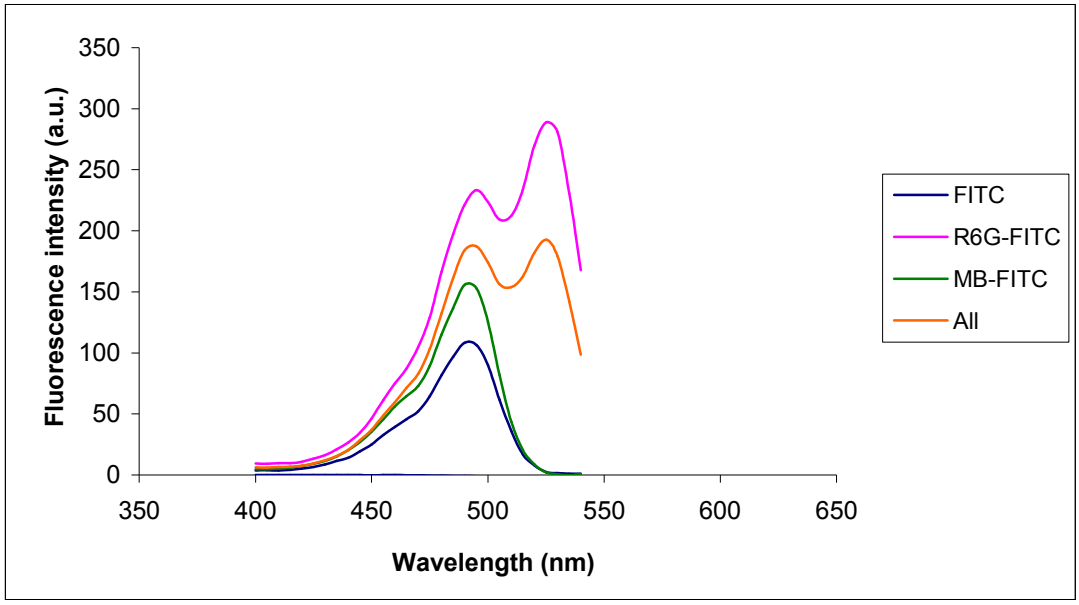

Figure 3-7: Emission spectra of FITC-doped and systems containing FITC and a second fluorophore.

3.3.2 Cell incubation and confocal microscopy

The second part of this chapter consisted in employing the new multifluorescent nanoparticles as contrast agents for confocal microscopy. Two different cell lines, prostate adenocarcinoma (PC3) and prostaste epithelial cells (PNT1A), were chosen for this study. Both cells lines possess distinctive morphologies: PNT1A are elongated and closely packed whilst PC3 are larger and more spherical (**Figure 3-8 A and B**). A preliminary study with FITC-doped nanoparticles synthesised by the Stöber method over a period of 1 to 3 days showed difference of particle uptake. After 1 day incubation, very few particles were detected near the nucleus but only after bleaching of the nuclear stain (**Figure 3-8 C and E**). Images were similar after 3 days, suggesting a low particle uptake for this specific cell line. Conversely, the uptake of particles by PC3 cells was important and immediately observed (**Figure 3-8 D and F**). The nucleus staining and cytoplasm counter-staining helped in locating the particles:

the images show large aggregates in the cytoplasm and isolated particles and small clusters in the vicinity of the nucleus. The acquisition of three-dimensional pictures further proved that the particles effectively penetrated within the cells and none of the clusters found close to the nucleus penetrated within the nuclear domain.

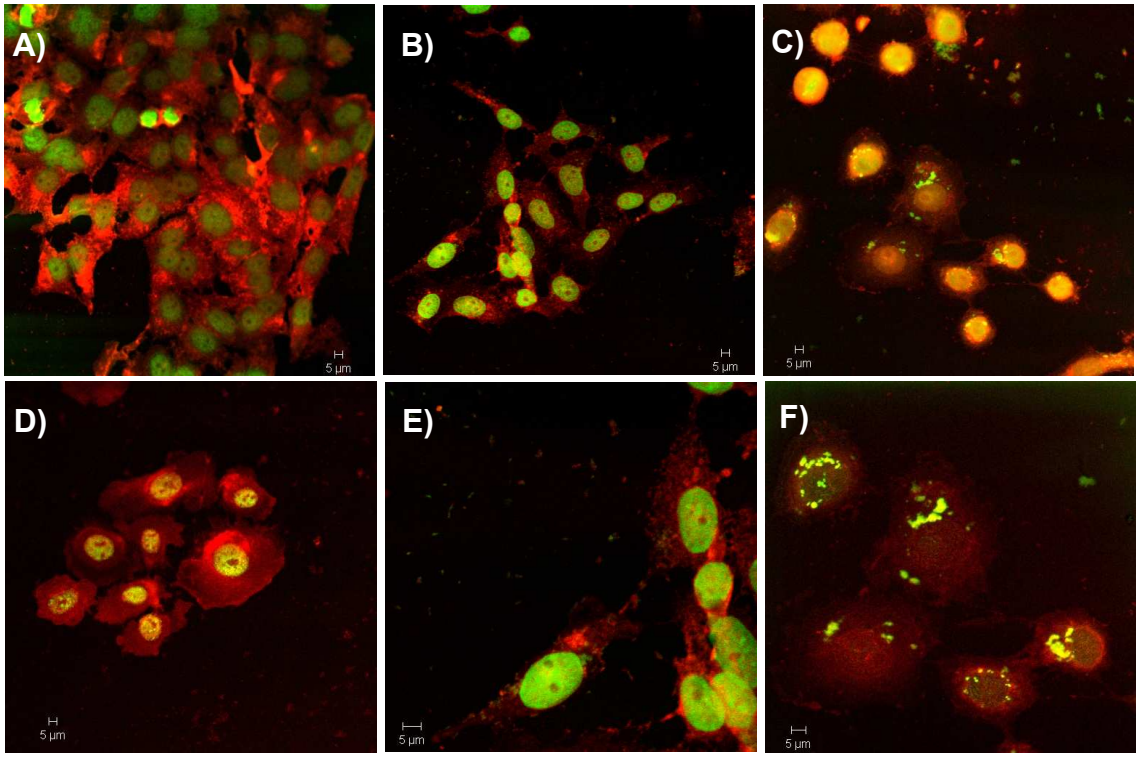

Figure 3-8: Confocal images of control PNT1A (A) and PC3 (D) cells after double staining and PNT1A (B and C) and PC3 (E and F) incubated for two days with FITC -doped silica.

Multifluorescent nanoparticles were tested in similar conditions over an incubation period of 12 hours. The staining of PNT1A did not proceed properly, possibly because the cells were kept for too long prior to imaging. The endosomes appeared very bright and the cells lacked of the smooth aspect previously observed. No particle was observed in the case of the nanoparticles containing a single fluorophores; however FITC-R6G and FITC-R6G-MB containing particles were detected in a few cells in the green channel (**Figure 3-9**). Reasons for this discrepancy are not known, especially since the particles

were synthesised following the same procedure. All that can be said is that the low particle uptake was once again observed, but additional experiments with flow cytometry are required to quantify this uptake and the imaging must be repeated to evaluate more clearly the location of the rare particles taken up by the cells.

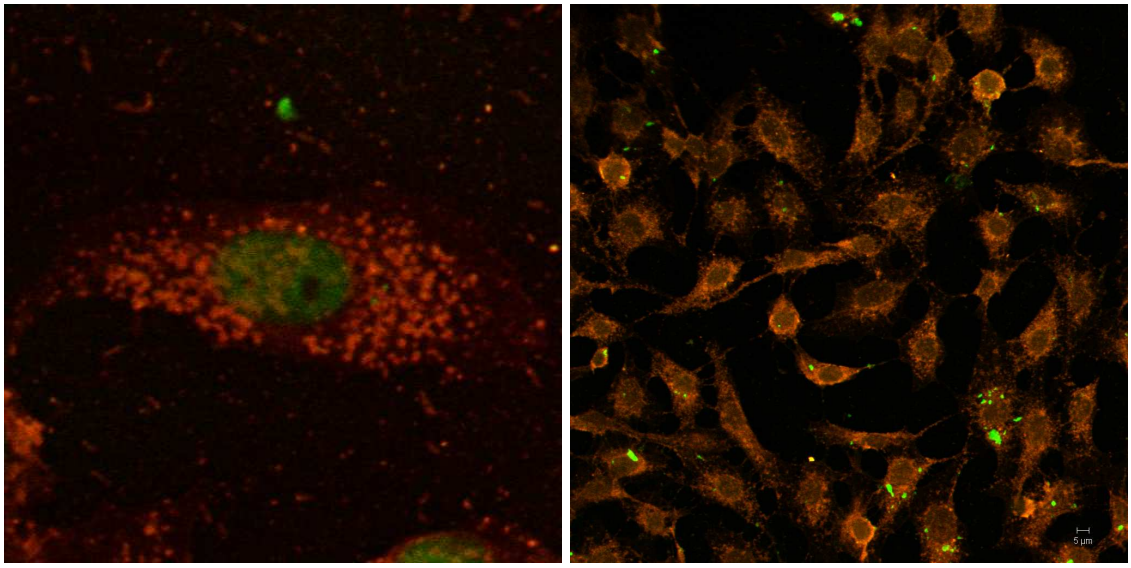

Figure 3-9: Confocal image of PNT1A cells incubated with FITC-R6G-combined particles (A) and particles containing the three dyes (B).

The results with PC3 cells were very different. Starting with R6G-doped particles, large aggregates were detected on the edges of the cells and generated a strong red signal that could be discriminated from the fluorescence of AF555, even though both dyes were detected in the red channel (**Figure 3-10 A**). The principal evidence of the particles presence is the higher fluorescence intensity of the FSNPs responsible for the bright red colour between the cells. The confocal microscope proposes additional functionalities to study cells in details. First of all, the fluorescence intensity can be scaled to map the fluorescence distribution in a picture. Here, the red channel depicts areas of high intensity that can be attributed to R6G because of their presence onto and between the cells whereas AF555 solely delimits the cytoplasm of cells and its intensity is weaker than that of R6G (**Figure 3-10 B**). The

scattergram is similar to the fluorescence distribution tool but enables to discriminate the signal with more precision by defining a minimal intensity level of interest (gating). It is clear from the pictures that the white signal – which correspond to the highest fluorescence intensity – are distinct from the stain signal and arise from R6G contained within the particles (**Figure 3-10 C**). The lack of distinction between R6G and AF555 hampered the construction of three-dimensional pictures: this option is less precise than the imaging of a single focal plane and the computer was not able to unmix the two dyes so that the cells appeared swollen and blistered, with no clear delimitation of each cell (**Figure 3-10 D**).

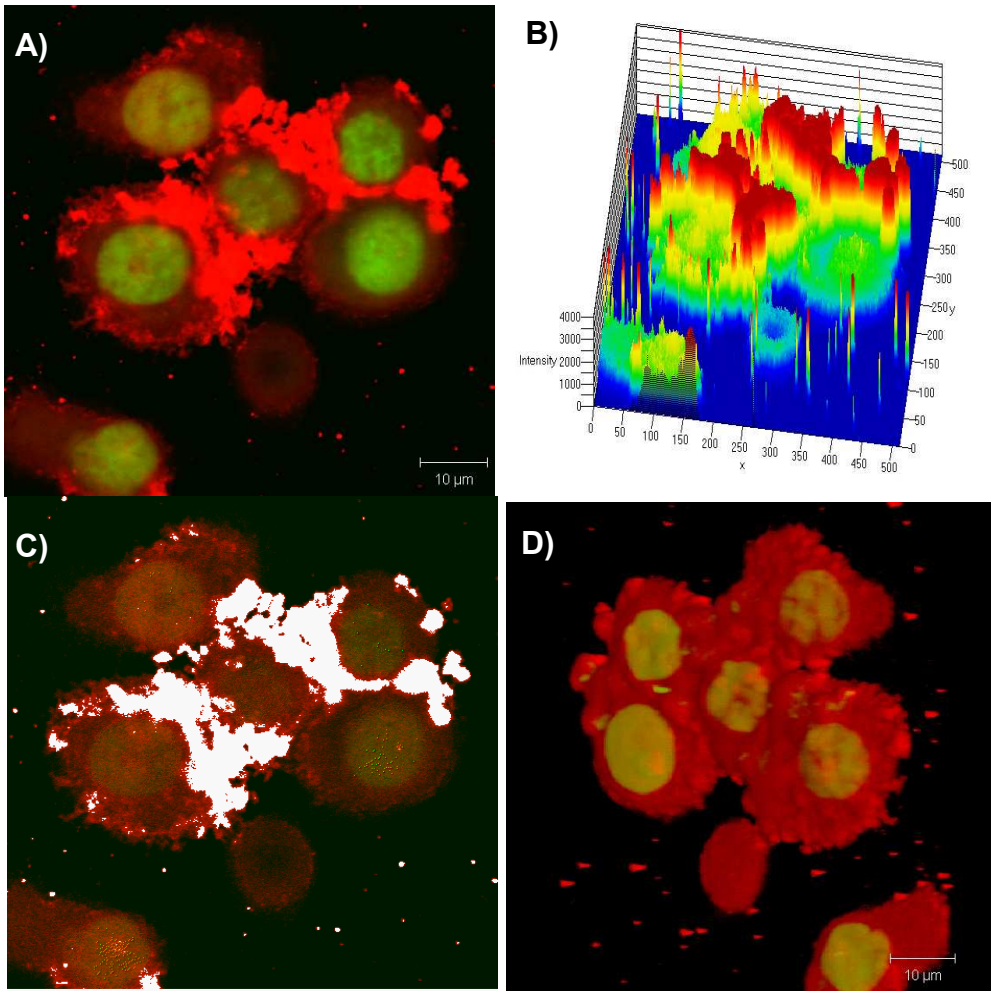

Figure 3-10: Confocal picture of PC3 cells labelled with R6G-loaded nanoparticles (A) , fluorescence intensity distribution in the red channel (B), scattergram (C), and three dimensional picture (D).

Better quality pictures can be acquired with longer acquisition time but this method increases the chances of AF555 bleaching. Note, however, that the confocal microscope used for this study proposes an option allowing distinguishing with more precision the difference of wavelength emission and to colour each signal with a different colour but it was not possible to use this upgrade at the time of the study.

The tracking of R6G-FITC particles within the PC3 cells proved easier because the particles were detected in the green and red channels so that the overlay of the pictures taken with the 488 and 543 nm sources ascribed a yellow colour to the particles (**Figure 3-11 A**).

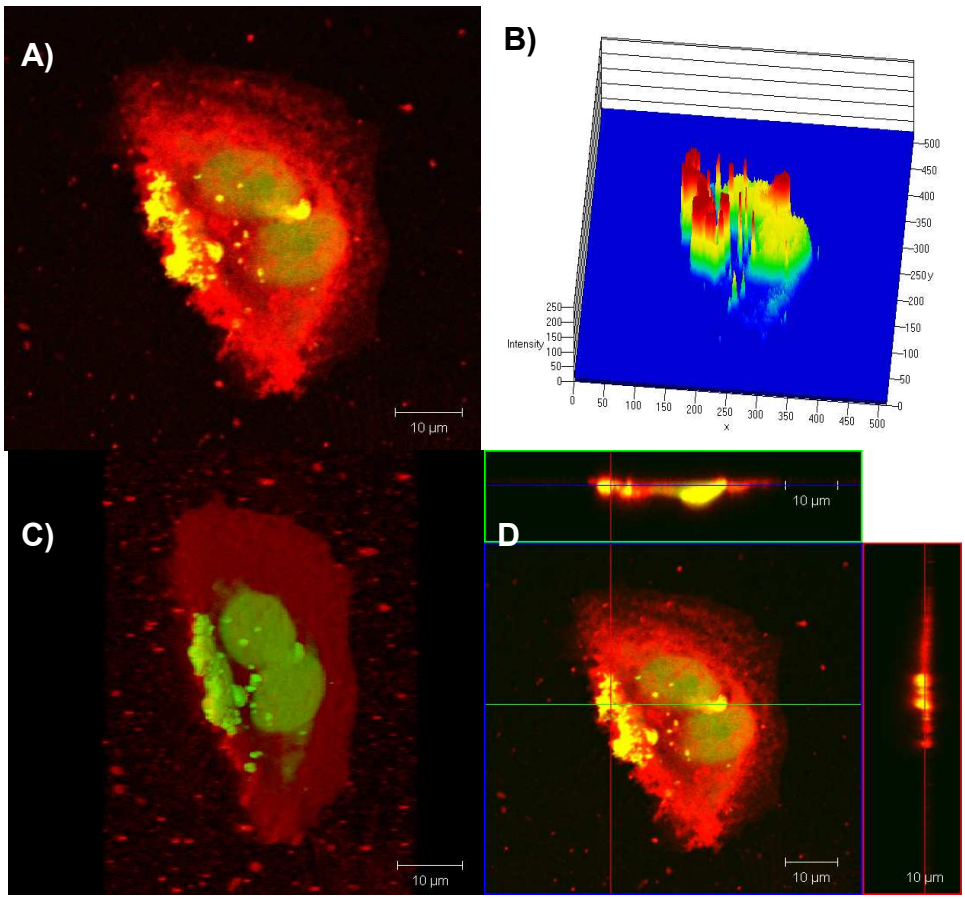

Figure 3-11: Confocal picture of PC3 cells labelled with R6G- and FITC-containing particles (A) and fluorescence intensity distribution in the green channel (B). The three dimensional picture was obtained after acquisition of images at different focal plane (C) and allows sagittal and transversal cuts to determine the localisation of the nanoparticles (D)

The tracking of R6G-FITC particles within the PC3 cells proved easier because the particles were detected in the green and red channels so that the overlay of the pictures taken with the 488 and 543 nm sources ascribed a yellow colour to the particles (**Figure 3-11 A**). The intensity distribution in the green channel depicted bright region matching the position of the yellow areas in the first pictures and contrasting with the mild signal of the acridine orange nuclear stain (**Figure 3-11 B**). The three dimensional image coupled to the sagittal and transversal cuts provided one more evidence that the particles were located within the cytoplasm. It also provided information about the location of the particles, present as aggregate along the internal cell membrane and a few clusters in the cytoplasm, but in no case the particles seemed to have entered the nucleus domain (**Figure 3-11 C and D**)

Finally, the particles containing all three dyes also generated a high signal in the red and green channels but the lack of MB fluorescence prevented its detection by the confocal microscope (**Figure 3-13 A**). However, there seemed to be two different populations of FSNPs: some areas were yellow due to the presence of both R6G and FITC but other areas remained green. This may be an indication that the APTES-FITC complex condensed into separate particles rather than condensed onto the already formed nuclei and tallies with the assumption that the suspension of particles are not optically homogeneous. This segregation was further highlighted by the fluorescence distribution that clearly shows that the strong green signal of the particles does not always superimpose on the fluorescence in the red channel (**Figure 3-13 B and C**). The three dimensional picture of the cells showed again that the internalised aggregates were localised close to the cell membrane whilst smaller particles migrated closer to the nucleus without penetrating into the nuclear membrane (**Figure 3-13 D**).

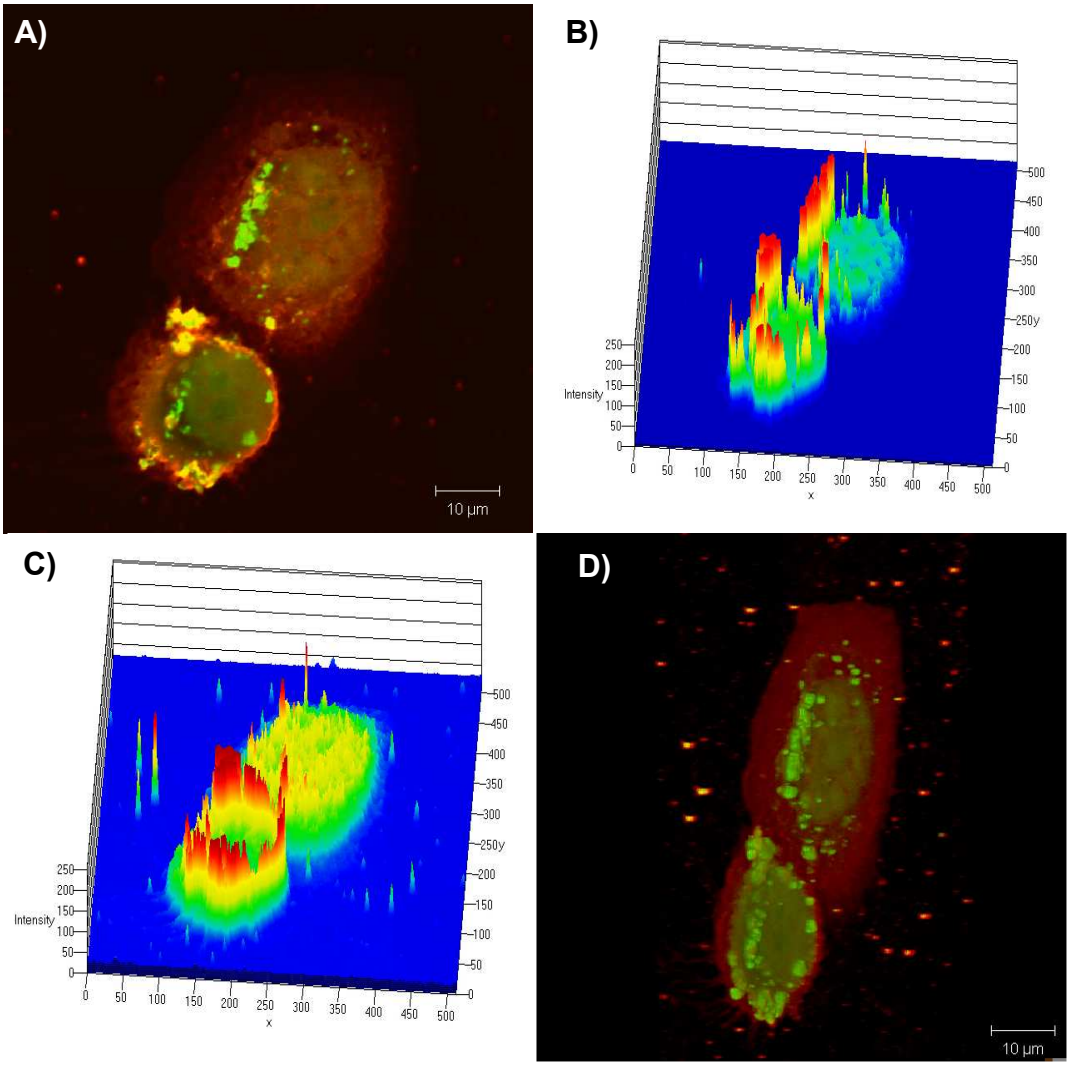

Figure 3-12: Confocal picture of PC3 cells labelled with R6G- FITC-MB-containing nanoparticles (A) and fluorescence intensity distribution in the green (B) and red channels (D). The last picture displays a three-dimensional representation of PC3 under a 45° angle (D).

3.4 Discussion

3.4.1 Nanoparticles synthesis

The aim of this chapter was to explore an alternative way to produce FSNPs and multifluorescent nanoparticles. The idea originated from the difficulty to obtain small fluorescent particles using conventional procedures as discussed in chapter 2. The amino acid route is still ill-explored, but appeared as an attractive and elegant method based on natural mechanisms encountered in certain organisms such as algae and glass sponges. The method possesses two distinct features:

- The replacement of the strong ammonium hydroxide by L-arginine;
- The replacement of organic and alcoholic solvents by water.

Arginine (and lysine) is a weaker base than ammonium hydroxide but the pH of the arginine solution of about 10 and the presence of two amine groups create favourable conditions for the condensation of TEOS into particles.

Here, DLS characterisation indicated that the initial seeds were circa 5 nm. These nuclei were further enlarged by iterative addition of TEOS to the system (also called seed regrowth) to create three additional silica layers. An additional step aimed at modifying the surface of the particles with amine and phosphonate groups to ensure stability via electrostatic repulsion and to express reactive groups for potential bioconjugation with ligands. The formation of new layers is made possible by the presence of free hydroxyl groups at the surface of the particles (silanol groups Si-OH) that groups act as anchors for the condensation of more silicon precursor molecules. DLS measurements showed an increase of the particle diameter from 5 to 11 nm that may be the result of the deposition of new layers onto the original nuclei, and the final surface modification brought the nanoparticles to about 20 nm in diameter. The quantities of TEOS added during each steps were calculated based on the equation [*Hartlen, 2008*]:

$$\left(\frac{Diameter_{final}}{Diameter_{seed}}\right)^3 - 1 = \frac{Mass_{TEOS,added}}{Mass_{TEOS,seed}}. \quad \textbf{(3-1)}$$

In theory, the quantity of TEOS added to the nuclei suspension was calculated to grow the nanoparticles by 20 nm after each step in order to bring the final particles up to a diameter of 80 nm. Practically, the diameter of the nanoparticles only increased by circa 5 nm 5 nm according to the DLS values. It must be ponted out that the equation ought to be modified to take into the consideration the difference of APTES hydrolysis and condensation rate since the silicon atom is connected to three alkoxide groups instead of four. One important observation is the small quantities of unmodified seeds obtained (1-2 mg approximately). It is difficult to assert why such a small amount was produced in view of the limited literature dedicated to this method. In contrast, about 200 mg of material was obtained at the end of the procedure, perhaps because of the nucleation of new particles occurring in parallel to the enlarging of the already formed nuclei.

The surface modification with THMPMP on silica nanoparticles aimed at stabilising the suspensions by creating repulsive interactions between the nanospheres owing to the negative charge of the phosphonate groups. APTES, on the other hand, is generally employed as coupling agent because its amine group is able to react with many other functional groups via conventional chemistry reactions. However, handling of THPMP was complicated because the compound formed a gel prior to its addition to the particle suspensions, which may have prevented its condensation onto the nanoparticles. Instead, the amine groups were free to cover the whole particle surface and may be responsible for the strong aggregation observed on the SEM images. This is due to the capacity of amine moieties to create hydrogen bonds with the silanol groups at the surface of the particles. The effect is reinforced because of the positive charge of the amine groups that attract the negatively charged silanols so that eventually, the particles are strongly attracted one to the others. Infrared spectroscopy proved that the amine groups were present in the sample but no phosphonate was detected. This absence may either originate from a screening

of the phosphonate peaks by the strong siloxane band or because the organosilane was unable to react with the particles in the first place. Additional measurements, in particular of the zeta potential, are required to follow up the surface modification of the particles and make sure that the suspensions are stable. Overall, the procedure must be refined to 1) increase the nuclei density, 2) control the particle diameter after each step, and 3) control the functional group densities to obtain stable suspensions.

One of the objectives was to design multifluorescent systems able to carry two or more fluorescent dyes. Such systems are rare in spite of the advantages that such system provides (multiplexing, multimodality, etc.). The MFSPNs exhibited strong colours depending on their fluorophore content, from the yellow, pink and blue of FITC, R6G, and MB, to the green, orange, and purple resulting from the dye combinations. FITC was chosen to test the covalent binding whereas MB and R6G were incorporated within the matrix by electrostatic interaction. These dyes were chosen due to their distinct emission wavelengths and their availability in the laboratory. Each of them was added at a different step of the procedure for integrating the dyes in separate layers when new silica layers were grown. Only the initial seed were kept free of fluorophores because of the small particle density. However, the absence of centrifugation (to remove excess dye molecules) means that MB and R6G are most likely present in several layers. In other words, it is necessary to carry out experiments once again while centrifugation between each step to confine each fluorophore in the separated layer.

Fluorescence measurements confirmed that the fluorophores were present in all samples Excitation and emission of FITC and R6G were distinguishable and the emission of the two dyes was obtained with a single wavelength. Nevertheless, the plate-reader gives an average of the excitation and emission of a suspension but the spectra do not ascertain that all the particles exhibit the same spectral signatures. In fact, there are chances that some particles may contain a single dye and some other contain combinations of fluorophores at different ratios. For example, confocal images (**Figure 3-14 A**) suggested that

some particles contained simultaneously FITC and R6G as shown by their yellow colour (overlay) but other particles only exhibited the green colour of FITC, proof that the particles do not possess uniform optical properties. Other techniques such as new generation of confocal microscopes, flow cytometry, and single molecule spectroscopy must be used to better characterise the optical properties of the nanoparticles and their dye content. The sensitivity of the last generations of confocal microscope is high enough to image single nanoparticles and they are able to unmix the signal of fluorophores localised in the same area. In other terms, the new generation confocal microscopes can image single particles and probe what dye(s) they contain. Likewise, flow cytometry may provide more information provided that the fluorophore emissions match the cytometer detectors, but the technique may not be able to record the signal of single particles. Finally, single molecule spectroscopy may be the most sensitive technique of the three and is potentially able to measure the optical properties of one or two particles at a time.

Overall, the core-shell architecture appears to contain more than one fluorophore and is a potential alternative to design multifluorescent systems without relying exclusively on covalent binding [*Wang, 2006*]. Additional experiments are necessary to gain a better control over the fluorescent pattern of the particles and to make sure that the dyes are sequestered in the appropriate layers. Moreover, more characterisation the optical properties of the suspensions is needed, especially to prove that the particles are spectrally uniform.

3.4.2 Cellular uptake

Before using the MFSNPs on cells, preliminary experiments were conducted with FITC-doped particles synthesised by the Stöber method (125 nm in diameter). The uptake of the PC3 and PNT1A cell lines qualitatively different: the internalisation of particles was reduced in the case of PNT1A but a large quantity of FSNPs was detected within the PC3 cytoplasm. Location of the

particles could be determined thanks to a double staining of the cells and the confocal images displayed a few particles or clusters close proximity to the nucleus after partial bleaching of the nuclear stain. Over three days, no difference of internalisation was noticed and it was concluded that PNT1A affinity for the FITC-doped particles was very limited. In comparison, PC3 cells gathered up the internalised particles to form large aggregates localised in the cytoplasm (close to the membrane) but the particles never seemed to cross the nuclear barrier.

Labelling with the multifluorescent nanoparticles showed a similar trend with little or no internalisation by PNT1A and an important uptake and aggregation with PC3, although experiments on the PNT1A must be repeated. The FITC signal of the MFSNPs was easily detected and discriminated from that of the nuclear stain. The signal of R6G was more difficult to detect, especially because R6G and AF555 were both detected in the red channel. The only way to discriminate the two fluorophores was by comparing the brightness of the particles to the uniform cytoplasm stain. Note, however, that the confocal microscope is equipped with a device called the META detector that is able to separate the emission signal into various wavelengths (10 nm increment) and to display each fluorophore separately on the picture (fingerprinting). This device would have enabled to unmix the signal of R6G and AF555 and may have revealed the nanoparticles on the 3D images. When both FITC and R6G were contained in the suspensions, the overlay created a yellow colour where the particles were located. The colocalisation of FITC and R6G was the main aim of this chapter and presumes that the nanoparticles can contain multiple fluorophores to generate distinct spectral signature. Selecting fluorophores appearing in different channels (or distinguishable by the META detector) or varying the dye ratios may create suspensions of particles with distinct signature. Moreover, it may be possible to target and simultaneously image different cell lines or organelles with appropriate bioconjugation of the MFSNPs. However, as discussed above, this step is not reached yet and a better control over the optical properties and stability of the suspensions must first be achieved before allowing multiplexed imaging. Furthermore, even though the

study has mostly explored a different strategy to design contrast agents, certain questions have been raised linked to the imaging of cells using nanoparticles as contrast agents.

3.4.3 The use of nanoparticles for cell imaging

Although one of the objectives of this chapter was to determine the location of the nanoparticles after internalisation, three questions were raised during the study:

- What cell line selecting?
- How can the surface modification and/or aggregation affect the cellular uptake?
- What is the particle fate after contact with the cell membrane?

PC3 is a cancerous prostate cell line and PNT1A is a prostate epithelial cell line. They were selected because of their availability in the laboratory and because one side project was focused on the specific targeting of PC3 using biopolymers (hyaluronic acid). However, it occurs that many *in vitro* studies are carried out on pulmonary epithelial cells or macrophages based on toxicological criteria. However, cell lines do not behave and do not respond to the presence of the nanoparticles in the same way. For instance, Tao et *al.* found that human T-cell lymphoma and neuroblastoma cells reacted differently to two types of mesoporous silica nanoparticles [*Tao, 2002*]: the particles elicited some toxicity in the first cell line, but the second was little affected by the treatment (except at high dosage). It is true that macrophages are the first line of defence against foreign bodies and as such deserved to be selected as a model for *in vitro* testing. Likewise, the selection of pulmonary cell lines makes sense when the particles are inhaled (anthropogenic particles, aerosol, etc.) but this choice is more arguable when the nanoparticles are to be injected or penetrate by a different route than inhalation, especially considering that most nanoparticles

with biomedical applications are engineered to be delay their recognition by the reticulo-endothelial system or for specific targeting. Furthermore, it is not possible to transpose the results from one cell line to the other. Here, the epithelial PNT1A did not take up large amount of FITC-doped particles and MFSNPs contrary to PC3 but it does not mean that the uptake will always be important in cancerous cell lines and limited in epithelial ones. There is no guideline as to what cell line using for *in vitro* study and care must be taken when comparing the toxicity or uptake of particles from one study to another.

The results of the FITC-doped particles and the MFSNPs could not be compared because their diameter was different and because the MFSNPs expressed amine groups (and perhaps phosphonate moieties too). However, these two parameters may completely modify the cellular affinity for the particles and the particle toxicity. For example, Tao observed that the mesoporous nanoparticle toxicity in human T-cell lymphoma and neuroblastoma cells was suppressed when the surface of the particles was modified with amine groups [*Tao, 2002*]. He et *al*. noted that the surface modification of silica nanoparticles with amine and phosphonate moieties affects the uptake rate [*He, 2006*]. They also showed that amine particles were internalised in higher amount and faster than unmodified silica particles whilst very little phosphonate-modified particles were taken up. The imaging study ought to be carried out once again, this time with different surface modification to assess how the presence of functional groups (or ligand) affects the particle internalisation. The aggregation of the MFSNPs was also an issue because it was not possible to assess whether the aggregates observed within PC3 existed before the particle internalisation or were formed by intracellular processes. It is true that DLS and SEM showed that the particles clustered but the size of the aggregate does not tally with the size of the particles taken up by PNT1A. Therefore, a new study must investigate the fate of the particles using well-dispersed suspensions of nanoparticles and to assess whether or not the cells gather up the particles intracellularly.

Finally, the fate of nanoparticles after their internalisation is not well documented. Many studies focuses either on the mechanisms underlying the particle uptake or highlight how particles accumulate in endosomes and lysosomes based on TEM pictures. However, no study has ever followed the whole process from endocytosis to exocytosis, partly because tracking one or more nanoparticles within the cells is technically difficult and partly because devices keeping the cells alive and fitting into the imaging modalities are not widespread. Sun et *al.* were able to follow a single mesoporous silica nanoparticle before and after endocytosis and showed how the particle crossed the membrane using differential interference contrast microscopy [*Sun, 2008*]. Yet, this study focused on a single particle and stopped shortly after the particle entered inside the cell. The work of Panyam focused on both endocytosis and exocytosis of PLGA nanoparticles and they observed that both mechanisms proceed simultaneously. In addition, they found that exocytosis occurred at one particular region of the cells and not through the whole membrane [*Panyam, 2003*]. This finding may explain why most of the nanoparticles within PC3 are gathered in one place, although no publication has reported such aggregation within cells. Chithrani was able to track the vesicles containing gold nanoparticles: the dynamic study by confocal microscopy showed that the particles are firstly gathered into endosomes and that the endosomes move away from the membrane into the cytoplasm where they fuse with lysosomes [*Chithrani, 2009*]. Afterward, the particles travel outward and are sent towards the membrane, probably in order to be exocytosed. The detection of small clusters close to the nucleus membrane in the images presented in this chapter (**Figures 3-12 and 3-13**) goes in that way but Chithrani's observation does not provide any information that could be related to the aggregation observed in PC3. The MFSNPs may shed some light on the particle fate if the appropriate set of fluorophore is selected. For example a single dye could be used to track down the particles whilst a fluorophore which emission is modified by the pH could inform on the particles encapsulation in endosomes or lyososomes, where the pH is more acidic. This in turn raises the question of whether silica

nanoparticles are able to carry all these fluorophores. It is known that silica is negatively charged and hydrophilic, but some fluorophores – in particular emitting in the near-infrared and the two photon dyes – are said to be hydrophobic and as such may be difficult to entrap within the multifluorescent particles. In this condition, it is necessary to alter the composition of the particles to take into account the potential hydrophobicity of the fluorophores in order to design universal dye carriers.

3.5 Conclusion

This chapter was divided into two parts: the development of multifluorescent nanoparticles following a new procedure, and the microscopy study of the particle uptake. The nanoparticles were obtained using the amino acid route and seed regrowth to produce small nanoparticles approximately 20 nm. The three dyes selected for this study (MB, R6G, and FITC) showed that a fluorophore can either be entrapped by covalent binding or electrostatic interactions. An interesting feature of the MFSNPs suspensions is their potential capacity to carry multiple fluorophores and possible tuning of their optical properties by controlling the type and concentration of fluorophores within the particles. However, this study remains exploratory and a more in-depth characterization of the particles properties is needed, in particular of the suspension stability and of the spectral homogeneity of the particles.

The *in vitro* study showed that the MFSPs are potential contrast agents for the optical imaging of cells. It was possible to detect the particles using a confocal microscope and the MFSNPs were localised in the cell cytoplasm. Interestingly, particles containing FITC and R6G saw the signal of the two fluorophores overlaid, suggesting that the MFSNPs could be used for multiplexing analysing using different sets of dyes or by varying the ratio of fluorophore. The study also revealed that the particle uptake is dependent on the cell line since PNT1A barely internalised any particles, contrary to the large uptake of particles by PC3. More has to be made about the follow-up of the particles after endocytosis and more importantly about the toxicity of the MFSNPs, an important criterion whenever the application is linked to the biomedical field.

Although the particles were able to contain FITC, R6G, and MB, it was not certain that interesting fluorophores such as NIR dyes, which are said to be hydrophobic, could be entrapped within the (hydrophilic) silica matrix. It seemed more judicious to alter the particle composition to take into account the possible hydrophobicity of the dyes. Fortunately, the sol-gel procedure allows the co-condensation of TEOS with organosilanes, and in our particular case, certain

organosilane possess a hydrophobic moiety that could be of help to stabilise hydrophobic fluorophores. The synthesis of these organically-modified silica nanocarriers is the subject of the next chapter.

Chapter 4

Synthesis of hybrid VTEOS-TEOS nanoparticles and surface modification for stabilisation and conjugation

4 Synthesis of hybrid VTEOS-TEOS nanoparticles and surface modification for stabilisation and conjugation

4.1 Introduction

Several teams have altered the original Stöber method to exert a higher control over the particle dimensions, to proceed in different solvents, or to replace the catalyst. In chapter 3, the amino acid route was tested to as a replacement to the traditional synthesis methods and is developed here in more into details. The amino acid catalysis route was firstly reported by Yokoi et *al.* in 2006 and is still in its early development [*Yokoi 2006*]. The Yokoi's original work was inspired by the natural ability of glass sponges and diatoms (algae) to create complex and highly organised silica structures using peptides, proteins, and other biomolecules, which led them to choose L-lysine to catalyse the sol-gel reactions. As a result, they obtained highly ordered silica particles 12 to 23 nm in diameter. They also discovered that a mixture of L-lysine and D-lysine could tune the size of the particles. Lastly, they tested other amino acids and came to the conclusion that only lysine and arginine lead to the formation of nanoparticles owing to their basic nature. Independently, Davis and co-workers reached the same conclusion the same year and synthesised 1 to 8 nm silica particles using L-lysine [*Davis, 2006*]. Later, Hartlen et *al.* extensively studied the synthesis conditions of silica nanoparticles with arginine and determined the effects of reaction parameters (amino acid concentration, stirring rate, etc.) on the final structure and dimensions of the nano-objects [*Hartlen, 2008*]. The amino acid route can be completed by seed regrowth, where the initial small seeds are enlarged to the desired size by incremental addition of silicon precursor. In principle, the amount of TEOS added is directly connected to the final diameter of the nanoparticles and enables a fine control of the nanoparticles diameter [*Giesche, 1994*]. By this mean Hartlen augmented the

size of his nanoparticles from 15 nm to 200 nm by successive deposition of silica layers, either through the amino acid route or following the Stöber method for the largest dimensions.

Yokoi has also studied with more details the mechanisms underlying the amino acid catalysis of silica nanoparticles [*Yokoi, 2009*]. SEM and SAXS (small-angle x-ray scattering) data indicated that the number of seeds becomes constant after 30 minutes and the size steadily builds up until it stabilises after 8 hours. In the same vein, ^{1}H and ^{29}Si NMR analyses showed that TEOS was completely hydrolysed and almost entirely consumed as the particles grew. Lysine was principally found at the surface of the nanoparticles rather than within the matrix. Yokoi's hypothesis is that the amino acid molecules interact with the silanol groups at the surface of the silica spheres via electrostatic bonds and/or via hydrogen bonds and direct and control the particle growth. However, the interactions between amino acid and silicon precursor/silica are not entirely elucidated and remain under investigation.

The nanoparticles synthesised following the amino acid catalysis route are composed of silica. Hartlen has shown that the particles can contain R6G and chapter 3 has shown that they could also contain FITC and MB [*Hartlen, 2008*]. However, it is unlikely that silica could be a universal carrier able to contain virtually any fluorophore. Due to its hydrophilic nature and overall negative charge, the silica matrix may repel certain dyes of interest with hydrophobic nature. In that case, it may be desirable to slightly modify the composition of the silica network and integrate an organic component with an affinity for particular categories of fluorophores. This class of hybrid ceramic material is referred to as ORMOSIL for Organically Modified SILica. ORMOSILs are generally found as xerogels (silica gels), but rarely as nanoparticles.

In fact, ORMOSIL nanoparticles are produced by oil-in-water emulsion, when a hydrophobic fluorophore must be encapsulated within silica nanocarriers. Because the particle growth occur in the organic phase, the hydrophilic TEOS must be replaced by a hydrophobic silicon precursor, typically vinyltriethoxysilane (VTES), to make sure that the silane enters into the

micelles. This strategy is common for the production of photosensitisers- and luminescent dye-doped silica nanoparticles [*Law, 2008; Kumar, 2008 and 2010; Roy, 2003*]. An major contribution to fluorescent ORMOSIL particles is the work of Theaker et *al.*, who co-condensed TEOS and Phenyltriethoxysilane (PhTEOS) following the Stöber method to encapsulate a variety of fluorescent dyes. They reached the conclusion that the stabilisation of fluorophores within the hybrid scaffold is related to the hydrophobic interactions between the planar rings of the biomolecules and the phenyl group of PhTEOS but also to the electrostatic interactions between the negatively charged silanols and the positive charges of certain of the fluorophores. Yet, the size of the particles was comprised between 400 and 500 nm and the particles were highly hydrophobic due to the abundance of phenyl groups [*Theaker, 2008*]. Vogel and co-workers followed a different approach to engineer fluorescent ORMOSIL by using the acid catalysis of sulphur-containing silane to create an emulsion, followed by a base-catalysed step where the hydrolysed silane reacted with rhodamine B isothiocyanate and formed particles 150 nm to 3 µm in size [*Vogel, 2007*]. From these studies, it seems difficult to produce ORMOSIL particles of small size, unless the synthesis proceeds by oil-in-water emulsion. However, the amino acid route may be able to solve the size problem, although it has never been attempted yet.

The second role of organosilanes is to improve stability by limiting or suppressing aggregation and to offer an anchor for other biomolecules to bind to the nanoparticles. Amine-, sulphur-, and carboxylic acid-modified silanes are the most common coupling agents, whilst a few other commercial silanes are already conjugated and ready for use without additional synthesis steps such as PEG-silane. Most of the coupling procedures involve one of these three groups and the techniques developed to coat thin films and micro- or macroscopic silica surfaces in general are transposable to the modification of nanoparticles. Antibodies have been the first ligands tethered to nanoparticles due to their recognition of specific antigens but the relatively large size of immunoglobulins considerably increases the final dimensions of the conjugated particles and affects their stability. Smaller molecules, for example peptides, carbohydrates

and vitamin, and small polymers and biopolymers were later used as ligands. Folic acid (FA) is one of these ligands that has gained importance: FA (or folate) is also known as vitamin B9 or pteroylglutamic acid is involvedand it intervenes in the nucleic acids synthesis and in particular in the synthesis of thymine due to the high folate requirement of certain cancer types. For this reason, FA is found in a certain number of studies to target certain cancer lines (ovaries, kidneys, lungs, thyroid, the fallopian tube and certain other ovarian cancers [*Xia, 2010*]. To date, iron oxide, gold, quantum dots, and silica nanoparticles have been conjugated to folic acid to target cancerous cells in vitro [*Geszke, 2011; Mansoori, 2010, Rosenholm, 2009; Santra, 2005 b; Zhang, 2002*;].

Hyaluronic acid (HA) is a polysaccharide present in nearly all biological fluids and tissues but only in substantial amounts in soft connective tissues and in the extracellular matrix of vertebrae [*Kogan, 2007*]. Hyaluronan (other name encompassing hyaluronic acid and the salt form sodium hyaluronate) is involved in many biological processes. The size of the polysaccharide chain triggers distinctive phenomena ranging from space filling and anti-angiogenesis for larger chains to anti-apoptosis and heat shock proteins inductions for small fragments [*Stern, 2006*]. HA and its derivatives have found numerous medical applications, for example in ophthalmologic surgery to protect eye tissues or to replace vitreous fluid, in orthopaedic surgery where its rheological properties are suitable joints replacement, in wound healing, or even plastic surgery [*Kogan, 2007*]. HA binds to CD44 and RHAMM receptors that are overexpressed in certain cancer types similarly to FA and is therefore a potential ligand to target CD44 [*Ossipov, 2010; Platt, 2008*]

The dyes employed in the previous multifluorescent nanostructures were three conventional fluorophores that are known to have a good affinity for the silica matrix. However, it is unlikely that the silica matrix may be suitable for all fluorophores, and the encapsulation of some dyes may be more challenging (in particular the hydrophobic dyes). A more efficient carrier may be obtained by altering the network composition to include regions with hydrophobic features

within the nanoparticles. The sol-gel chemistry allows mixing various silicon precursors, including organosilanes, to create hybrid inorganic-organic systems, or ORMOSILs, that combine the strength and robustness of silica to the flexibility of organic compounds. The co-condensation of TEOS with a silane bearing a hydrophobic moiety may favour the interactions between fluorophores and ceramic matrix and may be a good strategy for the encapsulation of dyes. However, the few studies focusing on the synthesis of ORMOSIL nanoparticles often yielded particles several hundred nm in diameter or require the use of oil-in-water emulsion.

The aim of this chapter is to design organically-modified silica nanoparticles with diameter inferior to 100 nm by exploiting the advantages of the amino acid catalysis. No fluorophore was incorporated yet because it was first necessary to synthesise the carrier. Still the idea was incorporate hydrophobic organic groups into the silica network to help stabilising fluorophores by creating particles with dual hydrophilic/hydrophobic nature and where dye molecules could locate according to their affinity.

Consequently, the objectives were:

- To verify that the amino acid route is suitable for the synthesis of ORMOSIL nanoparticles made of VTEOS and TEOS (referred to as VT hybrid). To do so, the experimental conditions (VTEOS content, amino acid concentration, and water content) were varied to tune both the matrix composition and the particle dimension.
- To modify the surface of the hybrid nanoparticles using APTES and THPMP in order to improve the suspension stability (avoiding aggregation) and make the surface reactive for further modification.

To conjugate the surface of the VT hyrbid particles with folic acid (FA) and hyaluronic acid (HA) via carbodiimide chemistry to target specifically cancerous cells, more precisely for the targeting of PC3 cells tested in Chapter 3.

4.2 Materials and methods

4.2.1 Materials

Chemical were purchased from commercial sources and used as received without any treatment. Tetraethyl orthosilicate (TEOS) was purchased from BDH. 3-aminopropyltriethoxysilane (APTES, >98 %), L-arginine (>98 %), dimethylsulfoxide (DMSO), folic acid (98 %, FA), heptane, N-hydroxysuccinimide (98 %, NHS), 4-(2-hydroxyethyl)-1-piperazineethanesulfonic acid (HEPES), (3-mercaptopropyl)trimethoxysilane (95 %, MPTMS), 2-(N-morpholino)ethanesulfonic acid (hydrate >99.5 %, MES), 3-(trihydroxysilyl) propyl methylphosphonate monosodium salt solution (42 wt.%, THPMP), vinyltriethoxysilane (>98 %, VTEOS) were obtained from Sigma Aldrich. Hyaluronic acid (HA) was acquired from Lifecore Biomedical. 1-ethyl-3-(3-dimethylaminopropyl)-carbodiimide (EDC) and N,N'-dicyclohexylcarbodiimide (DCC) were obtained from Thermo Scientific and Acros Organics respectively. Sodium hydroxide and triethylamine were purchased from Fisher Scientific. Highly purified water (Milli-Q) was obtained from a Millipore “Direct-Q 3” water purification system.

4.2.2 Nanoparticles preparation

- **Influence of VTEOS content**

Hybrid nanoparticles were prepared using the arginine-catalysed route. First, 18 mg L-arginine was dissolved in 7 mL Milli-Q water (15 mM) and 250 µL of heptane. After five minutes of vigorous stirring, up to 545 µL VTEOS and 775 µL TEOS were added, with concentrations ranging from 0 % (pure TEOS system) to 100 % (pure VTEOS system (**Appendix C**). The mixtures were magnetically stirred for 24 hours and the particles were centrifuged three times (1200 g, 15 minutes) and washed with distilled water between each step. In the end, the mass of particles was weight and the particles were suspended in Milli-

Q water. The same experiments were conducted with identical conditions 1) without heptane or 2) at 60°C.

- **Variation of the synthesis conditions**

Hybrid nanoparticles made of 50 % VTEOS and 50 % TEOS (VT-50) were prepared by dissolving 3.2 to 64 mg of arginine in 7 mL Milli-Q (2 to 50 mM) (**Appendix C**). After five minutes, VTEOS (150, 205, or 305 µL) and then TEOS (215, 290, or 430 µL) were added drop wise and the solutions were magnetically stirred for 12 hours or 1 day if the solution remained transparent. The particles were centrifuged three times (1200 g, 15 minutes) with washing in distilled water between each step and finally suspended in Milli-Q.

- **Surface modification**

VT-50 nanoparticles were prepared by addition of 275 µL of VTEOS and 385 µL of TEOS to 7 mL of arginine solution (15 mM) and magnetically stirred for 12 hours. Then, 5 mL of arginine solution (0.5 mM) was added to the nanoparticles suspension, followed by 200 µL TEOS. After 30 minutes, APTES and THPMP were added simultaneously (**Appendix D**) and the suspensions were magnetically stirred for additional 12 hours. The particles were recovered using the protocol described previously.

- **FA and HA modifications**

In a first protocol, three solutions containing FA (7 mg in 1.5 mL of DMSO), DCC (35 mg in 1.5 mL of DMSO), and NHS (4 mg in 1.5 mL of DMSO) were mixed before 50 mg of AP-00 hybrid nanoparticles (modification with 100 % APTES and 0 % THPMP) and 20 µL of triethylamine were added to the solution. The suspension was magnetically stirred for 4 hours, centrifuged, and left in the

oven overnight. The same experiments were carried out with AP-25 type particles (modification with 25 % THPMP and 75 % APTES) in water instead of DMSO.

The protocol was next modified. Reagent solutions were prepared as followed:

- 10 mg of FA was dissolved in 100 mL Milli-Q and produced a strong yellow-orange solution;
- 1.5 mg and 1.6 mg of EDC and NHS were both dissolved in 100 mL of Milli-Q;
- 2 mg of HA (11, 583, or 6457 disaccharides) was dissolved in 1 mL HEPES (10 mM, pH 7.0);

To conjugate FA and HA to hybrid particles, appropriate volumes of FA, NHS, and EDC solutions were diluted in arginine solution (**Appendix D**). Then, 1 or 2 mg of particles hybrid particles were subsequently added to the first solution and the reaction was left to proceed for 5 hours before the suspensions were centrifuged and the particles dried in an oven overnight.

The protocol was modified one last time. FA/HA, EDC, and NHS were diluted in MES buffer (4.88 g of MES dissolved in 100 mL Milli-Q and the pH was adjusted to 5.0) and stirred for 10 minutes before addition of 25 mg of particles (**Appendix D**). The reaction was left to proceed for 5 hours before the suspension were centrifuged and the particles dried in an oven overnight.

4.2.3 Characterisation

- **Scanning electron microscopy (SEM)**

The particle size and morphology were examined using scanning electron microscopy (SEM). The nanoparticle suspensions were firstly diluted: the samples were sonicated and subsequently 25 µL of suspension was poured in

an eppendorf and the total volume was increased to 500 µL with Milli-Q water so that the SEM samples were totally transparent. One drop of suspension was deposited into a silicon grid and let to dry in a desiccator for at least 24 hours. Finally, the particles were imaged using a high resolution FEI XL30 SFEG analytical SEM (Philips, Netherland).

- **Dynamic light scattering (DLS)**

The size and size distribution of the particles were measured by dynamic light scattering using a Zetasizer nano series S with an He/Ne laser of 633 nm wavelength (Malvern Instrument, UK). The particle suspensions were firstly diluted: 10 µL of the sample was poured in a quartz cuvette and completed with 1 mL Milli-Q. The refractive index and absorption of silica nanoparticles were fixed at 1.25 and 0.01 respectively. For each sample, four measurements of 20 runs (15 seconds each) were carried out, with temperature maintained at 25°C.

- **Fourier transform infrared spectroscopy (FTIR)**

The particle composition was analysed by infrared spectroscopy: a volume of nanoparticle suspension was taken, centrifuged, and dried in the oven for 1 day. The resulting powders were subsequently analysed in KBr powders using a Thermo Nicolet Avatar 370 spectrometer (Thermo Scientific). Infrared spectra were recorded over the wavenumber region 4000 to 400 cm^{-1} with a resolution of 4 cm^{-1}.

4.3 Results

4.3.1 Hybrid VTEOS-TEOS system

Silicon precursors, here VTEOS and TEOS, were co-condensed following a modification of Hartlen's protocol [*Hartlen, 2008*]. The percentage of VTEOS compared to TEOS was varied from 0 mol% (pure TEOS particles) to 100 mol% (pure VTEOS nanoparticles) by increment of 25 % and the samples were referred to as VT-X, where X is the molar percentage of VTEOS. In addition, the molar ratio L-arginine/silicon precursors/water ratio was kept as close to 0.02/1/150 as possible while a small quantity of heptane was added to the solution. A few hours after introduction of the silanes the solutions became turbid, except the VT-00 and VT-25 systems where the solutions remained clear. As the content of VTEOS increased, the turbidity became more important and the solution turned totally white above 50 % of VTEOS while large aggregates of white material floated in solution in the pure VTEOS sample. However, the method yielded only a few mg of VT-00 and VT-25, which is similar to what was observed with the multifluorescent particles. Increasing the reaction time or reducing the water volume did little to improve the yield of the synthesis.

The size and size dispersity measurements were conducted by dynamic light scattering (DLS): the hydrodynamic diameter graph of VT-00 and VT-25 displayed a first peak of low intensity around 8 nm and a second more intense at 255 and 320 nm respectively. In comparison, the other samples displayed a single peak at 100, 115, and 320 nm for VT-50, VT-75, and VT-100 respectively (**Figure 4-1**).

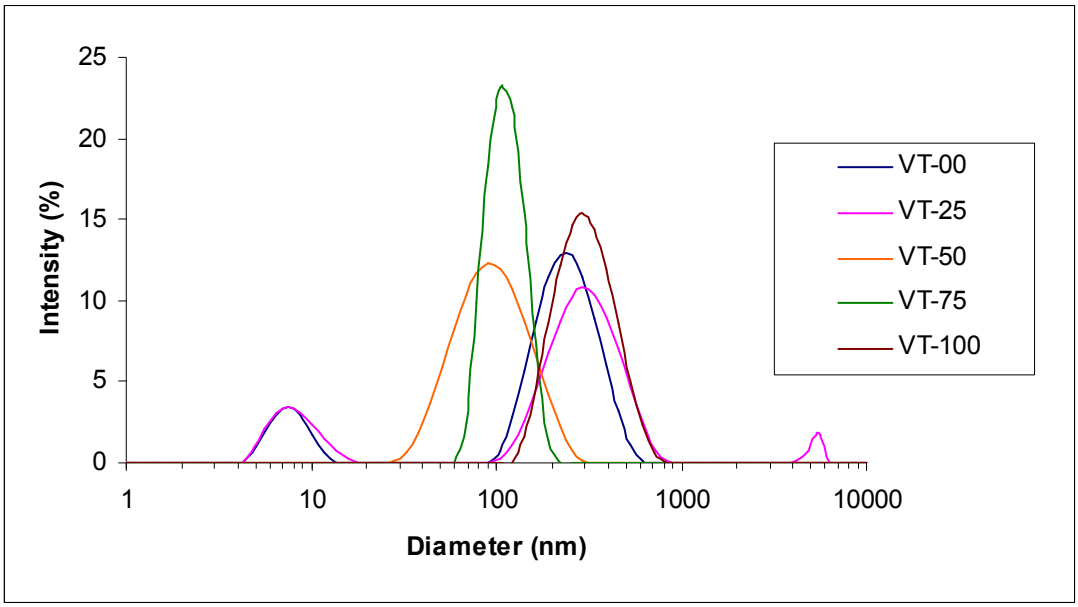

Figure 4-1: Variation of hybrid particles hydrodynamic diameter in presence of heptane.

For the first two samples (VT-00 and VT-25), the zetasizer warned that the conditions were not optimal – possibly due to the low particle concentration of the suspensions - and is corroborated by the high polydispersity index (**Table 4-1**). The large hydrodynamic diameter coupled to the high polydispersity index indicated that the particles clustered but the actual diameter is close to 8 nm. In comparison, VT-50 and above were easier to analyse and exhibited a very low polydispersity index, but the mismatch between the hydrodynamic and mean number diameter suggests that VT-50 and VT-100 had formed clusters of two or three particles.

Table 4-1: Experimental data acquired by dynamic light scattering of hybrid nanoparticles synthesised in presence of heptane.

Experiment	Hydrodynamic diameter	Hydrodynamic diameter (peak 2)	Number mean	Polydispersity index
VT-00	254.4 nm	7.6 nm	6.0 nm	0.774
VT-25	318.9 nm	8.2 nm	5.9 nm	1
VT-50	102.2 nm	X	44.8 nm	0.155
VT-75	114.1 nm	X	90.1 nm	0.031
VT-100	317.5 nm	X	243.7 nm	0.136

The composition of each sample was analysed by FTIR. The spectrum of the pure TEOS system possesses well-defined bands at 470, 791, and 1110 cm^{-1} that originate from siloxane bonds Si-O-Si, as well as a peak at 960 cm^{-1} due to the presence of silanol groups Si-OH (**Table 4-2**). Presence of VTEOS in the particles added more peaks characteristics of the vinyl moiety at 2975 (≡Si-**CH**=CH_2), 1600 (≡Si-**C**H=**C**H_2), and 1400 cm^{-1} (≡Si-CH=**CH_2**) (**Figure 4-2**) [*Ou, 1997*]. As the proportion of VTEOS increased, the vinyl peak intensity increased as well in comparison to the siloxane band, although the latter remained the most intense.

Table 4-2: Principal characteristic peaks on infrared spectra and related functional groups.

Wavenumber	Mode [a]	Structural unit
3060 cm^{-1}	ν_{as} (CH_2)	≡Si-CH=**CH_2**
2980 cm^{-1}	ν_{as} (C-H)	≡Si-**CH**=CH_2
2955 cm^{-1}	ν_s (CH_2)	≡Si-CH=**CH_2**
1630 cm^{-1}	δ (H-O-H)	H_2O
1600 cm^{-1}	ν_s (C=C)	≡Si-**C**H=**C**H_2
1400 cm^{-1}	δ (CH_2)	≡Si-CH=**CH_2**
1100 cm^{-1}	ν_{as} (Si-O-Si)	Si-O-Si
960 cm^{-1}	ν_{as} (Si-OH)	**≡Si-O**
930 cm^{-1}	ν_{as} (C-H)	-CH_2-R (residual alkoxide)
790 cm^{-1}	ν_s (Si-O-Si)	Si-O-Si
470 cm^{-1}	δ (O-Si-O)	O-Si-O

[a] *ν_s = symmetric stretching vibration; ν_{as} = asymmetric stretching vibration; δ = bending vibration.*

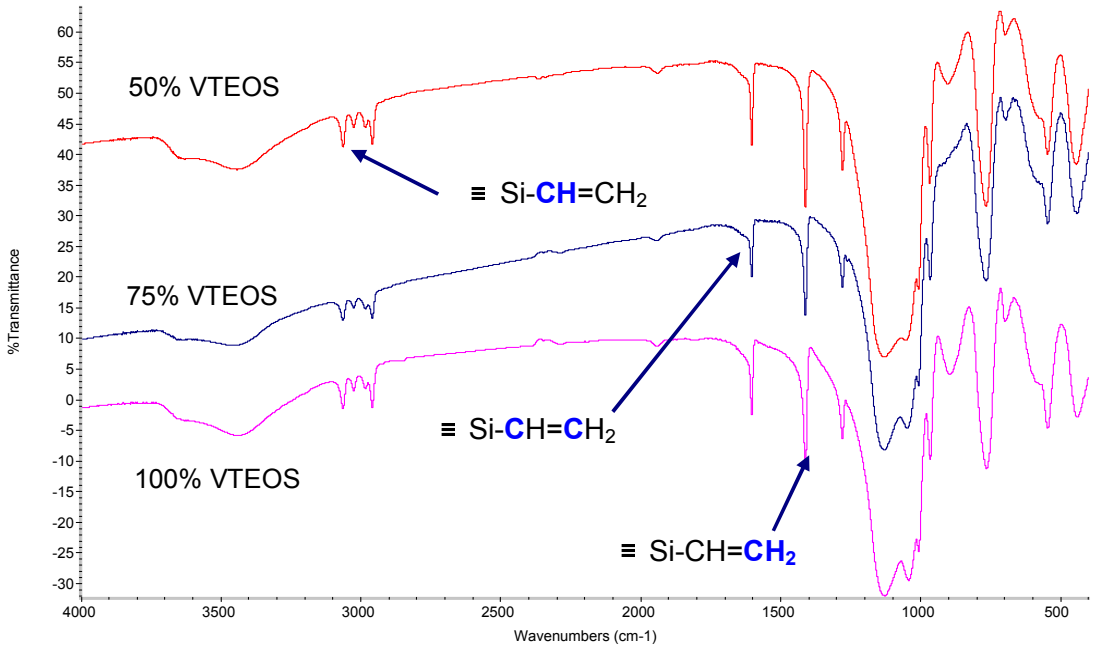

Figure 4-2: Infrared of hybrid spectra with 50 % (red), 75 % (blue), and 100 % VTEOS (pink).

During the centrifugation of the VT-75 and VT-100 samples, some particles remained in the top organic phase (heptane) instead of sedimenting at the bottom of the tubes and consequently the experiments were repeated in absence of heptane (samples are referred to as VTw-X). In that case, no segregation between the hydrophilic and hydrophobic particles was observed. The hydrodynamic radius steadily augmented with the VTEOS proportion and the VT-00 and VT-25 curves, which is similar to what was observed when heptane was added to the arginine solution (**Table 4-3**).

Likewise, the number diameter increased with the VTEOS/TEOS molar ratio: VTw-00 and VTw-25 were the smallest with diameters of 3.6 and 7.8 nm respectively. When the VTEOS proportion increased, the diameter rose to 113 nm for VTw-75 and more than 440 nm for pure VTEOS nanoparticles (**Figure 4-3**). The VTw-50 case has to be taken separately because of its polydispersity index slightly superior, which suggests that the objects detected by the

nanosizer were in fact small clusters of two or three particles so that the actual primary particle diameter was closer to 40 nm than 85 nm.

Table 4-3: Characteristic of the particles synthesised without heptane in the reacting medium.

Experiment	Hydrodynamic diameter	Hydrodynamic diameter (peak 2)	Number mean	Polydispersity index
VTw-00	5.7	418.6	3.6	0.328
VTw-25	6.8	658.4	7.8	0.253
VTw-50	143.5	X	85.4	0.179
VTw-75	142.0	X	113.9	0.022
VTw-100	480.2	X	445.4	0.069

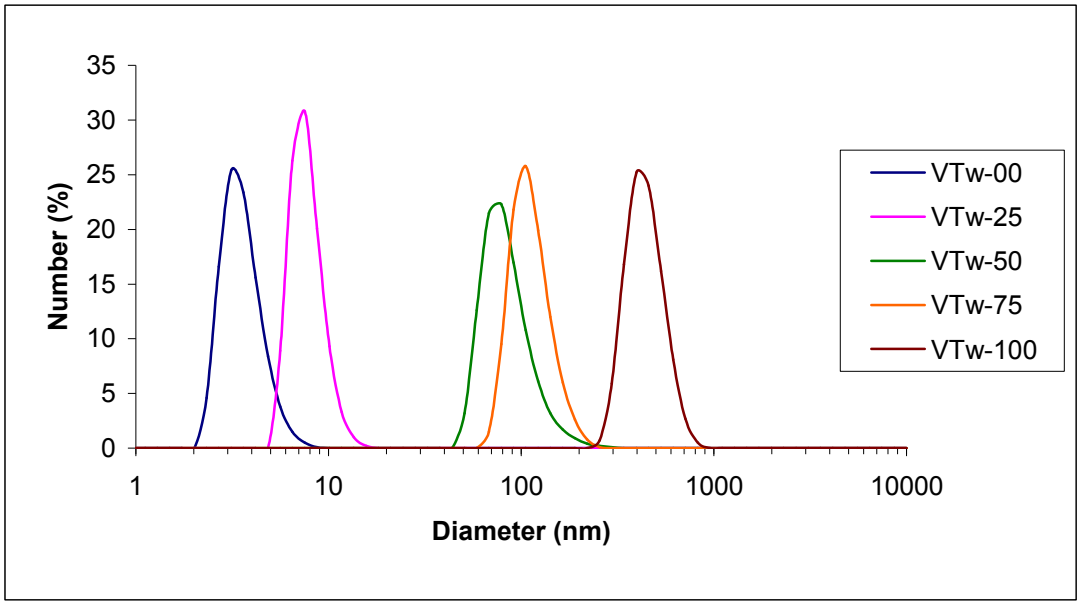

Figure 4-3: Variation of hybrid particles number diameter in absence of heptane.

SEM validated the DLS results since the images revealed a change of particle diameter according to the VTEOS/TEOS molar ratio (**Figure 4-4**). The VTw-00 and VTw-25 samples were the smallest and their dimensions were close to 10 to 13 nm respectively, larger than the value measured by the zetasizer. In

comparison, VTw-50 nanoparticles were 40 nm in size, smaller than the value detected by light scattering. The dimension of particles shifted to 110 and 480 nm for 75 and 100 % VTEOS in that order and are in good agreement with the DLS measurements. Two populations of particles co-exist on the SEM pictures because of cross-contamination during the SEM sample preparation. The pictures were selected nonetheless to highlight the difference of size that arises from a modification of VTEOS concentration. Other TEM images of VTw-100 confirmed the large particle size in comparison to the other hybrids (data not shown) whilst the 40 nm diameter of VTw-50 is in agreement with the SEM images displayed later in this chapter.

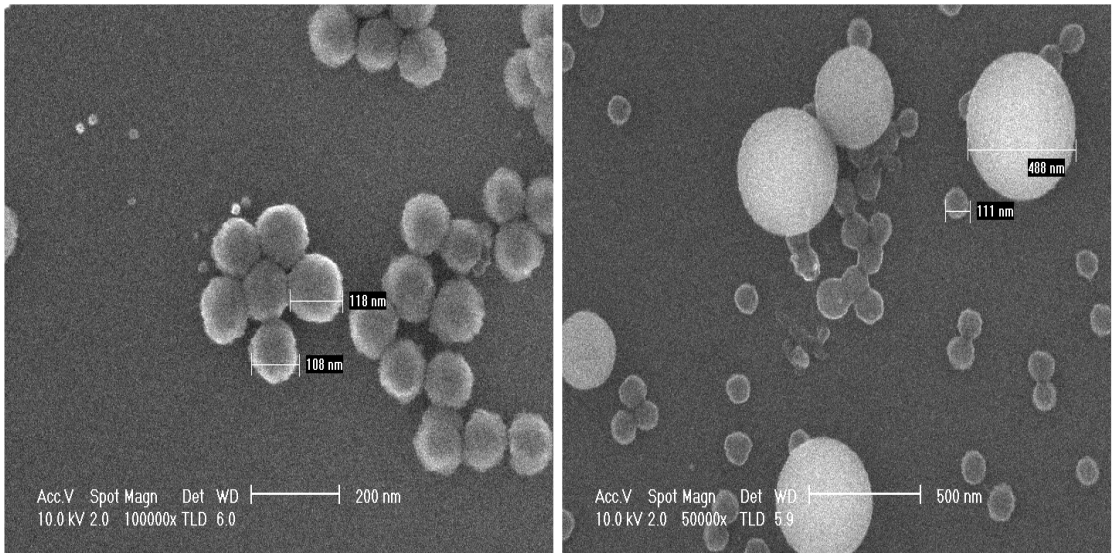

Figure 4-4: SEM micrographs of hybrid VTEOS-TEOS silica nanoparticles with 75% (left), and 100% VTEOS (right) in absence of heptane.

4.3.2 Variation of the experimental conditions

Other parameters than the VTEOS content were varied owing to their potential influence on the final particle dimensions. Stirring rate and reaction time were the first parameters probed: VT-50 particles were synthesised with the stirrer set at different speeds and aliquots (10 µL) were taken for light scattering measurement at periods ranging from 30 minutes to 2 or 3 days. At the two slowest speeds (300 and 600 rpm) values as high as 280 and 300 nm were

measured during the first hours but vanished after the fifth hours (**Figure 4-5**). After 5 to 10 hours, the zetasizer detected a signal but the seed diameter was centred around 20 nm and constantly grew until their size stabilised at circa 60 nm after about 30 hours. At higher speed (900 and 1200 rpm), the seeds appeared after 3 hours and reached the same threshold of 60 nm after 8 hours. Hence, the stirring rate seems to alter the particle formation kinetics rather than the diameter itself. However additional electron microscopy analyses are required to confirm that the nanoparticles maintain identical size.

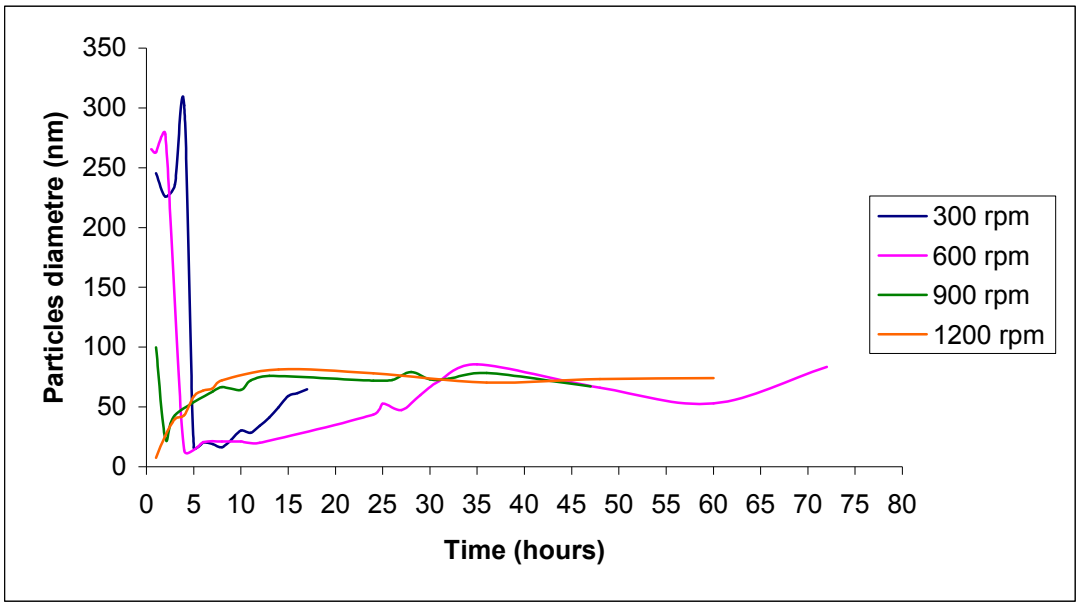

Figure 4-5: Variation of the particles diameter with time and in function of the stirring rate.

Other parameters of importance are the water and arginine concentrations. Silica-to-catalyst and silica-to-solvent molar ratios were attributed three values. The water volume was kept equal to 7 mL in all experiments and all structures were based on the VT-50 type. The first difference is the striking contrast time required to form the particles: at to obtain translucent solutions. Conversely, at a highest concentration of catalyst and lower concentration of water, the solutions became opalescent within a few hours of stirring. DLS measurements showed that lower arginine concentration yields particles with higher number diameter -

from 65 to 95 nm – whilst at higher concentration the particle diameter ranged between 25 and 40 nm (**Figure 4-6**). In all cases, the polydispersity index was inferior to 0.1 which means that the zetasiser measured the diameter of primary particles and not of clusters. It was not possible to image the particles by SEM (breakdown during several months) but these analyses are necessary to assess the particle diametre. In addition, the experiments were not carried out enough times (three times each) to be considered reproducible and more time has to be devoted to this part.

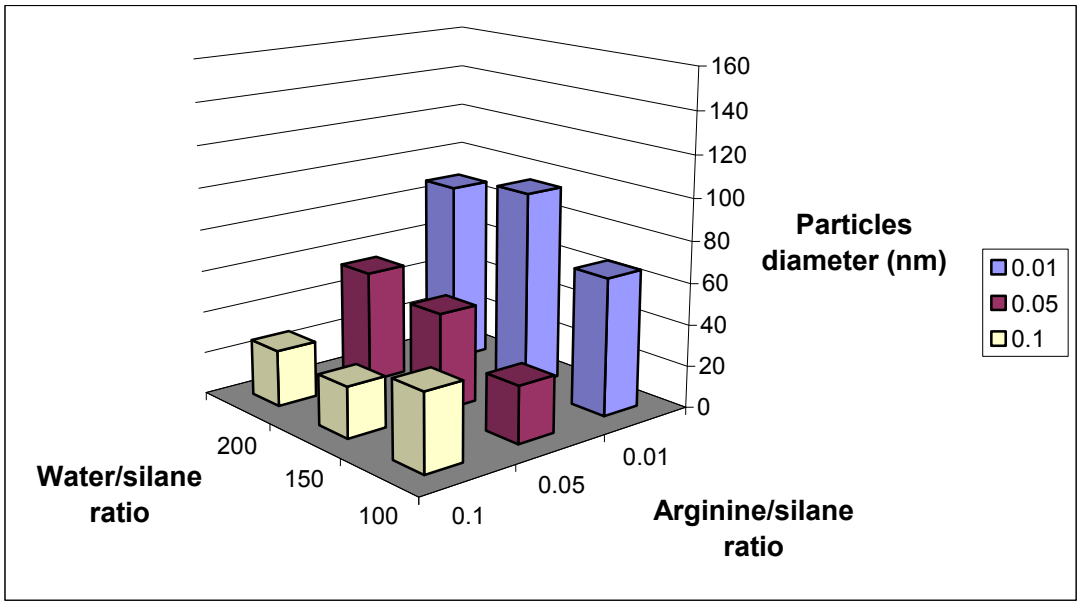

Figure 4-6: Particles diameter variations in function of arginine and water concentration.

In fact, the study was halted because an issue arose when a new VTEOS solution was used. First of all, the formation of silicic acid and of nanoparticles occurred within a few minutes while it required at several hours for the solutions to turn white previously. Secondly, the DLS curves differed significantly and the values increased to the micrometer range in almost all cases. Lastly, SEM pictures confirmed the high particle diameter and showed that in certain cases the particles shape was totally different and took on the form of “cups” (**Figure 4-7**).

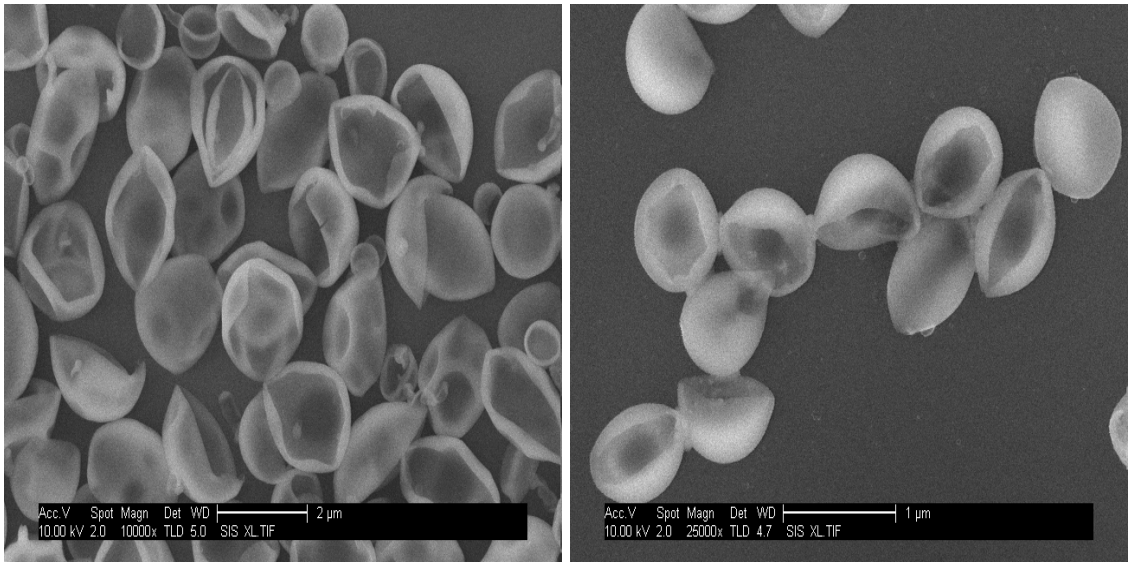

Figure 4-7: SEM pictures of VT-50 particles with arginine/silica/water ratio of 0.01/1/200 (left) and VT-75 (right) with the new VTEOS solution.

For the moment, it is not possible to determine whether the process is reproducible or not. There are strong evidences that the VTEOS solution was responsible for the change of morphology as the phenomenon was not observed on other hybrid (PhTEOS, THPMP, etc.) and because the spherical shape is in principle the most energetically favourable. One hypothesis could be that the solution was contaminated or altered and it is therefore required to synthesise new VT hybrids with different commercial VTEOS solutions or by varying the VTEOS concentration in comparison to TEOS. This is the only way to ensure that the process yields spherical particles and that the first results are the genuine particles.

Overall, the light scattering data of VT-50 samples (first samples) indicated a tendency for the particles to cluster. Aggregation is a common issue for nanoparticles and since the hybrid ones appear to be prone to this phenomenon, the next stage of development consisted in modifying the particle surface to make the suspension more stable and to progressively move towards their functionalisation.

4.3.3 Surface modification with APTES and THPMP

Aminopropyltriethoxysilane (APTES) was first chosen as coupling agent because it is the most common organosilane and its amine groups make it a powerful coupling agent. The hybrid seeds were synthesised based on the VT-50 protocol and the organosilane was added directly after the synthesis of the particles (no centrifugation). It seemed that more material was produced after addition of APTES compared to bare hybrid particles. At the same time, sedimentation was more pronounced and occurred faster than unmodified particles. DLS measurements indicated a high PdI and the SEM images displayed highly aggregated particles (**Figure 4-8**).

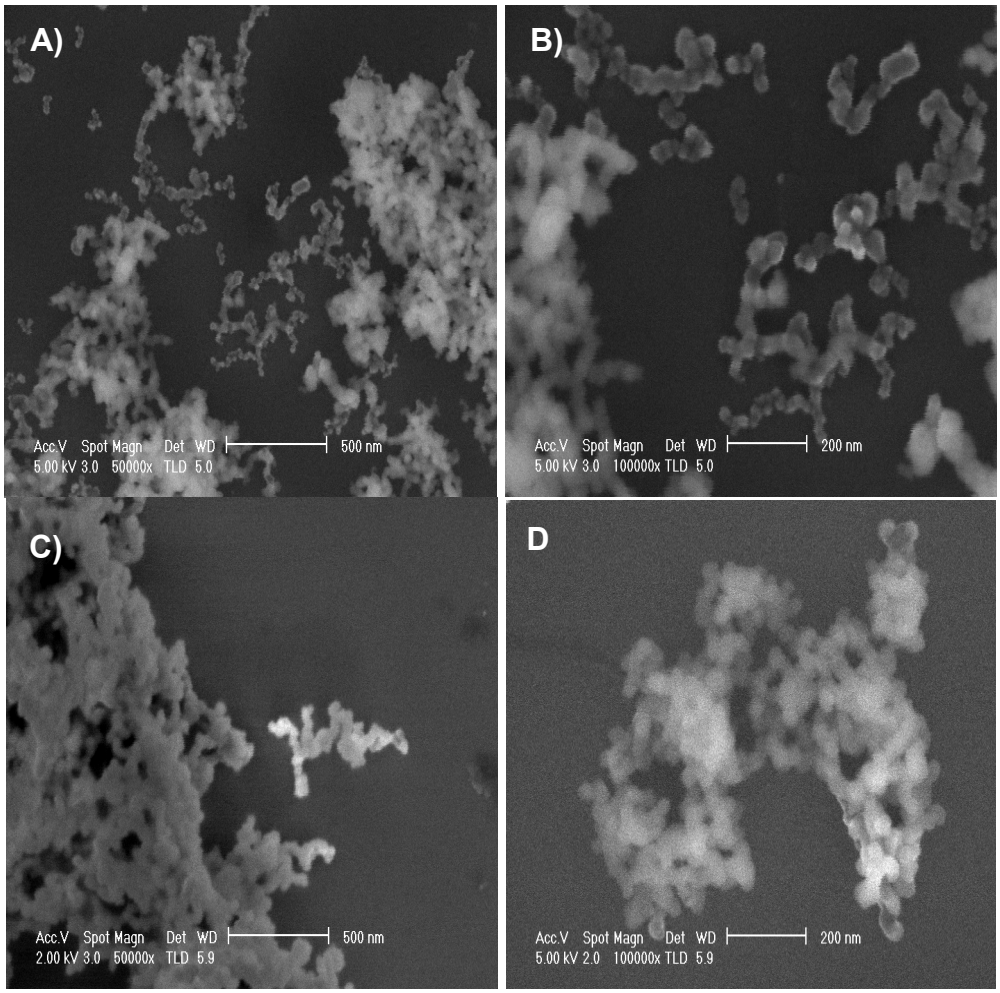

Figure 4-8: SEM pictures of silica nanoparticles after coating containing 1 % APTES (A and B), 25 % (C), and 50 % (D).

The smallest concentration of amine (1 % of the total silane concentration) led to small clusters but as the APTES-to-TEOS molar ratio increased, aggregation became more and more important and SEM pictures displayed large aggregates.

The infrared spectra after modification were different from that of unmodified VT-50: the intensity of the vinyl bands was somewhat lessened. A strong band appeared between 3500 and 3000 cm^{-1} as well as another peak around 1550 cm^{-1} confirmed the existence of the amine groups in or onto the particles, although this second peak was exclusively present at high APTES concentration (**Figure 4-9**).

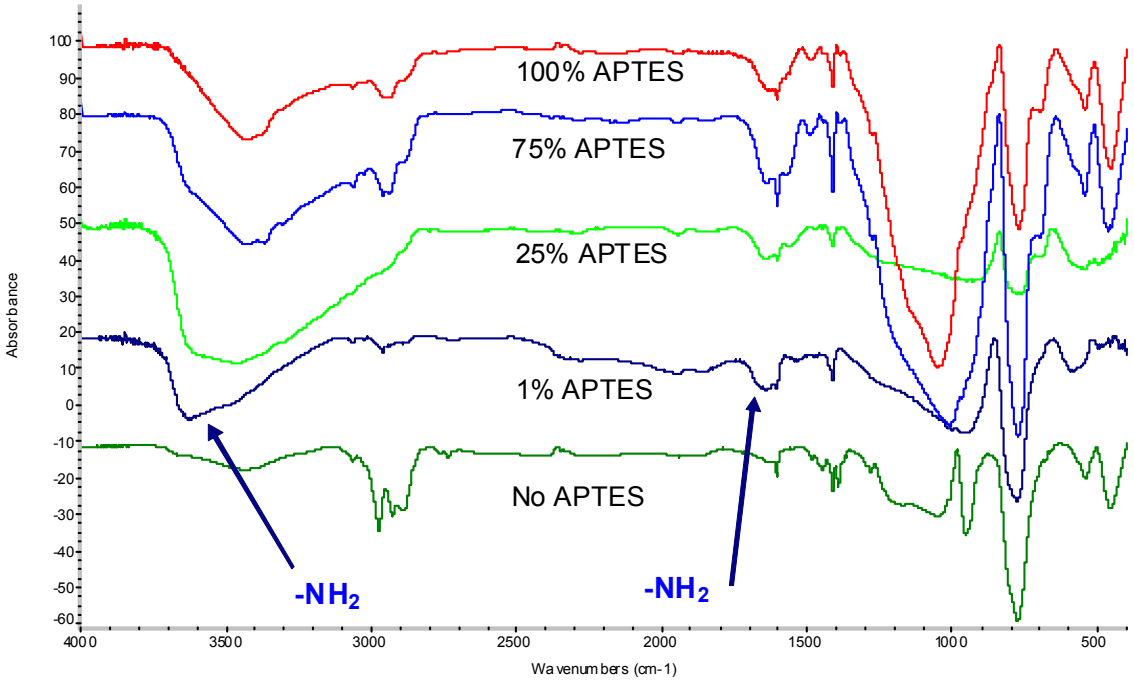

Figure 4-9: FT-IR spectra of nanoparticles after modification with increasing concentration of APTES.

To reduce the aggregation phenomenon, 3-(trihydroxysilyl) propyl methylphosphonate (THPMP) is generally co-condensed with APTES to counteract the action of hydrogen bonds by bringing negative charges that

promote the repulsion between nanospheres. Coatings with different proportions of APTES and THPMP were tested on VT-50 seeds and are referred to as AP-X, where X is the percentage of THPMP compared to APTES. DLS measurements showed that the increasing the THPMP content reduces the hydrodynamic diameter of the particles (**Figure 4-10**). Yet, the polydispersity index value of 0.2 of AP-75 and AP-100 suggest that small clusters of two to three particles were still present in solution and are comparable to unmodified VT-50 nanoparticles.

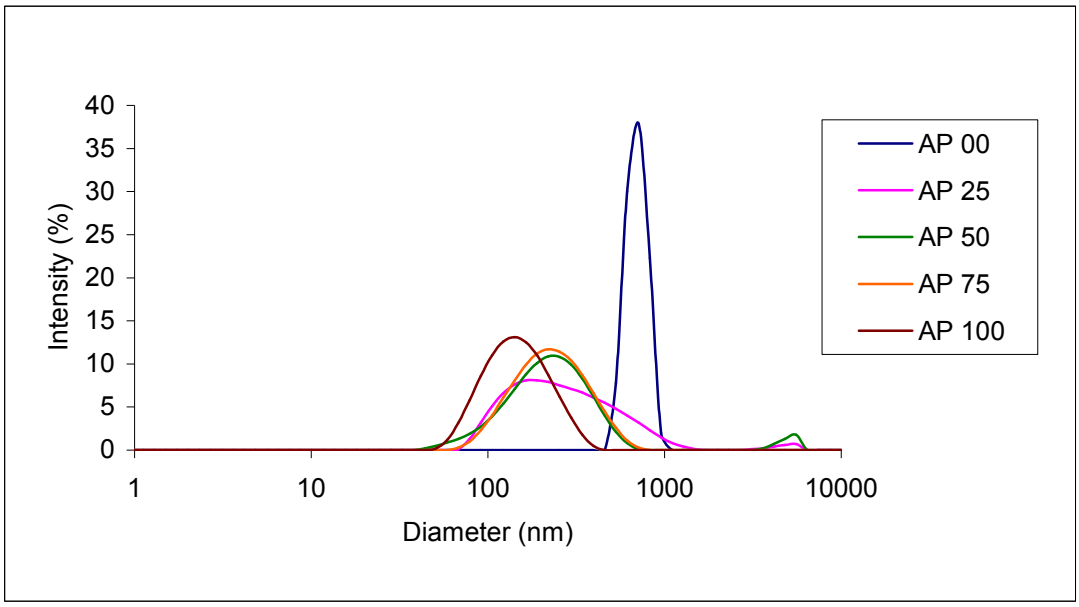

Figure 4-10: Hydrodynamic radius of hybrid particles after modification with increasing proportion of THPMP.

SEM pictures highlighted that: the presence of phosphonate at the surface improves the stability of particles. Where the aminated particles were strongly aggregated, samples with THPMP formed clusters made of a smaller number of particles and this number decreased with at high THPMP concentration up to the point that single particles 40 to 50 nm in diameter were present in the 75 % THPMP sample (**Figure 4-11**).).

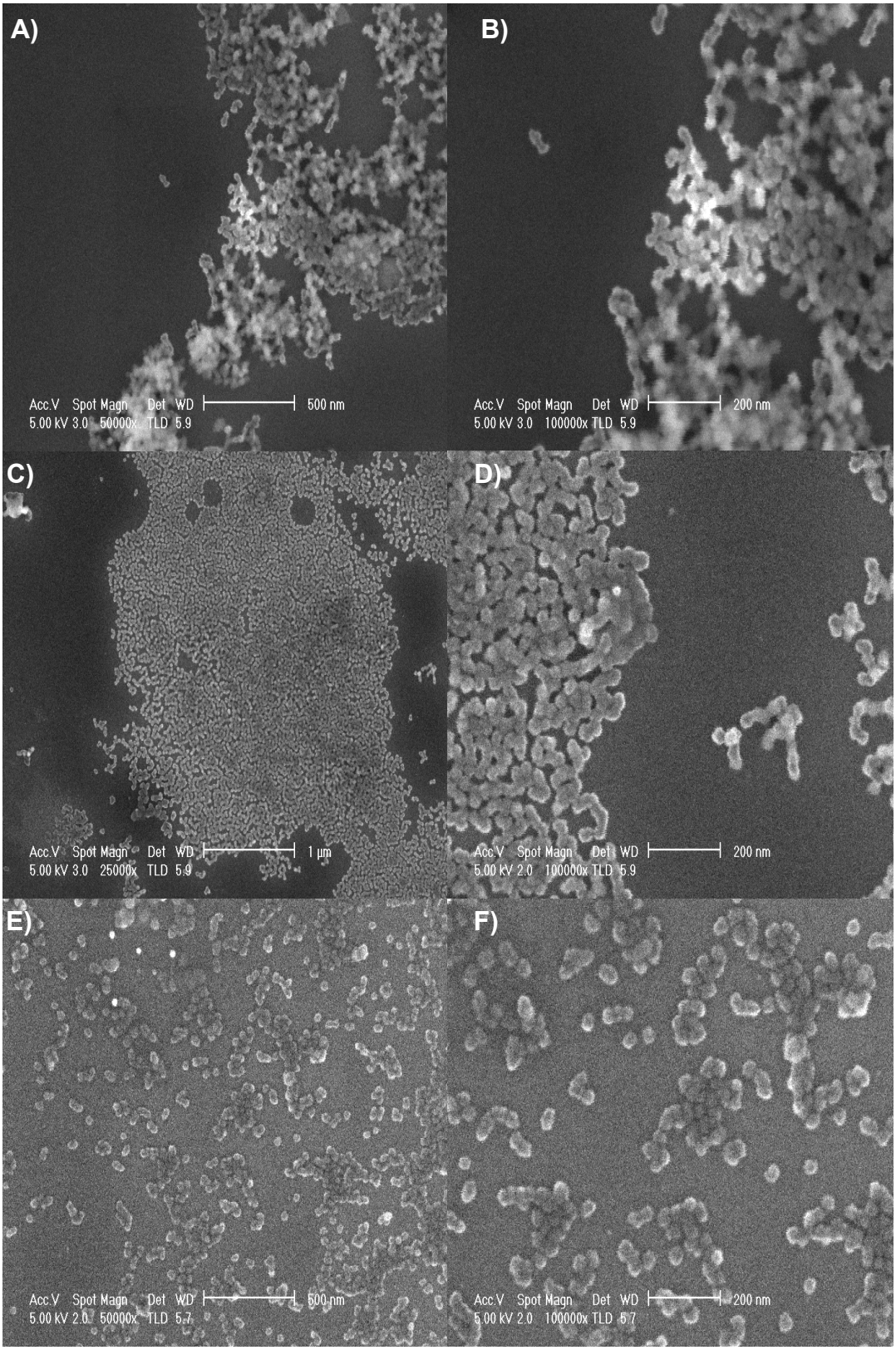

Figure 4-11: SEM of nanoparticles of AP-00 (A and D), AP-50 (B et E), et AP-75 (C and F).

Infrared analyses provided little information about the presence or absence of phosphonate. A piece of the xerogel was dried in the oven and analysed by FTIR (**Figure 4-12**) and the spectra were compared to the principal bond vibrations from the literature (**Table 4-4**) [*Pezzin, 2008; Bowen, 1988; Shagidullin, 2007*]. The siloxane bands overlap with most of the key peaks of the phosphonate moiety and hinder its identification, even with AP-100, where only THPMP is added. As a result, the infrared spectra of silica nanoparticles before and after reaction with organosilanes were similar, with a small signal from APTES but no obvious sign of THPMP (**Figure 4-13**).

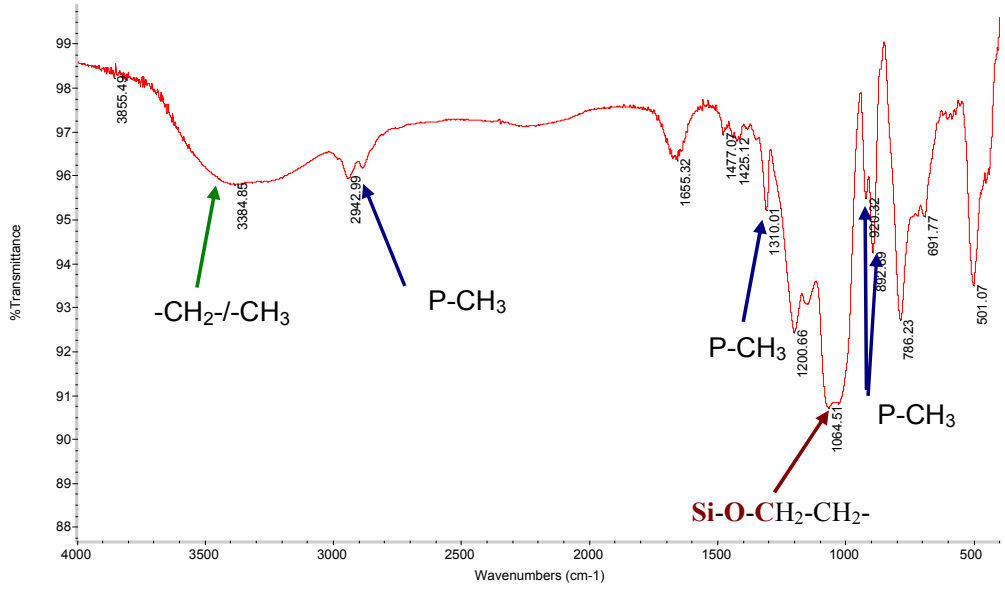

Figure 4-12: Infrared spectra of THPMP xerogel and characterisation of the major peaks and bands.

Additionally, THPMP may form a gel very quickly and its high viscosity that is not ideal for dilution and homogeneous reaction with the particles. Therefore, there are high chances that the modification with THPMP failed and would explain why the unmodified particles are similar to that after modification with the phosphonate-silane. The best method to detect the modification is in that case by measuring the zeta potential of the particles as THPMP-modification generates a strong negative charge whilst APTES generates a positive one.

Table 4-4: Principal characteristic peaks on infrared spectra and related functional groups.

Wavenumber	Mode [a]	Structural unit	Wavenumber	Mode [a]	Structural unit
2998 cm^{-1}	δ_s (CH_3-P)	≡P-CH_3	1026 cm^{-1}	ν_{as} (Si-O-C)	**Si-O-C**H_2-CH_2-
2930 cm^{-1}	δ_s (CH_3-P)	≡P-CH_3	916 cm^{-1}	ρ (CH_3-P)	≡P-CH_3
1420 cm^{-1}	δ_{as} (CH_3-P)	≡P-CH_3	895 cm^{-1}	ρ (CH_3-P)	≡P-CH_3
1316 cm^{-1}	δ_s (CH_3-P)	≡P-CH_3	824 cm^{-1}	ν (P-O)	O=P-OH
1244 cm^{-1}	ν (P=O)	≡P=O	791 cm^{-1}	ν (PO_2)	O=P-OH
1074 cm^{-1}	ν_s (Si-O-C)	**Si-O-C**H_2-CH_2-	768 cm^{-1}	ν_s (P-O-C)	-CH_2-**C**H_2-**O-P**
1050 cm^{-1}	ν_{as} (P-O-C)	-CH_2-**C**H_2-**O-P**	714 cm^{-1}	ν (P-C)	≡**P-C**H_3

[a] *ν_s = symmetric stretching vibration; ν_{as} = asymmetric stretching vibration; δ = bending vibration,* ρ = rocking.

Moreover, the zeta potential value is directly correlated to the aggregation as a strong charge typically prevents the phenomenon from occurring. As the reaction with coupling agent is crucial for conjugating nanoparticles with ligands, the experiments must be repeated to measure the zeta potential of the suspensions and verify whether the two organosilanes have reacted with the particles.

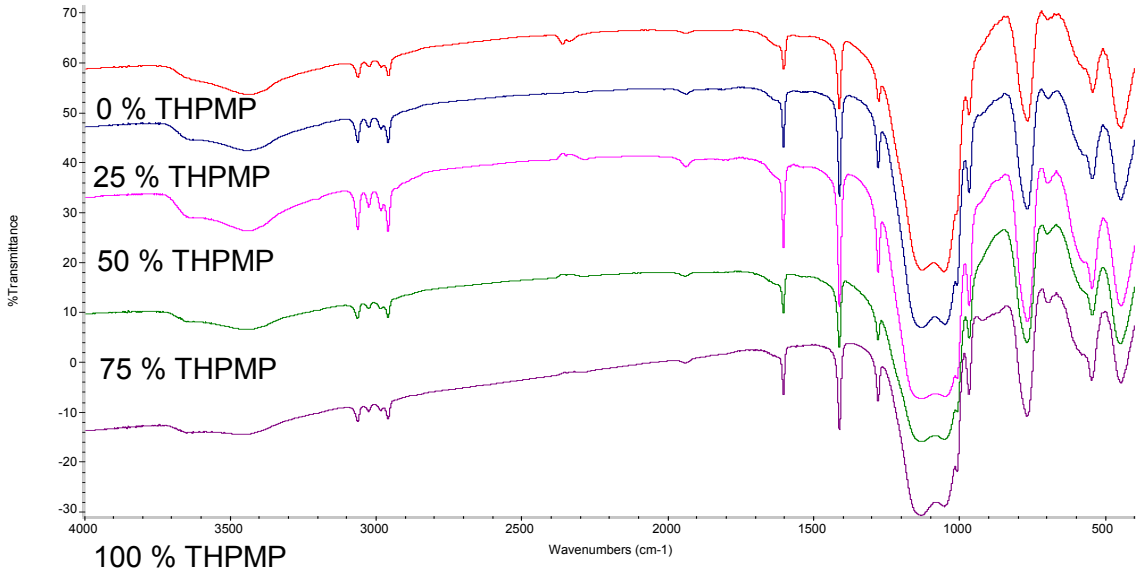

Figure 4-13: Infrared spectra of hybrid particles after modification with APTES and THPMP at different molar ratio.

4.3.4 Bioconjugation with FA and HA

In the last part, the conjugation of FA and HA was attempted using carbodiimide chemistry (**Appendix E**), where the aminated nanoparticles were reacted with one of the two biomolecules in presence of 1-ethyl-3-(3-dimethylaminopropyl)-carbodiimide (EDC) and N-hydroxysuccinimide (NHS). The chemical structure of FA is divided into three parts: a pterin ring (PT), para-amino benzoic acid (PABA) and glutamic acid (**Figure 4-14**) [*Zhang, 2002 and 2008; He, 2009 c*].

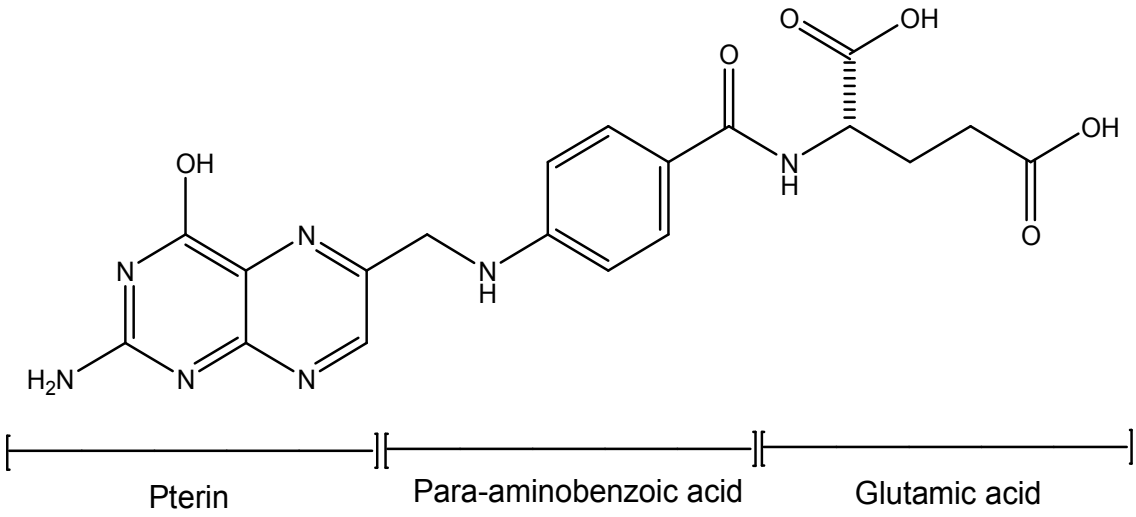

Figure 4-14: Chemical structure of folic acid that is divided into a pterin ring, para-aminobenzoic acid (PABA), and glutamic acid.

The complex structure of vitamin B9 gives rise to an elaborate infrared spectrum (**Figure 4-15**) but only few peaks are likely to appear after conjugation with the nanoparticles (**Table 4-6**), namely the benzene ring (1483 cm^{-1}) as well as the hydroxyl (3540 cm-1) and amine moieties (3414 cm^{-1}) of the pterin part. Moreover, the carboxylic acid peak around 1690 cm^{-1} should disappear after reaction with the aminated surface of the nanoparticles.

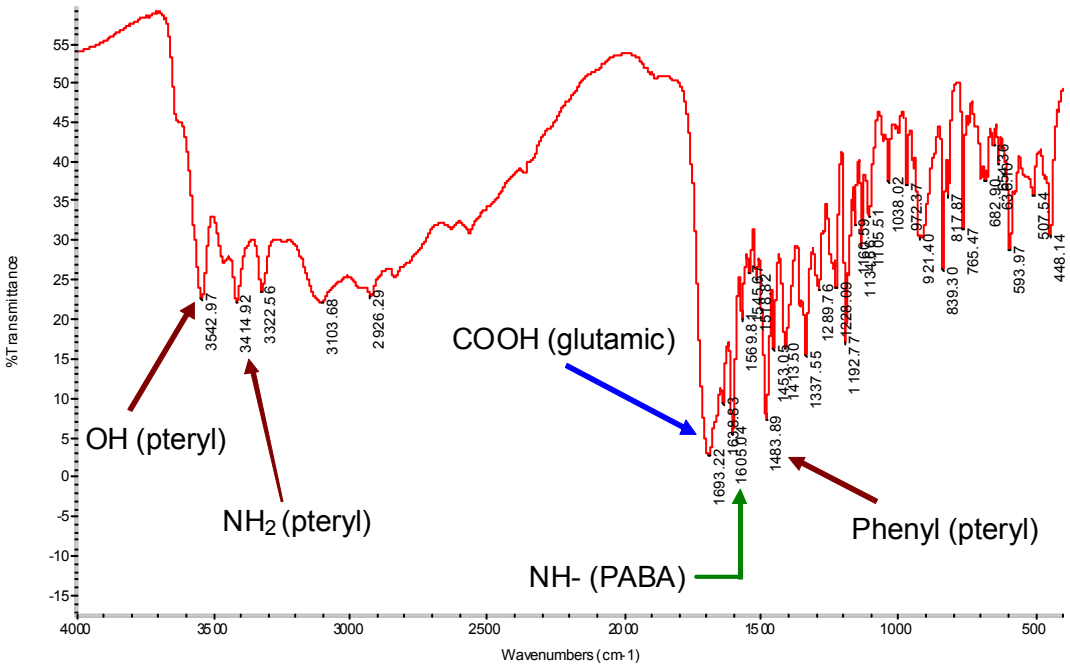

Figure 4-15: Infrared spectra of pure folic acid.

Table 4-5: Principal band appearing on the infrared spectrum of folic acid.

Wavenumber	Description[a]	Structural unit
3543 cm^{-1}	ν (O-H)	hydroxyl (glutamic acid)
3416, 3324 cm^{-1}	ν (N-H- - - H)	NH_2 (pterin)
2959, 2924, 2844 cm^{-1}	ν (C-H) and ν_s (C-H)	CH_2
1694 cm^{-1}	ν (C=O)	COOH
1640 cm^{-1}	ν (C=O)	COOH
1605 cm^{-1}	δ (NH_2) (bending)	NH_2
1484 cm^{-1}		Phenyl ring
1411 cm^{-1}	ν (O-H)	OH (phenyl skeleton)

[a] *ν = stretching vibration, δ = bending vibration.*

HA has a different structure consisting in the repetition of D-glucuronic acid and N-acetyl-D-glucosamine units bound by β 1-3 and β 1-4 linkages (**Figure 4-16**) [*Hargittai, 2007*]. For the purpose of this study, three chain sizes were selected: 11 disaccharides units (HA 11), 583 units (HA 583), and 6457 units (HA 6457).

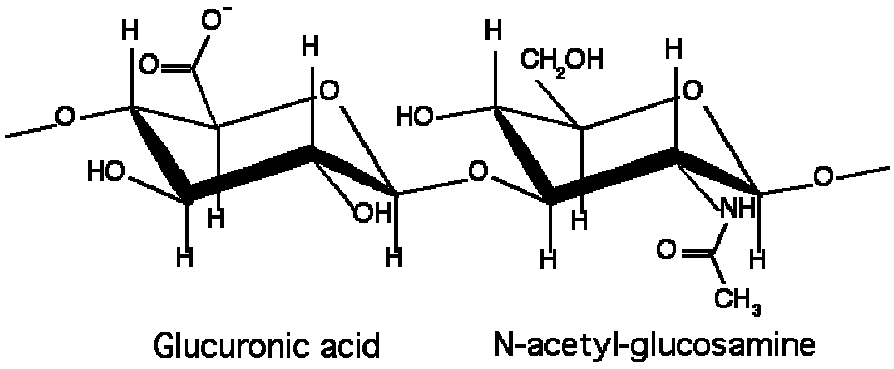

Figure 4-16: Chemical structure of the D-glucuronic acid and N-acetyl-D-glucosamine units that constitute hyaluronic acid.

The infrared spectrum of HA is simpler than that of FA(**Figure 4-17**): the principal reactive groups of the monomer are the carboxylic and amide groups as well as the glycosidic bond linking glucuronic acid and N-acetyl-D-glucosamine (**Table 4-7**) [*Alkrad, 2003; Donghui, 2006*].

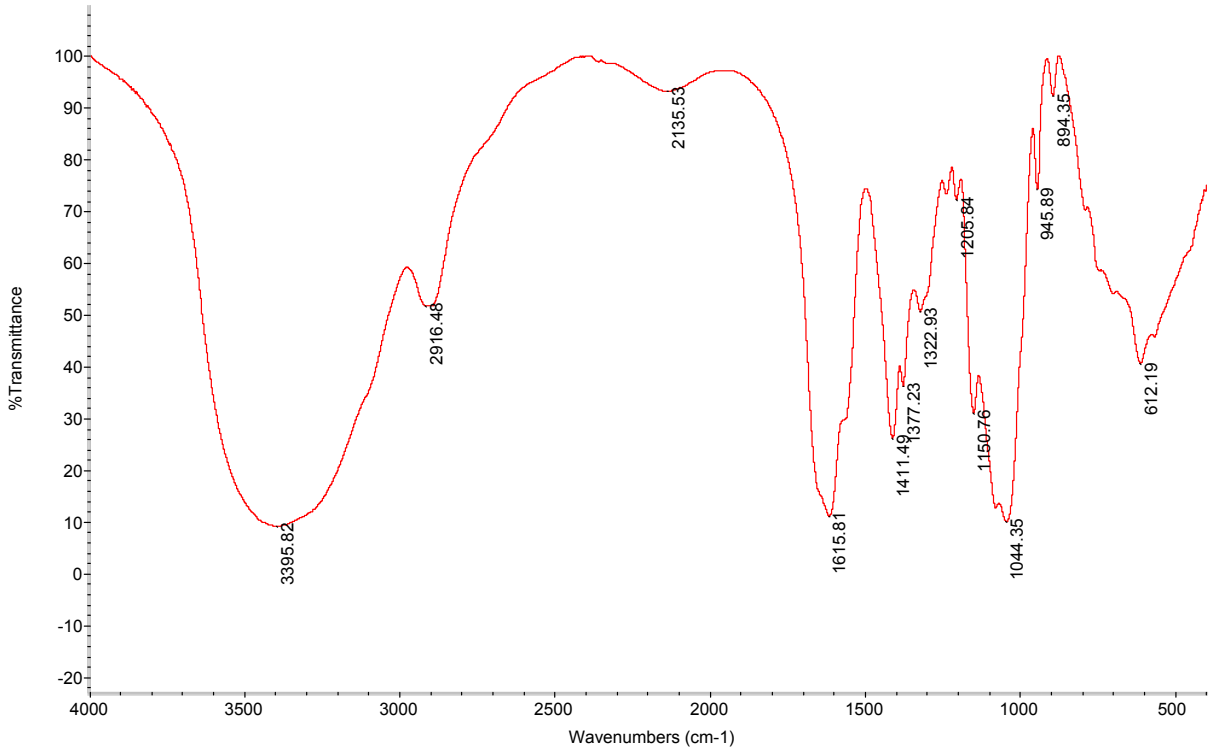

Figure 4-17: Infrared spectra of pure hyaluronic acid.

Table 4-6: Principal characteristic peaks on infrared spectra and related functional groups.

Wavenumber	Mode	Structural unit
3395 cm^{-1}	v (NH), v (OH)	OH and amide groups
2916 cm^{-1}	v (CH)	C-CH_2-C
1615 cm^{-1}	δ (NH)	Amide II and carboxyl
1411 cm^{-1}	v (CN) and δ (NH)	Amide III
1377 cm^{-1}	v (C=O)	Carboxyl -COOH
1044 cm^{-1}	v (C-O)	C-O-C
945cm^{-1}	δ (O-H) and v (C-C)	C-O-C (ring) and OH
612 cm^{-1}	ω (N-H)	Amide I

[a] *v = stretching vibration, δ = bending vibration,* ρ = rocking: ω = wagging.

The conjugation protocol was based on Santra's procedure and was gradually modified [*Santra, 2005 b*]. Initially, higher concentrations of folate, carbodiimide, and NHS than in Santra's protocols were used to initiate the esterification of the FA with NHS [*Santra, 2005 b*]. N,N'-dicyclohexylcarbodiimide (DCC) was used instead of EDC because this compound was available in the laboratory. In all cases, the suspensions had acquired a strong yellow colour characteristic of folic acid, but the high quantity of the ligand may result in adsorption rather than actual bonding with the amine moieties. Yet, some of the infrared spectra of the nanoparticles exhibited two very intense peaks at 1626 and 1574 cm^{-1} that replaced the 1690 and 1640 cm^{-1} peaks seen in the FA spectrum. These changes at 1626 and 1574 cm^{-1} are respectively caused by the C=O stretching vibration and the C-N stretching vibration of the amide group (**Figure 4-18**).

When the NHS, DCC, and FA/HA concentrations were decreased to match Santra's protocol, no significant changes on the particle spectra were observed in the infrared spectra and the conjugation failed. Consequently, the experiments were attempted once again under different conditions, in particular EDC was used instead of DCC and the arginine solution that was originally chosen was replaced by MES buffer (pH 5.5) because the reaction between FA and NHS is pH-dependent and the optimal conditions are between pH 4 and 6. New peaks appeared at 1700, 1680, 1535, and 1484 cm^{-1} (**Figure 4-19**). The

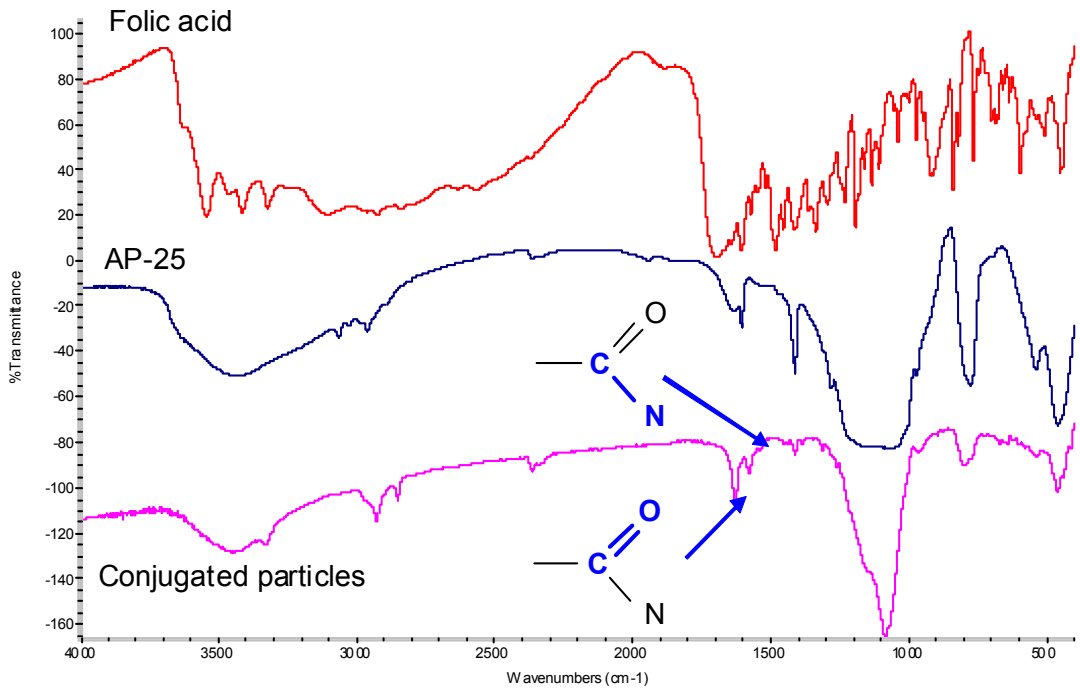

Figure 4-18: Infrared spectra of folic acid (red), hybrid particles with a 25 molar% APTES coating (blue) and FA-conjugated hybrid particles (pink).

peak at 1700 cm^{-1} corresponds to the carboxylic acid group (C=O stretching) of folic acid whilst the small peak at 1484 cm^{-1} is attributed to the phenyl ring of the same molecule [*Zhang, 2008; Asadishad, 2010*]. Unfortunately, none of the changes are the sign of a covalent bonding of FA to the nanoparticles (amidification) but are due to the adsorption of molecules onto the particles [*Kong, 2007*]. Variation of the EDC, NHS, and FA concentrations gave similar results and it was not possible to evidence the actual conjugation of FA (and HA) on the nanoparticles. It seems that the conditions were not optimal for the formation of amide groups, meaning that the experiments must be carried out again to detect what part of the process prevent the bioconjugation from occurring.

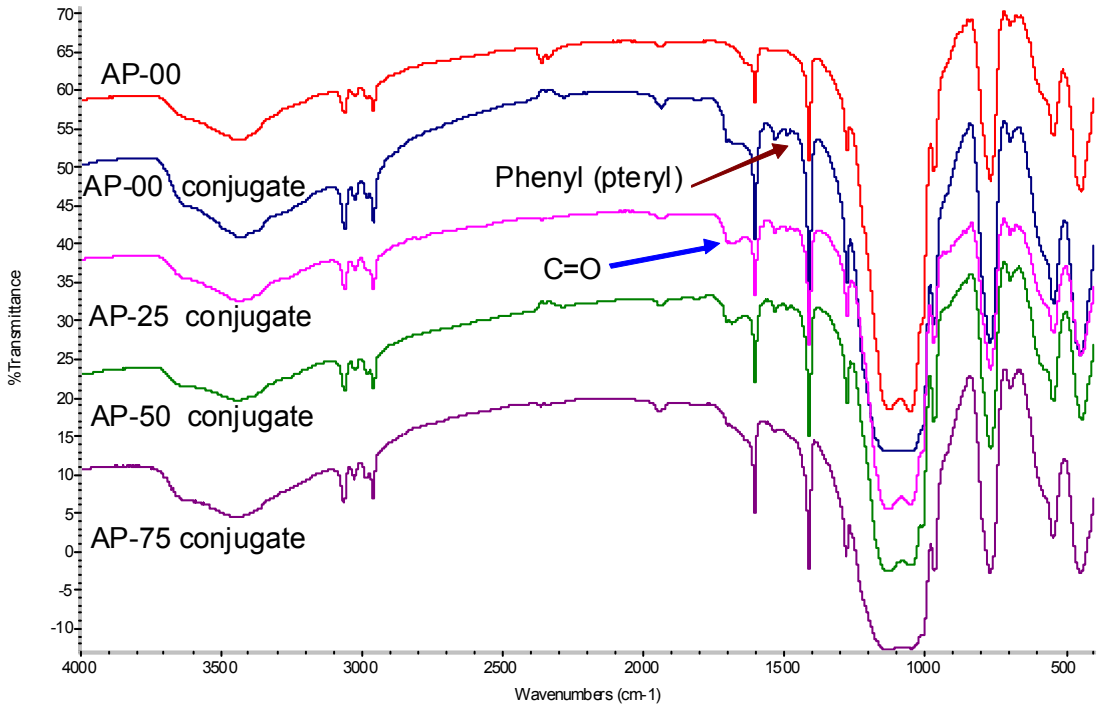

Figure 4-19: Infrared spectra of amine-modified hybrid particles (red) and AP-00 (blue), AP-25 (pink), AP-50 (green), and AP-75 (purple)

4.4 Discussion

The process developed by Yokoi, Davis, and Hartlen is very flexible [*Davis, 2006; Hartlen, 2008; Yokoi, 2006*] and this thesis reports for the first time the synthesis of amino acid-catalysed ORMOSIL nanoparticles. The choice of VTEOS stemmed from the idea of designing a structure with both hydrophilic and hydrophobic properties: since the amino acid catalysis is a one phase system where water is the only solvent, it was hypothesised that the hydrophobic VTEOS would seek protection from water and hence would create the core of the nanoparticles. TEOS would then surround the newly formed core in a sort of hydrophobic core-hydrophilic shell.

4.4.1 Structural characterisation of the hybrid particles

Since VTEOS and TEOS react differently with water, it seemed plausible that the VTEOS-TEOS molar ratio may affect the dimensions of the final particles. The first experiments showed a variation of the particle diameter with a change of VTEOS percentage: the original 10 nm seeds made of TEOS grew larger as the VTEOS/TEOS ratio increased and reached 115 nm with 75 % of VTEOS and more than 200 nm for pure VTEOS particles. VT-00 and VT-25 were produced in very small quantities even when the reaction time was prolonged up to two tor three days. This phenomenon was already observed in chapter 3 where 1 to 2 mg of seeds was produced but it is not clear why the yield is so small. Light scattering measurements indicated that the polydispersity indexes of VT-00 and VT-25 were high but the hydrodynamic diameter curves nonetheless indicated that the particles were circa 10 nm in diameter. This value is in agreement with what other studies using arginine and lysine reported (1 to 20 nm in diameter).

Interestingly, several tens of mg of VT-50, VT-75, and VT-100 were produced within 10 to 12 hours every time that the experiments were repeated. At the

same time, the particle size varied greatly from one composition to another. For instance, the hydrodynamic diameter of VT-75 was circa 115 nm (actual diameter close to 90 nm) with a polydispersity index of 0.1 characteristic of well-dispersed suspension. In contrast, VT-100's hydrodynamic diameter was closer to 300 nm (actual diameter around 250 nm) without aggregation. VT-50 nanoparticles were about 45 nm but the polydispersity index slightly superior to 0.1 is the sign of the formation of small clusters of 2 or 3 particles. This tendency was confirmed by electron microscopy since the images displayed numerous aggregates with VT-50 that were not observed with VT-75 and VT-100. Infrared spectroscopy confirmed the dual nature of the particles with the siloxane band(1200 to 1000 cm^{-1}) and vinyl peaks (1400 and 1600 cm^{-1}). The intensity of the vinyl peaks increased with increasing the VTEOS/TEOS molar ratio but remain less intense than the siloxane band in all cases.

At the beginning, heptane was added to the arginine solution because its presence supposedly slows down the hydrolysis of TEOS and favours the formation of a larger number of small nuclei [*Hartlen, 2008*]. This strategy is not suitable when a hydrophobic precursor is used because it splits the particles between hydrophilic and hydrophobic ones and induces segregation during the centrifugation step. This may be due to the fact that some particles with a high content of VTEOS must have formed in heptane rather than in water and the high density of vinyl moiety in these particles has imparted hydrophobicity. Therefore, when the suspensions were centrifuged, the hydrophobic nanoparticles were trapped between the organic phase and water. To synthesise homogeneous suspensions, heptane was suppressed. This time, no segregation was observed after centrifugation of all of the suspensions. DLS measurements and MEB images showed no significant difference with and without heptane, apart from VT-100 where the particle diameter nearly doubled. Infrared spectra of the particles were similar, indicating that the composition of the hybrid were unaffected by the change of conditions.

The VTEOS content exerts a strong influence over the nanospheres size and potentially on the hydrophobicity nature of the particles. It is unknown why VT-

75 and VT-100 changed so much but it might pertain to the high content of VTEOS and the use of water as solvent. More importantly, the amino acid route appears as an alternative to oil-in-water emulsion for the synthesis of ORMOSIL nanoparticles of small dimensions, though the experiments have focused on VTEOS only. Of the five compositions, VT-50 nanoparticles appeared as the most interesting due to their smaller size compared to VT-75 and because they were produced in larger amount than VT-00 and VT-25. For this reason, VT-50 was kept as the base structure for the next experiments.

4.4.2 Modifications of the experimental conditions

Since the reactions leading to the generation of nanoparticles remain sol-gel reactions, it is possible that the variation of parameters such as arginine concentration or water content could alter the particle diameter and/or composition. The stirring rate was selected as one such parameter and it also serves to assess the particle formation kinetics. Without stirring, silanes and water are not miscible and the hydrolysis of TEOS and VTEOS occurs at the interface between the two phases at a very slow pace. These conditions are impracticable since it would take too much time to eventually obtain the nanoparticles. The hydrodynamic and number diameters of VT-50 for all stirring speed converged towards the same values of 140 and 70 nm respectively. The polydispersity index of 0.179 indicated that in all cases, small clusters of VT-50 nanoparticles (primary particle diameter between 40 and 50 nm). The principal difference is the time necessary to reach the size threshold: the final particles were obtained after 8 to 10 hours at higher speed but take more than 24 hours at the lowest stirring speeds. The conclusion is that the stirring rate affects the time necessary to synthesise the hybrid seeds but not their dimensions and is not a parameter of influence when it comes to the structure of the seeds. However, the morphology of the particles must be studied with more details because they may lose their smooth spherical shape as noted by Hartlen [*Hartlen, 2008*].

Conversely, it was expected that the reagent concentrations - silanes, catalyst, and water – would have the deepest impact. It is well-known that these concentrations govern the size of the pores in gels and the diameters of sols/particles. The silica-to-arginine molar ratio was varied from 0.01 to 0.1 and the silica-to-water ratio from 100 to 200 whilst the volume of water was kept constant. The particle hydrodynamic and number diameters were larger at the highest arginine concentration and smaller at the lowest. The pH of all solutions fluctuated between 10 and 10.3 and could not be responsible for the changes and it is more likely that the number of arginine molecules in solution is directly connected to the variation of diameter. One hypothesis is that at low arginine concentration a limited number if nuclei are formed owing to an insufficient number of arginine molecules, and the remaining TEOS and VTEOS molecules are free to enlarge the seeds. The influence of water is less obvious since the diameter remain approximately the same at fixed arginine concentration. More experiments are required to clearly assess the influence of arginine and water because the particle shape changed when a new VTEOS solution was used. The Zetasizer detected micrometric particles in solution and MEB images displayed cup-shaped objects for each arginine and water concentrations. In absence of additives such as surfactant or growth-directing agents, it seems unlikely that the cup-shaped particles could be formed, especially because the sphere is the most energetically favourable form for the growth of particle in solution and because the co-condensation of TEOS with APTES, THPMP, or phenyltriethoxysilane (PhTEOS) as discussed in the next chapter did not create such shape. The VTEOS solution may have been contaminated at some point, which may explain the sudden change of morphology of the particles [*Champion, 2007; Gratton, 2008*].

It is not yet possible to affirm that the protocol is reproducible so long as the mechanism that led to the cup shape has not been elucidated. There are strong evidences that the initial small particles are the genuine particles and that the latter results are the products of some contamination of the VTEOS solution. From the preliminary results, the arginine catalysis seemed to confine the particle diameter below 100 nm and the arginine concentration appeared as the

parameter inducing the more significant variations of the nanoparticle dimensions. This must be compared to the Stöber method, where small variations of ammonium hydroxide may totally change the size of the final particle. However, the experiments must be repeated and the DLS measurements must be coupled to SEM and TEM images to clearly measure the diameter of the particles. Other techniques such as small angle x-ray scattering (SAXS) and RMN ought to be carried out to elucidate the kinetics of particle nucleation and how VTEOS and TEOS interact one with the other in the first steps.

4.4.3 Surface modification and bio-conjugation

Particle agglomeration and aggregation is a problem encountered with many nanomaterials. Here, it has been shown that VT-50 formed small clusters of a few primary particles but well-dispersed particles are usually preferable. Thus, the strategy consisted in modifying the surface and introducing groups that would promote the repulsion between particles. Additionally, some of the groups can be used as a way to conjugate ligands to the particles for specific targeting. In the case of silica-based systems, silicon precursors bearing sulphur, carboxylic, amine, and other organic groups can easily condense onto the silanol groups expressed at the surface of the particles. Here, APTES was first chosen and added to the VT hybrid suspensions after the particles were formed. The changes in the suspensions are immediately noticeable: during the centrifugation step, the supernatant was immediately clear and the quantity of material collected nearly doubled compared to the basic hybrid seeds. DLS measurements showed the presence of large particles in suspension, which was corroborated by SEM images that depicted highly aggregated samples. In other terms, the addition of APTES promoted the aggregation of the particles rather than their stabilisation.

The phenomenon has been rarely evoked in the literature, in spite of the extensive use of APTES and other aminated silanes to modify silica surfaces.

Bagwe et *al.* solved this issue and figured out that the amine groups bind to the silanol groups via hydrogen bonding [*Bagwe, 2006*]. Besides, the amine groups are positively charged and are attracted by the negatively charged silanols so that the outcome is a strong aggregation between particles. In the same study, they advocated the use of a second silane with a longer chain and a negatively charged group that can insert between amines and silanols to counteract the attraction between nanospheres (**Figure 4-20**). To prove their point, they co-condensed APTES with the phosophonated silane THPMP and showed that increasing THPMP proportion in comparison to APTES decreases the hydrodynamic radius and that the zeta potential of the system moves towards lower values and stabilise the suspensions. The only requirement for a successful condensation of the organosilane onto the silica sphere is that some TEOS is reacted with the colloidal suspension about 30 minutes before APTES and THPMP [*Deng, 2000*].

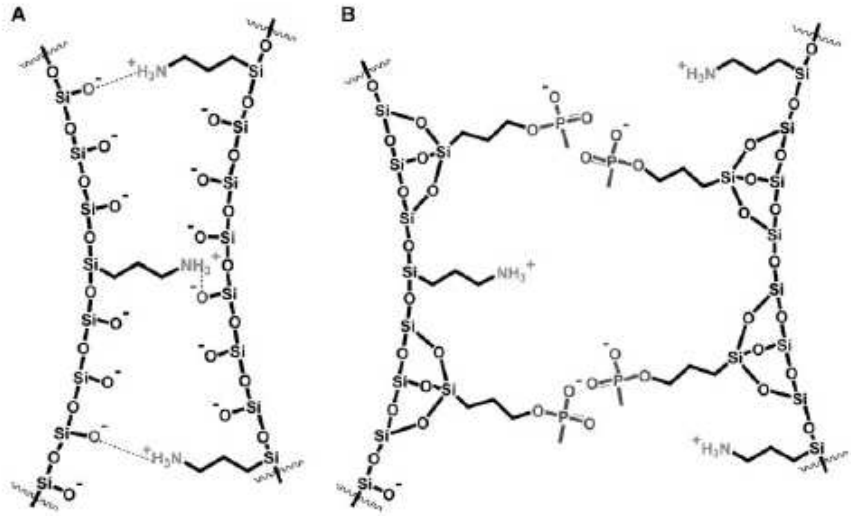

Figure 4-20: Hydrogen bond between amine and silanol at the surface of nanoparticles and action of PO4 inserted on the aminated particles.

Based on these findings, the two organosilanes were tested and both DLS and SEM tallied on the reduction of aggregation as THPMP concentration increased. One point remained obscured but could not be assessed: FTIR is not

sensitive enough to clearly detect the presence of phosphonate if THPMP condensed onto the particles (the IR peaks are hidden by the more intense siloxane bands). Since the presence of THPMP onto the particles remains hypothetic it is unclear whether the change of stability is linked to the phosphonate moieties or to the decreasing amount of APTES. Zeta potential measurements must be performed to follow the modification surface because the presence of phosphonate would lower the potential of the suspension. Zeta potential would also indicate whether the particle suspensions are stable or not.

Since the presence of APTES was certain, the bio-conjugation with FA and HA was attempted with the aim of specifically targeting cancerous cells. Folic acid (FA) was selected for its availability and because some studies suggest that FA can be use as a targeting agent. Hyaluronic acid was chosen for its capacity to link to CD44 receptors that are overexpressed in a number of cancers. The two molecules possess carboxylic acid groups and can react with aminated surface via carbodiimide chemistry. The first attempt with FA saw the appearance of peaks common to the nanoparticles and to folate, but also two intense peaks related to amide functions while the carboxylic acid peak of FA was no longer observed. Yet, amount of FA in the protocol was too high in comparison to the protocols detailed in the literature but it was impossible to detect any sign of amidification when the concentration of EDC, NHS, and FA were reduced. The mistake was to employ arginine solution and water as solvent. The reaction between EDC and the carboxylic acid of FA is pH-dependent and optimal 3.5 and 5.5 and the amine groups must be in their protonated state to react with the unstable O-urea [*Nakajima, 1995*]. The pH of arginine solution and pure water was too high to allow the reaction between amine and carboxylic acid to occur, plus the amine and carboxylic acid groups of arginine may interfere with EDC and FA.

MES was next used as a solvent to set the pH to a value of 5.5. A few changes were visible in the infrared spectra but the new peaks correspond to adsorbed or residual FA that was not washed away after centrifugation (solubility of folate in water is limited). The protocol developed in this thesis failed at conjugating

the biomolecules to the hybrid particles. More experiments with increased concentrations of FA and/or of EDC and NHS or adjusting the MES buffer pH to 4.5 to 5 may help in reacting carboxylic acid and NHS. Additional characterisation using thermogravimetry and electrophoresis could prove whether the coating of biomolecules is present or not. In particular, thermogravimetry may be sensitive enough to quantify the FA and HA density on the particles.

4.5 Conclusion

In this chapter, a novel method to synthesise ORMOSIL has been explored which appeared simpler (one phase system) and cleaner (no surfactant and organic solvent) than the oil-in-water emulsion. The hybrid particles were made of TEOS and of the hydrophobic VTEOS and their diameter appeared larger than that reported with pure silica nanoparticles, although the size remained secluded below or slightly above the 100 nm-threshold. Of the five compositions tested, VT-50 appeared as the most promising due to its hydrophilicity and to its diameter of about 45 nm. Although the effect of each parameter remain to be studied for the VT-50 particles, it occurred from the preliminary results that arginine concentration and water content variations do not induce large variation of the particle sizes.

Another aspect discussed in this chapter was the surface modification and the subsequent attempt to coat the particles with folic acid and hyaluronic acid. It was found that the use of APTES as coupling agents form amine groups at the surface of the particles but at the same induce a strong aggregation. In theory, the formation of hydrogen bonding can be countered by the addition of THPMP, but no phosphonate was detected with the characterisation techniques used in this study. The surface modification was not successful and requires more time to be refined as well as more characterization. This step is as important as the carrier because it is the bioconjugation of the nanoparticles that will decide of the application and allows specific targeting and specificity.

Despite of this problem, this chapter has seen the elaboration of ORMOSIL nanoparticles with a dual hydrophilic/hydrophobic nature. The idea is that the dual nature would help stabilising the fluorophores by providing an environment suitable to any dye regardless of its affinity for water. In particular, considering that the particle growth proceeds in water, t is expected that hydrophobic dye would go preferentially into the vinyl-rich regions of the particles. Now that the particle is ready, the carriage capacity and optical properties must be assessed.

Chapter 5

Applicability of the VTEOS hybrid particles to the carriage of organic fluorescent dyes

5 Applicability of the VTEOS hybrid particles to the carriage of organic fluorescent dyes

5.1 Introduction

Despite its promises, the capacity of silica nanoparticles to entrap fluorophores may be limited by its hydrophilic nature and the negative charge of its network. The fluorophores used in Chapters 2 and 3 were hydrophilic (or partially hydrophilic in the case of rhodamines), or sylilated to make the encapsulation easier. The effect was more obvious in the case of reverse microemulsions where the fluorophores were not able to penetrate within the micelles. A quick review of the FSNPs literature reveals that few of them are employed in comparison to the wide diversity of fluorescent dyes available and that: lanthanide chelates and isothiocyanate/maleimide derivatives of fluorescein and rhodamine represent the majority of the dyes studied. The entrapment of NIR dyes, and two-photon dyes is gaining momentum both as labels and photosensitisers but mostly via oil-in-water microemulsions towing to the hydrophobic nature of the dyes [*Bertazza, 2006; Herz, 2009; Miletto, 2010*]. Very few articles report the encapsulation of conventional fluorophores such as Nile red, crystal violet, or even rhodamine B and rhodamine 6G [*Mader, 2008; Qin, 2008; Sokolov, 2008; Theaker, 2008; Wang, 2009*].

There are two major procedures which can facilitate the incorporation of fluorophores within silica nanoparticles. The first requires the chemical modification of fluorophores for subsequent covalent binding with organosilane [*Gao, 2009; Ha, 2009; He, 2007; Langhals, 2009*]. Chemical modification of a fluorophore is often a heavy and complex procedure and this approach is usually discarded to the profit of more standard solutions. The second procedure uses an oil-in-water emulsion to produce ORMOSIL structures,

mostly for the encapsulation of hydrophobic compounds. Yet, oil-in-water emulsions face the same weaknesses as reverse microemulsion (organic solvent and surfactant, risks that the precursor or fluorophore are not soluble enough in the desired phase, etc.). The absence of a “universal” method to encapsulate fluorophores regardless of their hydrophobic or hydrophilic nature may explain why the design of multifluorescent nanoparticles is rarely reported. There are reports of microspheres loaded with quantum dots, but not with silica nanoparticles. The only major contribution to the synthesis of multifluorescent particles is the FRET system designed by Wang and Tan [*Wang, 2005 b*]. These particles contain 5-carboxyfluorescein, succinimidyl ester, 5-carboxyrhodamine 6G, succinimidyl ester, and 6-carboxy-X-rhodamine, succinimidyl ester at different ratio to modulate the spectral signature of the nanospheres. Nakamura et *al*. were able to co-encapsulate similar succinimidyl esters into submicrometric nanoparticles [*Nakamura, 2007*] but generally speaking multifluorescent nanoparticles with more than two fluorescent dyes remain ill-explored.

Development of a silica-based nanoplatform hosting multiple fluorophores simultaneously may be interesting multifunctional systems. The first application would be as a contrast agent for imaging: the combination of two or more dyes ascribes unique signature to the nanoparticles than can advantageously be used to image different targets simultaneously (multiplexing), for instance to distinguish different cell population in a sample or different organelles in single cells. Wang’s FRET system was to monitor *Escherichia coli*, *Salmonella typhimurium*, and *Staphylococcus aureus* by producing sets of particles with different dye ratios and conjugated to target on of the three bacteria [*Wang, 2007 a*].

Photoluminescent dyes for imaging are the principal dyes studies [*Estevez, 2009*] but the encapsulation of fluorophores with other physicochemical properties are generally underrated. Yet, certain fluorophores are suitable for photodynamic therapy (generation of singlet oxygen and radical species), some

are potential photoaccoustic agents, and some dyes commonly found in biology are sensitive to environmental parameters (pH, temperature, presence of ions, etc.). Of these three applications, the encapsulation of photosensitisers (PS) is the most documented because it overcomes the diffusion of the photosensitisers into the whole organism that make patients photosensitive [*He, 2009 b; Ohulchanskyy, 2007; Chen, 2009 b*]. Furthermore, these studies showed that oxygen is able to diffuse away from the particles through pores in the silica matrix but the dye molecules remain trapped inside the particles [*Roy, 2003*]. In other terms, the insulation of the dyes is partial and the smallest molecules and ions are able to diffuse through the matrix and reach the dyes, but larger molecules susceptible to quench or photodegrade the fluorophores cannot penetrate inside the particles.

The partial insulation is an important feature for the use of environmental dyes because it means that the fluorophore inside the ceramic matrix are still able to detect changes in the particle surrounding. Under their free form, sensor dyes are suitable for optical sensors as an alternative to electrochemical and electronic sensors to monitor multiple analytes in a sample and to detect specific environmental parameters such as calcium concentration, pH, generation of radicals, etc. [*Han, 2010; Moczko, 2009*]. Unfortunately, like most of the organic dyes, sensors fluorophores are prone to fast photobleaching. Their encapsulation within silica particles could lead to a new class of nanosensors able to probe the cellular environment *in situ*, detecting the potential change of pH or oxygen concentration, or simply measuring sodium or calcium ions concentration. Very few silica-based nanosensors have been reported so far. Platforms sensitive to pH are the most developed, mostly because FITC is a pH-sensitive dye (in the 4.0 to 8.0 pH range) but other fluorophores are potential candidates to probe different pH range [*Burns, 2006; Gao, 2007 and 2011*]. Temperature-sensitive sensors are emerging too: Peng et *al*. used a ratiometric nanoprobe to sense temperature between 25 and 45°C [*Peng, 2010*]. The objective is to design ideal sensing platform or PEBBLE (Probe Encapsulated By Biologically Localised Embedding) introduced by Kopelman and co-workers and where a whole range of sensing molecules are

embedded within a spherical carrier as a mobile and functional nanosensor [*Lee, 2009*]. However, nanosensors require at least two fluorophores (one sensing dye and one referent dye), which may explain the lack of silica sensor nanoparticles.

Taken individually, fluorescent, PS-loaded and sensor silica particles are all desirable for their respective applications (**Figure 5-1**), but to date a method bridging all these functionalities into a single structure is clearly missing. One can envision a single nanoplatform tracked by the NIR emission of a photoluminescent dye, measuring the emission of sensor dyes in search of anomalies, and reacting to correct any defects via photodynamic therapy whilst monitoring the changes in real-time.

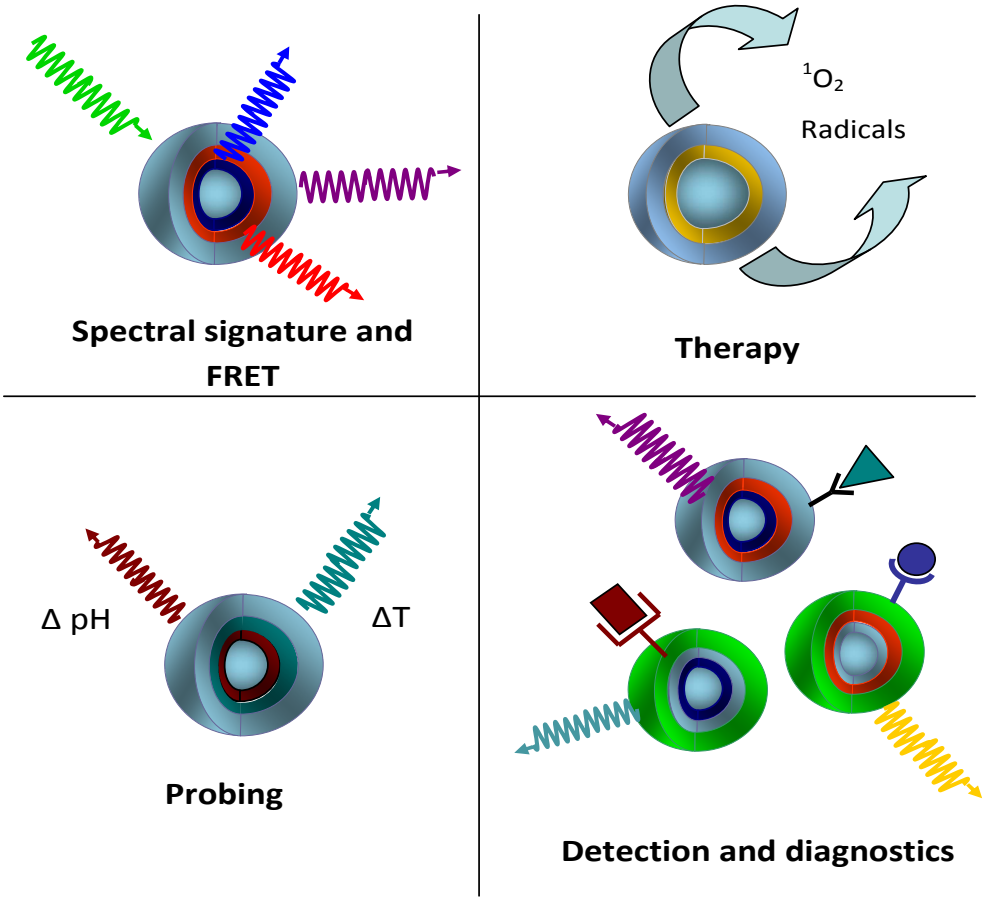

Figure 5-1: Schema of the potential applications of fluorescent and multifluorescent silica nanoparticles.

At a higher level, such multiplatform may not be limited to simple dyes but may include nanoparticles, drugs, or any other compounds that may be relevant from a biomedical point of view. Unfortunately, this hypothetic structure conflicts with the lack of flexibility when it comes to dye entrapment and there is a dramatic need to fill in the gaps that exist in the technology of FSNPs.

In summary, there is a lack of simple protocol suitable for the synthesis of FSNPs and MFSNPs suitable for hydrophobic and hydrophilic fluorophores indifferently. The hybrid VT nanoparticles of Chapter 4 were specifically developed for this purpose: the presence of hydrophobic regions rich in vinyl groups within the particles are supposed to help stabilising the hydrophobic dye whilst the silica network possesses a strong affinity for the hydrophilic fluorophores. The protocol developed in the previous chapter showed that it is possible to produce ORMOSIL particles with a diameter below 100 nm, but their capacity to entrap fluorophore has yet to be demonstrated.

The aim of this chapter is to verify whether the VT hybrids present an enhanced carriage capacity and are able to entrap a large diversity of fluorophores. The first objective was therefore to try encapsulating various fluorophores differing in term of excitation and emission wavelengths, water solubility, and charge. As will be shown, not all fluorophores were successfully integrated to the particles so that two more objectives were added (**Figure 5-2**):

- With the fluorophores showing a good affinity for the VT structure, the first objective was to combine them into multifluorescent nanoparticles with controlled fluorescence signature using a core-shell structure similar to that detailed in Chapter 3;

The second objective consisted in altering the particle composition as a way to encapsulate the remaining dyes with no or low affinity for the VT-structure. In particular, other organosilane were used instead of VTEOS and the optical properties of the new ORMOSIL nanoparticles were assessed.

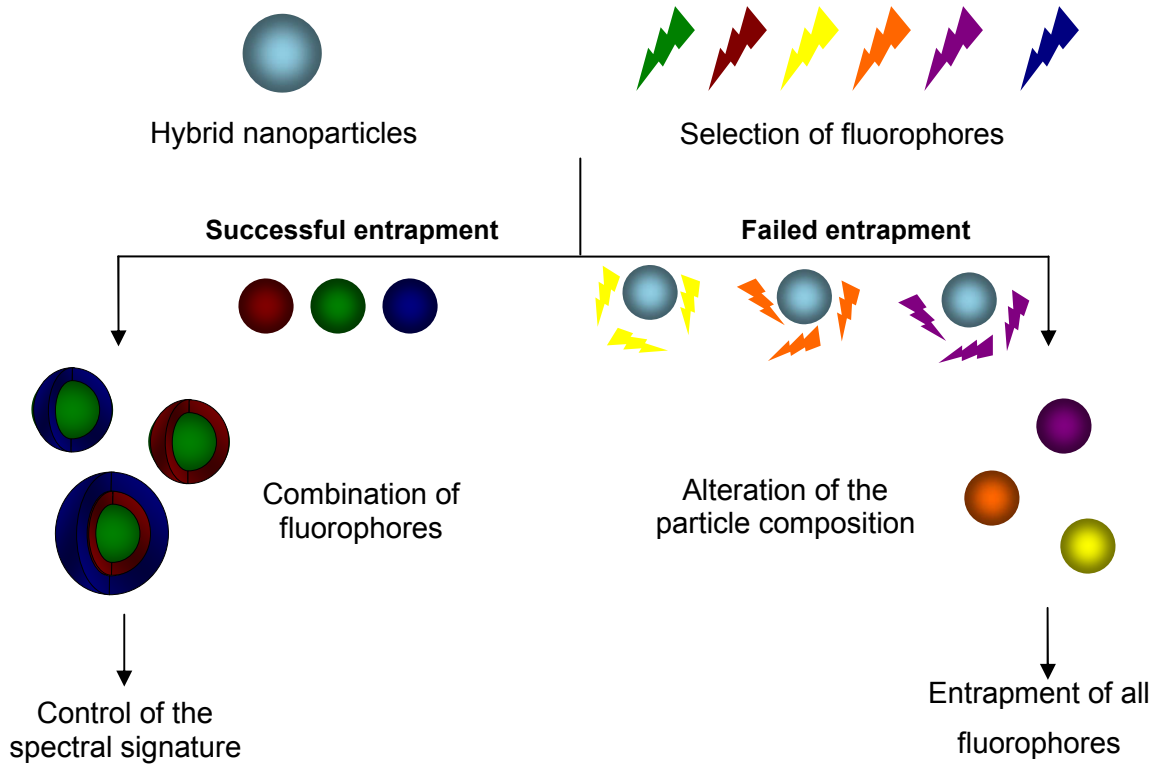

Figure 5-2: Schematisation of the chapter's objectives according to the fluorophore affinity for the hybrid silica nanoparticles.

5.2 Materials and methods

5.2.1 Materials

Chemical were purchased from commercial sources and used as received without any treatment. Tetraethyl orthosilicate (TEOS), malachite green (MG), neutral red (NR), and acridine orange (AO) were purchased from BDH. Absolute ethanol, L-arginine (>98 %), 3 aminopropyltriethoxysilane (>98 %, APTES), 3-(trihydroxysilyl)propyl methylphosphonate monosodium salt solution (42 wt.%, THPMP), vinyltriethoxysilane (>98 %, VTEOS), triethoxyphenylsilane (98%, PhTEOS), lucifer yellow (LY), and fluorescein (Fl) were obtained from Sigma Aldrich. Rhodamine B (RB) and rhodamine 6G (R6G) were purchased from Fluka and methylene blue (MB) from Fisher Scientific. Dextran, alexa fluor 647 (10000 M_W, AF647) and Oregon green 514 carboxylic acid (OG) was obtained from Molecular probes and Invitrogen respectively. Highly purified water (Milli-Q) was obtained from a Millipore “Direct-Q 3” water purification system.

5.2.2 Particles synthesis

- **Choice of dyes**

The fluorophores were selected firstly because they were available in the laboratory and secondly because they possess distinctive physical and chemical properties (**Table 5-1 and Figure 5-3**). All fluorophores solutions were prepared at a concentration of 1 mg/ml (unless specified otherwise) by diluting the dyes in Milli-Q water or in absolute ethanol in the case of oregon green and fluorescein.

Table 5-1: Physical properties of the chosen organic dyes.

Dye	Solvent	Mw (g.mol^{-1})	Excitation/Emission (nm)
Acridine orange	Water	265.35	502/526 nm
Dextran alexafluor 647	Water	10000 (dextran)	650/668 nm
Fluorescein	Acetone, methanol	332.31	490/520 nm
Lucifer yellow	Water	457	428/536 nm
Malachite green	Water	364.91	X
Methylene blue	Water, chloroform, partially in alcohols	373.9	609 and 668/X
Neutral red	Water	288.78	X
Oregon green 514	DMF	512.36	493/520 nm
Rhodamine 6G	Alcohol, water	479.02	525/555 nm
Rhodamine B	Water	479.01	555/580 nm

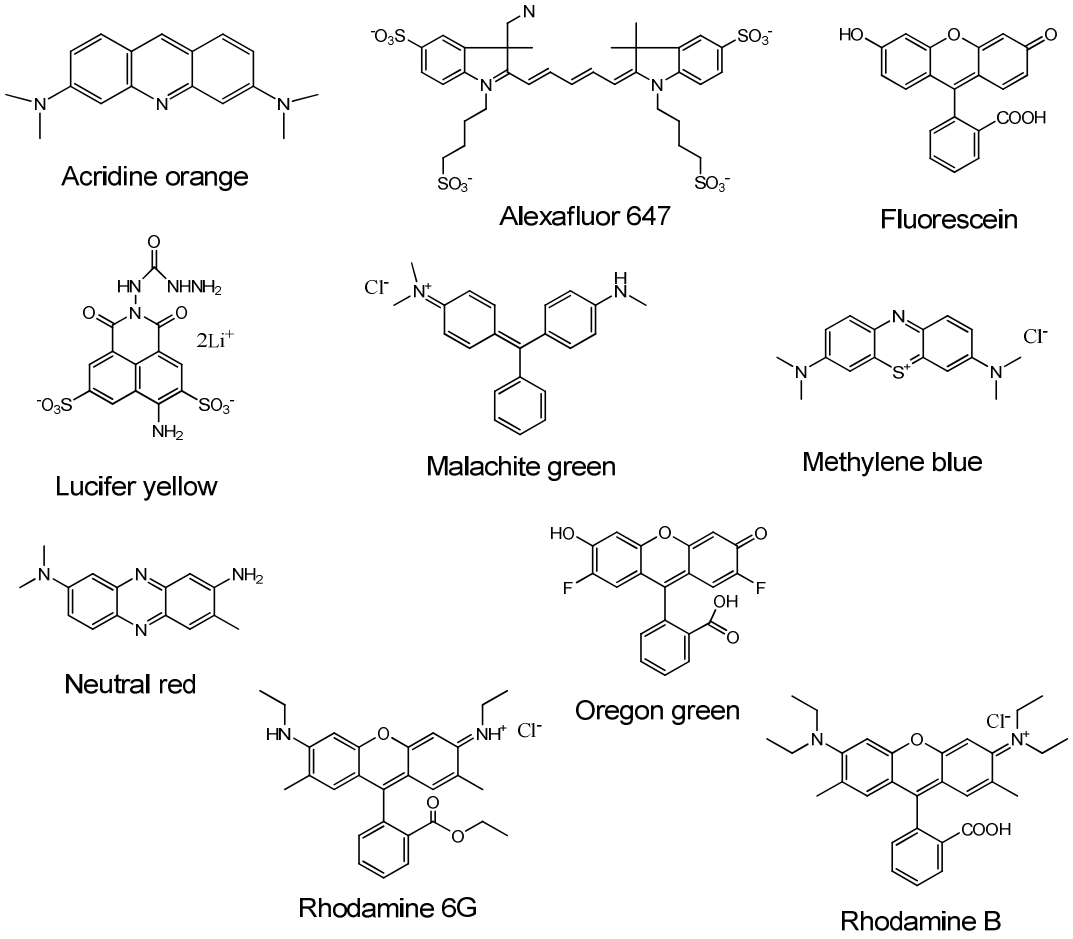

Figure 5-3: Chemical structure of the fluorophore and stains tested with the hybrid particles.

- **Synthesis of hybrid particles**

Hybrid nanoparticles were prepared following the VT-50 protocol detailed in the previous chapter. Typically, 50 µL of fluorescent dye solution (1 mg/mL) was diluted in 7 mL of arginine solution (15 mM) and covered with aluminium foil to protect from light. After 5 minutes, 275 µL of VTEOS and 380 µL TEOS were added dropwise to the fluorescent solution and left under magnetic stirring for at least 10 hours. In some embodiments, VT structures with various VTEOS/TEOS molar ratio were synthesised as described in Chapter 4 (**Appendix C**). The particle suspensions were centrifuged three times at 300 g for 15 minutes or until the supernatant remained transparent and washed with distilled water. The pellets were weighed and suspended in Milli-Q.

- **Synthesis of two- and three dyes-doped hybrid nanoparticles**

The synthesis of multi-layered structures containing two or more dyes started with the preparation of VT-50 seeds. Then, 10 mL of arginine solution (0.5 mM) and 50 µL of the second fluorescent dyes were added to the suspension immediately followed by 150 µL of TEOS to create a first fluorescent layer onto the seeds. The third layer was created by addition of 50 µL of the third fluorophore and 100 µL of TEOS. For each step, the reaction was left under magnetic stirring for at least 10 hours. The colloidal suspensions were centrifuged three times at 300 g for 15 minutes - or until the supernatant remained transparent - and washed with distilled water. The pellets were weighed and suspended in Milli-Q.

- **Variation over the hybrid particles composition**

PhTEOS hybrids with PhTEOS/TEOS molar ratio ranging from 25 to 100 % were obtained by co-condensing a volume of PhTEOS (from 65 to 640 µL) to TEOS (0 to 635 µL) in 7 mL of arginine solution (0.5 mM) (**Appendix F**).

THPMP-TEOS hybrid were obtained by mixing a volume of TEOS (660 to 735 µL) to THPMP (79 to 238 µL) in 7 mL arginine solution (0.5 mM) so that the THPMP molar ratio rose up to 15 molar%. Alternatively, VT-hybrids containing THPMP or APTES to a maximum of 10 molar% were synthesised by co-condensing VTEOS, TEOS, and the third silane following the VT-50 protocol. The recovery of the particles proceeded as described above.

5.2.3 Characterisation

- **Scanning electron microscopy (SEM)**

The particle size and morphology were examined using scanning electron microscopy (SEM). The nanoparticle suspensions were firstly diluted: the samples were sonicated and subsequently 25 µL of suspension was poured in an eppendorf and the total volume was increased to 500 µL with Milli-Q water so that the SEM samples were totally transparent. One drop of suspension was deposited into a silicon grid and let to dry in a desiccator for at least 24 hours. Finally, the particles were imaged using a high resolution FEI XL30 SFEG analytical SEM (Philips, Netherland).

- **Dynamic light scattering (DLS)**

The size and size distribution of the particles were measured by dynamic light scattering using a Zetasizer nano series S with an He/Ne laser of 633 nm wavelength (Malvern Instrument, UK). The particle suspensions were firstly diluted: 10 µL of the sample was poured in a quartz cuvette and completed with 1 mL Milli-Q. The refractive index and absorption of silica nanoparticles were fixed at 1.25 and 0.01 respectively. For each sample, four measurements of 20 runs (15 seconds each) were carried out, with temperature maintained at 25°C.

- **Fourier transform infrared spectroscopy (FTIR)**

The particle composition was analysed by infrared spectroscopy: a volume of nanoparticle suspension was taken, centrifuged, and dried in the oven for 1 day. The resulting powders were subsequently analysed in KBr powders using a Thermo Nicolet Avatar 370 spectrometer (Thermo Scientific). Infrared spectra were recorded over the wavenumber region 4000 to 400 cm^{-1} with a resolution of 4 cm^{-1}.

- **Fluorescence measurement**

Absorbance and fluorescence of FSNP were recorded in 96-well plates with a Varioskan Flash Spectral Scanning Multimode Reader (Thermo Fisher Scientific) equipped with a xenon flash lamp. All measurements were performed on 200 µL of 1 mg/mL suspensions of particles diluted in Milli-Q and at room temperature. Excitation and emission spectra of LY, FITC/AO/Fl/OG, R6G, and RB were acquired with fixed wavelength set 435/540, 450/530, 490/580, and 500/600 nm respectively. The excitation/emission spectra of samples containing AO and R6G and/or RB were obtained at 450/600 nm.

5.3 Results

5.3.1 Integration of usual and less common fluorophores

To fulfil the first objective (testing the carriage capacity of the VT-50 hybrid particles), 10 fluorophores - including MB, R6G, and RB already used in Chapter 3 – were selected due to their availability in the laboratory. These fluorophores differ in term of excitation and emission wavelengths and two of them are not soluble in water. Because the hybrid particles were designed to entrap a large variety of fluorophores without having recourse to sylilation or chemical modification, only electrostatic entrapment was tested to verify whether the dual nature of the material would help stabilising the dyes.

The colour of the particles at the end of the synthesis and centrifugation procedures was the first indicator of the incorporation of fluorophores or lack thereof. To begin with, the particles formed in presence of AO, R6G, and RB exhibited strong orange-yellow, reddish, and pink colours in that order. UV-visible spectroscopy revealed that the suspension absorbed light at 495, 525, and 550 nm respectively and detected fluorescence emission at 520, 555, and 580 nm (**Figure 5-4**). MB, MG and NR exhibited strong blue, weakly green, and pale orange colours in that order; the MB spectrum was the only one displaying a strong absorbance response with a first peak around 600 nm and a second larger one around 633 nm. NR and MG absorbance was very weak, with maxima circa 460 and 540 nm for NR and over 600 nm for MG. Conversely, the particles synthesised in presence of OG, Fl, LY, and AF 647 remained totally white and no optical properties were found.

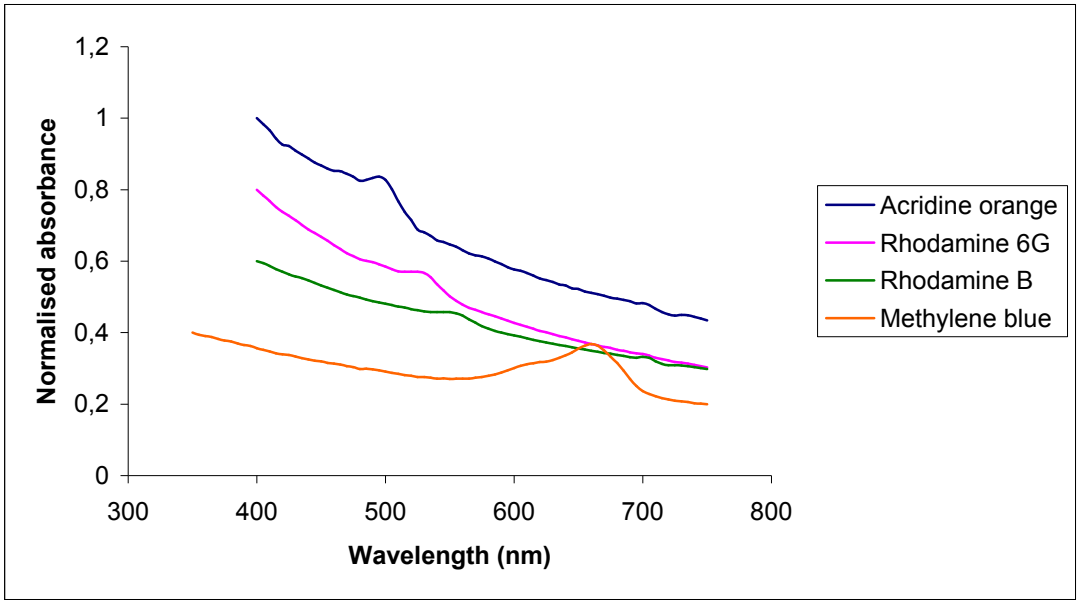

Figure 5-4: Normalised absorbance spectra of AO, R6G, RB, and MB-doped nanoparticles.

In order to investigate the effect of the matrix composition on the dye encapsulation, the experiments were carried out with other VT compositions (VT-00, VT-25, VT-75, and VT-100) and in presence of RB, LY, or OG. Similarly to VT-50, the experiments with RB yielded very bright pink particles, although the fluorescence of the particles cannot be compared directly due to the difference of diameter and of concentration (**Figure 5-5**). However, none of the compositions absorbed light or fluoresced in the case of LY and OG. These results suggest that the hydrophobicity may not be the characteristic governing the entrapment of dyes and in spite of the dual nature of the particles, another factor must be taken into consideration to create a universal carrier.

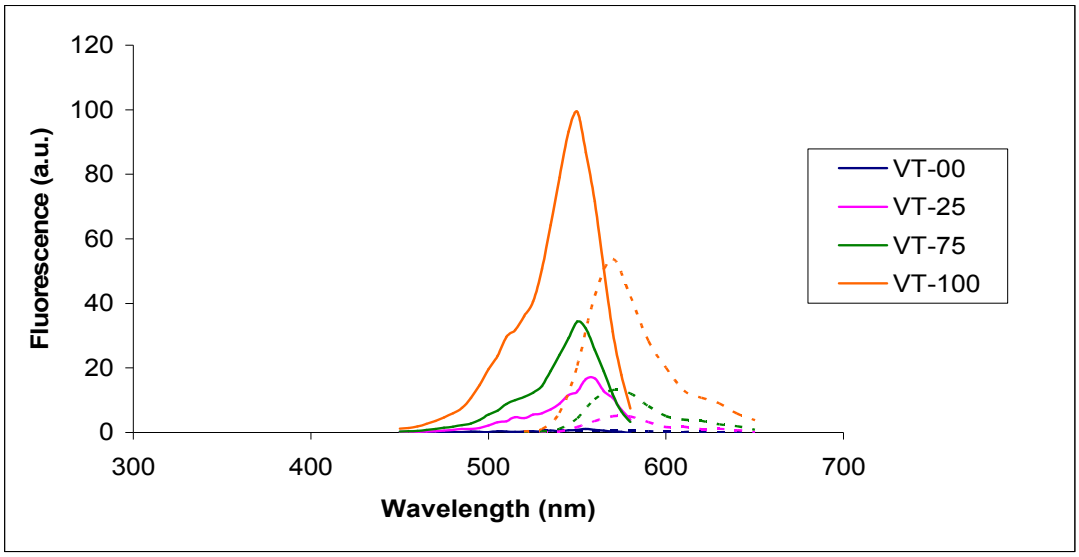

Figure 5-5: Fluorescence intensity of RB-doped hybrid particles at increasing VTEOS to TEOS molar ratio.

Due to the high concentration of fluorophore in the supernatant, it was decided to decrease the initial fluorophore concentration to reduce the losses of dyes. The experiments were conducted on RB and R6G owing to the strong fluorescence of the VT-50 particles obtained previously for molar concentration ranging from 2.10^{-9} to 2.10^{-6} mol. The particles diameter remained restricted between 40 and 60 nm but no correlation was found between the fluorescence intensity and the particle diameter in the case of R6G (**Figure 5-6**). The fluorescence neither increased with increasing the dye molar concentration nor reached any threshold. The main effect, though, was that the supernatant fluorescence was significantly reduced for the lowest dye concentration. In the case of RB; the fluorescence intensity was relatively low between 2.10^{-9} and 2.10^{-8} mol but the intensity suddenly rose for 2.10^{-7} mol (**Figure 5-7**). At higher concentration, the particle fluorescence decreased slightly but remained nonetheless more intense than at low fluorophore concentration. One would expect that the particle fluorescence would increase with increasing the initial fluorophore concentration. Two other possibilities may happen: (1) the fluorescence may reach a threshold corresponding to the maximum dye loading

or (2) the intensity may pass by a maximum above which the high fluorophore density into the particles may be responsible for quenching due to the close proximity between the molecules. Little can be concluded from these results and the experiments must be conducted another time to study with more precision the loading of particles and potentially to quantify the number of fluorophore per particles.

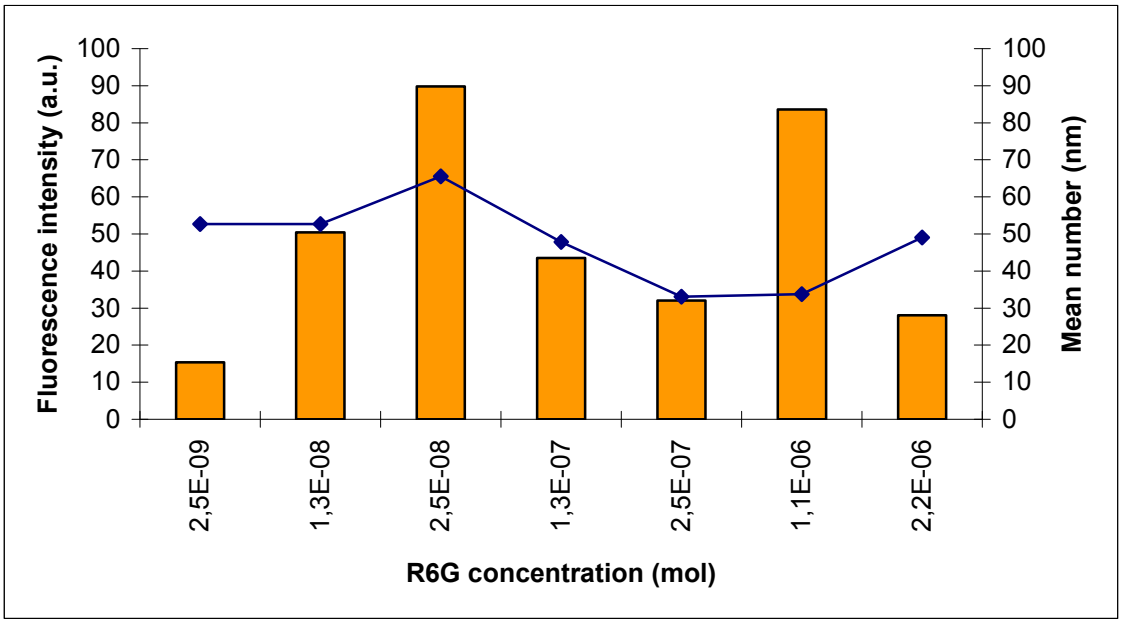

Figure 5-6: Mean number and fluorescence intensity of VT50 nanoparticles with various concentration of R6G.

An important feature of FSNPs is that they must retain the fluorophore throughout time, in particular because certain dyes may have toxic effects. Therefore, hybrid nanoparticles containing R6G and RB were synthesised and kept up to 1 month. The suspensions were centrifuged after periods ranging from 30 minutes to 1 hour and the fluorescence of the supernatant was measured to detect the trace of R6G and RB. No significant fluorescence was detected, even after 1 month, indicating that the particles effectively retain the fluorophores. Nevertheless, the plate reader may not be sensitive enough to detect trace amount of dyes and techniques such as single fluorophore microscopy ought to be used to verify that leakage does not occur at all.

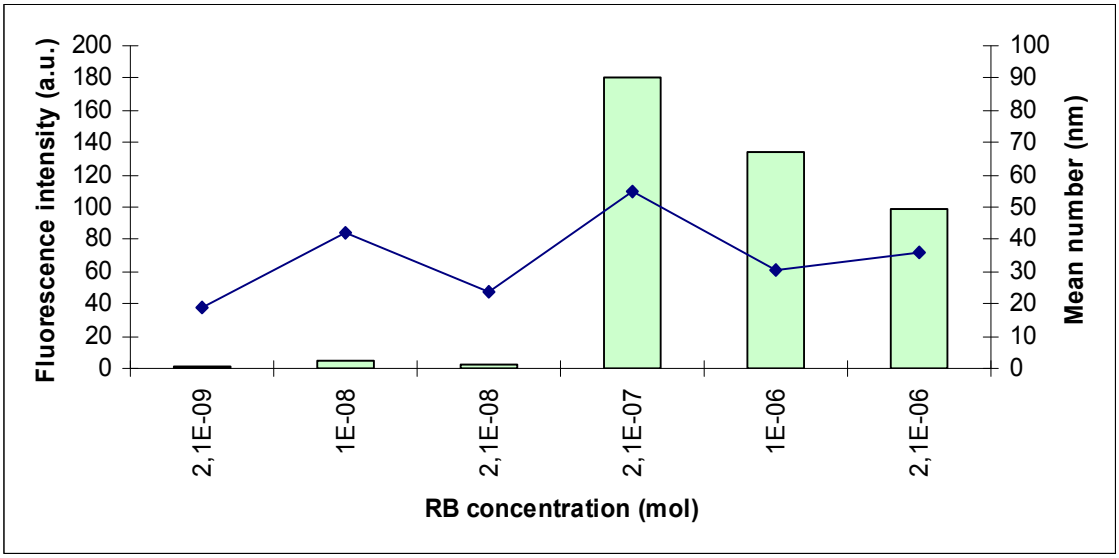

Figure 5-7: Mean number and fluorescence intensity of VT50 nanoparticles with various concentration of RB.

From the results presented so far, it occurs that the hybrid nanoparticles did not contain all fluorophores. Some such as RB, R6G, and AO were easily entrapped and yielded very bright nanoparticles. On the other hand, the particles failed at encapsulating dyes of interest such as LY, OG, or FI even when the particle composition was altered. The hypothesis that fluorescent dyes can be divided between hydrophobic and hydrophilic ones may not be correct, unless the hydrophobicity of the particles is not the parameter to take into account. From this point, the study of the optical properties is divided into two parts:

- On the one hand, combining AO, R6G, and RB (three fluorophores that were successfully entrapped) into a core-shell structure similar to the one detailed in Chapter 3. The objective was to control and tune the optical properties of the hybrid particles by variation of each dye concentration

- On the other hand, finding a solution to entrap Fl, OG, and the dyes that were not detected inside the hybrid particles via alteration of the nanoparticles composition.

Indeed, it is desirable to control the fluorescence of multifluorescent nanoparticles for ascribing distinctive spectral signature to the nanoparticles is crucial for the detection of multiple targets simultaneously, which explains the first objective. Moreover, the purpose of the hybrid particles is to encapsulate any fluorophore without modification of the protocol. This aspect is also important for the multifunctionality of the particles via entrapment of photosensitisers and luminescent and sensor dyes and is the objective of the second part.

5.3.2 Tuning of the spectral signature

One of the chapter's objectives is to design multifluorescent nanoparticles similar to that developed in Chapter 3 but with a larger diversity of fluorophores. Since there is still a limitation on the choice of fluorophore, the multifluorescent system was tested with R6G, RB, and AO, that produced bright particles. In a first time, AO was combined to either R6G or RB at different ratios in order to detect the alteration of the fluorescence pattern and to potentially tune the spectral signature of the nanoparticles. The structure was always based on an AO-containing hybrid core surrounded by a silica layer obtained from TEOS and entrapping one of the rhodamine dyes. The spectra obtained for single dye-doped particles clearly show that the emission and excitation of the fluorophores overlap (**Figure 5-8**). Note however that the spectra are normalised and that the excitation and emission of the three dyes will be modified according to the setups of the plate reader.

AO and R6G emission overlap and because of the close proximity of the excitation and emission of the two dyes, the spectra of particles containing simultaneously AO and R6G displayed a single broad peak. At low R6G

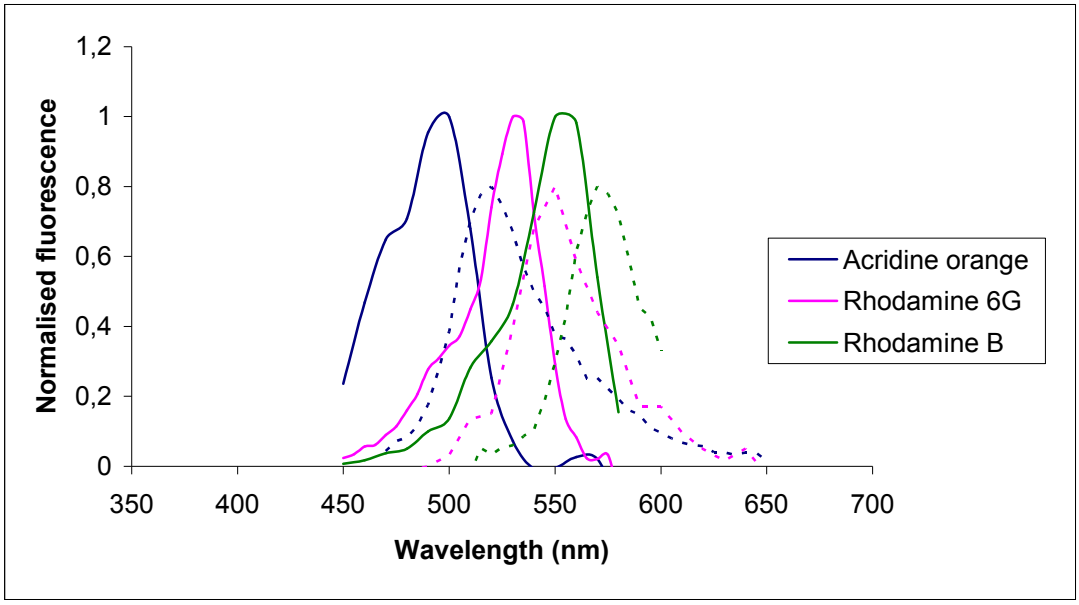

Figure 5-8: Normalised excitation (plain lines) and emission (dotted lines) of single dye-doped hybrid nanoparticles.

concentration (100 µL of AO and 10 µL of R6G), the fluorescence of AO dominated and the emission maximum was centred on 520 nm. At higher R6G content, the emission started to shift towards R6G maximum emission value while conserving some features of AO profile so that the maximum emission of the dual particles shifted between 520 and 555 nm.

In comparison, the fluorescence patterns of AO and RB were more separated and the effect of dye concentration was more obvious (**Figure 5-9**). Particles with high concentration of AO and low RB concentration (100-25) displayed a strong peak at 520 nm followed by a second les intense peak at 580 nm. When AO concentration decreased (75-25), the second peak rose to the same value than AO emission. The tendency continued this way until the AO contribution was a small shoulder before the RB peak.

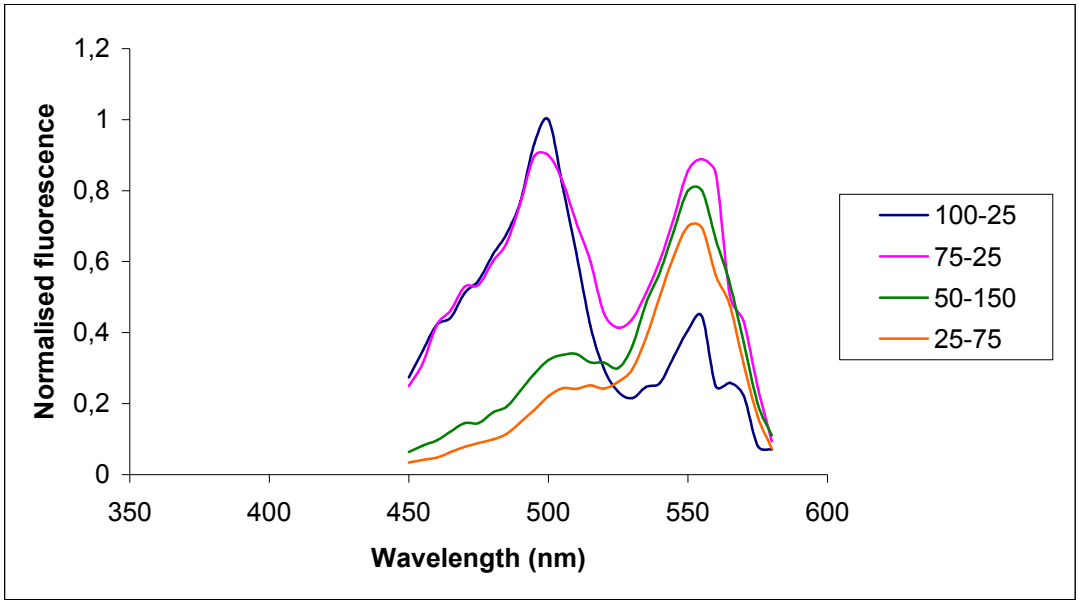

Figure 5-9: Normalised emission spectra of nanoparticles loaded with AO (first digit) and RB (second digit).

Next, the three dyes were included together into a single hybrid structure. AO was entrapped during the core formation whereas R6G and RB were added during the growth of the first and second silica layer synthesis in that order. DLS analyses showed that the particle diameter did not vary more than 5 nm and 10 nm for the second and third layer after each shell growth. Due to the close optical properties of the three fluorophores, the resulting excitation and emission spectra do not display any particular feature. Instead, AO and R6G form a first broad peak immediately followed by RB emission maximum (**Figure 5-10**). The emission band was broader than that of the dyes taken individually and covered the region between 450 and 600 nm. Yet, the choice of fluorophore was not ideal to study changes in the fluorescence pattern and dyes with more distant excitation and emission wavelengths ought to be tested instead. However, the results showed that the method can produce multifluorescent nanoparticles. Additional characterisation is needed, for example to verify of the dyes are homogeneously distributed between the nanoparticles. Furthermore, the experiments must be carried out with centrifugation between each step to

remove the excess of dye to avoid their presence in several layers simultaneously and to exert a higher control over the spectral signature.

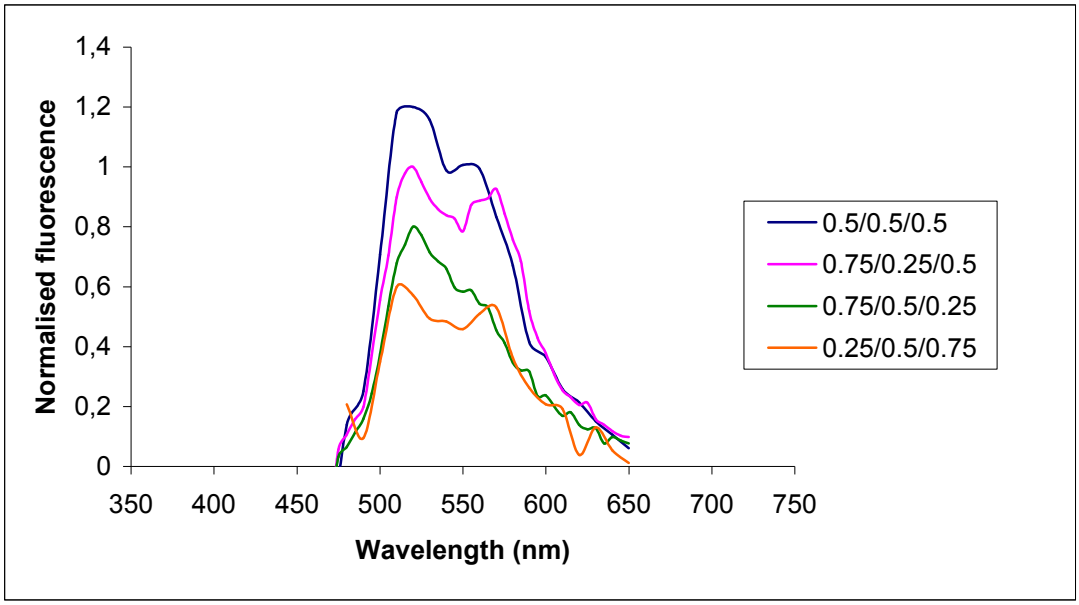

Figure 5-10: Emission spectra of the AO/R6G/RB hybrid nanoparticles at various ratios.

5.3.3 PhTEOS-TEOS and THPMP-TEOS nanostructures

The hybrid particles were initially designed based on the hypothesis that fluorophores can be divided into hydrophobic and hydrophilic dyes. This idea originates from the fact that, in the literature, some dyes require an oil-in-water emulsion for their encapsulation in silica nanoparticles whilst others need a water-in-oil emulsion. It was surmised that the dual nature of the particles would provide a suitable of environment for any fluorophore regardless of its nature. Yet, the first results presented in this chapter said otherwise and some of the dyes could not be encapsulated, even when the VTEOS/TEOS ratio was varied. This indicates that the hypothesis was not correct and two reasons may be proposed: (1) the hydrophobic nature of VTEOS is not strong enough, or (2) other interactions than hydrophilicity/hydrophobicity are involved in the stabilisation of the dye.

In a first time, VTEOS was substituted for phneyltriethoxysilane (PhTEOS) because of its bulkier moiety and potential stronger hydrophobicity. The change of hydrophobicity strength was especially obvious during the centrifugation because PhT-50 and hybrids containing more than 50 molar% PhTEOS were not longer soluble in water. Likewise, the particle diameter was modified with circa 30 nm in diameter for PhT-50 and 16 nm for PhT-75 whilst PhT-100 rose to more than 770 nm (**Figure 5-11**). Unlike the VT hybrids, where the particle diameter increased with increasing the VTEOS/TEOS ratio, the changes in PhT hybrid appeared more unpredictable. For instance, SEM picture of a PhT-10 structure displayed particles about 60-70 nm diameter (**Figure 5-12**). The particles remained spherical but with some aggregation as the particles bind one to the other.

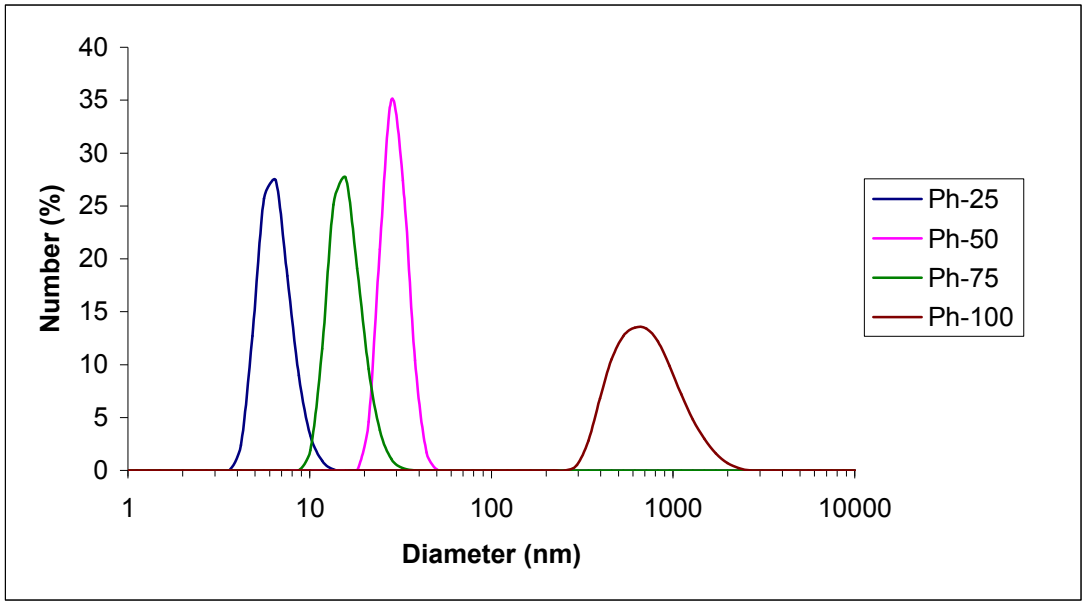

Figure 5-11: DLS measurement of PhTEOS-TEOS hybrid at various PHTEOS molar concentration.

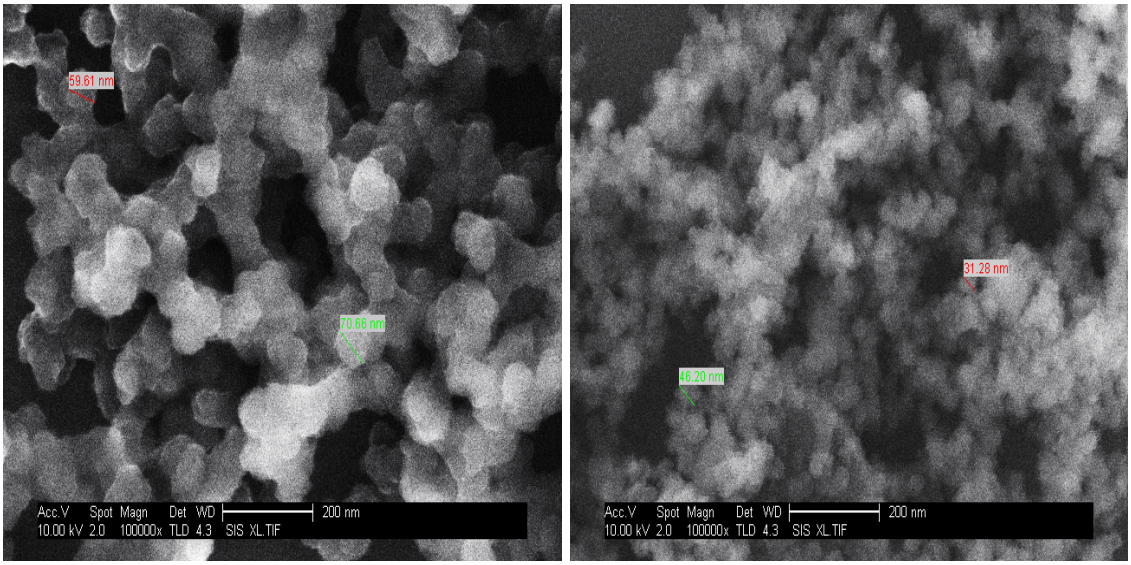

Figure 5-12: SEM pictures of TEOS-PhTEOS (10 molar% PhTEOS, left) and TEOS-THPMP (10 molar% THPMP, right) hybrid nanoparticles.

The phenyl group induces some modification to the infrared spectra compared to VT hybrids (**Figure 5-13**). The benzene ring signal shows up in three regions: three bands at 3070, 3051, and 2975 cm^{-1} originate from the stretching vibration of C-H whereas the peaks at 1596 and 1488 cm^{-1} are attributed to the ring stretch of C-C coupled to the C-H bending. Lastly, the out-of-the-plane C-H bending of the phenyl ring is responsible for the peaks at 736 and 694 cm^{-1}. Another important band arises at 1433 cm^{-1} and is the result of both the Si-C stretching and C-H bending of the ring (a coupling effect to the 736 and 694 cm^{-1}). All these peaks combined to the siloxane band and silanol peak indicate that the co-condensation of PhTEOS and TEOS proceeded and prove the hybrid nature of the particles. On the contrary, the presence of THPMP could not be detected and the infrared spectra reverted to a normal TEOS-based silica nanoparticle.

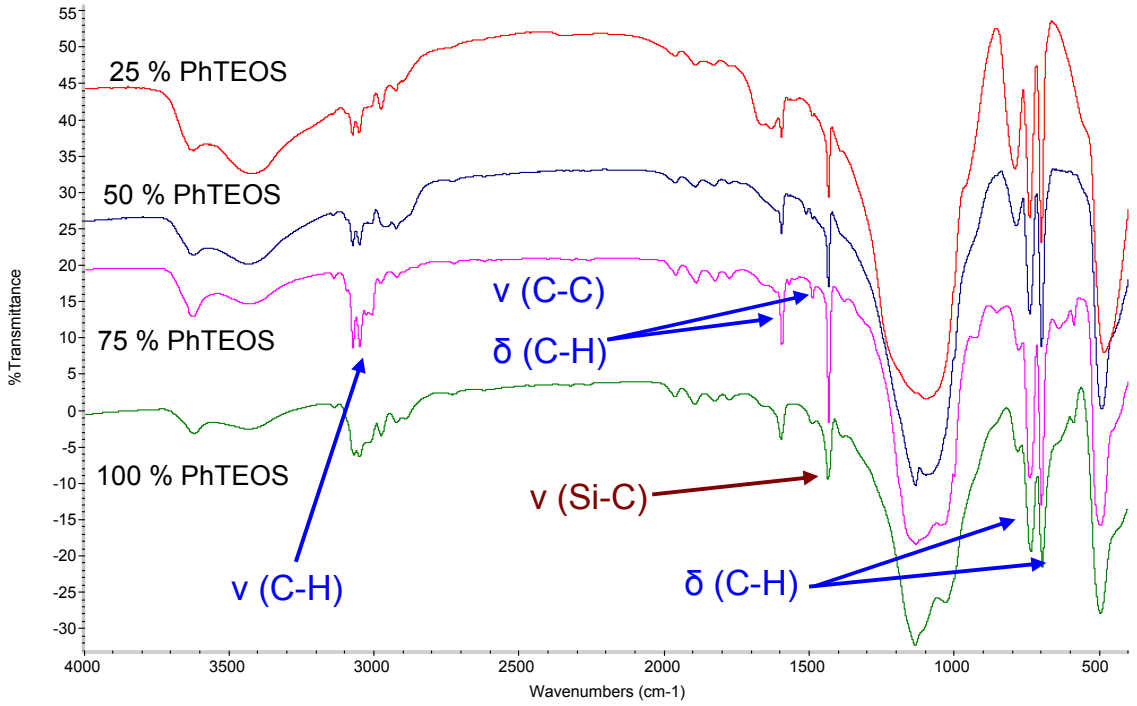

Figure 5-13: Infrared spectra of PhTEOS hybrid with 25 (red), 50 (blue), 75 (pink) and 100 molar % (green) of PhTEOS..

In spite of the structural alteration of the particle matrix, Fl, OG, and LY were still not contained within the PhT hybrids. Furthermore, the difficulty to recover the particles by centrifugation makes them more complicated to handle than the VT hybrids and the strong hydrophobicity of the particles may not be suitable for use *in vivo* (generally aqueous environments). PhTEOS was then replaced y THPMP and APTES as potential solutions. THPMP-TEOS hybrids produced small particles, for example 30-40 nm (10 % THPMP) as seen on SEM images (**Figure 5-12**). However, FTIR was not able to prove that the particles contained any phosphonate groups and, similarly to PhT hybrids, the particles were not able to entrap OG, LY, and Fl. APTES-TEOS hybrids were not tested in length because of the strong aggregation of the particles due to the hydrogen bonding settling between silanol and amine groups. However, the initial results seemed

to indicate that the particles were able to contain LY (the only de tested for these hybrids).

5.3.4 Alteration of the VTEOS-TEOS hybrid nanoparticles

A closer look at the chemical structure of the fluorophores provides a first reason to why some dyes remained out of the VT (and THPMP and PhT) hybrid nanoparticles. Acridine orange, malachite green, methylene blue, neutral red, and the two rhodamines are either positively charged or get protonated at pH 10 (arginine pKa). Owing to the negative net charge of the silica matrix, electro-attraction settles between nanoparticles and dyes which stabilises the molecules within the ceramic particles. On the other hand, alexafluor 647, fluorescein, lucifer yellow, and oregon green are not able to acquire the positive charge at high pH and are consequently repulsed by the siloxane network. To verify this hypothesis, small amount of APTES (less than 10 molar% of the total silane concentration) was added during the synthesis of VT-50 nanoparticles. The positively charged amine moiety of APTES would help attracting the fluorophores whilst the low organosilane concentration should limit aggregation.

The addition of APTES to TEOS and VTEOS did not alter the hydrodynamic diameter of the nanoparticles (around 50 nm) so long as the APTES proportion remains low. At 2.5 % APTES, a second peak little intense peak rose at about 700 nm but remained negligible. On the other hand, a strong aggregation was detected with 5 % APTES (polydispersity index of 1) and the particles diameter shifted to more than 400 nm (**Figure 5-14**).

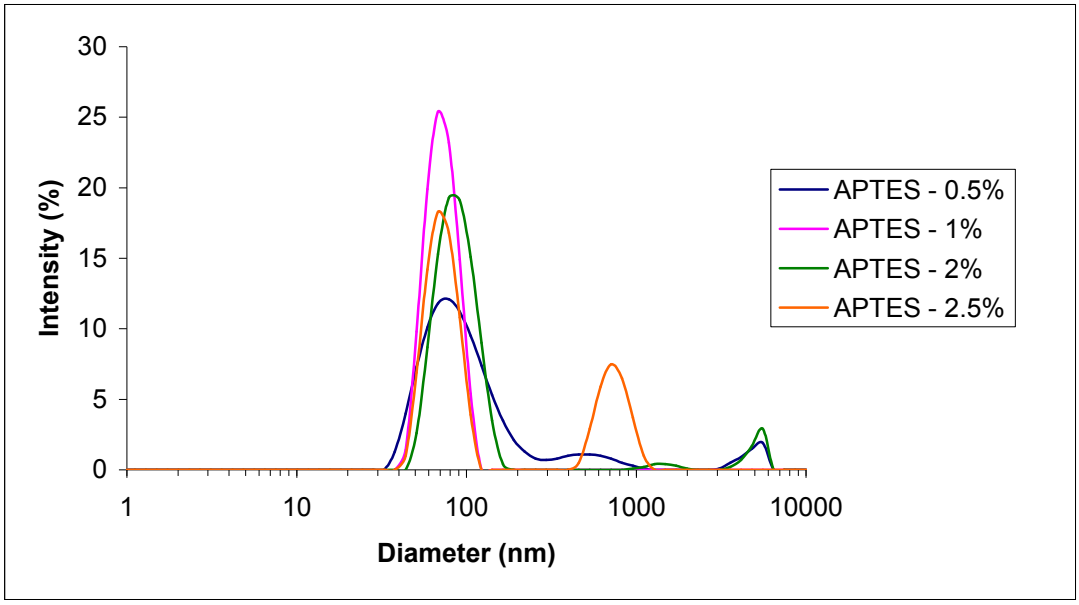

Figure 5-14: Hydrodynamic diameter of VT-hybrid containing APTES.

The diameter of the particles has observed by SEM seemed to correlate well with the DLS results, but SEM also revealed that large submicrometric and micrometric spheres were present as well. For instance, AP-5 picture (5 % APTES) principally 45 to 60 nm nanoparticles and occasionally 700 nm spheres (**Figure 5-15**) but AP-10 was composed of micrometric nanoparticles exclusively. Note however that some of the suspensions were prepared using the VTEOS solution responsible for the exotic shape of the particles described in Chapter 4. Therefore, the experiments must be carried out a second to verify whether the large particles result from hydrogen bonding (APTES effect) or by the contaminated VTEOS solution.

The effect of APTES on the particle fluorescence was immediately visible: the samples exhibited a yellow colour with lucifer yellow, which strongly contrasted with the former attempts with VTEOS and PhTEOS. The excitation measured at 440 nm and the emission at 525 nm further proved the presence of LY inside the ceramic matrix.

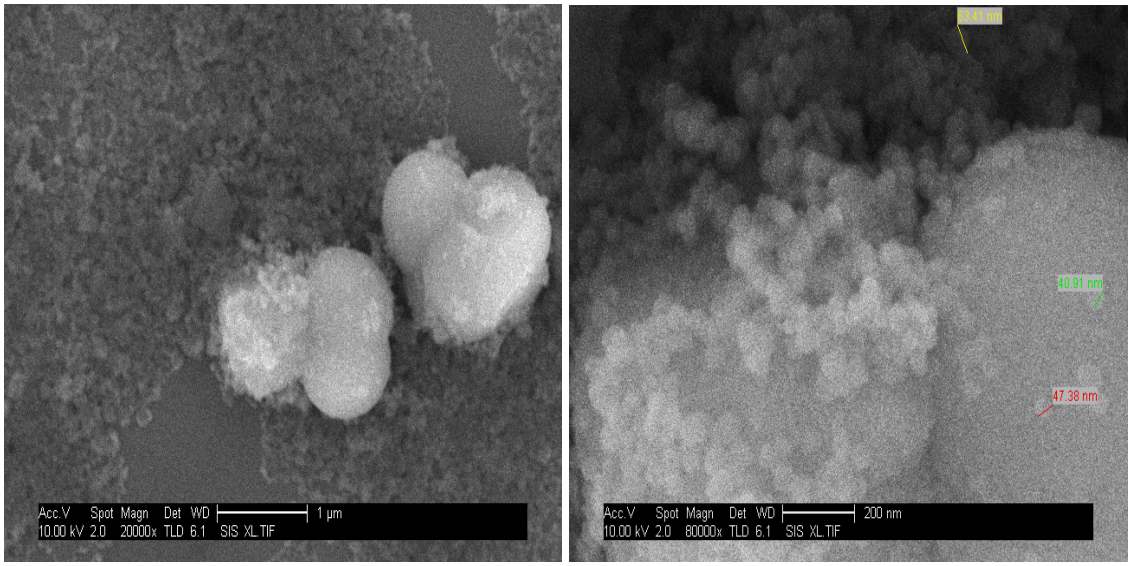

Figure 5-15: SEM pictures of VTEOS-TEOS particles with 5 % displaying some very large particles (left) but mostly composed of 45 nm nanoparticles (right).

The particle colour and fluorescence intensity seemed correlated to the APTES proportion in the network and the fluorescence augmented as the APTES was increased from 1 to 10 % (**Figure 5-16**). However, due to the aggregation in AP-10, characterisation must be conducted once again with suspension of the exact same to prove that fluorescence intensity is linked to the APTES concentration. However, if more APTES is beneficial for a better encapsulation of dyes, it likewise increases the chance of binding particles altogether or to create large structures because of the hydrogen bonding. The AP hybrids also successfully entrapped OG and FI, which is an important improvement in comparison to the VT and PhT nanoparticles. Furthermore, the present of APTES was not detrimental to the other fluorophores since AO, R6G, and RB were likewise detected in the AP-modified particles (**Figure 5-17**). Additional results showed that the nanoparticles could be recovered by silica layers to create two dye-doped systems. For example, some systems were made of a hybrid core containing LY and an extra layer entrapping RB and exhibiting the fluorescence of the two dyes. The structure still suffers from the same

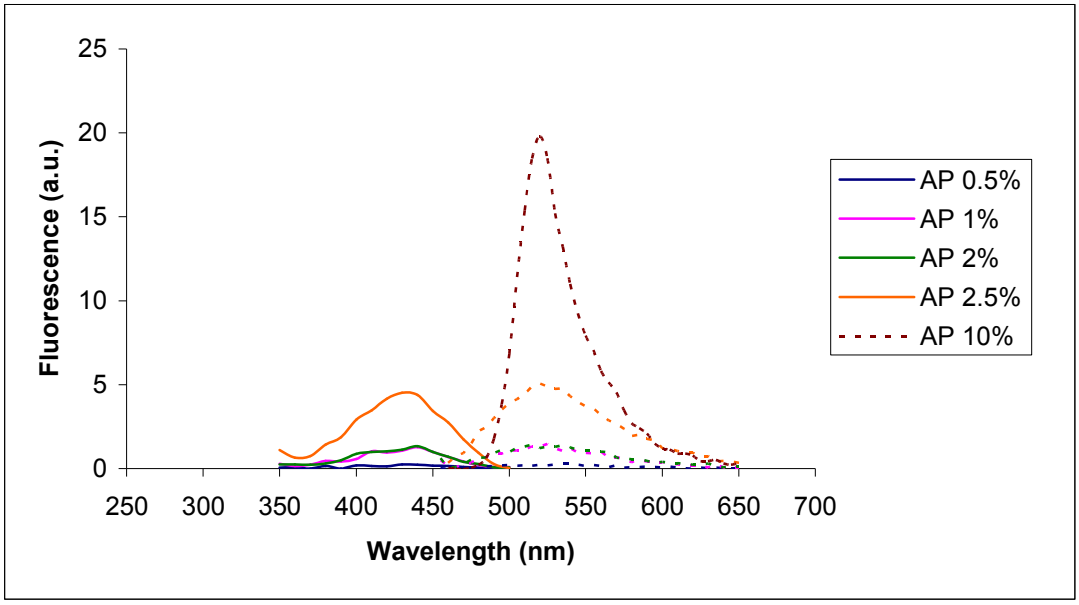

Figure 5-16: Excitation (plain lines) and emission (dotted lines) of AP-modified hybrid nanoparticles containing lucifer yellow.

uncertainty about the homogeneity of the particle content, i.e. it is not sure whether all the particles contain the two dyes and in the exact same proportion. As already mentioned, this must be assessed by single molecule microscopy and potentially by confocal microscopy of the last generation.

There was not time to assess whether multifunctional nanoparticles made of successive hybrid layers can be created. The LY-RB system was made possible by the good affinity of RB for silica but this strategy is not suitable for negatively charged fluorophores such as FI or OG. Therefore, the next experiments must include the design of multilayered nanoparticles composed of hybrid and silica layers. In summary, the AP-modified VT hybrids may be the solution to virtually entrap any fluorophore but the system is still limited by the threat of aggregation if too high APTES concentrations are employed. If this limitation can be overcome, the hybrid particles have the potential to become a novel class of fluorescent particles superior to silica nanoparticles.

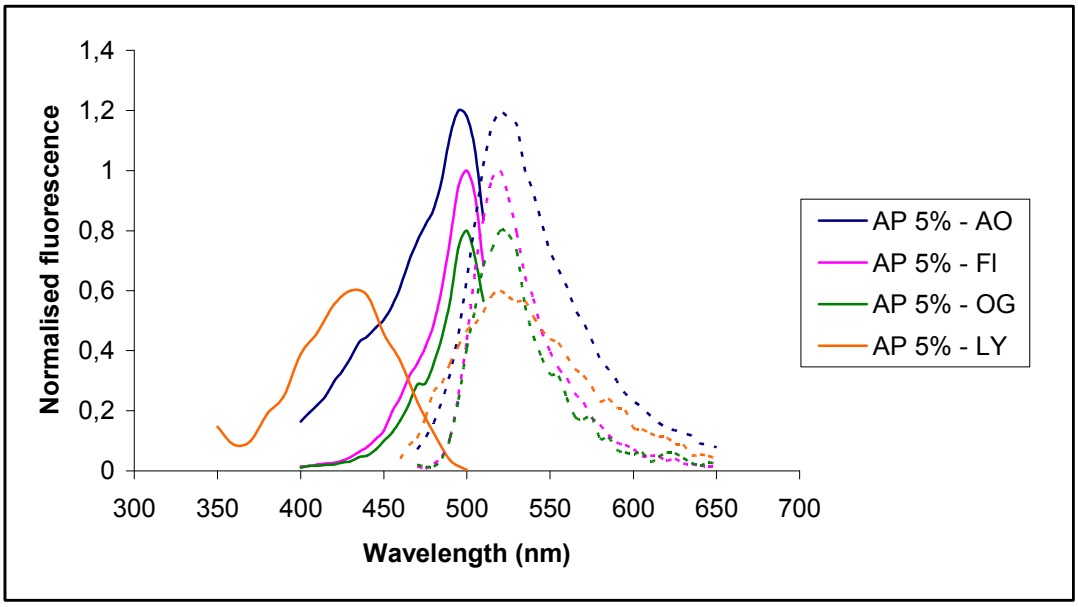

Figure 5-17: Excitation (plain lines) and emission (dotted lines) of hybrid nanoparticles with 5 molar% APTES and containing various range of fluorophores.

5.4 Discussion

Maleimide/isothiocyanate derivatives of fluorescein and rhodamine (suitable for covalent binding with organosilanes) and rare earth chelates (hydrophilic inorganic fluorophores) are the principal dyes combined with silica nanoparticles via the Stöber method and reverse microemulsion respectively. Additionally, more and more studies are devoted to the entrapment of NIR and two photon dyes via oil-in-water emulsion due to the hydrophilic nature of the fluorophores. It is virtually possible to encapsulate any fluorophore using one of the three synthesis method, however it is technically difficult to combine these approaches to create multifluorescent nanoparticles In that respect, the development of a more flexible method requiring a single solvent regardless of the hydrophilicity/hydrophobicity of a dye could be advantageous. This would preclude long purification process required to remove surfactant or problem of solubility and insolubility in aqueous or organic phase. Furthermore, core-shell structures similar to that of Chapter 3 could be easily designed and would be suitable for a large variety of fluorophore, including photosensitisers and sensor dyes.

The hybrid particles developed in Chapter 4 are envisioned as the basis for the “universal” carrier due to its dual nature. The presence of both hydrophilic and hydrophobic regions within the particles ought to create a suitable environment for all dye: it was hypothesised that the hydrophobic component (VTEOS) would seek to diminish its contact with water and ought to form the core of the nanoparticles, whilst the hydrophilic TEOS would cover the budding VTEOS seeds and create a protective shell. Consequently, the carriage capacity of the hybrid had to be assessed. To do so, the same dyes employed in Chapters 2 and 3 – namely AO, RB, R6G, and MB - were selected. Additionally, other fluorophore were found in the laboratory and tested: dextran alexafluor 647 (AF), fluorescein (FL), lucifer yellow (LY), malachite green (MG), neutral red (NR), and oregon green (OG). The choice of these dyes was motivated by different reasons:

- They possess different optical properties (excitation and emission wavelengths;
- Most fluorophores are soluble in water but some (LY, FL, and OG) are insoluble;
- The short excitation wavelength of LY makes it ideal for combination with other dyes into a single structure, for example LY/RB/MB that all match a different laser source of confocal microscopes;
- OG and FL are acid-sensitive dyes that could be interesting for the design of nanosensors.

Addition of all of the dyes led to contrasting results: MB and R6G were successfully detected within the nanoparticles but since they were already encapsulated in silica nanoparticles in Chapters 2 and 3, it may be assumed that the hydrophilic nature of the particle is responsible for their stabilisation. AO and RB gave similar results which is interesting because AO has the same optical properties as FITC and RB possesses a high quantum dye and matches perfectly the laser sources of confocal microscopes and flow cytometry. MG and NR led to pale green and red-orange nanoparticles and the lack of intense absorbance peak further confirms the weak optical properties of the nanoparticles. The dyes were not investigated further in details because their absence of fluorescence makes them less attractive for biomedical applications. Unfortunately, the other cases failed and no signal was detected with OG, FI, AF, or LY despite of the repeated attempts. The matrix composition was thus modified as a way to verify whether the VTEOS concentration can modulate the entrapment of the dyes. RB worked equally fine regardless of the network composition which sustains the hypothesis that RB has a natural good affinity for the silica matrix and that the presence or absence of the vinyl moiety seems inconsequential. Note that at the difference of some groups that relied on the covalent binding of RB to APTES, the hybrid nanoparticles are able to contain RB directly [*Gao, 2009*]. It was not possible to establish a direct comparison of fluorescence for all hybrid composition due to the very low concentration of VT-

00 and VT-25, but it may be interesting to determine the brightness and fluorescent molecule content of the nanoparticles. This may be obtained via a fluorescence calibration curve of the free dye of interest and by measuring the fluorescence of FSNPs suspension of known diameter and concentration. This calculation would in turn help determining if and how the VTEOS concentration affects the particle ability to carry fluorophore. Contrariwise, alteration of the particle matrix had no effect on OG encapsulation and the hybrid nanoparticles remained devoid of fluorophore. LY results were identical, although a very weak signal was measured but too low for practical purpose. Therefore, the hypothesis that generation of hydrophobic regions within the matrix may help in encapsulating a higher diversity of fluorophore is not valid, but the exact effects of VTEOS and potential enhancement it brings require additional experiments. From these tests, fluorophores can be divided into dyes with a strong affinity for the hybrid matrix (AO, RB, R6G, MB) and dyes that failed at being entrapped (OG, FL, LY principally). On the one hand, part of the study consisted in combining the first group of fluorophores into a single particle similarly to the system described in Chapter 3. On the other hand, the aim of creating a universal carrier had yet to be reached and part of the project was devoted to finding a solution to entrap the second group of fluorophores.

Before studying the combination of AO, R6G, and RB, the leakage of dye out of the particle had to be assessed along with the effect of the initial fluorophore concentration on the final optical properties of the particles. Indeed, it was found that most fluorescent molecules were not entrapped and were discarded after centrifugation the samples. These losses are an issue for dyes in small quantities, which are generally expensive. For low fluorophore concentration, the particle visual brightness was dim but supernatant was generally transparent whilst very bright particles were yielded at high initial concentration but the supernatant was highly fluorescent too. It was not possible to correlate the particle fluorescence intensity to the fluorophore concentration despite of the small size variation of the nanoparticle diameter. However, it seemed that the intensity reached a threshold above a concentration of $2*10^{-7}$ mol of dye in solution and the intensity decreased above this concentration. At some point,

the particle may become saturated in dye and the close proximity of the fluorophore may induce self-quenching, resulting in the decrease of fluorescence observed in the case of RB. In other terms, there may exist an optimal concentration where fluoresce predominates over quenching but additional measurement are required to confirm this hypothesis [*Gao, 2009; Imhof, 1999*]. The other reason to lower the dye concentration in particles is the potential interaction between nearby dye and is frequent in rhodamine dyes: these excimers tend to broaden and red-shift the emission band in comparison to the monomeric spectrum [*Ma, 2009*].

Leakage of cargo may be a source of concerns of FSNPs because of the potential weakness of the electrostatic interactions coupled to the natural porosity of silica nanoparticles. To verify whether the matrix retains the fluorophores, the particles were kept in PBS and water to a period up to one month during which the samples were regularly centrifuged and the supernatant fluorescent was measured. No leakage was detected in either PBS or water, indicating that the fluorophore do no diffuse away from the particles. The experiments may be repeated under harsher conditions such as higher temperature, a range of pH or highly saline solutions to test the robustness of the hybrid matrix but silica has a reputation of robustness and should not be degraded [*Gao, 2009; He, 2009 b*].

Among the ten fluorophores tested, AO, R6G, and RB were easily combined and produced very bright particles. Due to the successful incorporation, one of the two objectives of this chapter was to combine these three dyes into a core-shell structure similar to the multifluorescent system described in Chapter 3. The hybrid core always carried AO with the same initial volume and the volume of the second dye was varied. Due to the close proximity of AO and R6G excitation and emission, the effect of combining the two dyes is limited to a shift of the maximum emission wavelength and to a broadening of the emission band. In comparison, variation of RB at fixed AO concentration led to more obvious changes since AO and RB emissions are well separated. The

fluorescence of RB is very weak at the excitation wavelength set to measure the optical properties of the particles. As the RB concentration increased, the RB emission was more easily detected but it is unknown whether this effect is due to the higher RB concentration alone or AO emission was involved in the excitation of the rhodamine. The interest of the two-dye particles is the higher emission of R6G and RB when using the 488 nm source that is equivalent to producing systems with large Stokes shift – the difference between excitation and emission maxima – desirable to minimise issues with autofluorescence and self-quenching. Following this strategy, it may be possible to create systems emitting at long wavelength using conventional UV or visible excitation sources by exploiting the overlapping of emission and excitation of fluorophores into the particles. For instance, several populations of fluorescent nanoparticles with distinct emission wavelength could be used simultaneously with a single excitation source as a mean of multiplexing detection.

The only system containing three dyes has been designed by Wang et *al*. who precisely controlled the emission of particles containing FITC and two maleimide derivatives of rhodamine [*Wang, 2006*]. The covalent binding of dyes is ideal to tune the fluorophores composition of the particles and ensure that all fluorophores have been integrated to the particles. Their first attempts led to low FRET efficiency because each dye was present in a different layer due to their different hydrolysis rates. When the three sylilated fluorophores were pre-hydrolysed prior to adding TEOS, the FRET systems were created. This is due to the FRET dependency to the distance between dye molecules: because Wang's fluorophores were present in separated layers, FRET could hardly occur.

In the hybrid system, the fact that AO was present in the core and in the layers helped in bringing the acridine molecules close to the rhodamine ones and possibly helped in the energy transfer. It is not known whether removing the dyes after each growth step would impact the fluorescence of the particles and if the presence of dye in distinct layers would suppress the FRET phenomenon. If that were the case, it may be possible to tune the spectral pattern by adding

lower concentrations of dyes simultaneously during the original seed growth without need of additional silica layer. To verify this hypothesis, more experiments are required where excess of fluorophore is removed by centrifugation prior to creating new shells in order to prevent the presence of dye in multiple layers: since FRET is distance-sensitive, it is expected that the separation of AO, R6G and/or RB in distinctive regions of the particles hampers FRET.

The second objective was to find a solution to encapsulate LY, OG, and FI that had no affinity for the VT hybrids. The fact not all 10 dyes is the sign that the VT hybrids still not have the potential to be universal carriers and limit their multifunctionality. In other term, it is still necessary to find a way to make the encapsulation process more flexible and efficient. There are high chances that the major limitation lays in the poor affinity of fluorophores for the matrix. In his publication, Theaker was able to entrap a large number of fluorophores within PhTEOS-TEOS nanoparticles obtained via the Stöber method. Based on the chemical structure of the dyes that were encapsulated or remained in the solvent, they hypothesised that the particles retain the dyes because of both electrostatic interactions and steric hindrance [*Theaker, 2008*]. The phenyl group is more voluminous than VTEOS and may effectively increase the chances of incorporating LY and the other fluorophores. However, Theaker's particles suffered from two drawbacks: large diameter superior to 400 nm and high hydrophobicity that is not desirable for biological purposes. Considering the features of the amino acid routes, it was assumed that the method might help in resolving the diameter issue whereas tuning the PhTEOS to TEOS ratio might modulate the hydrophilicity or hydrophobicity of the particles as was seen – to some extent – with VTEOS.

Practically, the PhT particles are highly hydrophobic at 50 molar% of PhTEOS and above, but the diameter was much reduced than in Theaker's study and did not exceed 75 nm with the exception of pure PhTEOS particles that were more than 400 nm in diameter. Yet, the new organosilane modifies the particle

dimensions in a more unpredictable manner that VTEOS and no correlation was found between the PhTEOS/TEOS ratio and the size compared to the VTEOS case. Growing a pure silica layer may help in reducing the hydrophobicity of high PhTEOS-content particles but the best solution consists in using only a small proportion of PhTEOS. Even at 10 molar%, the size of the particles was found close to 50 nm (12 nm with VTEOS), sign that PhTEOS is able to exert a strong influence on the network. In spite of the modification induced by the presence of PhTEOS, the new hybrids were unable to encapsulate LY, OG, or Fl. This finding implies that the initial assumption that creating hydrophobic regions within the particles to stabilise the fluorophores is not correct and other interactions must take place. Looking at the chemical structure was the first hint: the common point between AO, R6G, RB, and the dyes that were combined with the hybrid particles is that they either possess or may gain a positive charge after protonation. The positive charge is ideal to stabilise the dyes within the matrix since silica is negatively charged. In contrast, the other dyes are not able to get protonated and remain negatively charged which creates repulsion with the inorganic network. Consequently, the organic component of the hybrid nanoparticles shifted from hydrophobic moieties to charged one. At first, THPMP and APTES were co-condensed with TEOS to impart a negative and positive charge to the network respectively. He et *al.* have shown in one occasion that co-condensation of THPMP and TEOS improves the loading with MB and the group even measured a strong fluorescence signal from MB where usual TEOS particles led to no significant fluorescence pattern [*He, 2009 b*]. Although the modification or doping of the matrix has been suggested, there is surprisingly no report of correlating the structure and charge of dyes with the net charge of the silica matrix [*Shibata, 1997*].

Here, TEOS-THPMP hybrids were small but could not entrap LY and Fl and this system was not further studied. Direct co-condensation of TEOS and APTES promoted the particle aggregation. Consequently, the VT structure was conserved as the main composition, but small amounts of APTES were incorporated to impart some positive charges to the network. The modified hybrid particles, referred to as AP hybrids, got a strong colour after reaction with

LY, OG, and LY and fluorescence measurement proved that the fluorophores were effectively encapsulated within the particles. The aminated silane did not disrupt the original VT structure and the particles retain similar dimensions (circa 50 nm), but agglomeration started to appear at 5 and 10 molar% of APTES, indicating that the third organosilane concentration must remain limited to avoid negative effects. There must be an optimal concentration that imparts good fluorescence without destabilising the colloidal suspensions. Indeed, the experiment involving LY showed that as the APTES percentage augmented, the fluorescence of the particles increased possibly because the positively charged amine helped in attracting and retaining more LY molecules. The effect was the same with the other fluorophores but a more consistent model has yet to be developed to understand the interactions at the heart of the encapsulation process. From the AP structure, it became possible to develop more advanced systems containing both LY and RB. At the difference to AO and RB, the excitation and emission of the two fluorophores are more distant and prevents FRET. With a third blue or NIR dye and the capacity to carefully tuned the fluorophore concentration in each layer, the number of combination, and by extension the number of analytes that could be simultaneously detected, increases. The possibility to co-encapsulate two fluorophores is particularly important in nanosensors: in general the sensor dye must be combined with a second referent dye to clearly assess the fluorescence modification induced by the changes of environmental conditions. This requirement may explain why silica-based nanosensors are rarely reported unless the sensor dye is FITC or a fluorophores easily silylated. Here, the AP particles may not suffer from such limitation since any fluorophores could theoretically be encapsulated by selected the appropriate composition (VT hybrid for positively-charged fluorophores and AP hybrid for the negatively-charged one).

A number of points remain to be investigated. First of all, it is necessary to test a wider range of fluorophores to validate the “charge hypothesis”. So far, the addition of APTES proved a valid strategy provided that the organosilane concentration is not so high that it starts inducing hydrogen bonding and aggregation. The employ of another organosilane with positively charged moiety

but unable to create hydrogen bonds may help circumventing the aggregation issue, albeit such new system would require a full characterisation. Another point is the necessity to exert a better control of the particles fluorescence signature as highlighted with the AO/R6G/RB system. More importantly, it is necessary to assess whether the AP composition may be used for the growth of additional layers to eventually obtain a universal carrier. The interesting point was the successful loading with FI and OG but there is no certainty that the loading results from the positive charges from APTES or whether the VTEOS presence is a requirement. More analysis with TEOS-APTES and APTES-hybrid matrix are necessary to attest of the silane influence. The principal setback of the particles reported so far is that the fluorophores were present throughout the whole process and were entrapped during the layers growth. The higher quantum yield of R6G and RB in comparison to AO was not an issue and was in a sense beneficial for the induction of a strong RB emission. However, it is less acceptable with expensive dyes or fluorophores supplied in small quantities such as AF647. This is also a requirement for ratiometric nanosensors where the concentration of the sensor dye and of the referent dye must be carefully controlled. Lastly, the next stage of the hybrid particles development will consist in transposing the hybrid composition of the core to the outer layers. So far, AO, R6G, and RB were entrapped during the layers growth because of their good vitreophilicity but other dyes are not likely to present similar affinity for the silica matrix. Although a three stages system (containing AO and RB plus another distinct fluorophore) already opens new possibilities, the number of permutations is still too limited for complete multiplexing arrays of nanoparticles.

5.5 Conclusion

This chapter lays the ground for a new generation of flexible FSNPs with enhanced carriage capacity. In spite of the versatility of silica chemistry, there has not been any report of a universal method for the design of nanoparticles able to contain virtually any organic dye. As the testing revealed, the VT hybrid nanoparticles are not as flexible as expected since some of the fluorophores tested were not contained with the particles. These mitigated results led to the exploration of two distinct ways. First, AO, R6G, and RB were combined in a core-shell structure similar to that detailed in Chapter 3. Although the three dyes were too close (in terms of excitation and emission), the results suggest that it is possible to tune the spectral signature of the particles by controlling the fluorophore concentration in the particles. It still remains testing the encapsulation of dyes with no excitation/emission overlap and to verify whether each layer contain a single fluorophore population.

Second, it was postulated that a better affinity of the fluorophores for the matrix could be achieved through an alteration of the particle composition. Indeed, neither VTEOS nor PhTEOS hybrids managed to encapsulate fluorescein, oregon green, and some other dyes in spite of the hydrophobicity of the two organosilanes. Instead, tuning the particles composition with a charged silane was more successful and it was possible to incorporate Fl, LY, and OG that failed the test of the VT-structure. Even though this approach requires more investigation, it is hypothesised that it is possible to encapsulate any fluorophore whenever the particle matrix possess an opposite charge.

In summary, the protocol still needs optimisation, notably verifying that a single layer can contain a single fluorophore and testing more fluorophores to ensure that the “charge hypothesis” is correct. If the hypothesis proved valid, then it would be possible to encapsulate any type of fluorophore, which in turns would open new possibility in confocal imaging, flow cytometry and possible other fluorescence-based imaging modalities and diagnostics tools. More importantly, the possibly to combine multiple dye into a single nanoparticle brings new

perspective with nanosensors able to sense changes in their environment and may play an important role in the development of new multifunctional and intelligent systems that will rely on the probing of their surroundings to match their effects.

Chapter 6

Development of multifunctional nanoparticles via the amino acid route and deposition-precipitation

6 Development of multifunctional nanoparticles via the amino acid route and deposition-precipitation

6.1 Introduction

Smart and reactive systems are often envisioned as a more advanced step in nanotechnology and nanomedicine development. So far, most nanomaterials of interest exhibit one or two key capacities but their potential becomes quickly limited and they are often not sufficient to be considered as a smart platform, with perhaps the exception of PEBBLE (Probe Encapsulated By Biologically Localised Embedding) structure. Combining the properties of nanomaterials or compounds into a single structure impart more flexibility and occasionally create synergies. Such multifunctional nanoparticles enable the use of a single nanoparticle for multiple purposes: in imaging smart particles act as contrast agents for two or more imaging modalities to retrieve information at the molecular and anatomical level simultaneously whereas theranostic systems are suitable for imaging and therapy to ensure that the nanoparticles have found their target and make treatments more specific and efficient [*Cheon, 2008; Kobayashi, 2010; Hahn, 2011*].

Gold and iron oxide (or other biocompatible magnetic nanomaterials) are key components of multifunctional nanoparticles as both are suitable for imaging and therapy indifferently. Their combination gives rise to a so-called magnetoplasmonic structure acting as contrast agent for MRI and for optical imaging; and for use in magnetically-guided photothermal therapy [*Ji, 2007; Xu, 2008*]. Moreover, gold is a versatile contrast agents and magnetoplasmonic is an invaluable tool for the development of combined imaging modalities such as MRI/CT [*Kim, 2009*]. Gadolinium-chelated gold nanoparticles were the first agents for dual MRI/CT imaging, but due to biocompatibility issues new

structures based on magnetite-gold core-shell structures as well as FePt alloys have already shown encouraging results, with FePt successfully being detected *in vivo* in mice [*Chou, 2010*]. Radio-labelled elements such as ^{64}Cu or ^{124}I are likewise conjugated to magnetic and metallic nanoprobes to take advantage of PET/CT, PET/optical, and PET/MRI dual modalities [*Glaus, 2010; Patel, 2011; Xie, 2010 b*]

More advanced agents have already been designed and tested on mice, for instance the trimodal gold-silica-Gd-Cy5.5 system of van Schooneveld (*2010*), suitable for MRI, CT, and optical imaging, or Hwang's (*2004*) quadruple imaging agent for luminescence, bioluminescence, PET, and MRI based on a cobalt-ferrite particle . In these two systems, gold and magnetic particles were not combined and in spite of their strengths, other routes are being explored. In that respect, quantum dots and fluorescent dyes are also combined with iron oxide and gold: quantum dots and dyes may be more detectable by optical means than gold nanostructures that are devoid of fluorescence (gold scatter light under plasmon resonance but the wavelength remains identical). The combination of quantum dots/dyes with superparamagnetic nanoparticles is ideal to take advantage of the high anatomical resolution of the magnetic modality to the sensitivity of fluorescence-based imaging as well as the high freedom in the design of particles morphology [*Mistlberger, 2010 a*]. For instance, Kircher et *al*. injected near-infrared dye/iron oxide nanocomposite into mice for the pre-operative detection of brain tumour in mice and as the intraoperative optical beacon to delineate the tumour [*Kircher, 2003*].

The better control of nanoparticles synthesis and especially of the surface engineering has allowed the progressive evolution from single particles for either detection or treatment into more versatile systems. Theranostic (or theragnostic) nanosystems are the next generation of targeting agents acting as both imaging/diagnostics and therapeutic tools: the term has been coined about 10 years ago but the field has only steadily grown over the last 5 to 6 years [*McCarthy, 2009*]. The specificity of nanoparticles after surface engineering is a tremendous advantage for the delivery of drug and many theranostics systems

are based on the vectorisation of active molecules or genes and the beaconing and/or magnetic guidance of the nanoparticles [*Xie, 2010 c*].

Theranostic agents may be suitable for dual imaging and therapy as well: for instance, Yang and co-worker developed a PET/MRI dual agent composed ^{64}Cu-labelled superparamagnetic nanoparticles and conjugated with an anticancer drug [*Yang, 2011*]. Likewise, the particles may help in the follow-up of the drug treatment: a common strategy consists in quenching the fluorescence or quantum dots or fluorophores in the initial stage due to the interaction with the drug. Once in the organism, the fluorescence emission is progressively recovered as the drug is released [*Bagalkot, 2007*]. Treatment triggered by external and controlled stimuli such as light and magnetic field have become attractive over time, especially because typical materials such as superparamagnetic nanoparticles and gold nanoshells are applicable for both applications and because at the difference of drug delivery, the treatment is delivered at will and better controlled [*Kim, 2006 b; Larson, 2007; Melancon, 2009*]. A hybrid solution consists in loading optically or magnetically active nanoparticles with PS and potentially sensing the changes by addition of sensor dyes [*Chen, 2009 b; Mistlberger, 2010 b*]. Hence, Kopelman and co-workers were able to track the particles and follow the mass shrinkage of rat brain tumour after action of PDT drug [*Kopelman, 2005*].

The *in vivo* applications of multifunctional nanoparticles are still limited by the mismatch between the dose necessary for imaging and for therapy. This is particularly true for radio-labelled and/or or drug-loaded nanoparticles but less of an issue when the particles properties are triggered by external stimuli. Conversely, multifunctional nanoparticles have found their place in *in vitro* studies and diagnostics as well, for exaple in cell/biomolecules separation, assays, or cellular and intracellular imaging [*Mistlberger, 2010 a*]. Luminescent magnetic particles are the most prominent multifunctional systems as they allow the magnetic manipulation of biological entities and their control and quantification via fluorescence-based techniques. The magnetic function may be to accumulate particles in the vicinity of a target cell line to favour their non-

specific uptake and then allow their imaging or alternatively manipulate the endosomes or sorting cells (for example metastasis) by magnetophoresis [*Bertorelle, 2006*].

In diagnostics, the typical approach consists in targeting non-luminescent magnetic particles for the detection of one analyte, separating the particles, and introducing a second population of luminescent but non-magnetic particles or molecule conjugated to a secondary antibody or DNA fragment [*Dressman, 2003; Mistlberger, 2010 a*]. One such example was the detection of drugs in fingerprints using antibody-conjugated magnetic particles to detect the drug, with a magnetic brush applied to remove any unreacted particles. Then, secondary antibodies modified with dyes were applied as a mean of detection and to provide a picture of the fingerprints at the same time [*Hazarika, 2008*]. Additionally, such procedure may be performed in microfluidic devices where the magnetic particles are separated from the rest of the sample and directed to a specific spot for read-out [*Vojtíšek, 2010*]. Although rare, the same effects were obtained with a single population of luminescent magnetic particles, for example Dosev used the luminescence of the particles for internal calibration in a competitive immunoassay and the system was extended to the detection of three analytes simultaneously [*Dosev, 2007; Nichkova, 2007*]. The assay relies on the binding of the analytes of interest followed by the addition of fluorophore-labelled secondary antibodies. After magnetic separation, the optical properties are measured and the intensity of the fluorophore(s) emission is reported to the nanoparticles intrinsic fluorescence, i.e. the fluorescence of the properties acts as an internal calibration and the measured signal is relative and not absolute. Finally, embedding of multiple quantum dots (or fluorescent dyes) onto magnetic particles paves the way for multiplexed assays with the design of nano-barcode where each population of nanoparticles display a specific fluorescence pattern similar to the quantum dots-loaded microspheres [*Wang, 2007 b*].

The aim of this chapter is to further expand the potential of the hybrid nanoparticles by integrating gold and/or iron oxide to impart plasmon resonance

and magnetic properties respectively. To do so, this chapter is divided into three parts (**Figure 6-1**):

- The assessment of the deposition-precipitation method (Appendix G) to coat the surface of the hybrid nanoparticles with small gold seeds and to further form a complete metallic layer;
- The coating of iron oxide nanoparticles with hybrid silica to design fluorescent-magnetic nanoparticles;
- The combination of the deposition-precipitation method and of the amino acid route to elaborate multifunctional nanoparticles composed of an iron oxide core, a thin silica coating, and an outer gold layer.

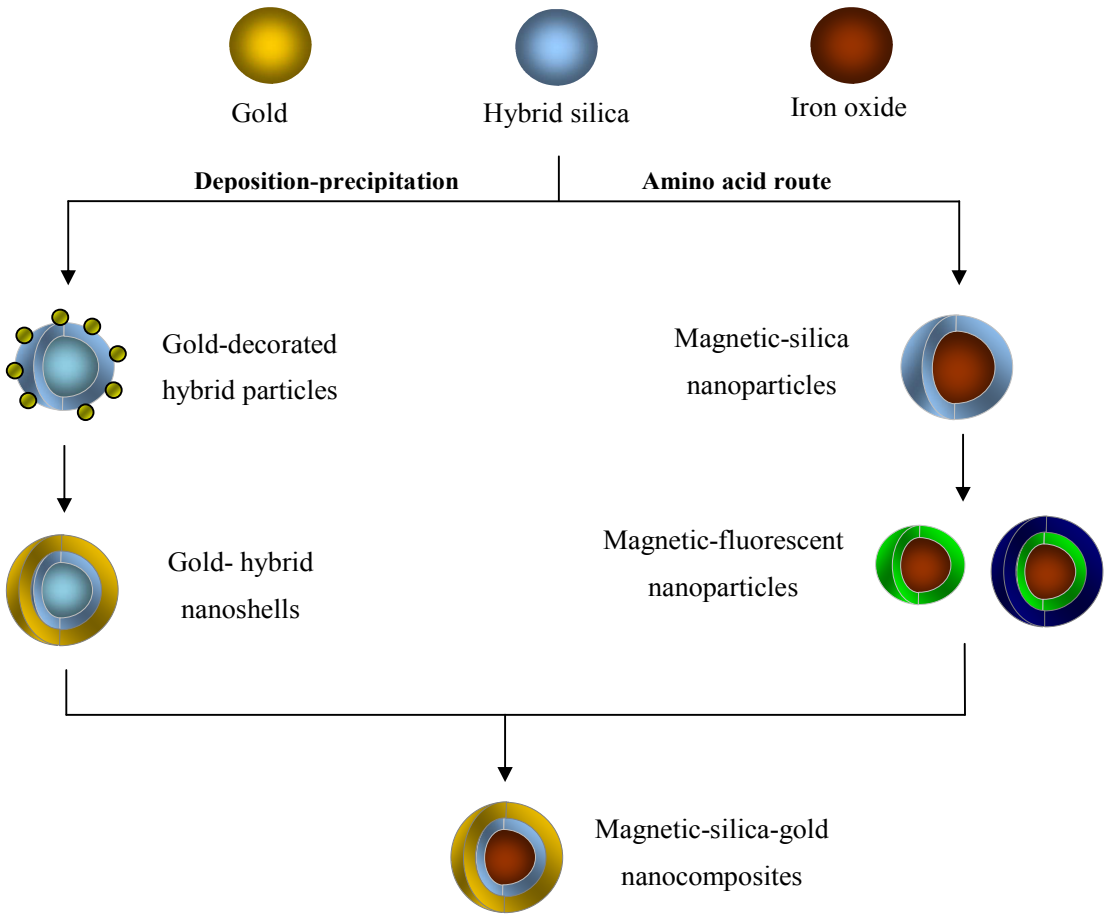

Figure 6-1: Strategies chosen to design gold/hybrid silica/iron oxide nanocomposites

6.2 Materials and methods

6.2.1 Materials

Chemical were purchased from commercial sources and used as received without any treatment. Tetraethyl silicate (TEOS), malachite green (MG), neutral red (NR), acridine orange (AO), and tri-sodium citrate were purchased from BDH. Absolute ethanol, L-arginine (>98 %), 3 aminopropyltriethoxysilane (APTES, >98 %), ammonium hydroxide (NH_4OH), 3-(trihydroxysilyl)propyl methylphosphonate monosodium salt solution (42 %, THPMP), vinyltriethoxysilane (>98 %, VTEOS), triethoxyphenylsilane (98 %, PhTEOS), hydrogen tetrachloroaurate trihydrate (>99.9 %, $HAuCl_4$), polyvinylpyrrolidone (40k Mw), sodium borohydride (~98 %, $NaBH_4$) lucifer yellow (LY), and fluorescein (Fl) were obtained from Sigma Aldrich. Rhodamine B (RB) and rhodamine 6G (R6G) were purchased from Fluka and methylene blue (MB), formaldehyde (CH_2OH) and sodium hydroxide (NaOH) from Fisher Scientific. Iron (II) chloride tetrahydrate (>99 %, $FeCl_2$) and iron (III) chloride hexahydrate (>99 % $FeCl_3$) were obtained from Acros Organics. Highly purified water (Milli-Q) was obtained from a Millipore “Direct-Q 3” water purification system.

6.2.2 Synthesis of gold nanoparticles and deposition-precipitation

- **Deposition-precipitation on hybrid seeds**

Hybrid silica seeds were synthesised using the protocol described in chapter 4: 275 µL of VTEOS and 385 µL of TEOS were mixed in 7 mL of arginine solution (15 mM) and left to stir for at least 10 hours. Next, 10 mL of arginine solution (0.5 mM) and 100 µL of TEOS were directly added to the suspension followed 30 minutes later by the organosilane(s):

- 40 µL APTES (AP-00)
- 30 of APTES and 20 µL THPMP (AP-25)

- 20 µL of APTES and 30 µL THPMP (AP-50)

Separately, a gold solution (6.35 mM) had been prepared by dissolving 125 mg of $HAuCl_4$ (trihydrate) in 50 mL Milli-Q. 100 or 500 µL of this solution was diluted in 7 mL of arginine (0.5 mM) and the pH was adjusted between 8 and 9. 1 mg of hybrid particles was added to this gold solution and the temperature was raised to 75°C. After 30 minutes reaction, the particles were collected by centrifugation at 150 g for 30 minutes, washed in water, and centrifuged a second time at 150 g for 15 minutes. Finally, the particles were suspended in 1 mL Milli-Q.

- **Growth of gold shells onto hybrid cores**

RB-doped silica nanoparticles were produced based on a VT-50 structure as described in chapter 5. Their surface was modified by addition of 30 µL TEOS followed 30 minutes later by 50 µL of THPMP and of APTES.

A gold platting solution was prepared by dissolving 60 mg of K_2CO_3 in 100 mL Milli-Q water to which 1.5 mL of a $HAuCl_4$ solution (25 mM) was added. The gold platting solution was left to stir overnight in the dark.

Gold seeds were nucleated onto the fluorescent nanoparticles following the protocol described previously. The particles were centrifuged two times at 150 g for 15 minutes and suspended in 1 mL of Milli-Q. The formation of a nanoshell was carried out by diluting 200 µL of the gold-decorated silica particle suspension into 5 mL of the gold-platting solution. Three different reductants (formaldehyde (CH_3OH), sodium borohydride ($NaBH_4$), and hydroxylamine (NH_2OH)) were used to reduce gold onto the particles. Likewise, the influence of some parameters was studied: variation of the gold platting volume (2, 5, 10, 15 mL), different reducing agent volume (100 µL to 1 mL), or variation of the deposition-precipitation reaction time (10 to 60 minutes).

6.2.3 Magnetite synthesis and magnetic nanocomposites

- **Synthesis of magnetite Fe_3O_4 and PVP-stabilised magnetite**

Iron oxide nanoparticles were prepared following a co-precipitation method: $FeCl_2$ (1.59 g) and $FeCl_3$ (2.16 g) were dissolved in 20 mL HCl solutions (0.2 M) each. Then, 1 mL of $FeCl_2$ and 2 mL of $FeCl_3$ and 400 mg of PVP were added to 30 mL of Milli-Q and stirred for 5 minutes at 60°C prior to addition of 2 mL of NH_4OH (conc.). The originally yellow-orange coloured solution turned immediately black. After 1 hour, the stirring was stopped and the solution was magnetically decanted (the particles sedimented at the bottom of the vessel after a few minutes). Then, a neodymium magnet was placed under the vessel to retain the particles within the glassware and the magnetite nanoparticles were washed two times with 20 mL of distilled water. The particles were finally suspended in 30 mL of Milli-Q (1 mg/mL).

- **Fluorescent-magnetic nanocomposites**

The PVP-stabilised iron oxide particles were sonicated for 15 minutes and a volume was diluted in arginine solution (0.5 mM) containing a fluorophore (1 mg/mL). After 5 minutes stirring, appropriate volumes of TEOS and VTEOS were added to the ferrofluid and the solutions were magnetically stirred for 8 hours before addition of APTES and THPMP. All conditions tested are summarized in the Appendix I (**Appendix I**). The composite particles were magnetically collected using a magnet and three times with distilled water before suspending the particles in 1 mL Milli-Q.

- **Deposition of an hybrid layer**

he exact same protocol was followed for the hybrid silica shell: 375 µL to 1 mL of ferrofluid was diluted in a volume of arginine (0.5 mM) and the required

amount of fluorophore solution (1 mg/mL). After 5 minutes, an appropriate volume of VTEOS and TEOS were added simultaneously (**Appendix I**) and the suspension was left to stir for 4 hours and collected as previously described.

- **Two dyes nanocomposites**

Nanocomposites composed of a magnetite core and a hybrid layer were synthesised as described above. After 10 hours reactions, half of each suspension was taken out for direct recording of the optical properties of the particles. The other half was washed in distilled water to remove the excess of fluorophore suspended in 5 mL of arginine solution (0.5 mM) containing a fluorophore (1 mg/mL). Then, TEOS was added, the solution were magnetically stirred overnight. The particles were washed and suspended as previously described. All condition tested are presented in the Appendix I (**Appendix I**).

6.2.4 Multifunctional nanoparticles

- **Deposition-precipitation on fluorescent nanocomposites**

New batches of iron oxide-silica nanoparticles were prepared by diluting 500 µL of sonicated ferrofluid in 35 mL of arginine solution (0.5 mM) to which 100 to 300 µL of TEOS was added. After 8 hours, the surface was modified with appropriate amount of APTES and THPMP and left to stir for additional 8 hours before collecting the particles (**Appendix J**).

Three solutions containing 5 mL of arginine solution (0.5 mM) and 300, 500, or 750 µL of $HAuCl_4$ (6.35 mM) and their pH was adjusted between 8.2 and 8.6. Then, 5 mL of the silica-iron oxide particle suspensions was washed and added to the gold solution. The suspensions were heated to 75°C and aliquots were taken at defined periods of time ranging from 30 minutes to 4 hours and washed in distilled water.

- **Growth of full gold layer**

Gold-decorated nanocomposites (Mg Au-1) were synthesised by diluting 750 µL of magnetite in 30 mL arginine solution (0.5 mM) to which 200 µL of TEOS and 75 µL MB .The surface was further modified 4 hours later by adding 40 µL of THPMP and 20 µL APTES. Next, 25 mL of the solution was washed and the particles were suspended in a solution composed of 30 mL of arginine (0.5 mM) and 3 mL of $HAuCl_4$ (6.35 mM) with a pH adjusted to 8.3-8.4. The solution was heated at 75°C for 4 hours and divided into 6 solutions, all washed in distilled water and suspended in Milli-Q. Two more gold-decorated nanocomposites (Mg Au-2 and 3) were prepared: in one case, the deposition-precipitation was varied between 1 and 2 hours and in the second case, 80 µL of THPMP was employed and the deposition-precipitation lasted 1h30.

Prior to the gold layer growth, fresh solution of sodium borohydride (6.9 mg $NaBH_4$ in 25 mL Milli-Q), formaldehyde (500 µL of formaldehyde in 10 mL Milli-Q) and hydroxylamine (16 mg in 25 mL Milli-Q) were prepared. The gold platting solution was prepared by dissolving 60 mg of K_2CO_3 in 100 mL Milli-Q water and by adding 1.5 mL of a $HAuCl_4$ solution (25 mM). The gold platting solution was left to stir overnight in the dark.

200 µL of particle suspensions was diluted in a volume of K-gold ranging from 2 to 40 mL. The growth of a full gold shell was studied by varying the type of reducing agent and the synthesis conditions as summarized in Appendix J (**Appendix J**).

6.2.5 Characterisation

- **Transmission and scanning electron microscopy (TEM/SEM)**

The particle size and morphology was examined using transmission electron microscopy (TEM) and scanning electron microscopy (SEM). The nanoparticle suspensions were firstly diluted: the samples were sonicated and subsequently

25 µL of suspension was poured in an eppendorf and the total volume was increased to 500 µL with Milli-Q water so that the SEM samples were totally transparent. One drop of suspension was deposited into a silicon grid and let to dry in a desiccator for at least 24 hours. Finally, the particles were imaged using a high resolution FEI XL30 SFEG analytical SEM (Philips, Netherland) or Philips CM20 Transmission Electron Microscope (Philips, Netherland).

- **Dynamic light scattering (DLS)**

The size and size distribution of the particles was measured by dynamic light scattering using a Zetasizer nano series S provided with an He/Ne laser of 633 nm wavelength (Malvern Instrument, UK). The particle suspensions were firstly diluted: 10 µL of the sample was poured in a quartz cuvette and completed with 1 mL Milli-Q. The refractive index and absorption of silica nanoparticles were fixed at 1.25 and 0.01 respectively. For each sample, four measurements of 20 runs (15 seconds each) were carried out, with temperature maintained at 25°C.

- **Fourier transform infrared spectroscopy (FTIR)**

The particles composition was analysed by infrared spectroscopy: a volume of nanoparticle suspension was taken, centrifuged, and dried in the oven for 1 day. The resulting powders were subsequently analysed in KBr powders using a Thermo Nicolet Avatar 370 spectrometer (Thermo Scientific). Infrared spectra were recorded over the wavenumber region 4000 to 400 cm^{-1} with a resolution of 4 cm^{-1}.

- **Fluorescence measurement**

Absorbance and fluorescence of FSNP were recorded in 96-well plates with a Varioskan Flash Spectral Scanning Multimode Reader (Thermo Fisher Scientific) equipped with a xenon flash lamp. All measurements were performed on 200 µL of 1 mg/mL suspensions of particles diluted in Milli-Q and at room temperature. Excitation and emission spectra of LY, FITC/AO/FI/OG, R6G, and

RB were acquired with fixed wavelength set 540/435, 530/450, 580/490, and 600/500 nm respectively.

6.3 Results

6.3.1 Gold nanospheres and gold-silica nanocomposites

Initially, the synthesis of gold-silica nanocomposites was attempted. Indeed, the synthesis of gold nanoparticles is easy and well-documented, producing bright red or purple suspension according to the particle size (**Figure 6-2**) corresponding to a plasmon resonance ranging from 520 to 560 nm. However, the elaboration of gold-silica core-shell structure was more challenging and the first attempts led to mixtures of gold, silica, and gold-silica nanoparticles altogether and their purification was difficult. For this reason, more attention was brought to the synthesis of silica-gold composites and gold nanoshells particles using the novel deposition-precipitation method.

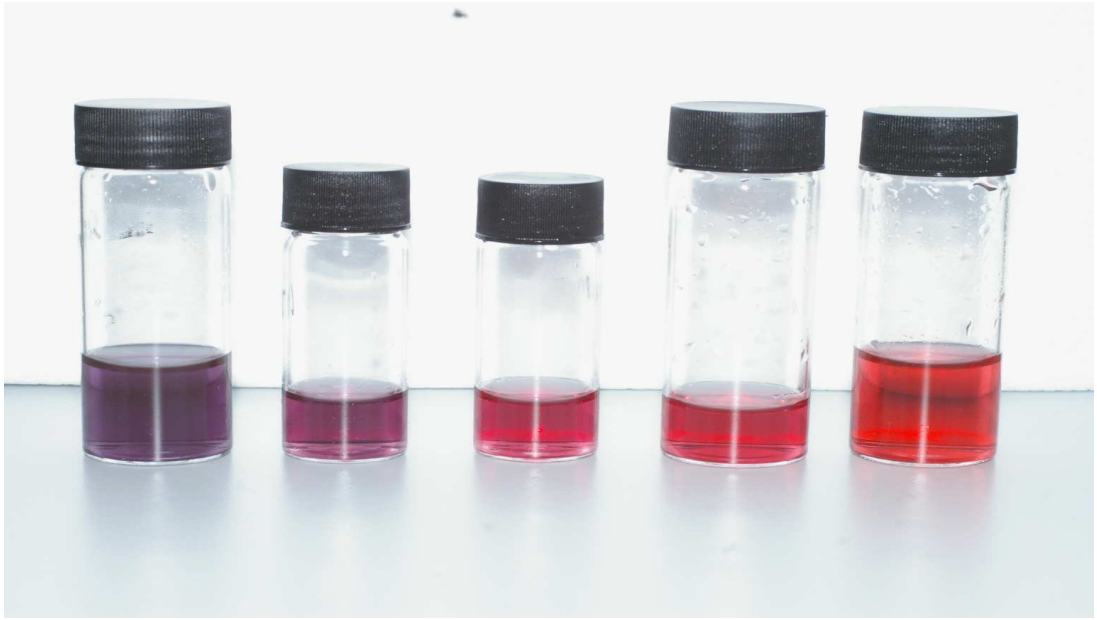

Figure 6-2: Example of gold nanoparticles suspension following the citrate-reduction protocol.

The deposition-precipitation process requires a “high” of the temperature and setting the pH of a gold solution at a specific value to favour the creation of seeds onto a surface. In a first time, the reaction time was fixed (30 minutes)

but the volume of gold solution used for the precipitation of gold seeds was varied [*Kah, 2008*]. Visually, the originally white suspension progressively gained a purple colour and became darker as the quantity of $HAuCl_4$ in the medium increased and aggregation was observed at the highest quantity of gold solution (500 µL). This change of colour was noticed for amine- and for amine-phosphonate-modified particles. The plasmon peak of gold progressively appeared on the spectra, although the peak was wider and slightly red-shifted than pure gold colloids and displayed a maximum absorption at 545 nm (**Figure 6-3**).

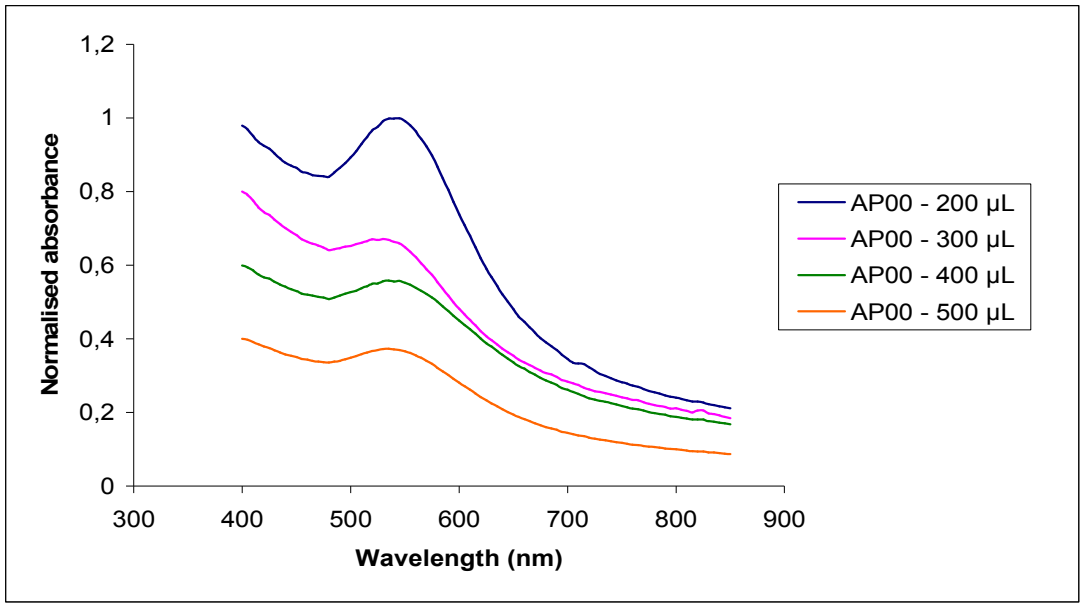

Figure 6-3 Absorbance spectra of AP-00 sample reacting with increasing volume of $HAuCl_4$ proceeded at 75°C for 30 minutes.

In a second time, the volume of gold solution was fixed and the reaction time was varied from 15 to 60 minutes. Moreover, RB-containing hybrid particles were used instead of blank one in order to observe the variation and potential effect of the gold seeds on the fluorescence properties of the FSNPs. The initially pink particles became more and more purple as the reaction time increased (**Figure 6-4**), indicating that a higher quantity of gold seeds or possibly bigger seeds were present at the surface of the nanoparticles.

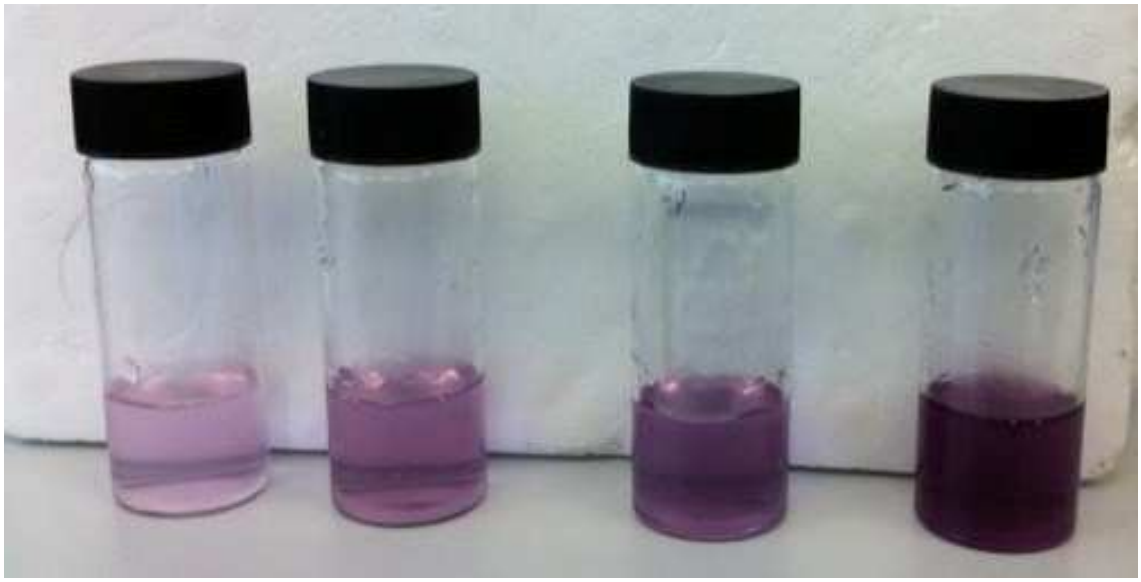

Figure 6-4: (from left to right) particles suspension after 15, 30, 45, and 60 minutes reaction time.

This assumption was further confirmed by the absorbance and fluorescence spectra. The hybrid nanoparticles displayed a peak at 555 nm, coupled to a weaker peak at 520 nm resulting from the gold seeds. When the reaction time increased, the plasmon peak widened covering most of the region between 500 and 600 nm but hiding the RB signal (**Figure 6-5**). This screening of the RB signal was also observed on the fluorescence spectra, where the emission of the fluorophore decreased and entirely disappeared after 30 minutes of deposition-precipitation time.

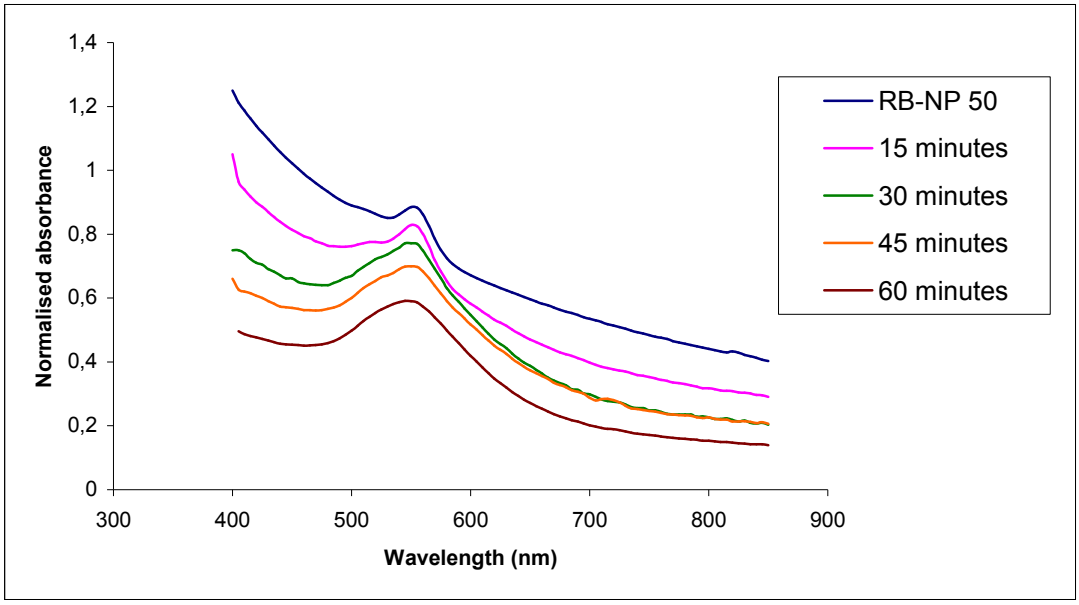

Figure 6-5: Evolution of the absorbance spectra of hybrid particles with the deposition-precipitation time.

The TEM images of the first batch of particles (30 minutes reaction, variation of the $HAuCl_4$ volume) showed the evolution of the nanoparticles morphology. At low volume (200 µL), black dots 1-2 nm peppered the surface of the particles (**Figure 6-6 A and B**). With 300 µL, these spots were no longer observed but energy-dispersive x-ray spectroscopy (EDX) indicated that gold was present in substantial amount and it may be assumed that gold recovered the hybrid nanoparticles and formed a layer of gold (**Figure 6-6 C**). At 500 µL, a few areas appeared darker than previously (higher electronic density) resulting from the aggregation of gold onto the hybrid particles (**Figure 6-6 D**). Unfortunately, it was not possible to performed electronic diffraction of the samples, which could have proved that gold was coating the particles and could have provided additional information about the phase in presence.

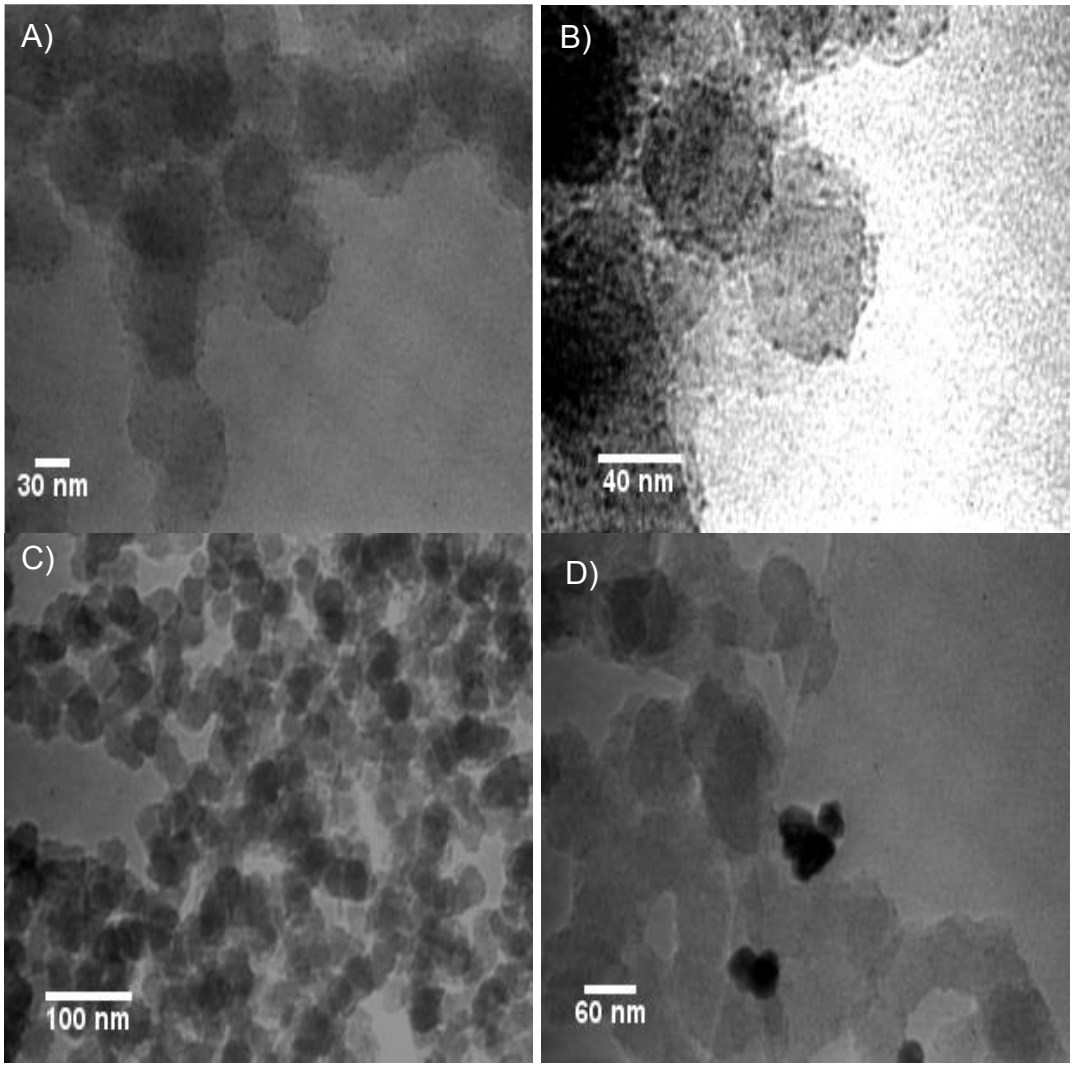

Figure 6-6: TEM pictures of hybrid particles after reaction for 30 minutes with 200 µL (A and B), 300 µL (C), and 500 µL of $HAuCl_4$ (D).

The deposition-precipitation is a transitional step towards the synthesis of gold nanoshells where the gold seeds act as support for the reduction of gold ions into a full layer. The gold plating concentration, and the reducing agent nature and concentration were investigated. Sodium borohydride ($NaBH_4$) and formaldehyde (CH_2OH) are two strong reducers but their mixing with the gold plating solution initiated the nucleation of pure gold particles, resulting in purple or red solution for all conditions tested. The measurement of the supernatant absorbance confirmed the presence of gold nanoparticles whereas the

absorbance of the “nanoshells” solely widened to cover the 500 to 600 nm region of the electromagnetic spectrum rather than being red-shifted to the near-infrared region.

Hydroxylamine hydrochloride (NH_2OH) was then substituted for $NaBH_4$ and CH_2OH due to its milder reducing capacities (and lower toxicity) [*Graf, 2002*]. The coloration of the gold plating solution was no longer immediate but occurred after a couple hours. After reduction of the gold from the gold platting solution, the spectra became modified: the plasmon resonance band was larger when the volume of reducing agent was increased and displayed a slight red-shift of the 520 nm-peak of the gold-seeded particles. The effect was maximal at the highest volume of NH_2OH with a peak at 585 nm. When hydroxylamine volume was fixed and the volume of gold plating solution increased, a similar red-shift was noted and the initial resonance at circa 525 nm rose up to 550, 590, and 595 nm (**Figure 6-7**). Yet, from the absorbance spectra, hydroxylamine was not able to form a complete layer because the plasmon resonance should go through an important red-shifting and easily reach the 700-900 nm. TEM analysis must be carried out to shed light on the particle morphology. According to the shape and wavelength of the plasmon resonance of the gold-hybrid “nanoshells”, no homogeneous layer has been created. Instead, it is likely that the gold seeds grew independently in all direction, creating large clusters, inducing a resonance between clusters, which explains the broad absorbance peak.

In summary, the deposition-precipitation approach is a powerful technique that easily covered the surface of hybrid particles with small gold seeds. The gold decoration is one step prior to growing a full metallic layer. Nevertheless, the results obtained here failed at creating a smooth gold layer and the plasmon resonance was only red-shifted to 590 nm at the maximum. Rather than continuing on this way, it was decided to first study the coating of iron oxide nanoparticles with hybrid silica. Since such particles are easier to manipulate, it would be easier to come back to the study of deposition-precipitation on

magnetic particles in order to better control the deposition-precipitation technique

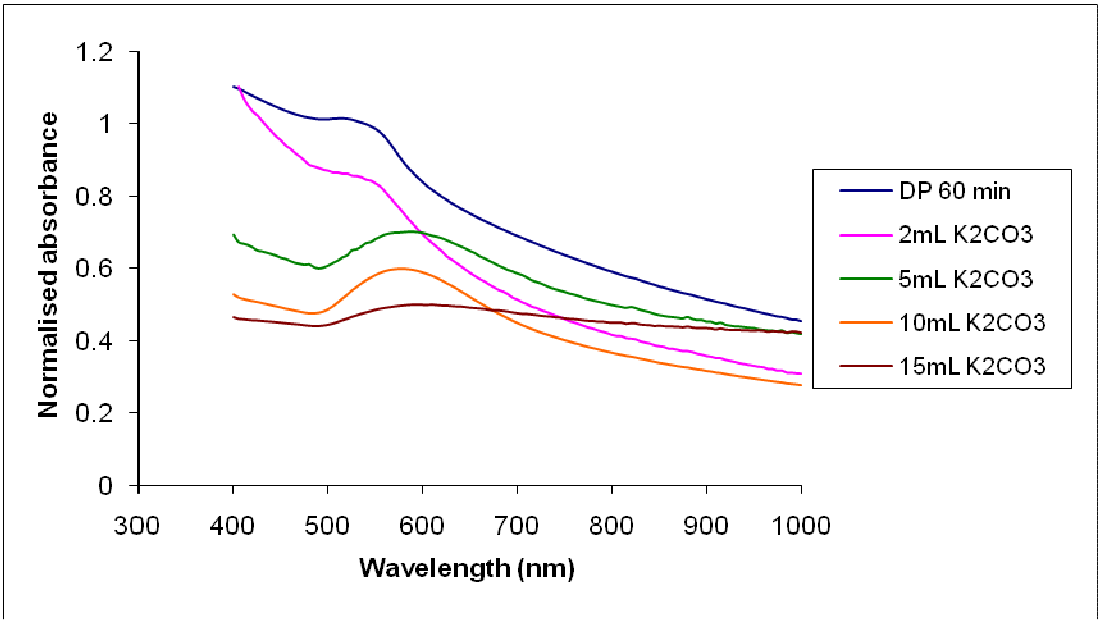

Figure 6-7: Absorbance spectra of gold-decorated hybrid nanoparticles after suspension in increasing volume of gold platting.

6.3.2 Synthesis of magnetite nanoparticles and magnetite-silica nanocomposites

The synthesis of iron oxide nanoparticles proceeded according to Massart's procedure, a co-precipitation-based method consisting in mixing iron salts (ferrous and ferric chlorides) under basic conditions. PVP was added at the end of the procedure to cap the particles and stabilise the suspension without hindering further coating [*Graf, 2003*]. One of the interesting properties of magnetic nanoparticles is their easy purification because the particles can be collected using an external magnet, which simplify the washing and suspension in water.

The FTIR-spectra of iron oxide displayed a characteristic band at 580 cm^{-1} that originates from the stretching vibration of Fe-O bonds in magnetite. The

adsorption of PVP was seen at 1660 cm^{-1} due to the C=O bond of the polymer and at 1289 cm^{-1} from the stretching vibration of C-N bonds (**Figure 6-8**) [*Arsalani, 2010; Sun, 2007*].

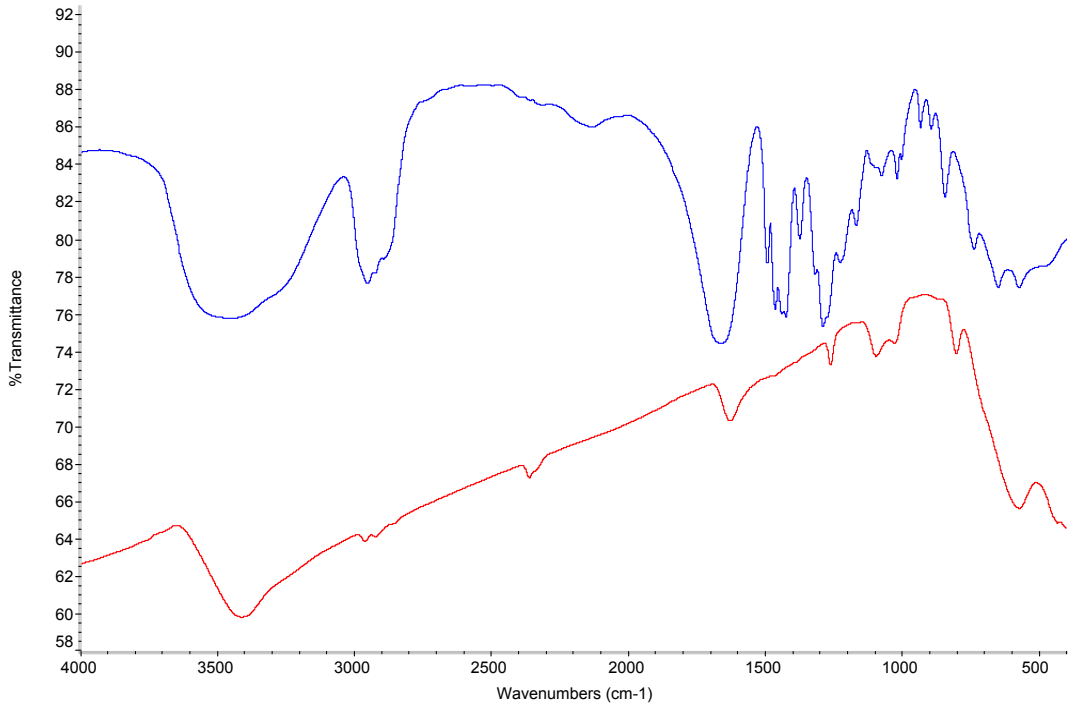

Figure 6-8: Infrared spectra of PVP 40k (blue) and PVP-stabilised magnetite (red).

Coating with SiO2 was then attempted by adding TEOS to the magnetic particles suspended in an arginine solution and MB was added as a visual and optical indicator. It must be pointed out that the coating of iron oxide with silica usually proceeds following the Stöber method but has never been reported with the amino acid route. Batches 1 and 2 were successful and the brown particles became green due to the presence of the fluorophore in the nanocomposite but none of the other batch seemed to contain the fluorophore. Yet, infrared spectroscopy revealed that both silica and magnetite were present in the samples since the spectra displayed the siloxane band at 1100 cm^{-1} and a reduced Fe-O stretching mode peak at 580 cm^{-1} (**Figure 6-9**).

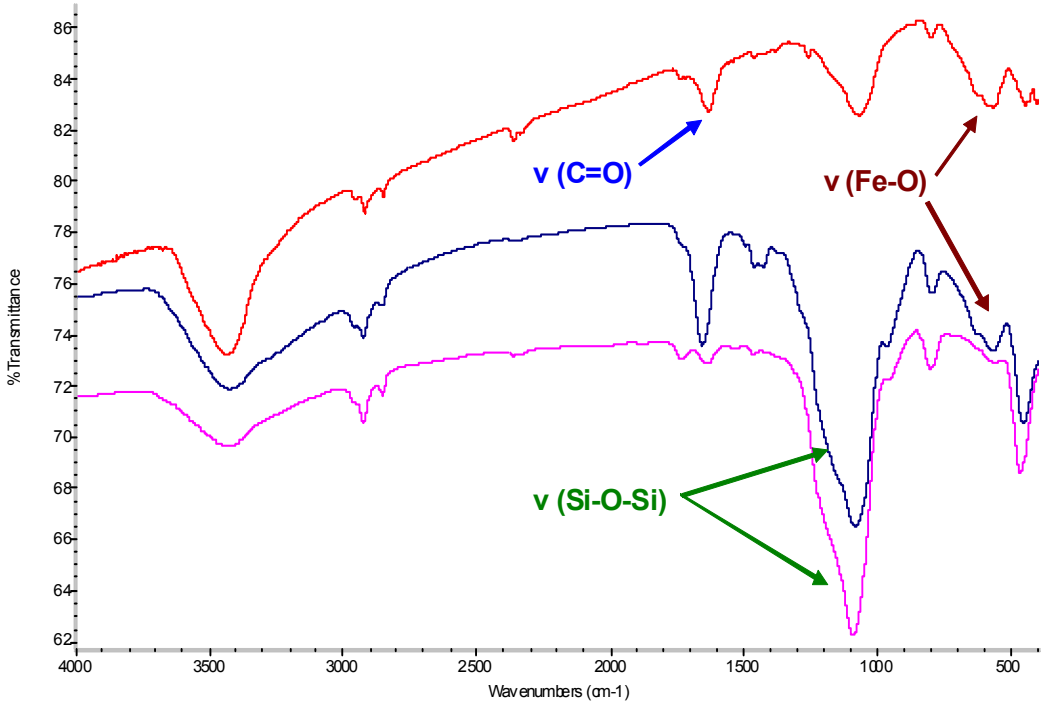

Figure 6-9: Infrared spectra of PVP-stabilised magnetite (red), and batch 1 (blue), and 6 (pink) obtained after reaction with TEOS.

SEM images displayed very small particles 9, 16, and 14 nmin diameter for batches 3, 4, and 5 respectively (**Figure 6-10**). The magnetite was highly aggregated in batches 3 whereas batch 5 was more dispersed. Iron oxide nanoparticles produced by co-precipitation are generally 6 to 9 nm in size and considering that silica was detected by FTIR the silica layer may not exceed 10 nm. The green colour was only detected in batches 1 and 2 but not in the other samples where the silica was composed of TEOS. The measurement of the suspension absorbance confirmed the presence of fluorophores in batches 1 and 2, but the other samples only displayed flat spectra. The difference may be attributed to the higher concentration of MB that was twice higher in the first two experiments but the other parameters were kept similar. On the other hand, R6G was present in the nanocomposites so the difference in MB case may be attributed for a low affinity of the dye for the matrix.

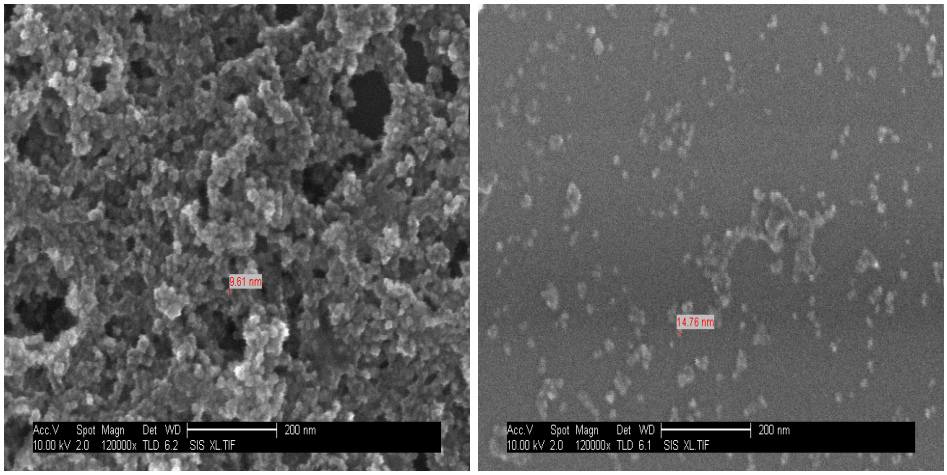

Figure 6-10: SEM pictures of silica-magnetite nanocomposite after reaction of the magnetic particles with 250 µL (left) and 1 mL (right) of TEOS.

Next, the coating with hybrid silica was tested following an identical protocol. Contrary to the previous experiments, the addition of VTEOS appeared to help in containing the dye within the coating since the samples exhibited a green colour after purification. The absorbance spectra of magnetite with hybrid coating possessed a peak at 660 nm. Similarly, batches 8, 11, and 12 that contained R6G emitted light at 555 nm whereas TEOS-THPMP and TEOS-APTES failed at incorporating MB and fluorescein respectively (**Figure 6-11**).

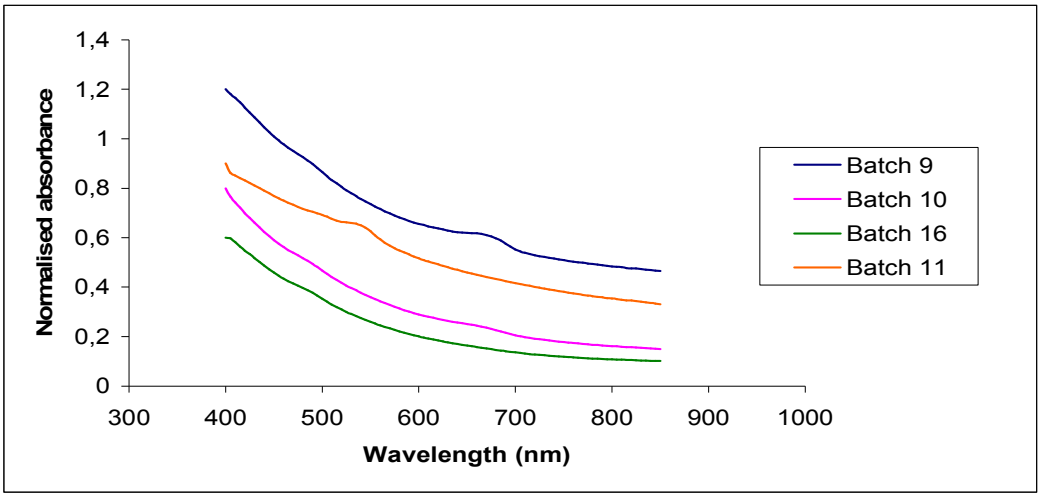

Figure 6-11: Infrared spectra of MB and R6G-doped nanocomposites composed of magnetic and hybrid VTEOS-TEOS layer.

Infrared spectra of batches 9 and 10 differed although both are made of VTEOS and TEOS: batch 9 spectrum is typical of hybrid VTEOS particles with strong peaks at 1600 and 1410 cm^{-1} but new peaks arise at 1461, 1413, and 1379 cm^{-1} in the second hybrid that may be due to residual PVP that was still present in the sample. In batch 16, no signal from THPMP was detected whereas the broad band in the 3500-3000 cm^{-1} region and the new peaks at 1547 and 1470 cm^{-1} are representative of APTES. In all cases, the 580 cm^{-1} originating from Fe-O was present (**Figure 6-12**).

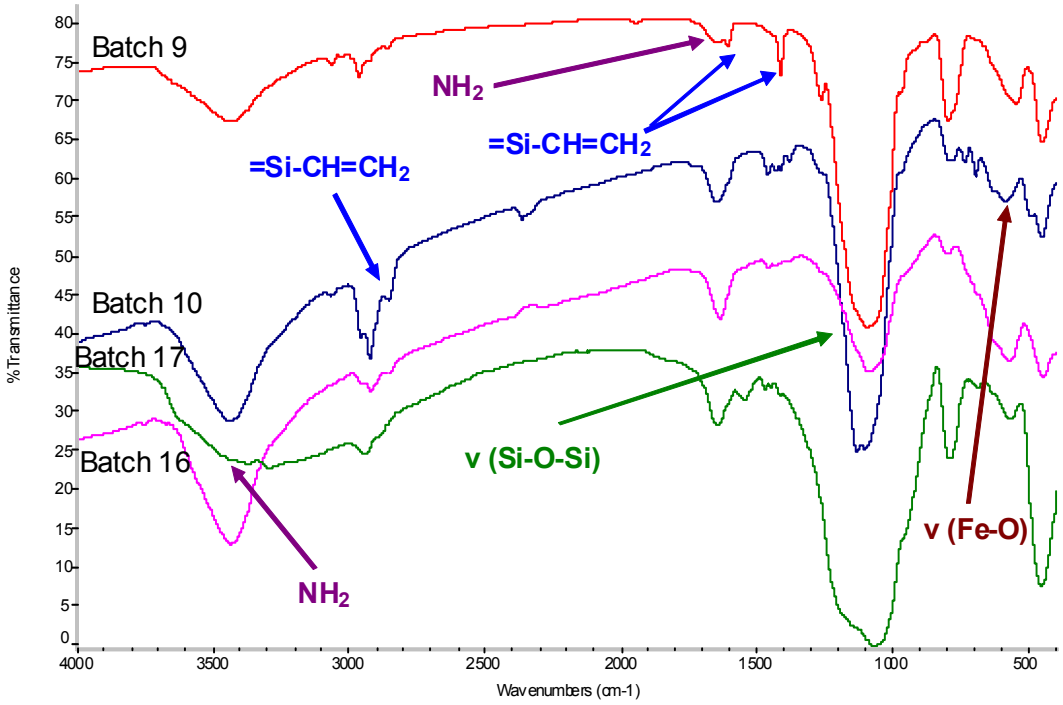

Figure 6-12: Infrared spectra of batches 9 and 10 (made of VTEOS and TEOS) and of batch 16 and 17 (made of TEOS-THPMP and TEOS-APTES respectively).

The procedure was extended by adding a second fluorescent layer to the previous particles. In a first time, batch 2 (700 µL ferrofluid reacted with 175 µL TEOS in presence of 75 µL MB) was used as a scaffold and already contained MB and a second layer made of TEOS or of VTEOS-TEOS and containing AO

was grown onto the nanocomposites. Where the original absorbance spectra only displayed a peak at 660 cm due to the presence of MB, the new magnetite-silica nanocomposites exhibited a second peak at 490 nm revealing the presence of the second dye (**Figure 6-13**). Although the signal was visible in all four spectra and the absorbance was of comparable intensities, the emission and excitation of the hybrid layer (batches 2-3 and 2-4) was lesser than that of pure TEOS.

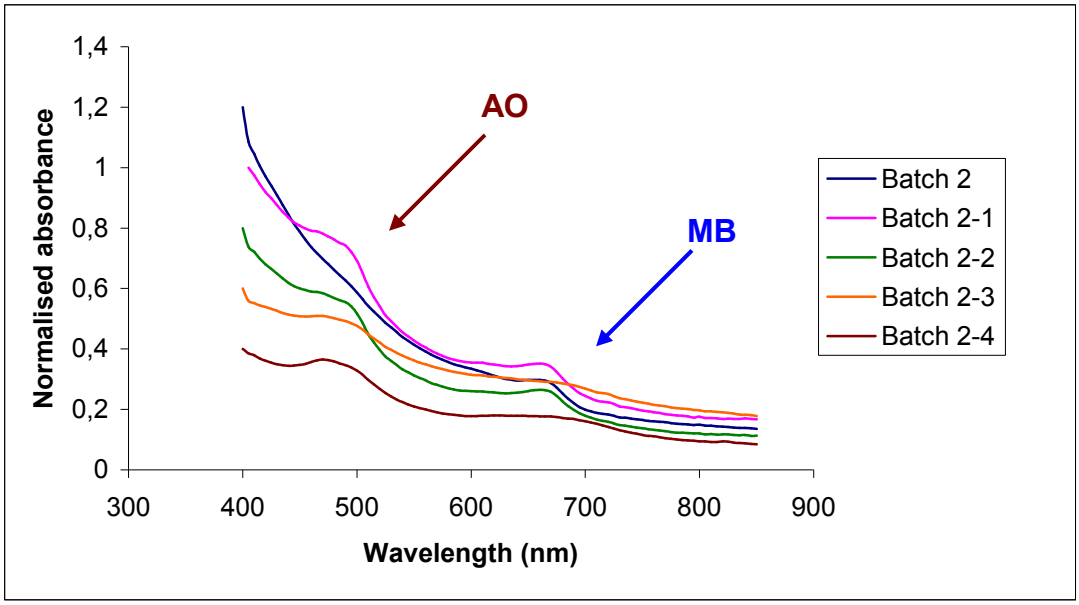

Figure 6-13: Absorbance spectra of MB-containing batch 4 before and after modification with either TEOS or TEOS-VTEOS.

The composition of the layer was modified to mimic that of the hybrid particles developed in the chapter 5. The samples were based on a similar structure where magnetite forms the core of the particles and was recovered by first a layer of hybrid silica and second by a pure silica coating. As observed in Chapter 5, the addition of APTES to the hybrid coating help in stabilising some of the fluorophores with low affinity for the VTEOS-TEOS composition, although the aggregation issue seemed amplifyied and the texture of the suspension was different, looking like “sand”.

The particles morphology was characterised by SEM: in batch 23 and 25, the images displayed two populations of particles with 140 nm spheres and 700 nm cup-shaped particles, whereas smaller spheres 100 nm diameter were visible in the same batch after growth of the second layer (**Figure 6-14**). In contrast, batch 26 was mainly composed of particles with size comprised between 100 and 140 nm after the first and second layer deposition, although the cup-shaped structures were occasionally observed. DLS did not provide clear information and detected objects nearly 1 µm in diameter – probably the large aggregates

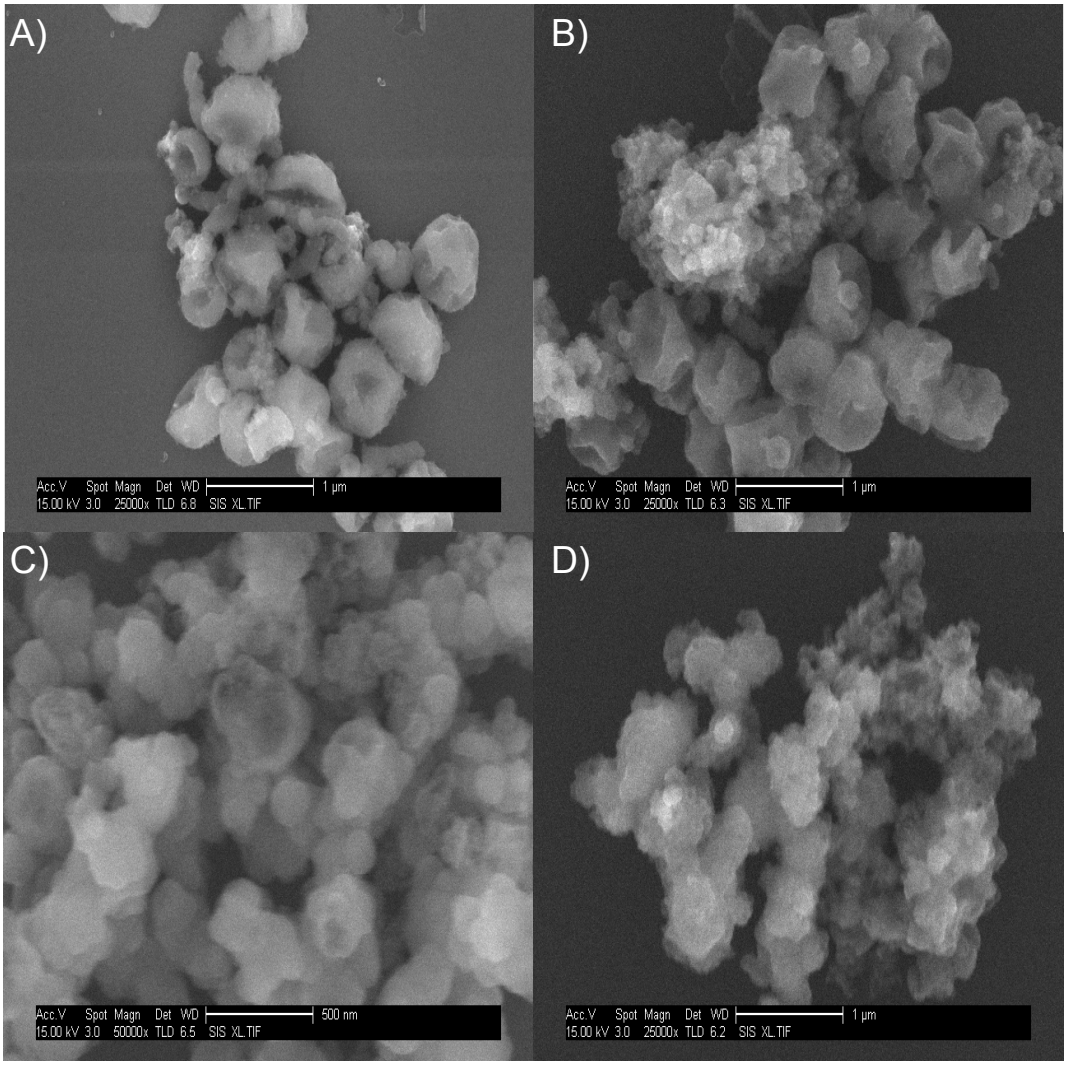

Figure 6-14: SEM pictures of the first hybrid and second TEOS layers of batch 23 (A and B), batch 25 (C and D), and batch 26 (E and F).

detected by electron microscopy - but the size was not necessarily larger after the growth of the second layer. In other words, the nanocomposites containing VTEOS suffered from the same problem encountered in Chapter 4 (the same VTEOS solution was used). For the same reason, it is necessary to repeat the experiment with a new VTEOS solution to verify whether the protocol developed in this chapter is able to produce nanoparticles rather than cup-shaped particles.

The hybrid nature of the particles was reflected by the characteristic peaks of vinyl on the infrared spectra at 1600 and 1410 cm^{-1} as well as the three peaks in the 2950-3050 cm^{-1} region. Although the 3500-3000 cm^{-1} band in batch 23 is narrower than in batches 25 and 26, the shoulder at 1668 cm^{-1} evidenced that APTES used during the first layer growth had been incorporated into the nanocomposite (**Figure 6-15**). The spectra of layer 1 and layer 2 were identical in all three cases.

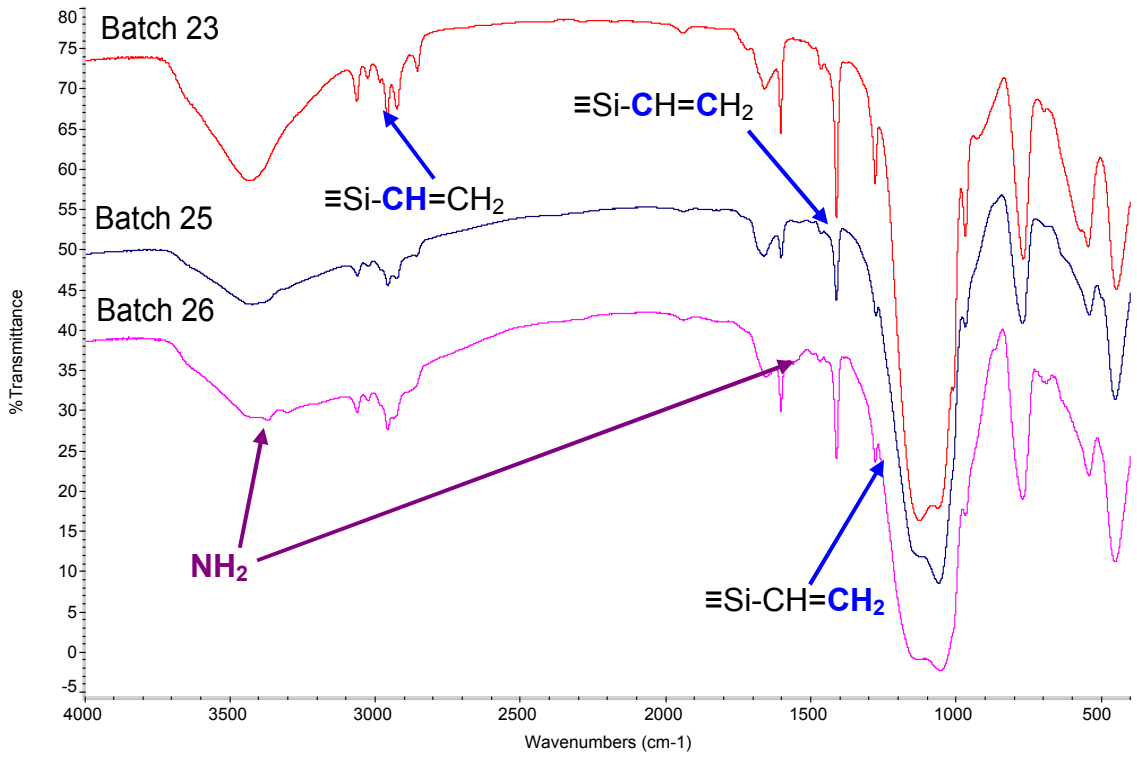

Figure 6-15: Infrared spectra of the final batches 23, 25, and 26 nanocomposites made of two silica layers.

The particles were synthesised in presence of R6G, MB, Fl, or LY for the inner layer and AO, R6G, or RB for the outer one. Batch 21, 22, and 24 contained LY and AO and the excitation and emission spectra indicated that the two fluorophores were present in the particles (**Figure 6-16**). The absorbance spectrum of batch 23 displayed a strong signal from MB and the excitation and emission spectra proved that AO was also present. Finally, the excitation and emission spectra of batches 25 and 26 displayed intense peaks of Fl as well as RB and R6G after the growth of the TEOS layer.

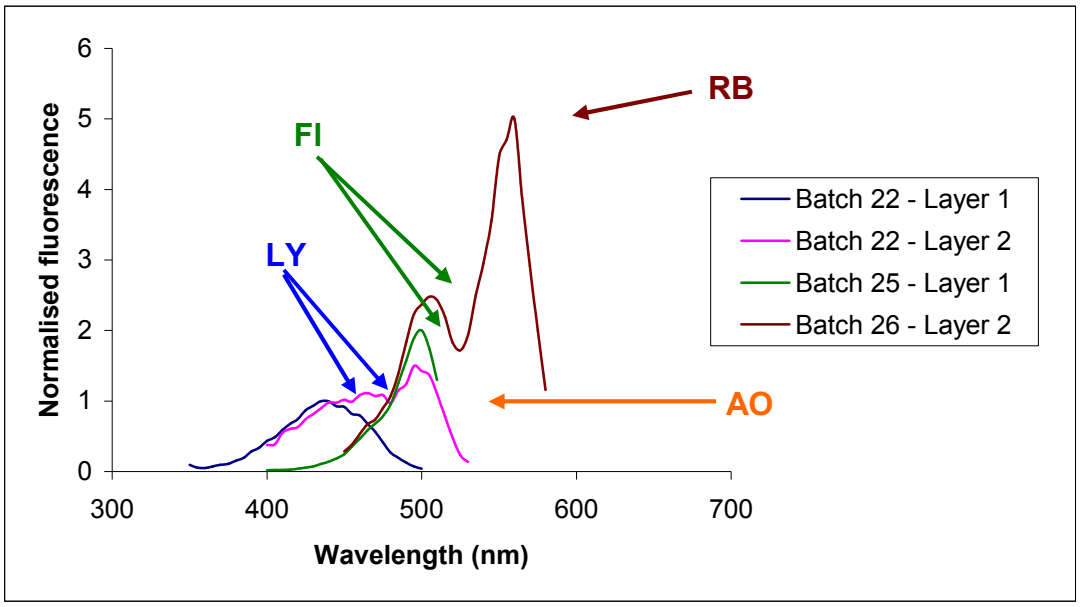

Figure 6-16: Excitation spectra of single- and two-layers magnetite-silica nanocomposites after coating with the hybrid and TEOS layers

All of these results suggest that the amino acid route is a potential candidate for the coating of iron oxide (and potential other material) with thin layers of silica. Moreover, the method is also suitable for the deposition of hybrid silica coatings in view of developing improved magnetico-fluorescent nanoparticles capable to carry a large diversity of fluorophores. Another interesting feature is the possibility to drag the particles with an external magnet: this feature may be helpful for the deposition precipitation, and more precisely to the formation of a homogeneous layer that may require reduction of gold in multiple steps.

6.3.3 Elaboration of iron oxide-silica-gold nanocomposites

Due to the easy handling of iron oxide nanoparticles, the deposition-precipitation process and growth of a gold nanoshell was tested on the magnetic-fluorescent nanocomposites. After adjustment of the pH and reaction from 15 to 60 minutes the results appeared random. For instance, batch 18 displayed a strong signal from R6G after 10 minutes and was supplanted by the plasmon resonance of gold after 20 minutes followed by a widening of the plasmon band over that time. On the contrary, batch 19 did not give sign of gold at all, even after 60 minutes (**Figure 6-17**). Compared to the hybrid particles, the decoration with gold seeds of the nancomposites requires more time to achieve similar results (usually several hours). This difference may be linked to a change of amine density at the surface of the particles or because the amine modification proceeded principally on silica particles nucleating as by-product during the coating and removed during the centrifugation preceding the deposition-precipitation stage.

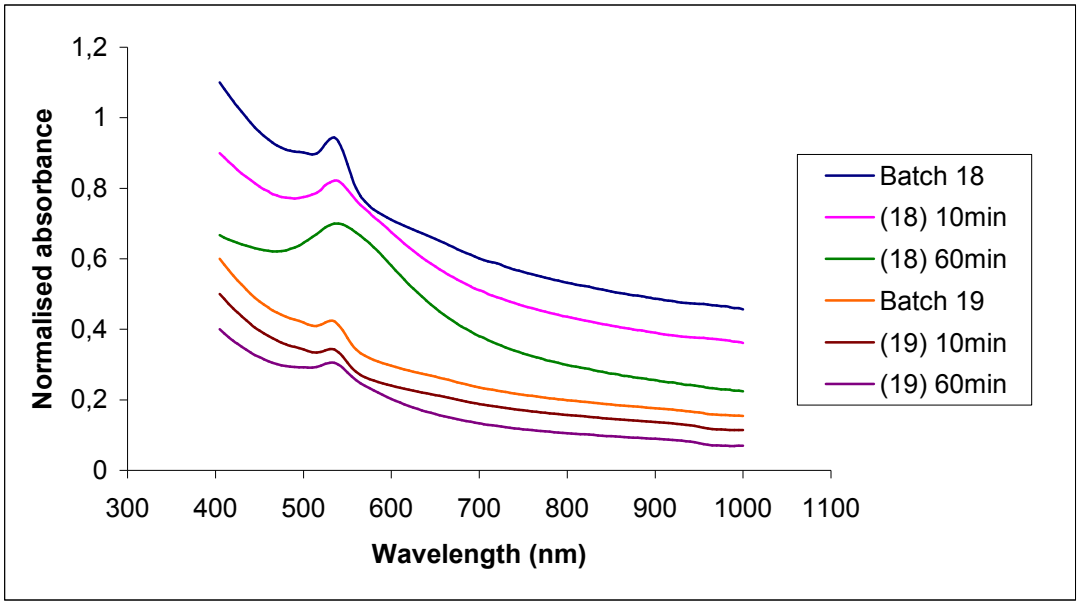

Figure 6-17: Evolution of the optical properties of fluorescent batches 18 and 19 after 10 and 60 minutes deposition-precipitation.

Some of the samples displaying a plasmon resonance were used for the growth of a full gold shell by reduction of gold salts from a platting solution. Formaldehyde, sodium borohydride, and hydroxylamine were all tested using the same protocol than reported earlier. Although all samples eventually displayed a large plasmonic band (even samples with very weak initial plasmon resonance), none possessed an absorbance over 600 nm but rather covered the whole 500-600 nm. As hypothesized earlier, it is likely that the nanocomposite are not coated with smooth and uniform gold layers but rather by clusters of various sizes. Due to their close proximity, the clusters are able to enter into resonance, which is known to produce a broad and slightly red-shifted plasmonic peaks.

A different approach called iterative hydroxylamine seeding, relying on the repetition of gold reduction, was then applied in order to create a complete layer of gold [*Lyon, 2004*]. Here, the gold reduction was repeated up to 7 times, i.e. the iron oxide-silica nanoparticles were suspended in first time in the gold platting solution and hydroxylamine was added. The particles were then collected, washed, and suspended once again in the gold platting solution. This was repeated up to 7 times, always with hydroxylamine to prevent the nucleation of pure gold seeds, in order to progressively create a homogeneous gold coating. For instance, batch Mg Au-3 was obtained by suspending the gold-decorated nanocomposites 4 times in the platting solution: although the initial particle did not display any plasmon resonance, a peak around 595 nm was visible after the initial reduction round and was shifted after to circa 650 nm after the second round. From the second to the fourth round, the spectra curvature changed and instead of a peak or a large band, the absorbance rose and formed a threshold spanning the 600-1000 nm that was closer to the signal from gold nanoshells (**Figure 6-18**).

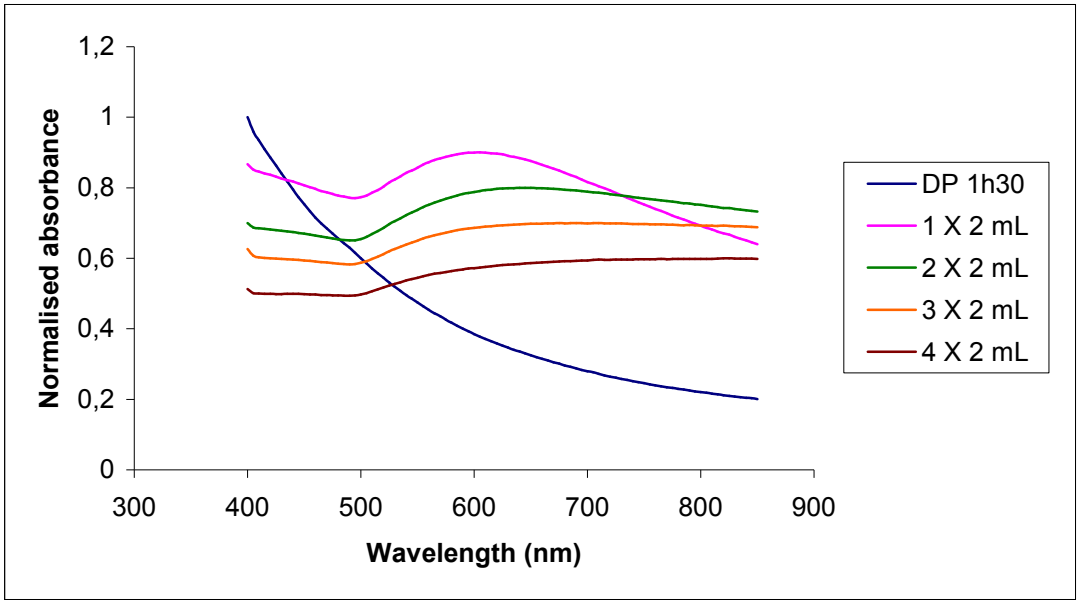

Figure 6-18: Absorbance spectra of Mg Au-3 after deposition-precipitation and iterative hydroxylamine seeding (4 times).

For all experiments proceeding following the iterative seeding, it was possible to red-shift the plasmon resonance over 600 nm as well as a broadening of the band that spanned the near-infrared region of the electromagnetic spectrum. Yet, the spectra eventually looked the same after 3 to 4 repetitions although the plasmon resonance should continue red-shifting as the “hypothetic” gold layer thickness increases. Consequently, another batch of particles was synthesised and the changes of morphology were followed by TEM. The spectra of the original composite and of the gold-decorated particles were similar and displayed the absorbance of R6G. A large plasmon resonance centred around 535 nm appeared after the first round of gold reduction and was shifted toward 585, 640, and 705 nm after the second, third, and fourth passages respectively with apparition of the absorbance threshold at the fourth round (**Figure 6-19**).

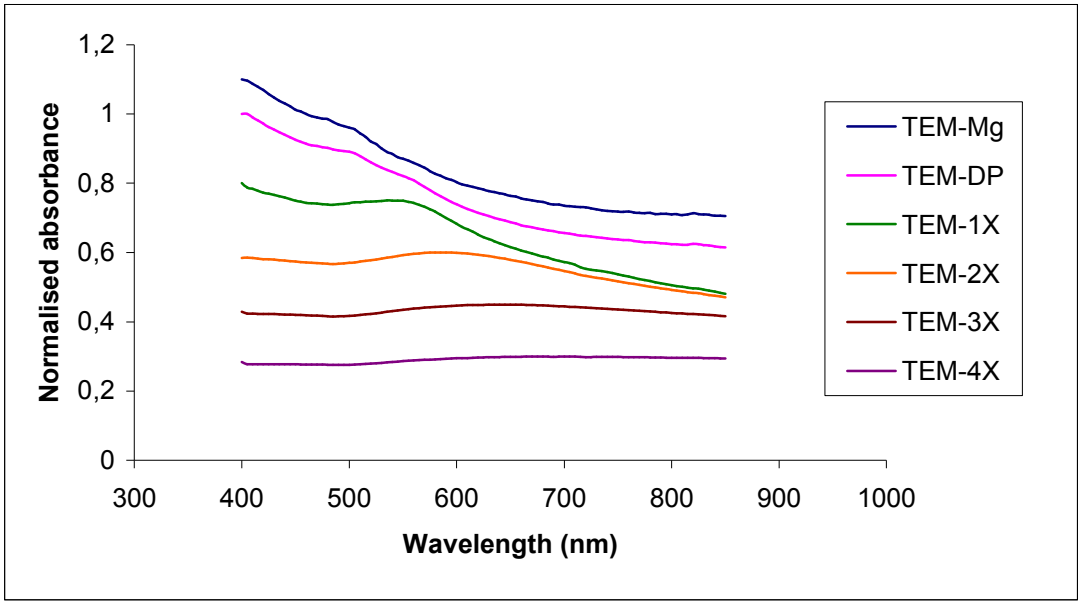

Figure 6-19: Absorbance spectra of the nanocomposite batch after deposition-precipitation and seed mediated regrowth

It was impossible to clearly assess the size of the nanoparticles by TEM because of the small size and high aggregation of the samples. The cause of the high aggregation may be attributed to both a high concentration during the TEM samples preparation and the natural tendency of iron oxide to aggregate in spite of the adsorption of PVP. Dark spots on the TEM image of the first round are the sign of gold but it does not seem that the particles are all coated. The density appeared to increase after 3 passages but the morphology of the final structure is not clear enough to verify whether a full layer has been grown and how homogeneous this layer might be (**Figure 6-20**). Unfortunately, these images are not exploitable but it was not possible to perform all of the characterization required (TEM, X-ray diffraction, etc.). In fact, the experiments must be repeated with a full set of characterisation after each step of the protocol to follow the changes occurring with the nanoparticles. For the moment, all that can be said is that coating of hybrid silica onto iron oxide via the amino acid route is possible and the deposition-precipitation and iterative

seeding are interesting strategies (still little used) for the formation of gold shells and are worth exploring further into details.

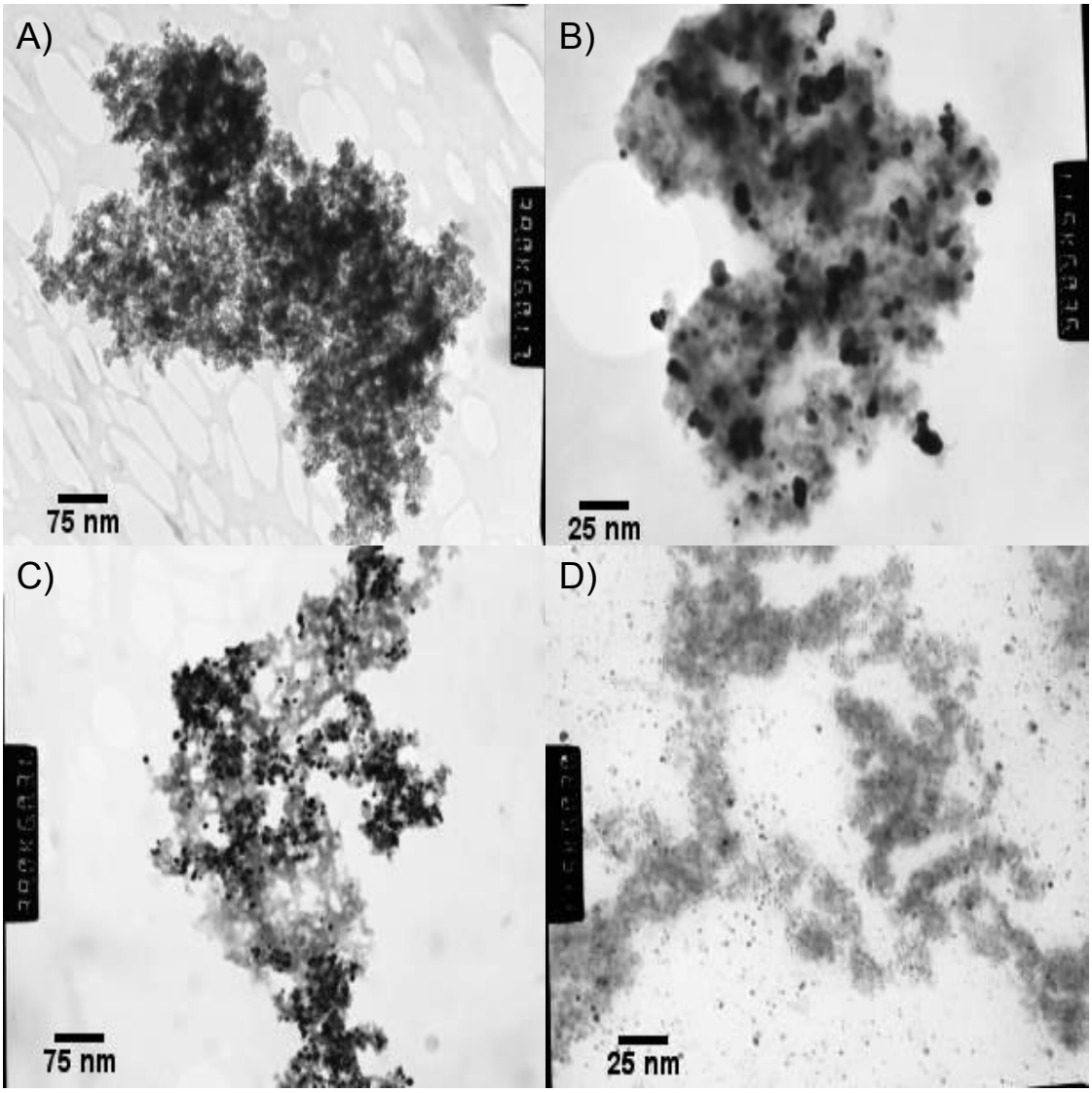

Figure 6-20: TEM picture of the final magnetite-silica batch (A) and after 1 round (B), 3 rounds (C), and 7 rounds (D) of seed mediated regrowth.

6.4 Discussion

6.4.1 Deposition-precipitation and gold nanoshells

The deposition-precipitation is a recent and still ill-explored method to coat nanoparticles. Initially, gold seeds were nucleated onto titanium dioxide to catalyse the decomposition of carbon monoxide but the work of Kah and co-workers proved that the technique is also suitable for coating the surface of silica nanoparticles, becoming a potential alternative strategy for the synthesis of gold nanoshells [*Kah, 2008*]. Contrary to the traditional synthesis protocol of gold nanoshells where very small gold seeds 1-2 nm needs are adsorbed onto (aminated) silica nanoparticles, the gold seeds grow onto the ceramic particles *in situ*. Kah's work identified the optimal conditions for the gold-deposition: pH comprised between 8 and 9 and a temperature exceeding 60°C maintained for 30 minutes are essential to obtain uniformly distributed 2 to 4 nm seeds. Longer periods of time promote the creation of clusters whereas absence of amine at the surface inhibits the deposition of gold particles.

The effect of phosphonate has not yet been investigated and it is unknown whether this moiety strategy may interfere with the deposition-precipitation due to its negatively charges that change the particles isoelectric point (IEP). Indeed the whole deposition-precipitation process is based on the difference of charged between the particle surface and the gold species. The first result showed that all samples were modified with gold seeds as seen by the change of colour, albeit the conjugation of THPMP has yet to be proved. The pH conditions are of utmost importance for the proper creation and precipitation of gold seeds. No changes were detected in experiments were this parameter was not controlled. This is because deposition-precipitation relies on the hydrolysis of the chloroauric ion $AuCl_4^-$ by the action of a base, resulting in the formation of anions of the form $[Au(OH)_xCl_{4-x}]^-$ [*Lee, 2002*]. The extent of hydrolysis depends on the pH but also on the temperature, which promotes the replacement of Cl^- with OH^-. Of all potential species, only $Au(OH)_3Cl^-$ precipitates and is able to deposit on silica or other substrate and $Au(OH)_3Cl^-$ mainly exists in the 8 to 9

pH range [*Kah, 2008*]. Haruta originally designed gold supported on titania surfaces for catalytic purposes but the method is suitable for other metal such as nickel on various metal oxide substrates [*Haruta, 1997*]. Nevertheless, the DP method does not function for all metal oxide surfaces as the IEP is another important critoerion. For example, the IEP of bare silica is equal to 2, meaning that the silica surface is negatively charged at higher pH and therefore repel the $Au(OH)_3Cl^-$ ions. To successfully create gold seeds onto silica nanoparticles, the surface must be modified with amine groups to raise the IEP of the particles to 9. In consequence, the particles become slightly positively charged below pH 9, which allows the deposition of $Au(OH)_3Cl^-$ and subsequent gold nucleation [*Phonthammachai, 2007*]. The advantage is that there is no risk of gold particles generation since no reducer is added to the solution and the $Au(OH)_3Cl^-$ specie exclusively reacts with the silica surface. The colour changes visible with the phosphonated-modified particles showed that the deposition-precipitation was achieved even though the surface was not strictly expressing amine groups. However, it is necessary to mesure the zeta potential of the potential to firstly prove the presence of phosphonate group and secondly to evaluate whether the change of IEP that may be detrimental for the procedure.

The optical properties of the gold-decorated hybrid particles highly depend on the gold ions concentration and on the reaction time: the higher concentration of $HAuCl_4$, the deeper the suspension colour and the broader the plasmon resonance band. The effects are equivalent when the reaction time is increased because of the structural changes in the particles surface. TEM and EDX evidenced the modification that occurred onto the nanoparticles: at low gold concentration or reaction time, small seeds were detected and turn into what appeared as full yet inhomogeneous layer of gold at medium concentration and/or time and finally evolved in the creation of large, dark areas onto the silica structures after 60 minutes reactions. The surface of the particles was covered of clusters of different sizes close one o the other and this proximity create a broad plasmonic band because a phenomenon of resonance between the

clusters. The presence of clusters is not desirable for the growth of a complete and smooth layer of gold because they compete with the small seeds as nucleation site. The deposition-precipitation reaction ought to be stopped based on visual and/or spectroscopic evidence to ensure of the optical properties quality and to avoid the formation of gold clusters. The main setback to the deposition-precipitation and to the coating of silica particles with gold in general is the screening of the fluorescence signal of dye contained in the hybrid matrix. It was found that as the plasmon resonance/seed density increased the fluorescence of dyes in the core of the diminished and was eventually screened the dyes fluorescence because gold is not optically transparent.

The logical next step is the growth of a uniform shell onto the gold nanocomposites via reduction of gold by action of a reducing agent. Sodium borohydride and formaldehyde are the principal reducing agents and were the first tested. Their addition to the gold platting solution immediately led to a red colour but centrifugation at low speed and recording of the supernatant absorbance showed that the colour originated from small gold nanoparticles that remained in suspension in the supernatant. The two reducing agents are too strong and their addition to the platting solution led to spontaneous nucleation of new gold nanoparticles. The sole effect on the nanocomposites was a slight broadening of the plasmon resonance peak at 530 nm but no nanoshell was created. Hydroxylamine hydrochloride, a weaker reducer, was also tested but to no avail: although no immediate gold nucleation occurred (but after a few hours reaction), no significant optical changes were observed with the nanocomposites [*Phonthammachai, 2008*].

Variation of reducer concentration, gold platting volume, and deposition-precipitation time had little effect and no absorbance spectra display the characteristic features of gold nanoshells (long wavelength plasmon resonance, etc.). In only one case, where a higher gold platting volume was used (15 mL), the maximum wavelength verged on 600 nm but overall no complete gold shell was created in any batch of nanoparticles. The synthesis of gold nanoshells

was paused for a while for investigating the production of iron oxide-silica nanocomposites.

6.4.2 Magnetic particles and magnetite-silica nanocomposites

The choice of moving to the magnetic particles rather than optimising the synthesis of gold-silica nanoparticles and gold nanoshells was motivated by the difficulty encountered with the purification of the samples. Iron oxide nanoparticles in that respect are easier to handle since they can be retrieved using an external magnet. Moreover, the deposition-precipitation revealed a powerful method and was supposed to be directly applicable with silica-coated iron oxide particles. The design of nanocomposites and multifunctional nanoparticles proceeded in three stages: growth of fluorescent silica and hybrid layers using the amino acid route, the functionalisation of the nanocomposites with gold seed following the deposition-precipitation approach, and the growth of a gold layer using hydroxylamine reduction and iterative seeding.

Several methods have been developed for the synthesis of iron oxide nanoparticles. The co-precipitation is the simplest and most frequent method and consists in mixing iron salts and to add ammonium hydroxide to precipitate iron under the form of magnetite nanoparticles. The method is able to produce very small particles 5 to 15 nm in large quantities but suffers from two major drawbacks: the relatively high size dispersity and the low crystallinity (high crystallinity goes in par with high magnetisation). Proceeding at higher temperature remedies to the size dispersity and low crystallinity, but requires another solvent withstanding 200 degrees. In the same way, controlling the aggregation of iron oxide nanoparticles helps in both controlling the size of clusters and increasing the saturation magnetisation, and render the particles more sensitive to moderate external magnetic field [*Ge, 2007*]. Nevertheless, co-precipitation is a perfectly acceptable method and was found suitable for the development of multifunctional nanoparticles.

Iron oxide nanoparticles can be stabilised by addition of polyvinylpyrrolidone (PVP) a biocompatible, neutral polymer that adsorbs onto the surface of the nanoparticles and promotes their steric repulsion. The adsorption is only provisory and the polymer chains exchange their place with other molecules or materials (ligand exchange) whenever the nanomaterial has to be coated [*Graf, 2003, Thanh, 2010*]. Yet, PVP effect was found limited in time and did not suppress the aggregation. It is however possible that the aggregation is in fact intrinsic to the method as the first particles are immediately formed with the first drop of ammonium hydroxide. This problem may be overcome by controlling the afflux of NH_4OH using a pump to ensure that the iron oxide salts are progressively transformed into nanoparticles.

The FTIR characterisation of the silica-coated iron oxide particles showed sign of silica but SEM pictures did not display significant changes of diameter before and after reaction with TEOS, suggesting that coating thickness may not exceed a few nm. Here again, the amino acid route may be interesting to produce thinner coating than the Stöber method and may reduce the chances of encapsulating multiple magnetite nanoparticles into a single silica particle (frequent with the Stöber method). The detection of silica prompted the testing of hybrid coating. Where pure silica showed difficulty to entrap MB (perhaps due to the thinness of the layer), hybrid VT-coating proved more successful since the particle displaying the 600 and 660 nm band found with free MB solution. The strategy developed in chapter 5 was attempted on the magnetic nanoparticles as well and incorporation of APTES to VTEOS and TEOS led to particles containing fluorescein and lucifer yellow (impossible with pure silica) as well as AO, RB, and R6G. It was likewise possible to combine all of these fluorophores by iterative deposition of hybrid silica, suggesting that core-shell structures are achievable. Considering that most fluorescent-magnetic particles require covalent binding, use of emulsion, or integration of quantum dots for the rest) [*Chen, 2009 b; Cho, 2010 c; Corsi, 2009, Zhang, 2010 a*], using hybrid silica coatings multiply the possibility of the magnetico-fluorescent systems for use in diagnostics, imaging, therapy, etc. However, it is necessary to conduct more experiments and to optimise the process. For instance, the SEM pictures

displayed large particles often with form of empty half spheres analogous to the VTEOS cups in Chapter 4 and imposes a change of VTEOS solution. The initial aggregation of iron oxide and the related instability are a problem and require a change of synthesis procedure (beyond the scope of this thesis). The fluorescence property and particle homogeneity (in terms of dye content) must be assessed. Overall, the experiments presented in this chapter must be taken as the first steps in the design of iron oxide-silica nanoparticles and a testing of the feasibility of the amino acid route to coat the magnetic particles and of the hybrid silica coating to enhance the fluorophore carriage capacity of the nanocomposites.

6.4.3 Multifunctional particles

The next evolution step towards the multifunctional systems consisted in coating the iron oxide-silica nanocomposite with a gold layer. The first step required the decoration of the fluorescent magnetic particles with gold seeds via deposition-precipitation. The initial experiments were unsuccessful and, although the plasmonic response was detected in a few samples, no pattern arose that could explain how the gold concentration and time affects the coverage. The solution came by increasing the reaction time from 60 minutes up to 4 hours where visual changes evidenced that the precipitation occurred. The process is still not well controlled and some samples needed less than 60 minutes to be covered with gold, perhaps because of a higher amine density onto the particles, or the thinness of the silica layer. Nevertheless, the apparition of a plasmon resonance peak (at 520 to 550 nm) may not be desirable: such signal mainly originates from gold clusters that handicap the nucleation of gold ions onto the small and result in heterogeneous gold layer [*Kah, 2008; Park, 2006 b*]. Therefore, measuring the absorption of the particles during the deposition-precipitation in order to stop the process before the resonance peak emerges may be required for a homogeneous gold coating.

Sodium borohydride and formaldehyde were found too strong and favoured the growth of pure gold particles to the detriment of the nucleation of gold onto the

seeds. The critical point in the formation of gold shell is that the rate of Au^{3+} reduction onto metallic surface must be greater than the rate of new particles nucleation [*Brown, 2000*]. Because of the reducing strength of the two compounds, the later is favoured and new particles nucleated instead of the reduction of gold ions onto the nanoparticles. For this reason, the plasmon resonance of the final nanocomposite did not differ much from that of the gold-decorated particles with either the apparition of the plasmonic phenomenon or a broadening of the plasmon band. Variation over the type of reducer and concentrations did not affect the optical properties of the multifunctional particles and the same response was obtained at all time. Hydroxylamine induced the same minor changes and it was also observed that the reduction of gold on magnetite-silica was achieved in absence of deposition-precipitation. A potential mechanism is the formation of small gold particles by the action of the reducing agents that were able to bind to the amine groups of the composites due to the good affinity of gold surface for this organic group. Although a strong resonance occurred, the changes are mainly the action of gold clusters and not that of a homogeneous layer. However, hydroxylamine is known to favour the reduction of gold ions on metallic surfaces metallic surface of the nucleation of discrete particles [*Brown, 1998 and 2000*] but the experiments in this chapter, be they with silica or nanocomposites, showed that pure gold particles were grown over time nonetheless. Therefore, the presence of gold onto the magnetic-silica particles may be the result of another mechanism that has yet to be elucidated.

Instead of applying a simple seed mediated regrowth, a different approach called iterative hydroxylamine seeding was tested. The method is suitable for the growth of homogeneous gold particles over 60 nm – technically difficult otherwise – and consists in applying hydroxylamine in multiple step to enlarge the particles step-by-step [*Brown, 2000*]. The principle is extendable to the growth of metallic shell so long as the surface already contains gold seeds. The method is very effective with magnetic particles as the nanomaterials are easily and quickly retrieved and suspended in gold platting without need of centrifugation or other complex procedure. By this mean, it was possible to red-

shift the plasmon resonance of the nanocomposite and reached 650 to 700 nm after 2 to 5 iterations. Two cases must be considered: when the samples exhibited a strong plasmon resonance after the deposition-precipitation, the final maximal resonance wavelength was not able to overpass 600 nm. Although the plasmon band spanned a larger region including part of the NIR region, the spectra are not that expected from smooth, homogeneous gold layer. In comparison, absence of original plasmon resonance led to a widening of the plasmon band followed by a distortion and a red-shift of the plasmon resonance as expected from a nanoshell. Salgueirino-Maceira designed similar multifunctional particles and the optical absorption of the particles passed through similar stages [*Salgueirino-Maceira, 2006; Zhang, 2010 b*]. In the case of inhomogeneous layer, the plasmon band was even broader and composed of multiple maxima that are the high order resonance contributions (mainly quadrupole) from clusters and particles of various dimensions [*Brinson, 2008; Graf, 2002*].

The works based on iterative hydroxylamine seeding applied more iterations than what was tested in this chapter (up to 18 in certain case), therefore continuing the regrowth might lead to full homogeneous layer. Nevertheless, it seems more plausible that the success or failure to tune the plasmon resonance is linked to the gold coverage and the deposition of gold-seed has been identified as the crucial step. The growth of a metallic layer is possible without the presence of silica between the two materials (although magnetite must be oxidised into maghemite for the gold to attach) but the response is similar to most of what has been obtained with deposition-precipitation and the impossibility to red-shift the resonance wavelength [*Lyon, 2004; Larson, 2007*]. Switching to a layer-by-layer self assembly technique where the particles surface is covered by polyelectrolyte may be an option and proved efficient to cover nanoparticles surface with a dense and homogeneous layer of gold nanoparticles [*Liang, 2003; Wang, 2008; Zhai, 2009*].

6.5 Conclusion

Two methods, the deposition-precipitation and amino acid route, were explored to design multifunctional nanoparticles incorporating simultaneously iron oxide, (fluorescent) silica, and gold. The former is a recent method that can coat a material with small gold seeds but remains ill-explored. The latter method has never been used to coat iron oxide (and other materials) nanoparticles. Therefore the aim of this chapter was to explore the feasibility to create nanocomposites by combining these two strategies.

The deposition-precipitation led to contrasted results: one the one hand, this method proved very efficient at coating the surface of the hybrid nanoparticles with small gold seeds, imparting at the same time plasmonic resonance. One the other hand, controlling the seed size and density proved difficult which prevented from creating homogeneous gold nanoshells and by extension it was not possible to design iron oxide-silica-gold nanocomposites. In other words, it has been shown that the deposition-precipitation could be applied on the hybrid particles but optimisation is required, notably a systematic SEM/TEM study to follow the influence of the various parameters on the gold seed morphology and density.

The synthesis of iron oxide-silica particles showed for the first time that the amino acid catalysis is suitable for coating magnetic nanoparticles with silica and hybrid silica. The results presented in this thesis suggest that the amino acid route can create a very thin silica layer, which can be an advantage over the Stöber method that is known to create thick layer encapsulating multiple iron oxide particles into a single structure. The coating with hybrid silica was also tested and the final magnetic-fluorescent composites were able to carry indifferently fluorescein, lucifer yellow, and rhodamine B. However, similarly to the deposition-precipitation, the procedure must be refined because some uncertainties still hang over. For instance, it is necessary to control the silica thickness (via SEM/TEM characterisation), verifying the particle morphology (problem of cup-shape particle), and assessing the optical properties of the

magnetico-fluorescent nanostructure (dye content of individual particles in particular, as discussed in the previous chapter).

Chapter 7

Final discussion

7 Final discussion

The aim of this thesis was to develop an alternative, more flexible method for the synthesis of fluorescent silica and multifunctional nanoparticles. The amino acid route that underlies the whole process was first tested to develop a multifluorescent structure (Chapter 3) and then used for the design of a TEOS-VTEOS hybrid structure (Chapter 4). The hybrid structure acted as a scaffold for the incorporation of a variety of fluorophores in order to fill a gap in the development of FSNPs (Chapter 5) and played a key role in the combination of nanomaterials into a Fe_3O_4-SiO_2-Au nanocomposite (Chapter 6).

Nanotechnology has the potential to impact on medicine and the biomedical field through three features: the new properties of nanomaterials, the surface engineering of nanoparticles, and the reduced scale of nanostructures comparable to biological species such as proteins. Classes of nanomaterials may be divided into particles with intrinsic properties such as iron oxide, gold, or quantum dots, and particles devoted to the carriage of molecules such as silica, dendrimers, etc.

Polymers and liposomes were among the first nanocarriers devised for the delivery of drugs and biomolecules in general but some compounds such as fluorescent dyes are best kept contained within the particles. Organic materials are known to break, degrade, or lose their integrity (swelling) when changing solvent or under basic/acid conditions. In that respect, silica nanoparticles offer certain advantages over polymers: ceramic nanoparticles are more robust and usually insensitive to changes of pH, temperature, and other environmental parameters. Furthermore, the silica matrix insulates its cargo and the whole effect can be modulated by controlling the porosity. Finally, the silica chemistry is highly versatile and allows for easy modification of the particle core or of its surface via use of organosilanes.

Silica is typically processed by sol-gel reactions and the formation of particles occurs when hydrolysis and condensation are catalysed by bases. The work of Stöber and Fink was the first thorough investigation of the parameters regulating the dimensions of silica particles [*Stöber, 1968*]. The procedure is fairly simple and only requires the mixing of silicon precursors, water, and ammonium hydroxide in an alcoholic environment. Yet, the particle dimension span the submicrometric and micrometric ranges which are not suited for all applications and do not strictly fall in the nanotechnology definition (as define by the NNI). Although reducing the particle dimension is possible by controlling the reagent concentration, the task of synthesising spheres smaller than 100 nm is typically allotted to reverse microemulsion. The particle growth is confined within micelles and ensures a high monodispersity of the samples. At the same time, the necessity to create an emulsion – implying the use of harsh organic solvent – and the long purification of the particles required to remove any trace of surfactant are limiting factors [*Osseo-Asare, 1990*].

Other factors arise during the incorporation of fluorescent dye: van Blaaderen modified the Stöber method, co-condensing sylilated fluorophores (FITC and RITC) with TEOS to produce bright particles; the hydrophobicity of most organic dyes hinders their incorporation into the growing nanoparticles by their inability to enter within the micelles [*van Blaaderen, 1992 c; Tan, 2004*]. In the end, fluorescent particles reported in the literature are limited almost exclusively to chemically-modified dyes and lanthanide chelates. Alternatively, the use of oil-in-water emulsions managed to take advantage of the hydrophobicity of organic fluorophores by ensuring that both silicon precursors and dyes are located in the same phase so that the final particles contain the fluorescent molecules. This method has been successful for the incorporation of near-infrared and two photon dyes as well as photosensitisers but still faces the long purification procedure and risk of remnant surfactant molecule adsorption [*Roy, 2003; Ohulchanskyy 2007 and 2010*]. Chapter 2 highlighted the ease of producing silica and fluorescent silica particles via the Stöber procedure and van

Blaaderen's alteration as well as the obstacle to the loading of common organic dye encountered with the reverse microemulsion approach and helped in identifying the current limitation of the FSNPs technology.

The apparent lack of fluorophore variety is not necessarily an issue: many groups such as van Blaaderen's, Wiesner's, Tan's, or Prasad's have established the strength of silica nanoparticles in cellular imaging, photodynamic therapy as well as in the tracking of particles in mice. All have perfected the Stöber and reverse and oil-in-water emulsions to the point of providing solutions to some of their initial limitations. For instance, C-dots are 20 nm FSNPs produced without recourse to emulsion but work only with sylilated fluorophores [*Burns, 2009; Ha, 2009, Zhao, 2004 b*]. Yet, two major gaps still exist and impede the progress of FSNPs: first of all emulsions remain the principal technique for the synthesis of small particles and ought to be substituted by cleaner methods. Secondly, the limited variety of fluorophores found in the literature does not make honour to the whole range of possibilities that dyes offer, be it in terms of luminescence or other physico-chemical properties.

A typical example is the near-absence of particles containing two dyes or more: Wang's FRET system is the only significant contribution to the field of multifluorescent particles: the system relied on the use of FITC and maleimide-derivatives of rhodamines co-condensed at a precise ratio to tune the fluorescence pattern of the nanoparticles [*Wang, 2006*]. By this means, Wang and co-workers demonstrated how the fluorophores can generate separate emissions or on the contrary how one dye can act as secondary excitation source by transfer of energy (FRET). Furthermore, they used a different set of FRET nanoparticles to label and simultaneously image four bacterial populations [*Wang, 2007 a*]. A few other studies have developed nanoparticles containing two dyes via the co-condensation of sylilated fluorophores or the combination of two lanthanide chelates but at present, Wang's particles are the only example of a system containing more than two dyes [*Nakamura, 2007; Xu,*

2010]. Yet, multifluorescent particles are necessary for multiplexed analyses where multiple analytes must be detected in a single sample but must meet three requirements:

- The variety of fluorophores must be broad enough to afford a large number of permutations;
- The dyes must cover the largest spectral region possible, from UV to infrared;
- The particles must potentially be small enough for the detection of minute amounts of analyte.

Even though silica nanoparticles are in theory able to contain virtually any dye by selecting the appropriate synthesis procedure, the encapsulation of two or more fluorophopores may become more challenging. For example combining a hydrophobic and a hydrophilic fluorophore requires first an oil-in-water emulsion followed by the purification of the particles and their suspension into a reverse microemulsion in view of incorporating the second dye. There is a lack of an easy and universal method that would enable the entrapment of the two dyes without having recourse to tedious or complex protocols such as emulsion or chemical modification of the fluorophores.

Yokoi and Davis have elaborated an alternative synthesis route involving lysine to catalyse the sol-gel reactions and their work was completed by Hartlen's study of the production of silica nanoparticles via arginine catalysis [*Davis, 2006; Hartlen, 2008; Yokoi, 2006*]. The amino acid route provides a solution to the size issue by producing very small seeds while the whole process is easier, cleaner, and more environmentally friendly than emulsions. The particularities of the amino acid route lies in the absence of organic and alcoholic solvents in favour of water and the substitution of the strong ammonium hydroxide by lysine or arginine. The milder conditions are such that the two amino acids are basic enough to direct the sol-gel reactions towards the creation of colloids while

limiting the particles sizes to a few tens of nanometres. In addition, the surface of silica nanoparticles expresses silanol groups Si-OH as well as unreacted alkoxide groups Si-OC_2H_5. The same silanol groups are at the heart of the sol-gel reactions and make the surface reactive to the introduction of more silicon precursors. For example, Hartlen proved that the initial small seeds could be enlarged by addition of more TEOS in an arginine environment or via a typical Stöber reaction in a process called seed regrowth [*Hartlen, 2008*].

From the seed regrowth approach germinated the idea of designing a core-shell structure where each compartment contains a specific fluorescent molecule resulting in the production of a multifluorescent nanoplatform. The particles were built up by iterative addition of TEOS and the addition of three dyes, each of them added at a separate step to integrate them in different layers. Each fluorophore highlighted a specific aspect: FITC was coupled to APTES for covalent binding to the silica network and R6G exemplified the electrostatic interaction with the matrix. The role of MB was different as it is commonly employed in staining procedures and is likely to be found in many laboratories. The choice of MB underpins the idea that silica nanoparticles ought to easily incorporate any fluorescent dye present in a laboratory and not exclusively isothiocyanate and maleimide derivatives or lanthanide chelates. FITC and R6G were both entrapped during the particle formation and generated a strong fluorescence signal whilst MB was also detected but did not fluoresce. It turned out that MB is a weak fluorophore but is a potential photosensitiser, i.e. the molecules potentially convert the light energy into radical species. In other terms, the structure designed in chapter 3 is a potential theranostic agent suitable for imaging and photodynamic therapy. The generation of singlet oxygen was not tested, albeit this capacity may be assessed via the use of an oxygen sensitive fluorophore [*He, 2009 b*]. The fact that the blue dye was added in the first layer raises the question of whether singlet oxygen would be able to diffuse away from the particles and if the radical species degrade the other dyes in their way.

The particles were not larger than 20 to 30 nm yet the seeds were based on Hartlen's protocol which supposedly produces 20 nm particles and the amount of TEOS added at each step was calculated to increase the diameter by about 10 nm based on a 20 nm seed hypothesis. Considering the very small amount of seed produced, it is not known whether the synthesis yield is small or requires more time for the particles to fully nucleate. However, the particle concentration steadily built up after each step to reach several micrograms at the end of the procedure. The reduced dimensions were not detrimental for the optical properties of the particles and each suspension exhibited very strong colour in accordance with the fluorophores they contained. Moreover, the fluorescence emission of the samples containing R6G and FITC displayed two maxima corresponding to each fluorophore and suggest that the combination of several dyes may help in tuning the emission pattern of the silica nanoparticles [*Wang, 2006; Xu, 2010*]. In summary, the system developed in the chapter 4 is an alternative way to produce multifluorescent nanoparticles in a simple way and suitable for the entrapment of some common fluorescent dyes and stains via electrostatic interactions and/or covalent binding while restricting the nanoparticles diameter below 50 nm.

The objective of designing small and fluorescent particles was achieved and their capacities as a contrast agent for imaging ought to be investigated. Two cell lines were selected prostate adenocarcinoma cell line (PC3) and its corresponding normal transferred line (PNT1A). The two cell-lines are well-characterised and their different state would be a first indicator of a possible cell-dependency of particle uptake, especially since cancerous cells are said to eagerly take up nanoparticles [*Trewyn, 2008*]. Many *in vitro* studies are based on lung epithelial cell lines, macrophages, or cancer cell lines. The choice of lung-related lines is motivated by the traditional assessment of particles where anthropogenic particles are inhaled and potentially interfere with the lungs. However, the inhalation of engineered nanoparticles is not automatic and many nanomaterials are synthesised under the form of hydro-colloids which thereby

limits the risk of inhalation. Furthermore, the entry routes are different for particles with biological applications and the nanoparticles would in all likelihood interact with other cells and tissues during their time in the organism before macrophages clear them from the blood stream and direct them in the spleen and liver, potentially in the lymph nodes and a few other organs when the nanostructures are small enough [*Vonarbourg, 2006*]. The complicating factor lies in the different cellular response towards the presence of nanoparticles: it has been shown that certain nanomaterials may not be toxic for epithelial cells but induce deleterious effects on other cells because the metabolism of each cell type is different [*Rabolli, 2010*]. Finally, surface engineering of nanoparticles reduces the chance of interactions with unwanted cells when in the organism, although macrophages recognition and clearance will eventually occur. Many systems aim at targeting cancerous cells via the conjugation with peptides, antibodies, carbohydrates, or biopolymers recognised by specific receptors overexpressed in cancerous cells. Here, PC3 cells are known to overexpress CD44 receptors that can be targeted by hyaluronic acid as discussed below [*Ossipov, 2010; Platt, 2006*].

The qualitative assessment of PC3 and PNT1A labelling with the multifluorescent nanoparticles was performed by confocal microscopy and showed two situations. In the PNT1A case, the uptake was considerably limited and only a few small particles were detected. In contrast, PC3 took up large amount of particles that formed aggregate within the cells. These findings highlight the difference that may exists between related cell lines and the impossibility to predict how a cell line will respond to nanoparticles. The result also raised questions about the intracellular fate of the particles: the fact that “primary” particles were localised in PNT1A whereas the same samples led to large aggregates in PC3 suggests that the cancerous cells may have gathered the particles into a specific region of the cytoplasm. The intracellular fate of nanoparticles is not well-characterised yet at the difference of the endocytosis pathways. In one occurrence, it was mentioned that particles were exocytosed in one region of the cells instead of throughout the whole membrane, which may be consistent with the evidence here [*Panyam, 2003*]. It is likely that the

particles remained encased within vesicles throughout the whole internalisation as escaping vesicles requires either the modification with evading peptides or the degradation of the particles and this encasement might explain how all of the particles are eventually gathered in the same region [*Nativo, 2008*].

The strong optical properties of the nanoparticles helped in their easy tracking within the cells. The emission of many fluorophores and cellular stains lies in the 500 to 600 nm range and due to a strong overlapping it becomes increasingly difficult to distinguish each fluorophore as their number augments. For instance, FITC, acridine orange, and sytox green emission are separated by 5 to 10 nm so that their identification is only possible via the difference of intensity when entrapped within silica nanoparticles or via the META detector for FITC and sytox green. Similarly, the signal from R6G was masked by that of AF555 although the META module would have easily deconvoluted the emission of the two dyes. The FITC-R6G-doped particles did not suffer from this limitation as the two fluorophores appeared in different channels and their signals were overlayed to produce a distinct colour. Coupled to the META detector, more two colours-coded populations of particles could be employed at the same time and clearly be distinguished, opening the field of multiplexed imaging. At another level, the robustness of the silica and the total dye insulation render the FSNPs photostable, allowing imaging for an extended period of time. This feature may be put into use for tracking in real-time the endocytosis, intracellular fate, and exocytosis of the particles.

The work reported in chapter 3 was only a first step in the cell labelling and opened new research possibilities. First of all, it is necessary to couple the evidence obtained by confocal microscopy to flow cytometry to quantitatively assess the labelling of PC3 and of PNT1A and prove the difference in uptake. In the same vein, it is necessary to assess the cellular response to the presence of nanoparticles via viability and apoptosis/necrosis assays as well as measuring the degree of oxidative stress and the generation of radical species within the cells. Lastly, the potential of the multifluorescent nanoparticles has yet to be investigated, notably via the coupling with appropriate ligands to target either

organelles or specific cell types for multiplexing analyses. Another point of interest is to investigate the effect of the particle surface as results produced during an MSC project showed a clear difference with a viability assay between bare FITC-doped particles produce by reverse microemulsion and the same particles modified with APTES [*Traver, 2010*].

Despite the flexibility and ease of production of the multifluorescent nanoparticles, the matrix remains composed of silica exclusively and is not ideal for certain organic dyes. One hypothesis was that the affinity of hydrophobic dyes – among others - for the inorganic matrix would not be strong enough and the particles would fail to contain such dyes. Therefore, a modification of the particles composition was tried to favour the stabilisation of the fluorescent molecules in the growing nanoparticles. Silica is ideal for this strategy due to the large number of silicon precursors commercially available and is already employed for the creation of ORMOSIL structures (organically modified silica) such as xerogel or simply to solubilise the silicon precursors in the oil phase of oil-in-water emulsions [*Li, 1992; Qian, 2009*]. This role is often devoted to vinyltriethoxysilane (VTEOS) that possess a hydrophobic vinyl moiety and this silicon precursor appeared as an interesting candidate for the modification of the silica matrix [*Law, 2008; Sharma, 2004*]. The procedure was kept similar to the multifluorescent particles and VTEOS was introduced simultaneously to TEOS and co-condensed to form nanoparticles.

The hybrid colloids displayed certain differences from TEOS-made particles:

- The seed diameter increases with the proportion of VTEOS and ranges from 10 nm at 25 molar% to 110 nm at 75 % and pure VTEOS particles are in the submicrometer rather than in the nanometer range;
- More material was recovered compared to TEOS particles;
- VT-50 consistently produced particles 40 to 50 nm in diameter;

- A change of the silane/arginine/water molar ratio does not induce large variation of the particle diameter in the VT-50 case.

Most ORMOSIL nanoparticles are obtained by mean of microemulsion, which automatically restricts their size to the tens of nanometre. Conversely, Dirè investigated the co-condensation of organosilane with short and long alkane chain moieties as well as amine, vinyl, and phenyl groups via the Stöber method, which yielded particles ranging from 100 to 1 µm according to the silane and the composition [*Dire, 2011*]. PhTEOS-TEOS systems have also been investigated and are known to create large particles of high hydrophobicity [*Bagwe, 2002; Theaker, 2008*]. Here, the PhTEOS hybrids were no more than 50 nm or lower according to the PhTEOS/TEOS ratio but a strong hydrophobicity was noted even at low ratio. Other hybrids such as THPMP-TEOS and TEOS-APTES were also small although the APTES hybrid was subject to a strong aggregation. Therefore, the amino acid route is suitable for the design of ORMOSILs and restrains the growth of particles to a few tens of nanometer without requiring any alteration of the synthesis procedure.

The change of diameter in comparison to the small TEOS seeds may originate from repulsive interactions between silica and the vinyl moieties that may distort the matrix and/or create larger pores than in silica nanoparticles. Although infrared spectroscopy proved that the vinyl moiety had been integrated to the silica matrix, the actual morphology of the particles remains unknown. The organosilane hydrolysis rate is different from that of TEOS and it influences their condensation. The difference of rate may lead to heterogeneous structures where the core is made of VTEOS or of TEOS and covered by a layer made of the second silane. For instance, Wang's initial attempts to create the FRET systems led to low FRET efficiency because each sylilated dye create a layer of its own [*Wang, 2006*]. The fact that the VTEOS particles were not hydrophobic – although a secondary hydrophobic population was detected in small quantity during the centrifugation step at high VTEOS concentration – discard the possibility that VTEOS creates an outer layer onto the TEOS seeds. In contrast, the hydrophobicity of PhTEOS at moderate PhTEOS/TEOS molar ratio

indicates that the organosilane may form an outer layer because of a slower hydrolysis rate. Ideally, VTEOS may form the core of the seeds and become protected by a hydrophilic layer made of TEOS. Such structure would be perfect for the embedding of hydrophobic dyes: due to the aqueous environment, the generation of hydrophobic seeds would provide a friendly environment for the fluorophores that would accumulate in the VTEOS core [*Deng, 20*06]. Next, TEOS would cover the seeds and protect the hydrophobic compounds, all without modifying the experimental conditions [*Rampazzo, 2007*]. In all likelihood, the hydrolysis rate of TEOS and VTEOS are similar and both precursors homogeneously condense during the seed nucleation. There may be two solutions to shed the light on the particles morphology: firstly, the nucleation and growth of particles can be followed by small angle x-ray scattering (SAXS) to determine the particle formation kinetics [*Yokoi, 2009*], but it is uncertain whether the technique can distinguish the organosilane contribution in the seeds. The second option consists in using ^{29}Si NMR and ^{1}H NMR in order to assess the composition of the seeds over time and whether the two silicon precursors are initially present in the seeds or if they enter at different stages of the particle growth.

It was only possible to determine the particles diameters at different arginine/arginine/water molar ratios using DLS but this technique gives an approximation and cannot provide an actual value as soon as the particles cluster. However, the hydrodynamic and “number” diameters did not exceed 100 nm, most likely due to the pH of 10 and the adsorption of arginine molecule that limit the particle growth. The principal issue was related to the unusual shape of the particles (submicrometric half-spheres with empty core). These shapes were not observed at all with the first organosilane solution but it is not certain that VTEOS is responsible for this phenomenon. The shape in itself is interesting and not necessarily a drawback: for example gold nanocages and nanostars exhibit new plasmonic behaviours whereas simulations have showed that shapes other than spheres and rods may have faster and optimal cellular uptake [*Champion, 2007; Gratton, 2008*]. At present, it is unknown whether these new particles may be of interest and the “cup-shaped” particles require

more investigation, firstly to reduce their dimensions, and secondly to probe their carriage capacities and functionalisation.

The first objective was partially fulfilled: it was demonstrated that the amino acid route is an easy way to synthesise ORMOSILs structures with better control over the particle dimensions than that reported with the Stöber method and without need for extensive purification. However, the mechanisms that led to the creation of the large and oddly shaped VTEOS particles are still obscure, although such changes were not observed with the other hybrid structures.

With the new hybrid particles developed, the next stage was to investigate their capacity to entrap fluorescent dyes by using a larger variety of fluorophores than commonly found in the literature. Increasing the number of fluorescent dyes adds more flexibility to the fluorescent silica nanoparticles in terms of excitation choice, but also in terms of combination into multifluorescent nanoparticles. More importantly, the nanoparticles could be used for other application than imaging (luminescence) such as photodynamic therapy (cf methylene blue) but also in sensing since the emission of certain fluorophores may be modified by a change of pH or temperature or react to the presence of oxygen, ions, or other species. The coupling of sensing dyes into a single matrix has been proposed via the PEBBLE structure which is based on ratiometric measurements, i.e. the sensing dye fluorescence intensity is brought back to that of a reference dye, which implies that such structure must contain at least two fluorophores [*Burns, 2006; Gao, 2011, Peng, 2010*]

As mentioned, few fluorophores have been investigated as van Blaaderen's procedure and the sylilation of dye is favoured. Yet, Theaker and co-workers used a PhTEOS-TEOS hybrid in order to embed a larger choice of dyes and stains used in forensic analyses (fingerprints) but not all dyes were entrapped. Likewise, of the ten fluorophores tested for this thesis, half were not encapsulated during the particle growth. The mixed results meant that the VTEOS-TEOS structure as such is not a universal carrier and could not contain

the hydrophobic fluorescein, oregon green, and lucifer yellow. Where the reverse microemulsion was unable to contain RB, R6G, and R6G – or more precisely led to poorly fluorescent particles – the VT-50 produced very bright particles in the range 40 to 50 nm with an excellent repeatability and smaller than the RB-doped particles obtained by the Stöber method. However, it was impossible to compare the hybrid particles with the typical silica particles obtained by the amino acid route because of the low particle density of the latter. The problem of fluorophore leakage is occasionally raised for the electrostatic entrapment of dyes but there is no strong evidence of such phenomenon in the literature and many groups noticed the absence of dye diffusion over long periods of time [*Estevez, 2009; He, 2009 b; Santra, 2006*] and leak tests in chapter 5 did not detect any diffusion of the dyes away from the matrix.

Based on a process similar to that developed for the multifluorescent nanoparticles, the hybrid seeds were enlarged by successive TEOS additions to form multi-layered structures. Each layer contained a different dye among AO, R6G, and RB; combined at different ratios in order to tune the spectral signature of the particles. By this means, the nanoparticles were able to emit light at long wavelength with high intensity by exciting the whole particles with the AO excitation whereas the excitation of R6G and RB only at the same wavelength is ordinary weak. The close proximity of AO and R6G had for principal effect a broadening of the emission band whereas combination of AO and RB produced patterns with two maxima, with relative intensity depending on the initial dye concentrations. The excitation and emission of the three dyes were too close to efficiently impart a distinctive signature and the whole system is not as efficient as Wang's and would require a third dye emitting at longer wavelength than RB [*Wang, 2006*].

The fact that the first and second dyes were present in multiple layers was initially believed to be a weakness and a lack of control exerted over the particle optical properties. However, the mix of dye in a same layer may help in promoting FRET. This effect is distance-dependent and quickly diminishes

when the distance between donor and acceptor augments but the presence of the two dyes in the same layers increased the chance of energy transfer. The opposite effects arise if the fluorophores are too close, in which case quenching occurs. In fact, of the major drawbacks of the experiments carried out in this thesis is the initial high concentration of dyes: most of the fluorophores remained in the supernatant and were discarded during the centrifugation step, undesirable for expensive dyes. On the other hand, the saturation of the silica matrix led to dimmer signal which usually causes a loss of intensity and emissions at lower wavelength, lost by nonradiative pathways or caused by quenching in non-fluorescent aggregates [*Anedda, 2007; Del Monte, 2000; Severino, 2003*]. Therefore, there is a need for both controlling the minimal dye concentration to avoid unnecessary losses and experiments showed that reducing 2 to 5 times the dye concentration led to particles with sufficient brightness.

The hybrid composition was modified as an answer to the failure to certain dyes incorporation. Theaker hypothesised that the dyes remained restrain within the particles by the combined action of steric hindrance and electrostatic interaction with the large and electron dense phenyl group [*Theaker, 2006*]. Certain studies such as that of Theaker and other teams focused on the co-condensation of TEOS and phenyltriethoxysilane (PhTEOS) for the encapsulation of dyes such as R6G or fluorescent dyes and stains of help in forensics [*Theaker, 2008*]. The hybrid structure had high fluorescence intensity and photostability but the very large and the hydrophobic nature of the particles quickly arose as the proportion of PhTEOS increased [*Bagwe, 2002*]. The same effect was noticed when PhTEOS substituted VTEOS and the particles became very hydrophobic at a molar ratio of 50% whereas no advantage was noticed in terms of dye entrapment. More importantly, where the particle size increased as the proportion of VTEOS increased no clear trends were noted but more experiments may be necessary to investigate this hybrid system. The solution arose from the addition of APTES to the hybrid structure: it was noted that the

use of this organosilane tended to augment the size of the particles and was noted by other groups as well [*Dire, 2011*], yet the presence of amine played a role in the stabilisation of fluorescein, lucifer yellow, and oregon green that were eventually included inside the silica matrix. The idea came from the comparison of the dye chemical structure and the three dyes all bore a negative charge and are consequently repulsed by the negatively charged silica matrix. The incorporation of amine creates regions of positive charges within the network and facilitates the stabilisation of the fluorophores and more brightness was obtained by increasing the APTES proportion.

In summary, the hybrid nanoparticles offer an easier alternative to the synthesis of FSNPs and were able to embed some bright fluorescent dyes such as rhodamine B and 6G. The dyes were restrained by electrostatic interactions, admittedly not as efficient as the covalent binding of van Blaaderen's method, but enough to partially tune the spectral signature of the nanoparticles. It may be interesting, though, to transpose van Blaaderen's protocol to the amino acid route in order to verify if the FSNPs get smaller. If the hypothesis of correlating the choice of organosilane with the fluorophore charge proves correct, the hybrid particles may virtually be able to contain any dye by simply selected the appropriate precursor while maintaining the exact same procedure. At present, two points still have to be investigated: the actual effect of the organosilane – in particular APTES - on the particle diameter could not be assessed because of the formation of cup-shaped particles. Similarly, the potential aggregation induced by APTES might be attenuated by the choice of a different amino-silane or by a positively charged silane unable to create hydrogen bonds with the silanol groups. The second point consists in translating the process to the growth of additional layer in order not to restrict the localisation of specific dyes into the hybrid core and add more flexibility with the aim of combining sensor dyes such as rhodamine B, fluorescein, or oregon green.

Finally, silica was used as a common matrix for the combination of iron oxide, gold, and/or fluorescent dyes in order to design multifunctional nanoparticles.

The objective was to develop a modular structure where each component may be positioned according to the use but it was not possible to coat gold particles with enough precision or to cover the surface of silica nanoparticles with iron oxide. Therefore, the final chapter aimed at designing a magnetite-silica-gold structure where the initial magnetic core helped in manipulating the particles throughout the whole process.

Gold is one of the most versatile nanomaterials for imaging, therapy and/or diagnostics but also for the creation of synergistic effects such as metal-enhanced fluorescence. For instance, gold nanoshells can be used in combined NIR imaging and photothermal therapy but also enter in the composition of immunoassays [*Hirsch, 2003 a and b*]. The formation of gold nanoshells is well-documented and typically requires the synthesis of small gold seeds that are then adsorbed onto a dielectric core such as silica followed by the reduction of gold ions to progressively form a homogeneous layer [*Oldenburg, 1998*]. The method is powerful but there exists the chance of seed desorption that could compromise the layer growth and/or adherence. Kah demonstrated that gold nanoshells can be produced without having recourse to the synthesis of gold seeds but instead by inducing their formation in situ onto the particles surface, suppressing at the same time the risk of desorption [*Kah, 2008*]. A part of the final chapter aimed at controlling the deposition-precipitation method in order to decorate the hybrid particles with gold seeds and to further create a full metallic layer. With this technique, the hybrid silica nanoparticles acquired plasmonic properties due to the decoration with small gold nanoparticles and the plasmon response depended on the gold ion concentration and reaction duration. In particular, the longer the reaction, the more clusters on the surface. It was found that the presence of clusters is detrimental for the creation of a uniform gold layer by promoting the growth in three-dimensions of the clusters rather than creating a smooth layer.

Like gold, iron oxide is a key material in nanomedicine and is often integrated into nanocomposites and multifunctional systems because of its manipulation with a magnet. There is a strong need for magnetic-fluorescent nanoparticles in

diagnostics where nanoparticles are able to detect analytes and to retrieve them by magnetic separation [*Mistlberger, 2010 a*]. Magnetic nanoparticles are frequently combined with quantum dots or fluorescent dyes but usually one type at a time which limits the potential for multiplexed analyses [*Hu, 2011; Wang, 2010*]. There exist two issues when synthesising magnetic-silica nanocomposites: first of all, the Stöber method employed to grow the silica layer produces relatively thick particles and generally entraps a random number of magnetite nanoparticles [*Claesson, 2005*]. Secondly, the magnetic properties of SPIO and USPIO, i.e. saturation magnetisation, are moderate but decrease with the presence of silica. Reverse microemulsion is a solution to make sure that each silica particle contains a single magnetic core but the amino acid route may provide a better and more flexible solution to the first issue by growing very thin layer of silica that reduces the chance of co-encapsulation of magnetite [*Narita, 2009*]. The second issue may be overcome by controlled aggregation of the iron oxide nanoparticles followed by the encapsulation of the resulting clusters into silica [*Larsen, 2008; Wan, 2010*]. Alternatively, the surface of silica may be decorated with iron oxide but the approach is not satisfactory for magnetic luminescent structures as the magnetic particles screen the fluorescence, unless a new layer of fluorescent silica is grown onto the structure. Chapter 6 reported for the first time the use of the amino acid route to coat iron oxide with silica and the first results seem to indicate that the layers are naturally thin. Furthermore, the protocol developed for the synthesis of hybrid nanoparticles was directly transposable and easily gave birth to multifluorescent magnetic nanoparticles containing two dyes and can be extended to more fluorophores. This new approach has the potential to enhance the magnetic luminescent particle potential by providing more flexibility to the structure and by multiplying their applications.

The second step consisting in engineering magnetoplasmonic structures was more contrasted: on the one hand, the deposition-precipitation worked well the iron oxide-silica structure were decorated with gold seeds and clusters, achieving the first stage towards a full multifunctional platform. However, it was here again impossible to obtain a smooth and homogeneous metallic shell

because of the presence of gold clusters. Instead, the plasmon resonance of the “magnetoplasmonic” nanoparticles was red-shifted up to 700 nm via the iterative hydroxylamine seeding. Direct coating of iron oxide with gold does not allow a modification of the plasmon resonance frequency more than a few tens of nm and rarely by-pass 600 nm [*Larson, 2007*]. The presence of silica is indispensable to red-shift the nanoparticles as the structure becomes similar to silica-gold nanoshell and the effect may be linked to the silica thickness. Shifting the plasmon resonance was only possible when the reduction of gold ions proceeded in several stages though iterative seeding.

One important point remains to be elucidated: the deposition-precipitation was originally developed by Haruta for catalytic purpose. The high specific surface and reactivity of small nanoparticles has a central role in “nanocatalysis” and gold seeds were initially used for the oxidation of amines and halogenated compounds, combustion of carbon monoxide and reduction of nitrogen oxides [*Haruta, 1997*]. Therefore, it is unknown how the multifunctional particles with incomplete gold shells or decorated with gold seeds would interact with the cell membrane. It is possible that, due to their reactivity, the gold seeds induces the oxidation of lipids or could play a role in damaging the plasma membrane. At the same time, the presence of clusters may reduce this effect but there are chances that such an incomplete structure may induce toxic effects. On the other hand, the close proximity of the clusters may create a resonance phenomenon between each aggregate and amplify the plasmonic response, in which case the decoration with gold may give rise to a powerful Raman spectroscopy probe.

One of the aims was to develop a modular platform, i.e. a structure where gold, silica, and iron oxide could be permuted at will to create any morphology (for instance gold-silica-iron oxide or iron oxide-gold-silica, etc.). The amino acid route would in theory grow very thin layer of silica, which would be ideal to position fluorophores at a distance where their emission or excitation could be amplified by the plasmon resonance of the metallic surface in their vicinity. In the same vein, the objective of synthesising gold nanoshells failed. However,

part of the chapter 6 was dedicated to the testing of the deposition-precipitation and proved a very efficient tool to decorate the surface of hybrid particles with small seeds.

The requirements for the development of magnetic-silica nanocomposites was met and led to multifluorescent magnetic particles. The novelty came from both the use of the amino acid route to coat with a thin layer of silica and the transposition of the hybrid structure to favour the incorporation of fluorophores. By extension, the deposition-precipitation functioned on the nanocomposites as well and led to a multifunctional platform where iron oxide, (fluorescent) silica, and gold were combined into a single structure with magnetic and plasmonic properties. The structure still needs to be optimised through the formation of a smooth gold layer and through the deposition of additional silica layer to impart fluorescence to the whole system. Moreover, the nanocomposites must be conjugated with targeting ligands for their use in biomedical applications. Attempts with folic acid and hyaluronic acid failed, yet the latter could have been directly employed to help in targeting PC3 cells and enhance the uptake of nanoparticles while reducing the aggregation. Both silica and gold surfaces possess a high affinity for a large variety of ligands and many procedures have been devised to conjugate these nanomaterials with antibodies, peptides, DNA, and polymers. This step is crucial for the biomedical applications of nanoparticles introduced in the first chapter.

Chapter 8

Final conclusion and future work

8 Final conclusion and future work

Nanoparticles offer promises in many field, including in medicine. The combination of optical, magnetic, and electrical properties of nanoparticles coupled to their dimensions similar to that of proteins makes them ideal to interact with the biological entities. More accurate and faster diagnostics, specific delivery of drugs or imaging probes, or direct treatment of diseases are some possibilities that nanoparticles offer. Among the biocompatible nanomaterials, inorganic nanoparticles have a distinct place: gold, iron oxide, quantum dots possess optical, magnetic, and electrical properties that can be of use in imaging, diagnostics and/or therapy whereas silica is a formidable carrier with a good affinity for virtually any material or compound.

The research study reported in this thesis was centred on two axes: the synthesis of a new class of silica-based nanoparticles with enhanced fluorophore carriage capacity and the development of alternative approach for the production of multifunctional nanoparticles. For both aims, the amino acid catalysis played a key role to control the silica chemistry and create either nanoparticles or coatings. Furthermore, the amino acid catalysis was completed by the deposition-precipitation method in view of decorating the surface of nanoparticles with very small gold seeds as basis to fully integrate the noble metal into the final nanocomposites and multifunctional nanoparticles.

The first part of the research focused on the understanding of the amino acid route and its difference with the other traditional synthesis methods. The amino acid route positions itself between the traditional synthesis approaches that are the Stöber and reverse microemulsion method: the particles were very small while obviating the necessity to use organic solvent and alcohols, which make the whole process easier, faster, and environmentally friendly. Furthermore, the

initial small seeds were easily enlarged by creation of successive silica layers to control the final particle diametre

The very small seeds acted as a scaffold for the growth of three successive silica layers, each containing a different fluorophore, and not larger than 30 nm. The capacity to carry multiple dyes illustrates the flexibility of the system as the fluorophores can be incorporated either via electrostatic interactions or via covalent binding to the inorganic network indistinctively while exhibiting strong optical properties. The nanoparticles were suitable for the labelling of cells and subsequent imaging by a confocal microscope. The capacity of carrying multiple fluorophores was helpful to create a distinct signal from the stains by appearing in multiple channels simultaneously and revealed a cell-dependency in the uptake of nanoparticles, where the internalisation of the normal epithelial was very low compared to that of he cancerous cell line.

Next, the silica particle composition was modified to take into account the different nature of fluorophores in order to create a universal carrier able to contain any dye. In particular, the hydrophilicity of many organic dyes governs the choice of the synthesis technique as the most hydrophobic fluorophores require a different emulsion. For this reason, the composition of the seeds was modified in order to incorporate vinyl moieties that ought to create hydrophobic sites within the silica matrix. ORMOSIL nanoparticles are generally several hundred of nanometres unless produced by oil-in-water emulsion, but the catalysis by arginine confined the particles in the 10 to 100 nm range. The optimisation of the procedure allowed the synthesis of 40 to 50 nm seeds with a good reproducibility.

The hybrid particles appeared as good fluorophore carriers able to contain dyes of interest such as rhodamine B and 6G. The core composition could be further modified in accordance to the chemical structures of the dyes in order to facilitate their incorporation and enabled the encapsulation of all 10 dyes tested. With this approach it is likely that one entrap any fluorophore by simply tuning the particle composition to match the dye electrical charge. More work is necessary to control the final optical properties but it was nonetheless possible

to entrap up to three dyes simultaneously and their relative concentrations enabled to modulate the fluorescence patterns of the FSNPs.

Finally, the hybrid nanoparticles acted as a linker to iron oxide and gold. The synthesis protocol of hybrid nanoparticles was directly transposed to the coating of magnetite and opens new possibilities for magnetic luminescent systems that suffer from a lack of fluorophore choice. The magnetic system was even able to contain two distinct fluorophores, which is rather unusual for magnetic luminescent nanocomposites. The incorporation of gold was linked to the deposition-precipitation technique and played a fundamental role in the design of multifunctional particles. Still, the system is incomplete as the final gold layer lack of homogeneity, although the plasmon resonance of the whole nanostructure was successfully red-shifted to 700 nm. More work is necessary for the design of a modular structure, whose composition can be tuned to meet ones requirement and where the three nanomaterials tested could be switched at will.

In conclusion, the main purpose of this research project was to develop a flexible method for the design of fluorescent silica nanoparticles. The procedure developed achieved this aim and lays the first stone for newer applications of silica nanoparticles in imaging and diagnostics by allowing the analysis of multiple targets simultaneously. The potential of the nanoparticles is further enhanced by the easy combination with magnetic and metallic nanoparticles. The requirements for the multifunctional systems are partially met and with some optimisation, the multifunctional nanoparticles will be able to evolve into one of smart systems envisioned for the second phase of nanotechnology development and play a role in the improvement of nanomedicine.

There exist several possibilities to improve the hybrid and multifunctional nanoparticles as well as to enhance their fluorescent properties. Moreover,

most of the experiments consisted in optimising the different types of nanoparticles and their applications have yet to be investigated. Here are some possibilities that could be exploredt.

- **Optimisation of the hybrid nanoparticles synthesis**

The synthesis of ORMOSIL by arginine catalysis developed in the chapters 4 and 5 is a novel approach and as such opens many possibilities. There exists a large variety of organosilanes and each of them could generate new effects. For instance, addition of THPMP might have an effect on the particle porosity due to the repulsion between phosphonate groups between them or with the negative silanol. Other positively charged silanes might suppress the formation of hydrogen bonds that APTES suffers from while preserving its capacity to attract certain fluorophores.

The assessment of VT-structures ought to be continued, for example to effectively analyse the influence of water and arginine on the actual particle diameter and to obviate the creation of large cup-shaped structures. Similarly, the PhTEOS hybrid might have a stronger effect on organic dyes but its hydrophobicity must be lowered to make them useful in aqueous environment. This could be achieved by growth of silica layers to improve the nanoparticle water solubility. In that respect, it was not possible to probe how to grow thicker layers of silica via the seed regrowth but this stage is highly important for the encapsulation of multiple targets in separate layers as well as for the creation of nanocomposites and multifunctional structures where silica acts as a linker. Moreover, the possibility to grow hybrid layers, in particular of APTES-TEOS layers, onto the seeds has yet to be determined.

- **Control of the carriage capacity and tuning of the optical properties**

Although the hybrid structures were able to entrap fluorescein and lucifer yellow, the production of FSNPs is still in its early stage. For of all, it is necessary to test NIR/IR and multiphoton dyes that are of interests in bio-imaging. There is no certainty how the fluorophores will react in the arginine solution and whether the molecules with aggregate before their containment – if it occurs – within the VTEOS core. It may be necessary to replace VTEOS by the more hydrophobic PhTEOS or by other silane that would enhance the affinity of the dyes for the inorganic matrix.

In the same vein, the initial fluorophore concentration must be decreased to limit the loss of free molecules as well as to control the fluorescence emission with more precision. Besides, the high concentration was responsible for some aggregation within the particles as the signal from dimer and other excimers was detected in some occasion. This step is fundamental for the development of nanosensors (PEBBLE) where the fluorescence of the sensing dye is reported to that of a referent fluorophores, meaning that the concentration of the two populations of molecules must be known with exactitude.

- **Development of nanocomposites and multifunctional nanoparticles**

Chapter 6 was a first attempt to produce nanoparticles composed of two or more nanomaterials. The coating of iron oxide, gold, and other surface with silica via arginine catalysis has never been tested so far but is potentially a good solution to produce very thin layer of ceramic. This point is crucial to ensure that only one nanoparticle is contained within the silica, a common issue in the synthesis of nanocomposites. However, the technique consisting in controlling the aggregation of iron oxide is worth exploring as it strongly enhances the magnetic properties of nanocomposites.

One of the aims was to design a modular structure, i.e. positioning iron oxide, gold, and/or silica in any order in function of the needs. So far, the coating of gold nanoparticles with silica failed which limits the modularity of the particles. Yet, gold-silica nanoparticles are interesting for fluorescence as it allows the right distance between metallic surface and fluorophores to take advantage of

the MEF effect, especially if the nanospheres were to be replaced by nanorods or nanostars due to their multiple plasmon resonance. Similarly, attempts to grow a full gold shell failed and more attention has to be paid to the deposition-precipitation to determine ito what extent this step affect the homogeneity of the gold layer. Overall, more time is needed to determine the effects of all of the parameters involved in the creation of the iron oxide-silica-gold particles, from the thickness of the silica layer to the deposition of gold seeds and the factors intervening in the growth of gold shells.

- **Surface engineering and applications**

Modifying the surface of nanoparticles is a requirement to fully take advantage of the particles properties. So far, the bio-conjugation with FA and HA failed and must be attempted again. For example, coating with HA would enable the precise targeting of CD44 receptors of PC3 cells and procedures exist for the conjugation of DNA/RNA, peptides, or polymers on gold or silica surfaces.

With the appropriate surface modification, the FSNPs and multifunctional structures could find multiple applications: the synthesis of multiple populations of particles with distinctive spectral properties may help in

- Targeting specific organelles or detecting different cell types or molecules within tissues and complex samples;
- The detection of biomolecules in blood for diagnostic purposes using magnetic properties to separate the analytes of interests and using fluorescence-based or Raman-based techniques for the analysis;
- Combined imaging/photodynamic or photothermal therapy as the photoactivity of MB still has to be assessed;
- Nanosensors could shed light on intracellular processes, including the probing of nanoparticles effects in the cytoplasm or simply as a follow-up

of the particles fate from their endocytosis to their exocytosis or their precise location.

The final point is related to the toxicity of the nanoparticles developed throughout this thesis. Although the materials selected are in principle biocompatible, it is impossible to predict how the hybrid and nanocomposite would interact with the cells. This is particularly true for the gold-decorated nanoparticles that might prove cytotoxic due to the high reactivity of the small gold seeds.

References

REFERENCES

Algar W.R., Krull U.J., “New opportunities in multiplexed optical bioanalyses using quantum dots and donor acceptor interactions”, *Anal. Bioanal. Chem.*, **398**, 2439-2449 (2010)

Alivisatos A.P., “Semiconductor clusters, nanocrystals, and quantum dots”, *Science*, **271**, 933-937 (1996)

Alkilany A.M., Murply C.J., “Toxicity and cellular uptake of gold nanoparticles: What we have learned so far?”, J*. Nanopart. Res.*, **12**, 2313-2333 (2010)

Alkrad J.A., Mrestani Y., Stroehl D., Wartewig S., Neubert R., “Characterization of enzymatically digested hyaluronic acid using NMR, Raman, IR, and UV/Vis spectroscopies”, *J. Pharm. Biomed. Anal.*, **31**, 545-550 (2003)

Anderson C.J., Bulte J.W.. Chen K., Chen X., Khaw B.A., Shokeen M., Wooley K.L. VanBrocklin H.F., “Design of targeted cardiovascular molecular imaging probes“, *J. Nucl. Med.*, **51** (5), 3S-17S (2010)

Anedda A., Carbonaro C.M., Corpino R., Ricci P.C., Grandi S., Mustarelli P.C., “Formation of fluorescent aggregates in Rhodamine 6G doped silica glasses”, *J. Non-Cryst. Solids*, **353**, 481-485 (2007)

Andrä W., Nowak H., *Magnetism in medicine: a handbook*, Wiley-VCH, 1998

Arbab A.S., Bashaw L.A., Miller B.R., Jordan E.K., Lewis B.K., Kalish H., Frank J.A., “Characterization of biophysical and metabolic properties of cells labelled with superparamagnetic iron oxide nanoparticles and transfection for cellular MR imaging”, *Radiology*, **229**, 838-846 (2003)

Arbab A.S., Wilson L.B., Ashari P., Jordan E.K., Lewis B.K., Frank J.A., “A model of lysosomal metabolism of dextran coated superparamagnetic iron oxide (SPIO) nanoparticles: implications for cellular magnetic resonance imaging”, *NMR Biomed.*, **18**, 383-389 (2005)

Arriagada F.J., Osseo-Asare K., “Synthesis of nanosize silica in a non-ionic water-in-oil microemulsion: Effects on the water/surfactant molar ratio and ammonia concentration”, *J. Colloid Interf. Sci.*, **211**, 210-220 (1999)

Arriagada F.J., Osseo-Asare K., “Controlled hydrolysis of tetraethoxysilane in non-ionic water-in-oil microemulsion: a statistical model of silica nucleation”, *Colloids Surf. A*, **154**, 311-326 (1999)

Arruebo M., Fernandez-Pacheco R., Ibarra M.R., Santamaria J., “Magnetic nanoparticles for drug delivery”, *Nanotoday*, **2** (3), 22-32 (2007)

Arsalani N., Fattahi H., Nazarpoor M., “Synthesis and characterization of PVP-functionalized superparamagnetic Fe3O4 nanoparticles as an MRI contrast agent”, *Express Polym. Lett*., **4** (6), 329-338 (2010)

Asadishad B., Vosoughi M., Alamzadeh I., Tavakoli A., “Synthesis of folate-modified, polyethylene glycol-functionalized gold nanoparticles for targeted drug delivery”; *J. Disper. Sci. Technol.*, **31** (4), 492-500 (2010)

Aslan K., Lakowicz J.R., Szmacinski H., Geddes C.D., “Metal-enhanced fluorescence solution-based sensing platform”, *J. Fluoresc.*, **14** (6), 677-679 (2004)

Bagalkot V., Zhang L., Levy-Nissenbaum E., Jon S., Kantoff P.W., Langer R., Farokhzad O.C., “Quantum dot-aptamer conjugates for synchronous cancer imaging, therapy, and sensing of drug delivery based on bi-fluorescence resonance energy transfer”, *Nano Lett.*, **7** (10), 3065–3070 (2007)

Bagwe R.P., Zhao X., Tan W., “Bioconjugated Luminescent Nanoparticles for Biological Applications”, *J. Disper. Sci. Technol.*, **24** (3), 453 — 464 (2002)

Bagwe R.P., Yang C., Hilliard L.R., Tan W., “Optimization of dye-doped silica nanoparticles prepared using a reverse microemulsion method”, *Langmuir*, **20** (19), 8336-8342 (2004)

Bagwe R.P., Hilliard L.R., Tan W., “Surface modification of silica nanoparticles to reduce aggregation and non-specific binding”, *Langmuir*, **22**, 4357-4362 (2006)

Bellin M. F., Beigelman C., Precetti-Morel S., “Iron oxide-enhanced MR lymphography: initial experience”, *Eur. J. Radiol.*, **34**, 257 (2000)

Bertazza L., Celotti L., Fabbrini G., Loi M.A., Maggini M., Mancin F., Marcuz S., Menna E., Muccini M., Tonellato U., “Cell penetrating silica nanoparticles doped with two-photon absorbing fluorophores”, *Tetrahedron*, **62**, 10434-10440 (2006)

Bertorelle F., Wilhelm C., Roger J., Gazeau F., Menager C., Cabuil V., “Fluorescence-modified superparamagnetic nanoparticles: Intracellular uptake and use in cellular imaging”, *Langmuir*, **22** (12), 5385–5391 (2006)

Bogush G.H., Zukoski C.F., “Uniform silica particle precipitation: An aggregative growth model”, *J. Colloid Interface Sci.*, **142** (1), 19-33 (1991)

Bohren C.F., Huffman D.R., *Absorption and Scattering of Light by Small Particles*, Wiley Science Paperback Series, 1998

Bowen J.M., Powers C.R., Ratcliffe A.E., Rockley M.G., Hounslow A.W., “Fourier transform infrared and raman spectra of dimethyl methylphosphonate adsorbed on montmorillonite”, *Environ. Sci. Technol.*, **22**, 1178-1181 (1988)

Brinker C.J., Scherer G.W., *Sol-Gel Science: The Physics and Chemistry of Sol-Gel Processing*, Academic Press Inc., 1990

Brinson B.E., Lassiter J.B., Levin C.S., Bardhan R., Mirin N., Halas N.J., “Nanoshells made easy: Improving Au layer growth on nanoparticle surfaces”, *Langmuir,* **24**, 14166-14171 (2008)

http://www.britishmuseum.org/explore/highlights/highlight_objects/pe_mla/t/the_lycurgus_cup.aspx

Brown K.R., Natan M.J., “Hydroxylamine seeding of colloidal Au nanoparticles in solution and on surfaces”, *Langmuir*, **14**, 726-728 (1998)

Brown K.R., Walter D.G., Natan M.J., “Seeding of colloidal Au nanoparticle solutions. 2. Improved control of particle size and shape“, *Chem. Mater.*, **12**, 306-313 (2000)

Burns A., Sengupta P., Zedayko T., Baird B., Wiesner U., “Core/shell fluorescent silica nanoparticles for chemical sensing: Towards single-particle laboratories”, *Small*, **2** (6), 723-726 (2006)

Burns A.A., Vider J., Ow H., Herz E., Penate-Medina O., Baumgart M., Larson S.M., Wiesner U., Bradbury M., “Fluorescent Silica Nanoparticles with Efficient Urinary Excretion for Nanomedicine”, *Nano Lett.*, **9** (1), 442-448 (2009)

Buyukhatipoglu K., Clyne A. M., “Superparamagnetic iron oxide nanoparticles change endothelial cell morphology and mechanics via reactive oxygen species formation”, J*. Biomed. Mater. Res. A*, **96** (1), 186-195 (2011)

Cai W., Gao T., Hong H., Sun J., “Applications of gold nanoparticles in cancer nanotechnology”, *Nanotechnology, Science and Applications*, **1**, 17-32 (2008)

Callister W.D., *Fundamentals of Materials Science and Engineering*, 5th edition, John Wiley & Sons, 2001

Celzard A., Marêche J.F., “Applications of the Sol-Gel Process Using Well-Tested Recipes”, *J. Chem. Ed.*, **79**, 854-859 (2002)

Champion J.A., Katare Y.K., Mitragotri S., “Particle shape: A new design parameter for micro- and nanoscale drug delivery carriers”, *J. Controlled Release*, **121**, 3-9 (2007)

Chan W.C., Maxwell D.J., Gao X., Bailey R.E.. Han M., Nie S., “Luminescent quantum dots for multiplexed biological detection and imaging”, *Curr. Opin. Biotechnol.*, **13**, 40-46 (2002)

Chang C., “The immune effects of naturally occurring and synthetic nanoparticles”, *J. Autoimmun.*, **34**, 234-246 (2010)

Chen F., Castranova V., Shi X., Demers L. M., “New insights into the role of nuclear factor-kappaB, a ubiquitous transcription factor in the initiation of diseases”, *Clin. Chem.*, **45**, 7–17 (1999)

Chen J., Saeki F., Wiley B., Cang H., Cobb H. M., Li Z., Au L., Zhang H., Kimmey M., Li X., Xia Y., “Gold nanocages: Bioconjugation and their potential use as optical imaging contrast agents”, *Nano Lett.*, **5** (3), 473-477 (2005)

Chen M., Von Mikecz A., “Formation of nucleoplasmic protein aggregates impair nuclear function in response to SiO2 nanoparticles”, *Exp. Cell Res.*, **305**, 51-62 (2005)

Chen Y.S., Hung Y.C., Liau I., Huang G.S., “Assessment of the in vivo toxicity of gold nanoparticles”, *Nanoscale Res. Lett.*, **4**, 858–864 (2009)

Chen Z.L., Sun Y., Huang P., Yang X.X., Zhou X.P., “Studies on preparation of photosensitizer loaded magnetic silica nanoparticles and their anti-tumor effects for targeting photodynamic therapy”, *Nanoscale Res. Lett.,* **4** (5), 400-408 (2009)

Chen H., Ming T., Zhao L., Wang F., Sun L.D., Wang J., Yan C.H., “Plasmon-molecule interactions”, *Nanotoday*, **5**, 494-505 (2010)

Cheon J., Lee J.H., “Synergistically integrated nanoparticles as multimodal probes for nanobiotechnology”, *Accounts Chem. Res.*, **41** (12), 1630-1640 (2008)

Chien W.Y., Szkopek T., “Multiple-multipole simulation of optical near-fields in discrete metal nanosphere assemblies”, *Opt. Express*, **16**, 1820-1835 (2008)

Chithrani B.D., Ghazani A.A., Chan C.W., “Determining the size and shape dependence of gold nanoparticle uptake into mammalian cells”, *Nano Lett.*, **6** (4), 662-668 (2006)

Chithrani B.D., Chan W.C., “Elucidating the mechanism of cellular uptake and removal of protein-coated gold nanoparticles of different sizes and shapes”, *Nano Lett.*, **7** (6), 1542-1550 (2007)

Chithrani B.D., Stewart J., Allen C., Jaffray D.A., “Intracellular uptake, transport, and processing of nanostructures in cancer cells*”, Nanomedicine: Nanotechnology, Biology, and Medicine*, **5**, 118-127 (2009)

Cho M., Cho W.S., Choi M., Kim S.J., Han B.S., Kim S.H., Kim H.O., Sheen Y.Y., Jeong J,, “The impact of size on tissue distribution and elimination by single intravenous injection of silica nanoparticles”, *Toxicol. Lett.*, **189**, 177-183 (2009)

Cho E.C., Glaus C., Chen J., Welch M.J., Xia Y., “Inorganic nanoparticle-based contrast agents for molecular imaging“, *Trends in Mol. Med.*, **16** (12), 561-573 (2010)

Cho E.B., Volkov D.O., Sokolov I., “Ultrabright fluorescent mesoporous silica nanoparticles”, Small, 20, 2314-2319 (2010)

Cho Y.S., Yoon T.J., Jang E.S., Hong K.S., Lee S.Y., Kim O.R., Park C., Kim Y.J., Yi G.C., Chang K., “Cetuximab-conjugated magneto-fluorescent silica nanoparticles for *in vivo* colon cancer targeting and imaging”, *Cancer Lett.*, **299**, 63-271 (2010)

Choi H.S., Liu W., Misra P., Tanaka E., Zimer J.P., Ipe B. I., Bawendi M.G., Frangioni J.V., “Renal clearance of nanoparticles”, *Nat. Biotechnol.*, **25** (10), 1165-1170 (2007)

Chou S.W., Shau Y.H., Wu P.C., Yang Y.S., Shieh D.B., Chen C.C., “*In vitr*o and *in vivo* studies of FePt nanoparticles for dual modal CT/MRI molecular imaging”, *J. Am. Chem. Soc.*, **132**, 13270-13278 (2010)

Claesson E.M., Philipse A.P., “Monodisperse magnetizable composite silica spheres with tunable dipolar interactions”, Langmuir, 21, 9412-9419 (2005)

Conner S.D., Schmid S.L., “Regulated portals of entry into the cell”, *Nature*, **422**, 37-44 (2003)

Connor E.E., Mwamuka J., Gole A., Murphy C.J., Wyatt M.D., “Gold nanoparticles are taken up by human cells but do not cause acute cytotoxicity”, *Small*, **1** (3), 325-327 (2005)

Corsi F., De Palma C., Colombo M., Allevi R., Nebuloni M., Ronchi S., Rizzi G., Tosoni A., Trabucchi E., Clementi E., Prosperi D., “Towards ideal magnetofluorescent nanoparticles for bimodal detection of breast-cancer cells”, *Small*, 5 (22), 2555-2564 (2009)

Davis T.M., Snyder M.A., Krohn J.E., Tsapatsis M., “Nanoparticles in lysine-silica sols”, *Chem. Mater.*, **18**, 5814-5816 (2006)

Deerinck T. J., “The application of fluorescent quantum dots to confocal, multiphoton, and electron microscopic”, *Toxicol Pathol.*, **36**, 112-116 (2008)

Del Monte F., Mackenzie J.D., Levy D., “Rhodamine fluorescent dimers adsorbed on the porous surface of silica gels”, *Langmuir*, **16**, 7377-7382 (2000)

Deng G., Markowitz M.A., Kust P.R., Gaber B.P., “Control of surface expression of functional groups on silica particles”, *Mater. Sci. Eng., C*, **11**, 165-172 (2000)

Deng T., Li J.S., Jiang J.H., Shen G.L., Yu R.Q., “Preparation of near-IR fluorescent nanoparticles for fluorescence-anisotropy-based immunoagglutination assay in whole blood”, *Adv. Funct. Mater*. **16**, 2147–2155 (2006)

Derfus A.M., Chan W.C., Bhatia S.N., “Probing the cytotoxicity of semiconductor quantum dots”, *Nano Lett.*, **4** (1), 11-18 (2004)

Dickinson D.A., Forman H.J., “Glutathione in defense and signaling: Lessons from a small thiol”, *Ann. NY Acad. Sci.*, **937**, 488–504 (2002)

Dimitriev Y., Ivanova Y., Iordanova R., “History of sol-gel science and technology (Review)”, *Journal of the University of Chemical Technology and Metallurgy*, **43** (2), 181-192 (2008)

Dirè S., Tagliazucca V., Callone E., Quaranta A., “Effect of functional groups on condensation and properties of sol–gel silica nanoparticles prepared by direct synthesis from organoalkoxysilanes”, *Mater. Chem. Phys.*, **126**, 909-917 (2011)

Dobson J., “Magnetic nanoparticles for drug delivery”, *Drug Dev. Res.*, **67**, 55-60 (2006)

Doherty G.J., McMahon H.T., “Mechanisms of endocytosis”, *Annu. Rev. Biochem.*, **78**, 857-902 (2009)

Donaldson K., Stone V., Borm P.J., Jimenez L.A., Gilmour P.S., Schins R.P., Knaapen A.M., Rahman I., Faux S.P., Brown D.M., MacNee W., “Oxidative stress and calcium signaling in the adverse effects of environmental particles”, *Free Radical Bio. Med.*, **34** (11), 1369-1382 (2003)

Donghui F., Beibei W., Zheng X., Qisheng G., “Determination of Hyaluronan by Spectroscopic Methods”, *J. Wuhan Univ. Technol. - Mater. Sci. Ed.*, **21** (3), 3-34 (2006)

Dosev D., Nichkova M., Dumas R.K., Gee S.J., Hammock B.D., Liu K., Kennedy I.M., “Magnetic/luminescent core/shell particles synthesized by spray pyrolysis and their application in immunoassays with internal standard”, *Nanotechnology*, **18** (5), 055102 (2007)

Dressman D., Yan H., Traverso G., Kinzler K., Vogelstein B., “Transforming single DNA molecules into fluorescent magnetic particles for detection and enumeration of genetic variations”, *Proc. Natl. Acad. Sci. USA*, **100** (15), 8817–8822 (2003)

Durr N. J., Larson T., Smith D.K., Korgel B.A., Sokolov K., Ben-Yakar A., “Two-photon luminescence imaging of cancer cells using molecularly targeted gold nanorods”, *Nano Lett.*, **7**, 941–945 (2007)

El-Sayed I.H., Huang X., El-Sayed M.A., “Surface plasmon resonance scattering and absorption of anti-EGFR antibody conjugated gold nanoparticles in cancer diagnostics: Applications in oral cancer”, *Nano Lett.*, ***5***, 829–834 (2005)

El-Sayed I.H., Huang X., El-Sayed, M.A. “Selective laser photo-thermal therapy of epithelial carcinoma using anti-EGFR antibody conjugated gold nanoparticles”, *Cancer Lett.*, **239**, 129-135 (2006)

Elias A., Tsourkas A., “Imaging circulating cells and lymphoid tissues with iron oxide nanoparticles”, *Hematology*, 720-726 (2009)

Eom H.J., Choi J., “Oxidative stress of silica nanoparticles in human bronchial epithelial cell, Beas-2B”, *Toxicol. in Vitro*, **23**, 1326-1332 (2009)

Erogbogbo F., Yong K.T., Roy I., Xu G., Prasad P.N., Swihart M.T., “Biocompatible luminescent silicon quantum dots for imaging of cancer cells”, ACS Nano, 2 (5), 873-878 (2005)

Estevez M. C., O’Donoghue M.B., Chen X., Tan W., “Highly fluorescent dye-doped silica nanoparticles increase flow cytometry sensitivity for cancer cell monitoring”, *Nano Res.*, **2**, 448-461 (2009)

European Commission, “The Sixth Framework Programme in brief”, December 2002

European Commission, “EU Policy for Nanosciences and Nanotechnologies”, 2006

European Technology Platform on NanoMedicine - Nanotechnology for Health, European Commission, November 2006

European Commission, “FP7 in Brief: How to get involved in the EU 7th Framework Programme for Research”, December 2007

European Commission, “Some Figures about Nanotechnology R&D in Europe and Beyond”, December 2008

Fadeel A., Garcia-Bennett A.E., “Better safe than sorry: Understanding the toxicological properties of inorganic nanoparticles manufactured for biomedical applications”, *Adv. Drug Deliver. Rev.*, **62** (3), 362-374 (2010)

Feynman R., “There's Plenty of Room at the Bottom”, *Engineering and Science Magazine*, XXIII (5) (1960)

Figuerola, R. Di Corato, L. Manna, T. Pellegrino, “From iron oxide nanoparticles towards advanced iron-based inorganic materials designed for biomedical applications”, *Pharmacol. Res.*, **62,** 126-143 (2010)

Foglia S., Suber L., Righini M., “Size tailoring of CdS nanoparticles by different colloidal chemical techniques”, *Colloids Surf., A*, **177**, 3-12 (2001)

Frangioni V., “In Vivo near-infrared fluorescence imaging”, *Curr. Opin. Chem. Biol.*, **7**, 626-634 (2003)

Gao X., Cui Y., Levenson R.M., Chung L.W., Nie S., “In vivo cancer targeting and imaging with semiconductor quantum dots”, *Nat. Biotechnol.*, **22**, 969-976 (2004)

Gao F., Tang L., Dai L., Wang L., “A fluorescence ratiometric nano-pH sensor based on dual-fluorophore-doped silica nanoparticles”, *Spectrochim. Acta A*, **67**, 517-521 (2007)

Gao X., He J., Deng L., Cao H., “Synthesis and characterization of functionalized rhodamine B-doped silica nanoparticles”, *Opt. Mater.*, **31**, 1715-1719 (2009)

Gao F., Chen X., Ye Q., Yao Z., Guo X., Wang L., “Core-shell fluorescent silica nanoparticles for sensing near-neutral pH values”, *Microchim. Acta*, **172**, 327-333, (2011)

Ge J., Hu Y., Biasini M., Beyermann W. P., Yin Y., “Superparamagnetic magnetite colloidal nanocrystal clusters”, *Angew. Chem. Int. Ed.*, **46**, 4342-4345 (2007)

George S., Pokhrel S., Xia T., Gilbert B., Ji Z., Schowalter M., Rosenauer A., Damoiseaux R., Bradley K.A., Mädler L., Nel A.E., “Use of a rapid cytotoxicity screening approach to engineer a safer zinc oxide nanoparticles through iron doping”, *ACS Nano*, **4** (1), 15-29 (2010)

Gerion D., Chen F., Kannan B., Fu A., Parak W.J., Chen D.J., Majumbar, A., Alivisatos A.P. , “Room-temperature single-nucleotide polymorphism and multiallele DNA detection using fluorescent nanocrystals and microarrays”, *Anal. Chem.*, **75**, 4766–4772 (2003)

Geszke M., Murias M., Balan L., Medjahdi G., Korczynski J., Moritz M., Lulek J., Schneider R., “Folic acid-conjugated core/shell ZnS:Mn/ZnS quantum dots as targeted probes for two photon fluorescence imaging of cancer cells”, *Acta Biomater.*, **7** (3), 1327-1338 (2011)

Giesche H., “Synthesis of monodispersed silica powders II. Controlled growth reaction and continuous production process”, *J. Eur. Ceram. Soc.*, **14**, 205-214 (1994)

Glaus C., Rossin R., Welch M.J., Bao, G., “In vivo evaluation of ^{64}Cu-labeled magnetic nanoparticles as a dual-modality PET/MR imaging agent”, *Bioconjugate Chem.*, **21**, 715-722 (2010)

Gobin A.M., Lee M.H., Halas N.J., James W.D., Drezek R.A., West J. L., “Near-infrared resonant nanoshells for combines optical imaging and photothermal therapy”, *Nano Lett.*, **7** (7), 1929-1934 (2007)

Gök E., Olgaz S., “Binding of fluorescein isothiocyanate to insulin: A fluorimetric labelling study”, *J. Fluoresc.*, **14** (2), 203-206 (2004)

Goldman E.R, Clapp A.R., Anderson G.P., Uyeda H.T., Mauro J.M., Medintz I.L., Mattoussi H., “Multiplexed toxin analysis using four colors of quantum dot fluororeagents”, *Anal. Chem.*, **76**, 684-688 (2004)

Goodman C.M., McCusker C.D., Yilamz T., Rotello V.M., “Toxicity of gold nanoparticles functionalized with cationic and anionic side chains”, *Bioconjug. Chem.*, **15** (4), 897-900 (2004)

Gould P., “Nanomagnetism shows in vivo potential”, *Nanotoday*, **1** (4), 34-39 (2006)

Govorov A.O., Richardson H.H., “Generating heat with metal nanoparticles”, *Nanotoday*, **2**, 30-38 (2007)

Graf C., van Blaaderen A., “Metallodielectric colloidal core-shell particles for photonic applications”, *Langmuir*, **18**, 524-534 (2002)

Graf C., Vossen D.L., Imhof A., van Blaaderen A., “A general method to coat colloidal particles with silica”, *Langmuir*, 19, 6693-6700 (2003)

Gratton S.E., Ropp P.A., Pohlhaus P.D., Luft J.C., Madden V.J., Napier M.E., DeSimone J.M., “The effect of particle design on cellular internalisation pathways”, *Proc. Natl Acad. Sci. USA*, **105** (33), 11613-11618 (2008)

Ha S.W., Camalier C.E., Beck G.R., Lee J.K., “New method to prepare very stable and biocompatible fluorescent silica nanoparticles”, *Chem. Commun.*, **20**, 2881-2883 (2009)

Häfeli U.O., Riffle J.S., Harris-Shekhawat L., Carmichael-Baranauskas A., Mark F., Dailey J.P., Bardenstein D., “Cell uptake and *in vitro* toxicity of magnetic nanoparticles suitable for drug delivery”, *Mol. Pharmaceutics*, **6** (5), 1417-1428 (2009)

Hahn M.A., Singh A.K., Sharma P., Brown S.C., Moudgil B.J., “Nanoparticles as contrast agents for in-vivo bioimaging: Current status and future perspectives”, *Anal. Bioanal. Chem.*, **399**, 3-27 (2011)

Han M., Gao X., Su J.Z., Nie S., “Quantum-dots-tagged microbeads for multiplexed optical coding of biomolecules”, *Natur. Biotechnol.*, **19** (7), 631-635 (2001)

Han J., Burgess K., “Fluorescent Indicators for Intracellular pH”, *Chem. Rev.*, **110**, 2709-2728 (2010)

Hardman R., “A toxicologic review of quantum dots: Toxicity depends on physicochemical and environmental factors”, *Environ. Health Persp.*, **114** (2), 165-172 (2006)

Hargittai I., Hargittai M., “Molecular structure of hyaluronan: An introduction”, *Struct. Chem.*, **19**, 697-717 (2007)

Hartlen K.D., Athanasopoulos A.P., Kitaev V., “Facile preparation of highly monodisperse small silica spheres (15 to > 200 nm) suitable for colloidal templating and formation of ordered arrays”, *Langmuir*, **24**, 1714-1720 (2008)

Haruta M., “Size- and support-dependency in the catalysis of gold”, *Catal. Today*, **36**, 153-166 (1997)

Hauck T.S, Anderson R.E., Fischer H.C., Newbigging S., Chan W.C., “In vivo quantum-dot toxicity assessment”, *Small*, **6** (1), 138-144 (2010)

Hazarika P., Jickells S., Wolff K., Russell D., “Imaging of latent fingerprints through the detection of drugs and metabolites”, *Angew. Chem. Int. Ed.*, **120 (**52), 10321–10324 (2008)

He X., Liu F., Wang K., Ge J., Qin D., Gong P., Tan W., “Bioeffects of different functionalized silica nanoparticles on HaCaT cell line”, *Chinese Sci. Bull.*, **51** (16), 1939-1946 (2006)

He X., Chen J., Wang K., Qin D., Tan W., “Preparation of luminescent Cy5 doped core-shell SFNPs and its application as a near-infrared fluorescent marker”, *Talanta*, **72**, 1519-1526 (2007)

He Q., Zhang Z., Gao Y., Shi J., Li Y., “Intracellular localization and cytoxicity of spherical mesoporous silica nano- and microparticles”, *Small*, **5** (23), 2722-2729 (2009)

He X., Wu X., Wang K., Shi B., Hai L., “Methylene blue-encapsulated phosphonate-terminated silica nanoparticles for simultaneous in vivo imaging and photodynamic therapy”, *Biomaterials*, **30**, 5601-5609 (2009)

He Y.Y., Wang X.C., Jin P.K., Zhao B., Fan X., “Complexation of anthracene with folic acid studied by FTIR and UV spectroscopies”, *Spectrochim. Acta A*, **72**,, 876–879 (2009)

Helmchen F., Denk W., “Deep tissue two-photon microscopy”, *Nat. Methods*, **2**, 932-940 (2005)

Herz E., Ow H., Bonner D., Burns A., Wiesner U., “Dye structure-optical property correlations in near-infrared fluorescent core-shell silica nanoparticles”, *J. Mater. Chem.*, **19**, 631-6347 (2009)

Hirsch L.R., Jackson J.B., Lee A., Halas N.J., West J.L., “A whole blood immunoassay using gold nanoshells”, *Anal. Chem.*, **75**, 2377–2381 (2003)

Hirsch L.R., Stafford R.J., Bankson J.A., Sershen S.R., Rivera B., Price R.E., Hazle J.D., Halas N.J., West J.L., “Nanoshell-mediated near-infrared thermal therapy of tumors under magnetic resonance guidance”, *Proc. Natl. Acad. Sci.*, **100** (23), 13549-13554 (2003)

Hirsch L.R., Gobin A.M., Lowery A.R., Tam F., Drezek R.A., Halas N.J., West J.L., “Metal nanoshells”, *Ann. Biomed. Eng.*, **34** (1), 15-22 (2006)

Hu J., Xie M., Wen C.Y., Zhang, Z.L., Xie H.Y., Liu A.A., Chen Y.Y., Zhou S.M., Pang D.W, “A multicomponent recognition and separation system established via fluorescent, magnetic, dual encoded multifunctional bioprobes”, *Biomaterials*, **32** (4), 1177-1184 (2011)

Huang X., El-Sayed I.H., Qian W., El-Sayed M.A., “Cancer cell imaging and photothermal therapy in the near-infrared region by using gold nanorods”, *J. Am. Chem. Soc.*, **128**, 2115-2120 (2006)

Huang X., Teng X., Chen D., Tang F., He J., “The effect of the shape of mesoporous silica nanoparticles on cellular uptake and cell function”, *Biomaterials*, **31** (3), 438-448 (2010)

Hwang D.W., Ko H.Y., Kim S.K., Kim D., Le D.S., Kim S., “Development of a quadruple imaging modality by using nanoparticles”, *Chem. Eur. J.*, **15**, 9387-9393 (2009)

Imhof A., Megens M., Engelberts J.J., de Lang D.T., Sprik R., Vos W.L., “Spectroscopy of fluorescein (FITC) dyed colloidal silica spheres”, *J. Phys. Chem. B*, **103**, 1408-1415 (1999)

Jain P.K., Lee K.S., El-Sayed I., M. El-Sayed, “Calculated absorption and scattering properties of gold nanoparticles of different size, shape, and composition: applications in biological imaging and biomedicine”, *J. Phys. Chem. B,* **110**, 7238 -7248 (2006)

Jain P.K., El-Sayed I.H., El-Sayed M.A., “Au nanoparticles target cancer”, *Nanotoday*, **2**, 18-28 (2007)

Jeon Y.H., Kim Y.H., Choi K., Piao J.Y., Quan B., Y.S. Lee, Jeong J.M., Chung J.K., Lee D.S., Lee M.C., Lee J., Chung D.S., Kang K.W., “In vivo imaging of sentinel nodes using fluorescent silica nanoparticles in living mice”, *Mol. Imaging Biol.*, **12**, 156-162 (2010)

Ji X., Shao R., Elliott A.M., Stafford R.J., Esparza-Coss E., Bankson J.A., Liang G., Luo Z.P., Park K., Markert J.T., Li C., “Bifunctional gold nanoshells with a superparamagnetic iron oxide−silica core suitable for both MR imaging and photothermal therapy”, *J. Phys. Chem. C*, **111** (17), 6245-6251 (2007)

Jiang W., Singhal A., Kim B.Y., Zheng J., Rutka J.T., Wang C., Chan W.C., “Assessing near-infrared quantum dots for deep tissue, organ, and animal imaging applications”, *J. Clin. Lab. Automat.*, **13** (1), 6-12 (2008)

Jiang H., Wang G., Zhang W., Liu X., Ye Z., Jin D., Yuan J., Liu Z., “Preparation and time-resolved luminescence bioassay application of multicolour luminescent lanthanide nanoparticles”, *J. Fluoresc.*, **20,** 321-328 (2010)

Jun Y.W., Seo J.W., Cheo J., “Nanoscaling laws of magnetic nanoparticles and their applicabilities in biomedical sciences”, *Accounts Chem. Res.*, **41** (2), 179-189 (2008)

Kah J.C., Phonthammachai N., Wan R.C., Song J., White T., Mhaisalkar S., Ahmad I., Sheppard C., Olivo M.., “Synthesis of gold nanoshells based on the deposition-precipitation process”, *Gold bull.*, **41**, 23-36 (2008)

Karin M., Liu Z., Zandi E., “AP-1 function and regulation”, *Curr. Opin. Cell Biol.*, **9**, 240–246 (1997)

Kim J.S., Yoon T.J., Yu K.N., Kim B.G., Park S.J., Kim H.W., Lee K.H., Park S.B., Lee J.K., Cho M.H., “Toxicity and tissue distribution of magnetic nanoarticles in mice”, *Toxicol. Sci.*, **89** (1), 338-347 (2006)

Kim J., Park S., Lee J.E., Jin S.M., Lee J.H., Lee I.S., Yang I., Kim J.-S., Kim S.K., Cho M.H., Hyeon T., “Designed fabrication of multifunctional magnetic gold nanoshells and their application to magnetic resonance imaging and photothermal therapy”, *Angew. Chem. Int. Ed.*, **45**, 7754-7758 (2006)

Kim D., Park S., Lee J.H., Jeong Y.Y., Jon S., “Antibiofouling polymer-coated gold nanoparticles as a contrast agent for in vivo x-ray computed tomography imaging”, *J. Am. Chem. Soc.*, **129**, 7661-7665 (2007)

Kim D.K., Kim J.W., Jeong Y.Y., Jon S., “Antibiofouling polymer coated Gold@Iron oxide nanoparticle (GION) as a dual contrast agent for CT and MRI”, *Bull. Korean Chem. Soc.*, **30** (8), 1855-1857 (2009)

Kimura N., Umemura J., Hayashi S., “Polarized FT-IR spectra of water in the middle phase of triton X100-water system”, *J. Colloid Interf. Sci.*, **182**, 356-364 (1996)

Kircher M.F., Mahmood U., King R.S., Weissleder R., Josephson L., “A multimodal nanoparticle for preoperative magnetic resonance imaging and intraoperative optical brain tumor delineation”, *Cancer Res.*, **63** (23), 8122–8125 (2003)

Klichko Y., Liong M., Choi E., Angelos S., Nel A.E., Stoddart J.F., Tamanoi F., Zink J.I., “Mesostructured silica for optical functionality, nanomachines, and drug delivery”, *J. Am. Ceram. Soc.*, **92**, S2-S10 (2009)

Knopp D., Tang D., Niessner R., “Review: Bioanalytical applications of biomolecule-functionalized nanometer-sized doped silica particles”, *Anal. Chim. Acta*, **647**, 14-30 (2009)

Kobayashi H., Hama Y., Koyama Y., Barrett T., Regino C.A., Urano Y., Choyke, P.L. “Simultaneous multicolor imaging of five different lymphatic basins using quantum dots”, *Nano Lett.*, **7**, 1711-1716 (2007)

Kobayashi H., Longmire M.R., Ogawa M., Choyke P.L., Kawamoto S., “Multiplexed imaging in cancer diagnosis: applications and future advances”, *Oncology*, **11**, 588-595 (2010)

Kogan G., Soltes L., Stern R., Gemeiner P., “Hyaluronic acid: A natural biopolymer with a broad range of biomedical and industrial applications“, *Biotechnol. Lett.*, **29**, 17-25 (2007)

Kohen R., Nyska A., “Oxidation of biological systems: Oxidative stress phenomena, antioxidants, redox reactions, and methods for their quantification”, *Toxicol. Pathol.*, **30**, 620- 650 (2002)

Kong J., Yu S., “Fourier Transform Infrared Spectroscopic Analysis of Protein Secondary Structures”, *Acta Bioch. Biophys. Sin.*, **39** (8), 549–559 (2007)

Koole R., van Schooneveld M.M., Hilhorst J., de Mello Donega C.,'t Hart D.C., Van Blaaderen A., Vanmaekelbergh D., Meijerink A., "On the incorporation mechanism of hydrophobic quantum dots in silica spheres by a reverse microemulsion method", Chem. *Mater*., **20**, 2503-2512 (2008)

Kopelman R., Lee K.Y., Philbert M., Moffat B.A., Ramachandra R.G., McConville P., Hall D.E., Chenevert T.L., Bhojani M.S., Buck S.M., Rehemtulla A., Ross B.D., "Multifunctional nanoparticle platforms for in vivo MRI enhancement and photodynamic therapy of a rat brain cancer", *J. Magn. Magn. Mater.*, **293** (1), 404–410 (2005)

Kroemer G., "Mitochondrial control of apoptosis: An introduction", *Biochem. Bioph. Res. Co.*, **304**, 433-435 (2003)

Kubin R. F., Fletcher A. N., "Fluorescence quantum yields of some rhodamine dyes", *J. Lumin.,* 27, 455-462 (1982)

Kumar R., Roy I., Ohulchanskky T.Y., Goswami L.N., Bonoiu A.C., Bergey E.J., Tramposch K.M., Maitra A., Prasad P.N., "Covalently dye-linked, surface-controlled, and bioconjugated organically modified silica nanoparticles as targeted probes for optical imaging", *ACS Nano*, **2** (3), 449-456 (2008)

Kumar R., Roy I., Ohulchanskky T.Y., Vathy L.A., Bergey E.J., Sajjad M., Prasad P.N., "In vivo distribution and clearance studies using multimodal organically modified silica nanoparticles", *ACS Nano*, **4** (2), 699-708 (2010)

Kwon J.T., Hwang S.K., Jin H., Kim D.S., Minai-Tehrani A., Yoon H.J., Choi M., Yoon T.J., Han D.Y., Kang Y.W., Yoon B.I., Lee J.K., Cho M.H., "Body distribution of inhaled fluorescent magnetic nanoaprticles in the mice", *J. Occup. Health*, **50**, 1-6 (2008)

Labhasetwar V., Leslie-Pelecky D.L., Biomedical applications of nanotechnology, Wiley-Interscience, 2007

Lakowicz J.R., "Radiative decay engineering 5: Metal-enhanced fluorescence and plasmon emission", *Anal. Biochem.*, **337**, 171-194 (2005)

LaMer V.K., Dinegar R.H., “Theory, Production and Mechanism of Formation of Monodispersed Hydrosols”, *J. Am. Chem. Soc.*, **72** (11), 4847-4854 (1950)

Langhals H., Esterbauer A.J., Kinzel S., “Red shining silica: Macroscopic pigments and nanoparticles by silylation”, *New J. Chem.*, **33**, 1829-1832 (2009)

Larsen B.A., Haag M.A., Serkova N.J., Shroyer K.R., Stoldt C.R., “Controlled aggregation of superparamagnetic iron oxide nanoparticles for the development of molecular magnetic resonance imaging probes”, *Nanotechnology*, **19**, 265102 (2008)

Larson D.R., Zipfel W.R., Williams R.M., Clark S.W., Bruchez M.P., Wise F.W., Webb W.W., “Water-soluble quantum dots for multiphoton fluorescence imaging in vivo”, *Science*, **300**, 1434-1436 (2003)

Larson T.A., Bankson J., Aaron J., Sokolov K., “Hybrid plasmonic magnetic nanoparticles as molecular specific agents for MRI/optical imaging and photothermal therapy of cancer cells”, *Nanotechnology*, **18**, 325101 (2007)

Larson D.R., Ow H., Vishwasrao H.D., Heikal A.A., Wiesner U., Webb W.W., “Silica nanoparticles architecture determines radiative properties of encapsulated fluorophores”, *Chem. Mater.*, **20**, 2677-2684 (2008)

W.C. Law, K.T. Yong, I. Roy, G. Xu, H. Ding, E.J. Bergey, H. Zeng, P.N. Prasad, “Optically and magnetically doped organically modified silica nnoparticles as efficient magnetically guided biomarkers for two-photon imaging of live cancer cells”, *J. Phys. Chem. C*, **112**, 7972-7977 (2008)

Law W.C., Yong K.T., Roy I., Xu G., Ding H., Bergey E.J., Zeng H., Prasad P.N., “Optically and magnetically doped organically modified silica nnoparticles as efficient magnetically guided biomarkers for two-photon imaging of live cancer cells”, *J. Phys. Chem. C*, **112**, 7972-7977 (2008)

Lee S.J., Gavriilidis A., “Supported Au catalysts for low-temperature CO oxidation prepared by impregnation”, *J. Catal.*, **206**, 305-313 (2002)

Lee J.H., Huh Y.M., Jun Y., Seo J., Jang J., Song H.T., “Artificially engineered magnetic nanoparticles for ultra-sensitive molecular imaging”, *Nat. Med.*, **13**, 95–99 (2007)

Lee Y.E., Kopelman R., Smith R., “Nanoparticle PEBBLE sensors in live cells and in vivo”, *Annu. Rev. Anal. Chem.*, **2**, 57-76 (2009)

Leslie-Pelecky D.L., Rieke R.D., “Magnetic properties of nanostructured materials”, *Chem. Mater.*, **8**, 1770-1783 (1996)

Levy M., Wilhelm C., Siaugue J.M., Horner O., Bacri J.C., Gazeau F., “Magnetically induced hyperthermia: size-dependent heating power of gamma-Fe_2O_3 nanoparticles”, *J. Phys.-Condens. Mat.*, **20**, 204133 (2008)

Levy M., Lagarde F., Maraloiu V.-A., Blanchin M.G., Gendron F., Wilhelm C., Gazeau F., “Degradability of superparamagnetic nanoparticles in a model of intracellular environment: follow-up of magnetic, structural and chemical properties”, *Nanotechnology*, **21**, 395103 (2010)

Lévy R., Shaheen U., Cesbron Y., Sée V., “Gold nanoparticles delivery in mammalian live cells: A critical review”, *Nano Reviews*, **1**, 4889 -5006 (2010)

Li C.Y., Tseng J.Y., Morita K., Lechner C., Hu Y., Mackenzie J.D., “Ormosils as Matrices in Inorganic-organic Nanocomposites for Various Optical Applications”, *Proc. SPIE*, **1758**, 410-419 (1992)

Li N., Hao M., Phalen R.F., Hinds W.C., Nel A.E., “Particulate air pollutant and asthma: A paradigm for the role of oxidative stress in PM-induced adverse health effects”, *Clin. Immun*., **109**, 250-265 (2003)

Li P.C., Wei C.W., Liao C.K., Chen C.D., Pao K.C., Wang C.R., Wu Y.N., Shieh D.B., “Photoacoustic imaging of multiple targets using gold nanorods”, *IEEE Trans. Ultrason. Ferroelectr. Freq. Control.*, **54**, 1642–1647 (2007)

Li T., Guo L., Wang Z., “Microarray based Raman spectroscopic detection with gold nanoparticle probes”, *Biosens. Bioelectron.*, **23**, 1125-1130 (2008)

Liang Z., Susha A., Caruso F., “Gold nanoparticle-based core-shell and hollow spheres and ordered assemblies thereof”, *Chem. Mater.*, **15**, 3176-3183 (2003)

Lin W., Huang Y.W., Zhou X.D., Ma Y., “In vitro toxicity of silica nanoparticles in human lung cancer cells”, *Toxicol. Appl. Pharm.*, **217**, 252-259 (2006)

Lin M.M., Kim H.H., Kim H., Muhmmed M., Kim D.K., “Iron oxide-based nanomagnets in nanomedicine: Fabrication and applications”, *Nano Reviews*, **1**, 4883 (2010)

Liong M., Lu J., Kovochich M., Ruehm S.G., Nel A.E., Tamanoi F., Zink J.I., “Multifunctional inorganic nanoparticles for imaging, targeting, and drug delivery”, *ACS Nano*, **2** (5), 889-896 (2008)

Liu X., Sun J., “Endothelial cells dysfunction induced by silica nanoparticles through oxidative stress via JNK/P53 and NF-kB pathways”, *Biomaterials*, **31**, 8198-8209 (2010)

Lodish H., Berk A., Matsudaira P., Kaiser C.A., Kriger M., Scott M.P., Zipursky L., Darnell J., *Molecular Cell Biology*, fifth edition, W.H. Freeman, 2003

Lunov O., Syrovets T., Büchele B., Jiang X., Röcker C., Tron K., Nienhaus G.U., Walther P., Mailänder V., Landfester K., Simmet T., “The effect of carboxydextran-coated superparamagnetic iron oxide nanoparticles on c-Jun N-terminal kinase-mediated apoptosis in human macrophages", *Biomaterials*, **31**, 5063-5071 (2010)

Lyer A.K., Khaled G., Fang J., Maeda H., “Exploiting the enhanced permeability and retention effect for tumor targeting”, *Drug Discov. Today*, **11**, 812-818 (2006)

Lyon J.L., Fleming D.A., Stone M.B., Schiffer P., Williams M.E., “Synthesis of Fe oxide core/Au shell nanoparticles by iterative hydroxylamine seeding”, *Nano Lett.*, 4 (4), 719-723 (2004)

Ma D., Kell A.J., Tan S., Jakubek Z.J., Simard B., “Photophysical properties of dye-doped silica nanoparticles bearing different types of dye-silica interactions”, *J. Phys. Chem. C*, **113**, 15974-15981 (2009)

Mader H., Li X., Saleh S., Link M., Kele P., Wolfbeis O.S., “Fluorescent silica nanoparticles”, *Ann. N.Y. Acad. Sci.*, **1130**, 218-223 (2008)

Maenosono S, Suzuki T, Saita S., “Superparamagnetic FePt nanoparticles as excellent MRI contrast agents”, *J. Magn. Magn. Mater.*, **320**, 79–83 (2008)

Mahmoudi M., Simchi A., Imani M., “Cytotoxicity of uncoated and polyvinyl alcohol coated sueprparamagnetic iron oxide nanoparticles”, *J. Phys. Chem. C*, **113**, 9573-9580 (2009)

Maier S.A., *Plasmonics Fundamentals and Applications*, Springer, 2007

Mansoori G.A., Brandenburg K.S., Shakeri-Zadeh A., “A comparative study of two folate-conjugated gold nanoparticles for cancer nanotechnology applications”, *Cancers*, **2**, 1911-1928 (2010)

Marquis B.J., Love S.A., Braun K.L., Haynes C.L., “Analytical methods to assess nanoparticle toxicity”, *Analyst*, **134**, 425-439 (2009).

Maysinger D., Behrendt M., Lalancette-Hébert M., Kriz J., “Real-time imaging of astrocyte response to quantum dots: In vivo screening model system for biocompatibility of nanoparticles”, *Nano Let*t., **7** (8), 2513-2520 (2007)

Mazzoli-Rocha F., Fernandes S., Einicker-Lamas M., Zin W. A., “Roles of oxidative stress in signaling and inflammation induced by particulate matter“, *Cell. Biol. Toxicol.*, **26**, 481-498 (2010)

McCarthy J.R., “The future of theranostic nanoagents”, *Nanomedicine*, **4** (7), 693-695 (2009)

McBain S.C., Yiu H., Dobson J., “Magnetic nanoparticles for gene and drug delivery”, *Int. J. Nanomedicine*, **3** (2), 169-180 (2008)

McNeil S.E., “Nanotechnology for the biologist”, *J. Leukocyte Biol.*, **78**, 585-594 (2005)

Medley C.D., Smith J.E., Tang Z., Wu Y., Bamrungsap S., Tan W., “Gold nanoparticle-based colorimetric assay for the direct detection of cancerous cells”, *Anal. Chem.*, **80**, 1067–1072 (2008)

Melancon M., Lu W., Li C., “Gold-based magneto/optical nanostructures: Challenges for *in vivo* applications in cancer diagnostics and therapy”, *Mater. Res. Bull.*, **34** (6), 415-421 (2009)

Meng H., Xia T., George S., Nel A.E., “A predictive toxicological praradigm for the safety assessment of nanomaterials”, *ACS Nano*, **3** (7), 1620-1627 (2009)

Miletto I., Gilardino A., Zamburlin P., Dalmazzo S., Lovisolo D., Caputo G., Viscardi G., Martra G., “Highly bright and photostable cyanine dye-doped silica nanoparticles for optical imaging: Photophysical characterization and cell tests”, *Dyes Pigments*, **84**, 121-127 (2010)

Mirkin C.A., Letsinger R.L., Mucic R.C., Storhoff J.J., “A DNA-based mehod for rationally assembling nanoparticles into macroscopic materials”, *Nature*, **382**, 607–609 (1996)

Mistlberger G., Klimant I., “Luminescent magnetic particles: Structures, syntheses, multimodal imaging, and analytical applications”, *Bioanal. Rev.*, **2**, 61-101 (2010)

Mistlberger G., Koren K., Scheucher E., Aigner D., Borisov S.M., Zankel A., Pölt P., Klimant I., “Multi-functional magnetic optical sensor particles with tunable

sizes for monitoring metabolic parameters and as basis for nanotherapeutics", *Adv. Funct. Mater.*, **20** (11), 1842–185(2010)

Moczko E., Meglinski I.V., Bessant C., Piletsky S.A., "Dye array for measuring physico-chemical parameters", *Anal. Chem.*, **81**, 2311-2316 (2009)

Mornet S., Vasseur S., Grasset F., Duguet E., "Magnetic nanoparticle design for medical diagnosis and therapy", *J. Mater. Chem.*, **14**, 2161-2175 (2004)

Nahrendorf M., Keliher E., Marinelli B., Waterman P., Feruglio P.F., Fexon L., Pivovarov M., Swirski F.K., Pittet M.J., Vinegoni C., Weissleder R., "Hybrid PET-optical imaging using targeted probes", *Proc. Natl. Acad. Sci.*, **107** (17), 7910-7915 (2010)

Nakajima N., Ikada Y., "Mechanism of amide formation by carbodiimide for bioconjugation in aqueous media", Bioconjugate *Chem.*, **6**, 123-130 (1995)

Nakamura M., Shono M., Ishimura K., "Synthesis, characterization, and biological applications of multifluorescent silica nanoparticles", *Anal. Chem.*, **79**, 6507-6514 (2007)

Napierska D., Thomassen L.C., Rabolli V., Lison D., Gonzalez L., Kirsch-Volders M., Martens J.A., Hoet P.H., "Size-dependent cytotoxicity of monodisperse silica nanoparticles in human endothelial cells", *Small*, **5** (7), 846-853 (2009)

Napierska D., Thomassen L.C., Lison D., Martens J.A., Hoet P.H., "The nanosilica hazard : Another variable entity", *Part. Fibre Toxicol.*, **7**, 39-71 (2010)

Narita A., Naka K., Chujo Y., "Facile control of silica shell layer thickness on hydrophilic iron oxide nanoparticles via reverse micelle method", *Colloids Surfaces A*, **336**, 46–56 (2009)

National Nanotechnology Initiative, 2011 budget, http://www.nano.gov/NNI_2011_budget_supplement.pdf

Nativo P., Prior I.A., Brust M., “Uptake and intracellular fate of surface-modified gold nanoparticles”, *ACS Nano*, **2** (8), 1639-1644 (2008)

Nehl C.L., Liao H., Hafner J., “Optical properties of star-shaped gold nanoparticles”, *Nano Lett.*, **6** (4), 683-688 (2006)

Nel A., Xia T., Mädler L., Li N., “Toxic potential of materials at the nanolevel”, *Science*, **311**, 622-627 (2006)

Nel A.E., Mädler L., Velegol D., Xia T., Hoek E.M., Somasundaran P., Klaessig F., Castranova V., Thompson M., “Understanding biophysicochemical interactions at the nano-bio interface”, *Nat. Mat.*, **9**, 543-557 (2009)

Neuberger T., Schöpf B., Hofmann H., Hofmann M., von Rechenberg B., “Superparamagnetic nanoparticles for biomedical applications: Possibilities and limitations of a new drug delivery system”, *J. Magn. Magn. Mater.*, **293**, 483-496 (2005)

Nichkova M., Dosev D., Gee S.J., Hammock B.D., Kennedy I.M., “Multiplexed immunoassays for proteins using magnetic luminescent nanoparticles for internal calibration”, *Anal. Biochem.*, **369** (1), 34–40 (2007)

Nie S., “Understanding and overcoming major barriers in cancer nanomedicine”, *Nanomedicine*, **5** (4), 523-528 (2010)

Nooney R.I., McCahey C.M., Stranik O., Guevel X.K., McDonagh C., MacCraith B.D., “Experimental and theoretical studies of the optimisation of fluorescence from near-infrared dye-doped silica nanoparticles”, *Anal. Bioanal. Chem.*, **393**, 1143-1149 (2009)

Oberdörster G., Maynard A., Donaldson K., Castranova V., Fitzpatrick J., Ausman K., Carter J., Karn B., Kreyling W., Lai D., Olin S., Monteiro-Riviere N., Warheit D., Yang H., “Principles for characterizing the potential human health effects from exposure to nanomaterials: elements of a screening strategy”, *Part. Fibre Toxicol.*, **2**, 8-43 (2005)

Oberdörster G., Stone V., Donaldson K., “Toxicology of nanoparticles: A historical perspective”, *Nanotoxicology*, **1** (1), 2-25 (2007)

Ohkuma S., Poole B., “Fluorescence probe measurement of the intralysosomal pH in living cells and the perturbation of pH by various agents”, *Proc. Natl Acad. Sci. USA*, **75**, 3327–3331 (1978)

Ohulchanskyy T.Y., Roy I., Goswami L.N., Chen Y., Bergey E.J., Pandey R.K., Oseroff A.R., Prasad P.N., “Organically modified silica nanoparticles with covalently incorporated photosensitizer for photodynamic therapy of cancer”, *Nano Lett.*, **7** (9), 2835-2842 (2007)

Ohulchanskyy T.Y., Roy I., Yong K.T., Pudavar H.E., Prasad P.N., “High-resolution light microscopy using luminescent nanoparticles”, *Wiley Interdiscip. Rev. Nanomed. Nanobiotechnol.*, **2** (2), 162–175 (2010)

Oldenburg S.J., Averitt R.D., Westcott S.L., Halas N.J., “Nanoengineering of optical resonances”, *Chem. Phys. Lett.*, **288**, 243-247 (1998)

Osseo-Asare K., Arriagada F. J., “Preparation of SiO_2 nanoparticles in a non-ionic reverse micellar system”, *Colloids Surf.*, **50**, 321 (1990)

Ossipov D.A., "Nanostructured hyaluronic acid-based materials for active delivery to cancer", *Expert Opin. Drug Deliv.*, **7** (6), 681-703 (2010)

Ou D. L., Seddon A.B., “Near- and mid-infrared spectroscopy of sol-gel derived ormosils: Vinyl and phenyl silicates”, *J. Non-Cryst. Solids*, **210**, 187-203 (1997)

Ow H., Larson D.R., Srivastava M., Baird B.A., Webb W.W., Wiesner U., “Bright and stable core-shell fluorescent silica nanoparticles”, *Nano Lett.*, **5** (1), 113-117 (2005)

Oyelere A.K., Chen P.C., Huang X., El-Sayed I.H., El-Sayed M.A., “Peptide-conjugated gold nanorods for nuclear targeting”, *Bioconjug. Chem.*, **18**, 1490–1497 (2007)

Pan Y., Neuss S., Leifert A., Fischler M., Wen F., Simon U., Schmid G., Brandau W., Jahnen-Dechent W., “Size-depedent cytotoxicity of gold nanoparticles“, *Small*, **3**, 1941-1949 (2007)

Pan Y., Leifert A., Ruau D., Neuss S., Bornemann J., Schmid G., Brandau W., Simon U., Jahnen-Dechent W., “Gold nanoparticles of diameter 1.4 nm trigger necrosis by oxidative stress and mitochondrial damage”, *Small*, **5** (18), 2067-2076 (2009)

Pankhurst Q.A, Connolly J., Jones S.K., Dobson J., “Applications of magnetic nanoparticles in biomedicine”, *J. Phys. D: Appl. Phys.*, **36**, R167-R181 (2003)

Panyam J., Labhasetwar V., “Dynamics of endocytosis and exocytosis of poly(D,L-Lactide-co-Glycolide) nanoparticles in vascular smooth muscle cells”, *Pharmaceut. Res.*, **20** (2), 212-220 (2003)

Park S.K., Kim K.D., Kim H.T., “Preparation of silica nanoparticles: determination of the optimal synthesis conditions for small and uniform particles”, *Colloids Surf., A*, **197**, 7-17, (2002)

Park S.I., Lim J.H., Kim J.H., Yun H.I., Kim C.O., “Toxicity estimation of magnetic fluids in a biological test”, *J. Magn. Magn. Mater.*, **304**, e406-e408 (2006)

Park S.E., Park M.Y., Han P.K., Lee S.W., “The effect of pH-adjusted gold colloids on the formation of gold clusters over APTMS-coated silica cores”, *Bull. Korean, Chem. Soc.*, **27** (9), 1341-1345 (2006)

Park S., Hamad-Schifferli K., “Nanoscale interfaces to biology”, *Curr. Opin. Chem. Biol.*, **14**, 1-7 (2010)

Patel D., Kell A., Simard B., Xiang B., Lin H.Y., Tian G., “The cell labeling efficacy, cytotoxicity and relaxivity of copper-activated MRI/PET imaging contrast agents”, *Biomaterials*, **32**, 1167-1176 (2011)

Peng H.S., Huang S.H., Wolfbeis O.S., “Ratiometric fluorescent nanoparticles for sensing temperature”, *J. Nanopart. Res.* **12**, 279-2733 (2010)

Pervaiz S., Olivo M., “Art and science of photodynamic therapy”, *Clin. Exp. Pharmacol. P.*, **33**, 551-556 (2006)

Petri-Fink A., Chastellain M., Juillerat-Jeanneret L., Ferrari A., Hofmann H., “Development of functionalized superparamagnetic iron oxide nanoparticles for interaction with human cancer cells”, *Biomaterials*, **26**, 2685-2694 (2005)

Petri-Fink A., Hofmann H., “Superparamagnetic iron oxide nanoparticles (SPIONs): From synthesis to in vivo studies—A summary of the synthesis, characterization, in vitro, and in vivo investigations of SPIONs with particular focus on surface and colloidal properties”, *IEEE Trans. Nanobiosci.*, **6** (4), 289-297 (2007)

Pezzin S.H., Stock N., Shishatskiy S., Nunes S.P., “Modification of proton conductive polymer membranes with phosphonated polysilsesquioxanes”, *J. Membrane Sci.*, **325**, 559–569 (2008)

Phonthammachai N., White T.J., “One-step synthesis of highly dispersed gold nanocrystals on silica spheres”, *Langmuir*, **23**, 11421-11424 (2007)

Phonthammachai N., Kah J.C., Jun G., Sheppard C.J., Olivo M.C., Mhaisalkar S.G., White T.J., “Synthesis of continuous silica-gold core-shell structures: Critical parameters and processes”, *Langmuir*, **24**, 5109-5112 (2008)

Piao Y., Burns A., Kim J., Wiesner U., Hyeon T., “Designed fabrication of silica-based nanostructured particle systems for nanomedicine applications”, *Adv. Funct. Mater.*, **18**, 3745-3758 (2008)

Pileni M.P., “Reverse micelles as microreactors”, *J. Phys. Chem.*, **97** (27), 6961-6973 (1993)

Pissuwan D., Valenzuela S.M., Cortie M.B., “Therapeutic possibilities of plasmonically heated gold nanoparticles”, *Trends Biotechnol.*, **24** (2), 62-67 (2006)

Platt V.M., Szoka F.C., “Anticancer therapeutics: Targeting macromolecules and nanocarriers to hyaluronan or CD44, a hyaluronan receptor”, *Mol. Pharm.*, **5** (4), 474-486 (2008)

Poland C. A., Duffin R., Kinloch I., Maynard A., Wallace W. A., Seaton A., Stone V., Brown S., MacNee W., Donaldson K., “Carbon nanotubes introduced into the abdominal cavity of mice show asbestos-like pathogenicity in a pilot study”, *Nat. Nanotechnol.*, **3**, 423-428 (2008)

Pollard T.D., Earnshaw W.C., Lippincott-Schwartz J., Cell Biology; 2nd Edition, Elsevier Health Sciences, 2007

Prasad P.N., *Introduction to Biophotonics*, Wiley-Interscience, New-York, 2003

Pustovalov V.K., Smetannikov A.S., Zharov V.P., “Photothermal and accompanied phenomena of selective nanophotothermolysis with gold nanoparticles and laser pulses”, *Laser Phys. Lett.*., **11**, 775-792 (2008)

Qian J., Chen Q., Cai F., Kong S.K., Ho H.P.,He S., “Quantum-dots-doped ORMOSIL nanoparticles as optical probes for total internal reflection fluorescence imaging of cancer cells”, *IEEE J. Quantum. Elect.*, **15** (5), 1374-1379 (2009)

Qiao R.R., Yang C.H., Gao M.Y., “Superparamagnetic iron oxide nanoparticles: From preparations to in vivo MRI applications”, *J. Mater. Chem.*, **19**, 6274–6293 (2009)

Qiao, Z.A.; Zhang, L., Guo, M., Liu, Y., Huo, Q., “Synthesis of mesoporous silica nanoparticles via controlled hydrolysis and condensation of silicon alkoxide”, *Chem. Mater.*, **21**, 3823-3829 (2009)

Qin J., Li X., Wei M., Gao X., Xu Z., He S., “Bio-molecule-conjugated fluorescent organically modified silica nanoparticles as optical probes for cancer cell imaging”, *Opt. Express*, **16** (24), 19568-19578 (2008)

Rabolli V., Thomassen L.C., Princen C., Napierska D.A., Gonzalez L., Kirsch-Volders M., Hoet P.H., Huaux F., Kirschhock C.E., Martens J.A., Lison D., “Influence of size, surface area and microporosity on the *in vitro* cytotoxic activity of amorphous silica nanoparticles in different cell types, *Nanotoxicology*, **4** (3), 307-318 (2010)

Rahman I.A., Vejayakumaran P., Sipaut C.S., Ismail J., Abu Bakar M., Adnan R., Chee C.K., “An optimized sol-gel synthesis of stable primary equivalent silica particles”, *Colloids Surf., A*, **294**, 102-110 (2007)

Rampazzo E., Bonacchi S., Montalti M., Prodi L., Zaccheroni N., “Self-organizing core-shell nanostructures: Spontaneous accumulation of dye in the core of doped silica nanoparticles”, J. Am. Chem. Soc., 129, 14251-14256 (2007)

Rao K.S., El-Hami K., Kodaki T., Matsuhige K., Makino K., “A novel method for synthesis of silica nanoparticles”, *J. Colloid Interf. Sci.*, **289**, 125-131 (2005)

Rechberger W., Hohenau A., Leitner A., Krenn J.R., Lamprecht B., Aussenegg F.R., “Optical properties of two interacting gold nanoparticles“, *Opt. Commun.*, **220**, 137-141 (2003)

Renn O., Roco M.C., “Nanotechnology and the need for risk governance”, *J. Nanopart. Res.*, **8**, 153-191 (2006)

Rosenholm J.M., Meinander A., Peuhu E., Niemi R., Eriksson J.E., Sahlgren C., Linden M., “Targeting of Porous Hybrid Silica Nanoparticles to Cancer Cells”, *ACS Nano*, **3** (1), 197-206 (2009)

Roy I., Ohulchanskyy T.Y., Pudavar H.E., Bergey E.J., Oseroff A.R., Morgan J., Dougherty T.J., Prasad P., “Ceramic-based nanoparticles entrapping water-

insoluble photosensitizing anticancer drugs: A novel drug-carrier system for photodynamic therapy", *J. Am. Chem. Soc.*, **125** (26), 7860–7865 (2003)

Salata O.V., "Applications of nanoparticles in biology and medicine", *J. Nanobiotechnol.*, **2** (3), 1-6 (2004)

Salgueirino-Maceira V., Correa-Duarte M.A., Farle M., Lopez-Quintela A., Sieradzki K., Diaz R., "Bifunctional gold-coated magnetic silica spheres", *Chem. Mater.*, **18**, 2701-2706 (2006)

Santra S., Dutta D., Walter G.A., Moudgil B.M., "Fluorescent nanoparticles probes for cancer imaging", *Technol. Cancer Res. T.*, **4** (6), 593-602 (2005)

Santra S., Dutta D., Moudgil B.M., "Functional dye-doped silica nanoparticles for bioimaging, diagnostics and therapeutics", Food Bioprod. Process., 83 (2), 136-140 (2005)

Santra S., Liesenfeld B., Bertolino C., Dutta D., Cao Z., Tan W., Moudgil B.M., Mericle R.A., "Fluorescence lifetime measurements to determine the core-shell nanostructure of FITC-doped silica nanoparticles: An optical approach to evaluate nanoparticle photostability", *J. Lumin.*, **117**, 75-82 (2006)

Sayes C.M., Wahi R., Kurian P.A., Liu Y., West J.L., Ausman K.D., Warheit D.B., Colvin V.L., "Correlating nanoscale titania structure with toxicity: a cytotoxicity and inflammatory response study with human dermal fibroblasts and human lung epithelial cells", *Toxicol. Sci.*, **92**, 174–185 (2006)

Schiepers C., Dahlbom M., "Molecular imaging in oncology: The acceptance of PET/CT and the emergence of MR/PET imaging", *Eur. Radiol.*, **21**, 548-554 (2011)

Schubert U., Hüsing N., Lorenz A., "Hybrid inorganic-organic materials by sol-gel processing of organofunctional metal alkoxides", *Chem. Mater.*, **7**, 2010-2027 (1995)

Schulze K., Koch A., Schöpf B., Petri A., Steintz B., Chastellain M., Hofmann M., Hofmann H., von Rechenberg B., " Intraarticular application of superparamagnetic nanoparticles and their uptake by synovial membrane—an experimental study in sheep", *J. Magn. Magn. Mat.*, **293**, 419-432 (2005)

Seger R., Krebs E.G., "The MAPK signaling cascade", FASEB J., **9**, 726–735 (1995)

Semelka R. C., Helmberger T.K., "Contrast agents for MR imaging of the liver", *Radiology*, **218**, 27-38 (2001)

Severino D., Junqueira H.C., Gugliotti M., Gabrielli D.S., Baptista M.S., "Influence of negatively charged interfaces on the ground and excited state properties of methylene blue", *Photochem. Photobiol.*, 77 (5): 459–468 (2003)

Seydel C., "Quantum dots get wet", *Science*, **300**, 80-81 (2003)

Shagidullin R. R., Vandyukova I. I., Zvereva E. E., Vizel A. O., Shchukina L. I., Garaev R. S., "Molecular structure and properties of oxime phosphonates: An FTIR and quantum chemical study", *Russ.Chem.Bull., Int.Ed.*, **56** (7), 1298-1304 (2007)

Sharma R.K., Das S., Maitra A., "Surface modified ormosil nanoparticles", *J. Colloid Interf. Sci*., **277** (2004) 342–346

Sharma P., Brown S., Walter G., Santra S., Moudgil B., "Nanoparticles for bioimaging", *Adv. Colloid Interfac.*, **123**, 471-485 (2006)

Shi H., He X., Yuan Y., Wang K., Liu D., "Nanoparticle-based biocompatible and long-life marker for lysosome labelling and tracking", *Anal. Chem.*, **82**, 2213-2220 (2010)

Shibata S., Taniguchi T., Yano T., Yamane M., "Formation of water-soluble dye-doped silica particles", *J. Sol-Gel Sci. Technol.*, **10**, 263-268 (1997)

Shukla R., Bansal V., Chaudhary M., Basu A., Bhonde R.R., Sastry M., “Biocompatibility of gold nanoparticles and their endocytotic fate inside the cellular compartment: A microscopic overview”, *Langmuir*, **21**, 10644–10654 (2005)

Slowing I.I., Trewyn B.G., Giri S., Lin V.S., “Mesoporous silica nanoparticles for drug delivery and biosensing applications”, *Adv. Funct. Mater.*, **15**, 1036. (2005)

Singh N., Jenkins G.J., Asadi R., Doak S.H., “Potential toxicity of superparamagnetic iron oxide nanoparticles (SPION)”, *Nano Reviews*, **1**, 5358-5353 (2010)

Smith A.M., Dave S., Nie S., True L., Gao X., “Multicolour quantum dots for molecular diagnostics of cancer”, *Expert Rev. Mol. Diagn.*, **6** (2), 232-244 (2006)

Sokolov K., Follen M., Aaron J., Pavlova I., Malpica A., Lotan R., Richards-Kortum R., “Real-time vital optical imaging of precancer using anti-epidermal growth factor receptor antibodies conjugated to gold nanoparticles”, *Tech. Cancer Res. Treatment*, **2** (6), 491-504 (2003)

Sokolov K., Aaron J., Hsu B., Nida D., Gillenwater A., Follen M., MacAulay C., Adler-Storhz K., Korgel B., Descour M., Pasqualini R., Arap W., Lam W., Richards-Kortum R., “Optical Systems for In Vivo Molecular Imaging of Cancer, *Tech. Canc. Res. Treat.*, **2**, 491-504 (2003)

Sokolov I., Naik S., “Novel fluorescent silica nanoparticles: Towards ultrabright silica nanoparticles”, *Small*, **4** (7), 934-939 (2008)

Sonnichsen C., Franzl T., Wilk T., von Plessen G., J. Feldmann, “Suppression of interband damping of plasmons in gold nanorods”, *Phys. Rev. Lett.*, **88** (7), 077402 (2002)

Sperling R.A., Rivera Gil P., Zhang F., Zanella M., Parak W.J., “Biological applications of gold nanoparticles”, *Chem Soc. Rev.*, **37**, 1896-1908 (2008)

Stern R., Asari A.A., Sugahara K.N., “Hyaluronan fragments: An information-rich system”, *Eur. J. Cell Biol.*, **85**: 699-715(2006)

Stöber W., Fink A., “Controlled growth of monodisperse silica spheres in the micron size range”, *J. Colloid Interf. Sci.*, **26**, 62-69 (1968)

Sugimoto T., “Underlying mechanisms in size control of uniform nanoparticles”, *J. Colloid Interface Sci.*, **309**, 106-118 (2007)

Sun J., Zhou S., Hou P., Yang Y., Weng J., Li X., Li M., “Synthesis and characterization of biocompatible Fe_3O_4 nanoparticles”, *J. Biomed. Mater. Res.*, **80** (2), 333-341 (2007)

Sutter U., Loeffler J., Bidmon M., Valadon H., Ebner R., *Roadmap Report Concerning the Use of Nanomaterials in the Medical & Health Sector*, Nanoroad SME, March 2006

Sun W., Fang N., Trewyn B.G., Tsunoda M., Slowing I.I., Lin V.S., Yeung E.S., “Endocytosis of a single mesoporous silica nanoparticle into a human lung cancer cell observed by differential interference contrast microscopy”, *Anal. Bioanal. Chem.*, **391**, 2119-2125 (2008)

Tada H., Higuchi H., Wanatabe T.M., Ohuchi N., “*In vivo* real-time tracking of single quantum dots conjugated with monoclonal aAnti-HER2 antibody in tumors of mice”, *Cancer Res.*, **67**, 1138-1144 (2007)

Tada D.B., Vono L.L., Duarte E.L., Itri R., Kiyohara P.K., Baptista M.S., Rossi L.M., “Methylene blue-containing silica-coated magnetic particles: A potential magnetic carrier for photodynamic therapy”, *Langmuir*, **23**, 8194-8199 (2007)

Thanh N.T., Green L.A., “Functionalisation of nanoparticles for biomedical applications, *Nano Today*, **5**, 213-30 (2010)

Tan W., Wang K., He X., Zhao X., Drake T., Wang L., Bagwe R., “Bionanotechnology based on silica nanoparticles”, *Med. Res. Rev.*, **24**, 621-638 (2004)

Tao Z., Toms B., Goodisman J., Asefa T., “Meosporosity and functional group dependent endocytosis and cytotoxicity of silica nanomaterials”, *Chem. Res. Toxicol.*, **22**, 1869-1880 (2002)

Tao Z., Morrow M.P., Asefa T., Sharma K.K., Duncan C., Anan A., Penefsky H.S., Goodisman J., Souid A.K., “Mesoporous silica nanoparticles inhibit cellular respiration”, *Nano Lett.*, 8 (5), 1517-1526 (2008)

Taroni P., Pifferi A., Torricelli A., Comelli D., Cubeddu R., “In vivo absorption and scattering spectroscopy of biological tissues”, *Photochem. Photobiol.*, **2**, 124-129 (2003)

Te Velde E.A., Veerman T., Subramaniam, Ruers T., “The use of fluorescent dyes and probes in surgical oncology”, *Eur. J. Surg. Oncol.*, **36**, 6-15 (2010)

Thanh N.T., Green L.A., “Functionalisation of nanoparticles for biomedical applications”, *Nano Today*, **5**, 213-230 (2010)

The Project on Emerging Nanotechnologies, http://www.nanotechproject.org/inventories/consumer/

Theaker B.J., Hudson K.E., Roswell F.J., “Doped hydrophobic silica nano- and micro-particles as novel agents for developing latent fingerprints”, *Forensic Sci. Int.*, **174**, 26-34 (2008)

Thiesen B., Jordan A., “Clinical applications of magnetic nanoparticles for hyperthermia”, *Int. J. Hyperthermia*, **24** (6), 467-474 (2008)

Traver E.R., *Specific targeting of silica nanoparticles to cancer cells using CD44hyaluronic acid interactions*, MSC thesis, Cranfield health, 2010

Trewyn B.G., Nieweg J.A., Zhao Y., Lin V.S., “Biocompatible mesoporous silica nanoparticles with different morphologies for animal cell membrane penetration”, *Chem. Eng. J.*, **137**, 23-29 (2008)

Tromberg B.J., Shah N., Lanning R., Cerussi A., Espinoza J., Pham T., Svaasand L., Butler J., “Non-invasive in vivo characterization of breast tumors using photon migration spectroscopy”, *Neoplasia*, **2**, 26-40 (2000)

Tsoli M., Kuhn H., Brandau W., Esche H., Schmid G., “Cellular uptake and toxicity of Au55 clusters”, *Small*, **1**, 841–844 (2005)

Unfried K., Albrecht C., Klotz L.O., von Mikecz A., Grether-Beck S., Schins R.P., “Cellular response to nanoparticles: Target structures and mechanisms”, *Nanotoxicology*, **1** (1), 52-71 (2007)

Unger S.A., “Photodynamic therapy: A bench-to-bedside success story”, *Buffalo Physician*, 8-19 (2004)

Van Blaaderen A., Kentgens A.P., “Particle morphology and chemical microstructure of colloidal silica spheres made from alkoxysilanes”, *J. Non-Cryst. Solids*, **149**, 161–178 (1992)

Van Blaaderen A., van Geest J., Vrij A., “Monodisperse colloidal silica spheres from tetraethoxysilanes: Particles formation and growth mechanism”, *J. Colloid Interface Sci.*, **154** (2), 481-501 (1992)

Van Blaaderen A., Vrij A., “Synthesis and characterization of colloidal dispersions of fluorescent, monodisperse silica spheres”, *Langmuir*, **8**, 2921-2931 (1992)

Van Schooneveld M.M., Cormode D.P., Koole R., van Wijngaarden J. T., Calcagno C., Skajaa T., Hilhorst J., ‘t Hart D.C., Fayad Z.A., Mulder W.J., Meijerink A., “A fluorescent, paramagnetic and PEGylated gold/silica nanoparticle for MRI, CT and fluorescence imaging”, *Contrast Media Mol. Imaging*, **5** (4), 231-236 (2010)

Verhaegh N.A., van Blaaderen A., “Dispersions of rhodamine-labeled silica spheres: Synthesis, characterization, and fluorescence confocal scaning laser microscopy”, *Langmuir*, **10**, 1427-1438 (1994)

Verma A., Stellacci F., “Effect of surface properties on nanoparticle-cell interactions”, *Small*, **6** (1), 12-21 (2010)

Vogel R., Surawaski P.P., Littleton B.N., Miller C.R., Lawrie G.A., Battersby B.J., Trau M., “Fluorescent organosilica micro- and nanoparticles with controllable size”, *J. Colloid and Interf. Sci.*, **310**, 144-150 (2007)

Vonarbourg A., Passirani C., Saulnier P., Benoit J.P., “Parameters influencing the stealthiness of colloidal drug delivery systems”, *Biomaterials*, **27** (24), 4356-4373 (2006)

Vojtíšek M., Iles A., Pamme N., “Rapid, multistep onchip DNA hybridisation in continuous flow on magnetic particles”, *Biosens. Bioelectron.*, **25** (9), 2172–2176 (2010)

Wagner M.K., Li F., Li J., Li X.F., Le C., “Use of quantum dots in the development of assays for cancer biomarkers”, *Anal. Bioanal. Chem.*, **397**, 3213-3224 (2010)

Walling M.A., Novak J.A., Shepard J.R., “Quantum dots for live cell and in vivo imaging”, *Int. J. Mol. Sci.*, **10**, 441-491(2009)

Wan J., Meng X., Liu E., Chen K., „“Incorporation of magnetite nanoparticles clusters in fluorescent silica nanoparticles for high-performance brain tumor delineation”, *Nanotechnology*, **21**, 235104 (2010)

Wang H.F., Huff T.B., Zweifel D.A., He W., Low P.S., Wei A., Cheng J. X., “*In vitro* and *in vivo* two-photon luminescence imaging of single gold nanorods”, *Proc. Natl. Acad. Sci. U.S.A*., **102**, 15752–15756 (2005)

Wang L., Yang C., Tan W., “Dual-luminophore-doped silica nanoparticles for multiplexed signalling”, *Nano Lett.*, **5** (1), 37-43 (2005)

Wang L., Tan W., “Multicolor FRET silica nanoparticles by single wanvelength excitation”, *Nano Lett.*, **6** (1), 84-88 (2006)

Wang L., Zhao W., O'Donoghue M.B., Tan W., "Fluorescent nanoparticles for multiplexed bacteria monitoring", *Bioconjugate Chem.*, **18**, 297-301 (2007)

Wang Q., Liu Y., Lin C., Yan H., "Layer-by-layer growth of superparamagnetic, fluorescent barcode nanospheres", *Nanotechnology*, **18** (40), 405604 (2007)

Wang L. Y., Bai J. W., Li Y. J., Huang Y., "Multifunctional nanoparticles displaying magnetization and near-IR absorption", *Angew. Chem. Int. Ed.*, **47**, 2439- 2442 (2008)

Wang M., Mi C., Zhang Y., Liu J., Li F., Mao C., Xu S., „"NIR-responsive silica-coated NaYbF4:Er/Tm/Ho upconversion fluorescent nanoparticles with tunable emission colors and their applications in immunolabeling and fluorescent imaging of cancer cells", *J. Phys. Chem. C*, **113**, 19021-19027 (2009)

Wang G., Gao Y., Huang H., Su X., "Multiplex immunoassays of equine virus based on fluorescent encoded magnetic composite nanoparticles", *Anal. Bioanal. Chem.*, **398**, 805–813 (2010)

Wilhelm C., Billotey C., Roger J., Pons J.N., Bacri J.C., Gazeau F., "Intracellular uptake of anionic superparamagnetic nanoparticles as a function of their surface coating", *Biomaterials*, **24**, 1001-1011 (2003)

Wilhelm C., Gazeau F., "Universal cell labelling with anionic magnetic nanoparticles", *Biomaterials*, **29**, 3161-3174 (2008)

Wood S., Jones R., Geldart A., *The Social and Economic Challenges of Nanotechnology*, Economic & Social Research Council, 2004

Wu L.Z., Tang X.J., Jiang M.H., Tung C.H., "Two-photon induced fluorescence of novel dyes", *Chem. Phys. Lett.*, **315**, 379-382 (1999)

Xia T., Kovochich M., Brant J., Hotze M., Sempf J., Oberley T., Sioutas C., Yeh J.I., Wiesner M.R., Nel A.E., "Comparison of the abilities of ambient and manufactured nanoparticles to induce toxicity according to an oxidative stress paradigm", *Nano Lett.*, **6** (8), 1794-1807 (2006)

Xia T., Kovochich M., Liong M., Zink J.I., Nel A.E., “Cationic polystyrene nanosphere toxicity depends on cell-specific endocytic and mitochondrial injury pathways”, *ACS Nano*, **2** (1), 85-96 (2008)

Xia W., Low P.S., “Folate-targeted therapies for cancer”, *J. Med. Chem.*, **53**, 6811-6824 (2010)

Xiao G.G., Wang M., Li N., Loo J.A., Nel A.E., “Use of proteomics to demonstrate a hierarchical oxidative stress to diesel exhaust paricle chemicals in a macrophage cell line”, *J. Biol. Chem.*, **278** (50), 50781-50790 (2003)

Xie G., Sun J., Zhong G., Shi L., Zhang D., “Biodistribution and toxicity of intravenously administered silica nanoparticles in mice”, *Arch. Toxicol.*, **84** (3), 183-190 (2010)

Xie H., Wang Z.J., Bao, A., Goins B., Phillips W.T., “In vivo PET imaging and iodistribution of radiolabeled gold nanoshells in rats with tumor xenografts”, *Int. J. Pharm.*, **395**, 324-330 (2010)

Xie J., Lee S., Chen X., “Nanoparticle-based theranostic agents”, *Adv. Drug Deliver. Rev.*, **62**, 1064-1079 (2010)

Xu C., Xie J., Ho D., Wang C., Kohler N., Walsh E.G., Morgan J.R., Chin Y.E., Sun S., “Au-Fe_3O_4 dumbbel nanoparticles as dual-functional probes”, *Angew. Chem. Int.*, **47**, 173-176 (2008)

Xu J., Liang J., Li J., Yang W., “Multicolor Dye-Doped Silica Nanoparticles Independent of FRET”, *Langmuir*, **26** (20), 15722-15725 (2010)

Yamauchi H., Ishikawa T., Kondo S., “Surface characterization of ultramicro-spherical particles of silica prepared by W/O microemulsion method”, *Colloids Surf.*, **37**, 71-80 (1989)

Yan J., Estevez M.C., Smith J.E., Wang K., He X., Wang L., Tan W., “Dye-doped nanoparticles for bioanalysis”, *Nanotoday*, **2** (3), 44-50 (2007)

Yang, W., Zhang, C.G., Qu, H.Y., Yang, H.H., Xu, J.G., “Novel fluorescent silica nanoparticle probe for ultrasensitive immunoassays”, *Anal. Chim. Acta*, **503** (2), 163-169 (2004)

Yang X., Hong H., Grailer J.J. , Rowland I.J. , Javadi A., Hurley S.A., Xiao Y., Yang Y., Zhang Y., Nickles R.J., Cai W., Steeber D.A., Gong S., “cRGD-functionalized, DOX-conjugated, and ^{64}Cu-labeled superparamagnetic iron oxide nanoparticles for targeted anticancer drug delivery and PET/MR imaging”, *Biomaterials*, **32**, 1-10 (2011)

Yao G., Wang L., Wu Y.R., Smith J., Xu J.S., Zhao W., Lee E., Tan W., “FloDots: luminescent nanoparticles”, *Anal. Bioanal. Chem.*, **385**, 518–524 (2006)

Yezhelyev M.V., Al-Hajj A., Morris C., Marcus A.I., Liu T., Lewis M., Cohen C., Zrazhevskiy P., Simons J.W., Rogatko A., “In Situ Molecular Profiling of Breast Cancer Biomarkers with Multicolor Quantum Dots”, *Adv. Mater.*, **19**, 3146-3151 (2007)

Yguerabide J., Yguerabide E.E., “Light-scattering submicronic particles as highly fluorescent analogs and their use as tracer labels in clinical and biological applications I. Theory”, *Anal. Biochem.*, **262**, 137-156 (1998)

Yokoi T., Sakamoto Y., Terasaki O., Kubota Y., Okubo T., Tastumi T., “Periodic arrangement of silica nanospheres assisted by amino acids”, *J. Am. Chem. Soc.*, **128**, 13664-13665 (2006)

Yokoi T., Wakabayashi J., Otsuka Y., Fan W., Iwama M., Watanabe R., Aramaki K., Shimojima A., Tatsumi T., Okubo T., “Mechanism of formation of uniform-sized silica nanospheres catalyzed by basic amino acids”, *Chem. Mater.*, **21**, 3719-3729 (2009)

Zhai Y., Zhai J., Wang Y., Guo S., Ren W., Dong S., “Fabrication of iron oxide core/gold shell submicrometer spheres with nanoscale surface roughness for

efficient surface-enhanced Raman scattering", *J. Phys. Chem. C*, **113**, 7009-7014 (2009)

Zhang Y., Kohler N., Zhang M., "Surface modification of superparamagnetic magnetite nanoparticles and their intracellular uptake", *Biomaterials*, **23**, 2553-2561 (2002)

Zhang J., Rana S., Srivastava R.S., Misra R.D.K, "On the chemical synthesis and drug delivery response of folate receptor-activated, polyethylene glycol-functionalized magnetite nanoparticles", *Acta Biomaterialia*, **4**, 40-48 (2008)

Zhang G., Feng J., Lu L., Zhang B., Cao L., " Fluorescent magnetic nanoprobes: Design and application for cell imaging", *J. Colloid Interf. Sci.*, **351**, 128-133 (2010)

Zhang Q., Ge J., Goebl J., Hu Y., Sun Y., Yin Y., "Tailored synthesis of superparamagnetic gold nanoshells with tunable optical properties", *Adv. Mater.*, **22**, 1905-1909 (2010)

Zhao, X., Tapec R., Tan W., "Ultrasensitive DNA Detection Using Highly Fluorescent Bioconjugated Nanoparticles", *J. Am. Chem. Soc.*, **125**, 11474 - 11475 (2003)

Zhao X., Hilliard L.R., Mechery S., Wang Y., Bagwe R., Jin S., Tan W., "A rapid bioassay for single bacterial cell quantitation using bioconjugated nanoparticles", *Proc. Natl. Acad. Soc. U.S.A.*, **101**, 15027-15032 (2004)

Zhao X.J., Bagwe R.P., Tan W.H., "Development of organic-dye-doped silica nanoparticles in a reverse microemulsion", *Adv. Mater*. **16**, 173–176 (2004)

Zharov V.P., Galitovskaya E.N., Johnson C., Kelly T., "Synergistic enhancement of selective nanophotothermolysis with gold nanoclusters: Potential for cancer therapy", *Laser Surg. Med.*, **37**, 219-226 (2005)

Zharov V.P., Mercer K.E., Galitovskaya E.N., Smeltzer M.S., “Photothermal nanotherapeutics and nanodiagnostics for selective killing of bacteria targeted with gold nanoparticles”, *Biophys. J.*, **90**, 619-627 (2006)

Zhou M., Wang B., Rozynek Z., Xie Z., Fossum J.O., Yu X., Raaen S., “Minute synthesis of extremely stable gold nanoparticles”, *Nanotechnology*, **20**, 505606 (2009)

Appendices

Appendix A Supplementary materials for the synthesis of FNSPs by the Stöber and reverse microemulsion approaches

A.1 Preparation of blank and FITC-doped nanoparticles following the Stöber method

Table A-1: Parameters for the preparation of FITC-doped silica nanoparticles

Experiment	V (TEOS)	V (NH_4OH)	V (FITC-APTES)	V (H_2O)	V (EtOH)
Blank 1	1.5 mL	2.8 mL	X	X	35 mL
Blank 2	2.5 mL	2.8 mL	X	X	35 mL
Blank 3	1.5 mL	2.8 mL	X	5 mL	35 mL
Blank 4	2.5 mL	2.8 mL	X	5 mL	35 mL
Stöb 1	500 µL (0.5 M)	100 µL	250 µL	X	10 mL
Stöb 2	250 µL (0.5 M)	100 µL	250 µL	X	10 mL
Stöb 3	250 µL (0.5 M)	50 µL	250 µL	X	10 mL
Stöb 4	250 µL (0.5 M)	100 µL	100 µL	X	10 mL

A.2 Dye-doped nanoparticles via the reverse microemulsion route

Table A-2: Parameters for the preparation of fluorophores-doped silica nanoparticles.

Experiment	w (TX100)	V (cyclohexane)	V (hexanol)	V (NH_4OH)	V (H_2O)	V (TEOS)
Mic-RB 1	1.77 g	7.5 mL	1.6 mL	150 µL	500 µL	500 µL
Mic-RB 2	1.77 g	7.5 mL	1.6 mL	300 µL	500 µL	500 µL
Mic-R6G	1.77 g	7.5 mL	1.6 mL	150 µL	1 mL	500 µL
Mic-AO	1.77 g	7.5 mL	1.6 mL	300 µL	1 mL	500 µL

Appendix B Principles of dynamic light scattering

Dynamic light scattering (DLS) is a technique measuring the size of submicrometric particles through correlation with Brownian motion (the random movement of particles within a liquid due to the collision with the solvent molecules). DLS relies on the illumination of particles in a liquid and analysis of the fluctuation of light scattered by the particles.

Small and large particles do not drift similarly in a liquid, and small particles tend to move more quickly than the larger one. Speed and size of particles in a liquid are related by the Stokes-Einstein relation:

$$D_H = \frac{kT}{3\pi\eta D} \qquad \textbf{(B-1)}$$

where D_H is the hydrodynamic diameter of the particles, k is the Boltzmann constant (1.3806504 x 10^{-23} $J.K^{-1}$), η is the solvent viscosity, T is the absolute temperature, and D is the diffusion coefficient.

The correlation curve obtained through DLS measurements contains the information to determine the diffusion coefficient of particles and therefore to measure their hydrodynamic diameter. The Stokes-Einstein equation is based on the assumption that particles in solution are spherical; otherwise the Perrin factor is necessary to estimate the particles dimension. A DLS instrument uses a correlator, i.e. a component that compares the intensity of a signal at particular points in time to build the correlation curve of a sample. When recording the signal at an instant (t) and comparing it with the signal at an instant (t + δt), the two signals have high chances to be very similar provided that the instant δt is very short (**Figure B-1**).

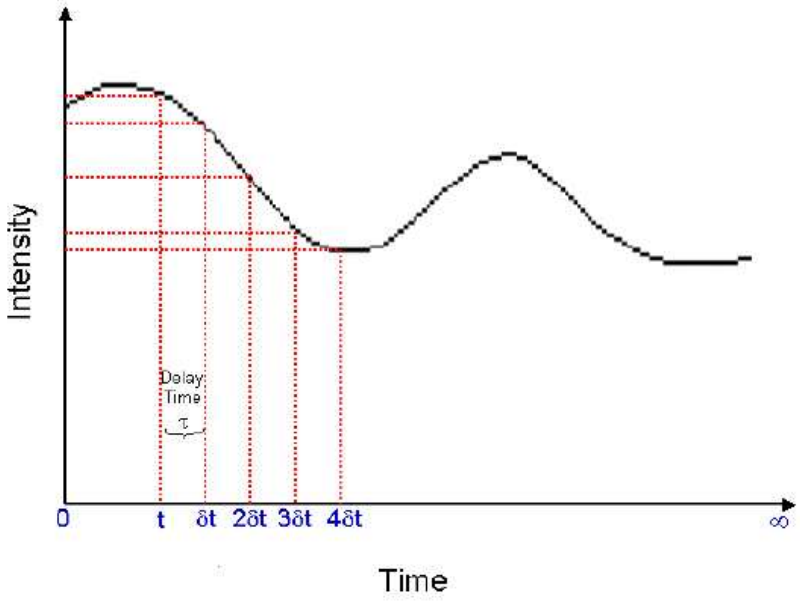

Figure B-0-1: The intensity of light scattered is recorded at different time intervalles (t), (t+dt), (t+2dt), etc. in order to build the correlation curve necessary to measure the sioze of particles.

At an instant (t + 2δt), the correlation between (t) and (t + 2δt) decreases because the particles have slightly moved and the intensity of light scattered is accordingly modified. As the signal at the instant (t) is compared with longer the signal, the correlation will continue to decrease until there is no correlation anymore. The correlation curve is built by measuring correlation at different time (t), (t + δt), (t + 2δt), (t + 3δt), (t + 4δt), etc. When comparing the signal at (t) with itself, the correlation is perfect and is reported as 1; when no correlation exists, the value is 0. Because of the difference of motion between small and large particles, their respective correlograms will be different: small particles move quickly so that the fluctuation of intensity is very fast so that the rate of decay of the correlation function will be much faster than for the slower large particles (**Figure B-2**).

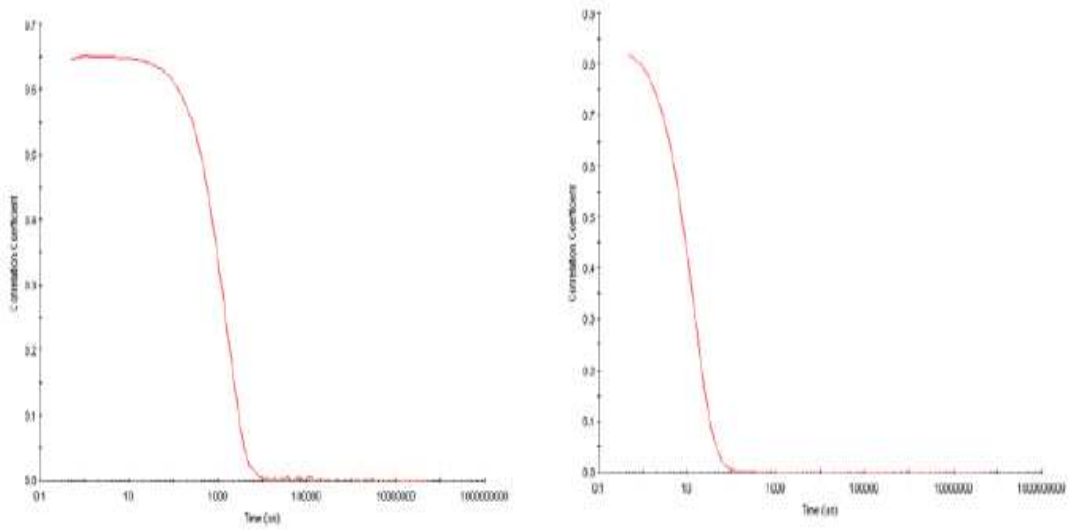

Figure B-0-2: Correlograms values range between 1 and 0 and indicate the presence of small or large particles according to the rate of decay. Hence, small particles move more quickly and the decay rate occurs earlier than for large, slower particles.

Once the correlation function is measured, size of particles is calculated using the Stokes-Einstein equation or more precisely the size distribution of particles in a sample. Typical DLS graph displays the relative intensity of light scattered compared to size distribution, also called intensity distribution. From the intensity distribution, volume distribution and number distribution can be extrapolated using Mie theory. In general, d(intensity) > d(volume) > d(number), which is easily understand when considering a sample containing two sizes of particles (for example 5 and 50nm) at the same concentration (**Figure B-3**). In that case, the number distribution displays two peaks of same intensity since both populations are in equal number. When considering the volume distribution, the 50nm particle population present a peak 1,000 times larger than the 5nm peak. The volume of sphere is equal to $4/3\pi r^3$, meaning that the volume of 50 nm spherical sphere is 10^3=1000 times higher than that of 5 nm particles. Finally, 50nm particles present a peak 1,000,000 times larger than the peak of 5 nm particles because

large particles scatter more light than small particles ($I \alpha d^6$ in the Rayleigh theory)

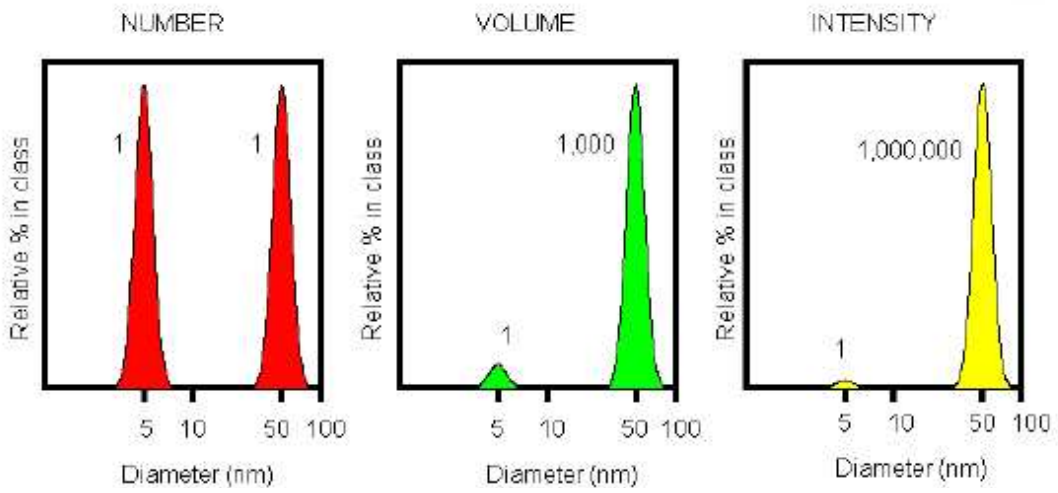

Figure B-0-3: (From left to right) Number, volume, and intensity size distribution of a sample containing 5 and 50 nm particles at the same concentration.

Appendix C Supplementary materials for the synthesis of hybrid VTEOS-TEOS nanoparticles

C.1 Influence of VTEOS content

Table C-1: Volume of silicon precursors for the study of VTEOS concentration effect.

	mol (VTEOS)	V (VTEOS)	mol (TEOS)	V (TEOS)	VTEOS composition
VT-00	0 mmol	0 µL	3.5 mmol	775 µL	0% VTEOS
VT-25	0.88 mmol	135 µL	2.6 mmol	580 µL	25% VTEOS
VT-50	1.8 mmol	275 µL	1.8 mmol	385 µL	50% VTEOS
VT-75	2.6 mmol	410 µL	0.88 mmol	195 µL	75% VTEOS
VT-100	3.5 mmol	545 µL	0 mmol	0 µL	100% VTEOS

C.2 Study of influencing parameters

Table C-2: Concentration of reagents for the study of the arginine and water effects.

V (VTEOS)	V (TEOS)	w (arginine)	V (water)	Silane/arginine/water molar ratio
305 µL	430 µL	6.4 mg	7 mL	1/0.01/100
205 µL	290 µL	4.3 mg	7 mL	1/0.01/150
150 µL	215 µL	3.2 mg	7 mL	1/0.01/200
305 µL	430 µL	32 mg	7 mL	1/0.05/100
205 µL	290 µL	21 mg	7 mL	1/0.05/150
150 µL	215 µL	16 mg	7 mL	1/0.05/200
305 µL	430 µL	64 mg	7 mL	1/0.1/100
205 µL	290 µL	43 mg	7 mL	1/0.1/150
150 µL	215 µL	32 mg	7 mL	1/0.1/200

Appendix D Supplementary materials for the surface modification of hybrid nanoparticles

D.1 Surface modification with APTES and THPMP

Table D-1: Volumes of TEOS, APTES, and THPMP for the surface modification of silica nanoparticles with amine.

V (TEOS)	*V (APTES)*	*V (THPMP)*	*V (arginine)*	*Organosilane %*
220 µL	3 µL	X	5 mL	1 % APTES
200 µL	25 µL	X	5 mL	10 % APTES
165 µL	60 µL	X	5 mL	25 % APTES
110 µL	115 µL	X	5 mL	50 % APTES
55 µL	175 µL	X	5 mL	75 % APTES
X	235 µL	X	5 mL	100 % APTES
30 µL	20 µL	0 µL	5 mL	0% THPMP
200 µL	15 µL	10 µL	5 mL	25% THPMP
30 µL	10 µL	20 µL	5 mL	50% THPMP
30 µL	5 µL	30 µL	5 mL	75% THPMP
30 µL	0 µL	40 µL	5 mL	100% THPMP

D.2 FA and HA bio-conjugation in arginine solution

Table D-2: Volume of reagents employed for the bioconjugation of FA onto hybrid nanoparticles.

V (FA)	V (EDC)	V (NHS)	W (NP)	Arginine
250 µL	720 µL	860 µL	100 mg	5 mL
250 µL	1.08 mL	1.29 mL	100 mg	5 mL
250 µL	1.44 mL	1.72 mL	100 mg	5 mL
500 µL	720 µL	860 µL	100 mg	5 mL
500 µL	1.08 mL	1.29 mL	100 mg	5 mL
500 µL	1.44 mL	1.72 mL	100 mg	5 mL
500 µL	1.8 mL	2.15 mL	100 mg	5 mL
750 µL	1.08 mL	1.29 mL	100 mg	5 mL
750 µL	1.44 mL	1.72 mL	100 mg	5 mL
750 µL	1.8 mL	2.15 mL	100 mg	5 mL

1 mL	1.44 mL	1.72 mL	100 mg	5 mL
1 mL	1.8 mL	2.15 mL	100 mg	5 mL

D.3 FA and HA bio-conjugation in MES buffer

Table D-3: Volume of reagents used for the MES-solvated bioconjugation of FA and HA onto hybrid nanoparticles.

V (FA)	V (EDC)	V (NHS)	V (MES)	W (SiNP)	Arginine
0.5 mL (FA)	720 µL	860 µL	10 mL	2 mg	10 mL
1.5 mL (FA)	720 µL	860 µL	10 mL	2 mg	10 mL
2 mL (FA)	1.08 mL	1.29 mL	10 mL	2 mg	10 mL
2 mL (FA)	1.44 mL	1.72 mL	10 mL	2 mg	10 mL
2 mL (FA)	1.8 mL	2.15 mL	10 mL	2 mg	10 mL
5 mL (FA)	720 µL	860 µL	10 mL	2 mg	10 mL
5 mL (FA)	1.8 mL	2.15 mL	10 mL	2 mg	10 mL
250 µL (HA)	1.08 mL	1.29 mL	10 mL	2 mg	10 mL
250 µL (HA)	1.44 mL	1.72 mL	10 mL	2 mg	10 mL

Appendix E Carbodiimide coupling chemistry

Conjugation of nanoparticles requires two steps: firstly, the surface of the silica structure must be modified by a linker, usually an organosilane. Then, the chosen ligand can be bound to the surface in order to generate a nanoparticle targeting specific species. Frequently, APTES is used as linker for various species containing carboxylic groups such as folic acid. In that case, carbodiimide chemistry is employed to bind aminated surface and biomolecules. The first step of this process consists in activating the carboxylic groups via 1-Ethyl-3-(3-dimethylaminopropyl)-carbodiimide (EDC) following the equation:

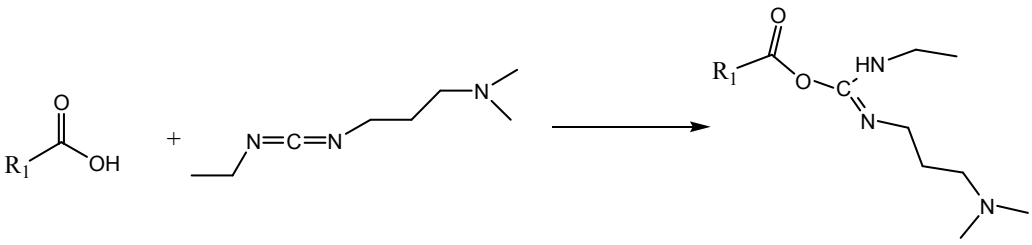

Then N-hydroxysuccinimide is introduced to react with the resulting unstable O-urea derivative. Following a condensation reaction between the carboxylic group and NHS, an ester is formed:

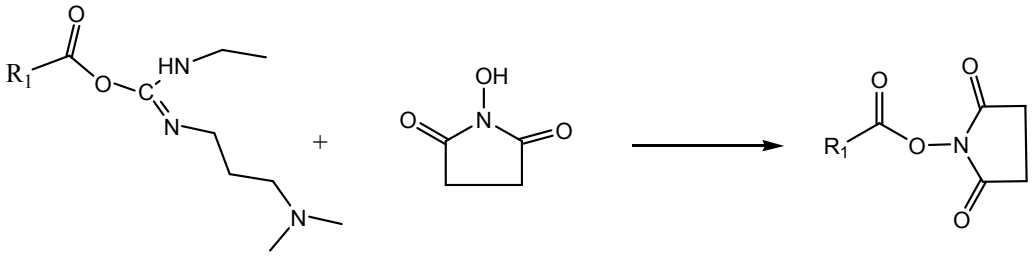

The ester group reacts with the amine functional groups at the surface of the nanoparticles and finally form amide bond:

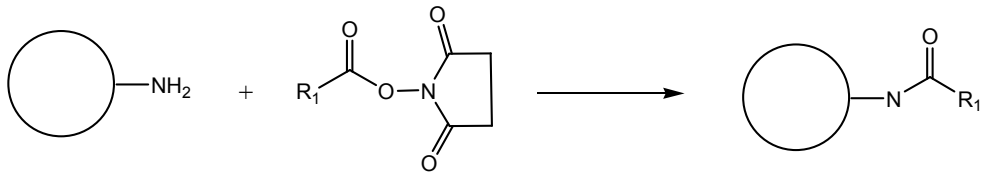
NH2
+
R1
O
N
O
O
O
N
O
R1

Appendix F Supplementary materials for the modification of hybrid composition

Table F-1: Parameters for the preparation of hybrid silica nanoparticles

Type	V (TEOS)	V (PhTEOS)	V (VTEOS)	V (organosilane)	composition
Ph-10	635 µL	65 µL	X	X	10% PhTEOS
Ph-25	430 µL	160 µL	X	X	25% PhTEOS
Ph-50	285 µL	320 µL	X	X	50% PhTEOS
Ph-75	145 µL	480 µL	X	X	75% PhTEOS
Ph-100	X	640 µL	X	X	100% PhTEOS
TH-05	735 µL	X	X	79 µL (THPMP)	5 % THPMP
TH-10	700 µL	X	X	158 µL (THPMP)	10 % THPMP
TH-15	660 µL	X	X	238 µL (THPMP)	15 % THPMP
VT-TH 5	370 µL	X	260 µL	79 µL (THPMP)	5 % THPMP
VT-TH 10	350 µL	X	245 µL	158 µL (THPMP)	10 %THPP
VT-AP 1	383 µL	X	270 µL	8 µL (APTES)	1 % APTES
VT-AP 2	380 µL	X	267 µL	16 µL (APTES)	2 % APTES
VT-AP 5	368 µL	X	259 µL	41 µL (APTES)	5 % APTES
VT-AP 10	349 µL	X	246 µL	83 µL (APTES)	10 % APTES

Appendix G Deposition-precipitation

Deposition-precipitation is based on the hydrolysis of the chloroauric ion $AuCl_4^-$ under the action of a base, resulting in the formation of anions of the form $[Au(OH)_xCl_{4-x}]^-$. The extent of hydrolysis depends on the pH but also on the temperature that promotes the replacement of Cl^- with OH^-. Of all potential species, only $Au(OH)_3$ precipitates and is able to deposit on silica or other substrate – the other species remaining in solution - so that the control of pH is crucial for the proper decoration with gold seeds (**Figure G-1**). The optimal conditions for the generation of $[Au(OH)_3Cl]^-$ species and their precipitation onto the substrate surface are a pH comprised between 8 and 10 and a temperature in the range 60 to 80°C.

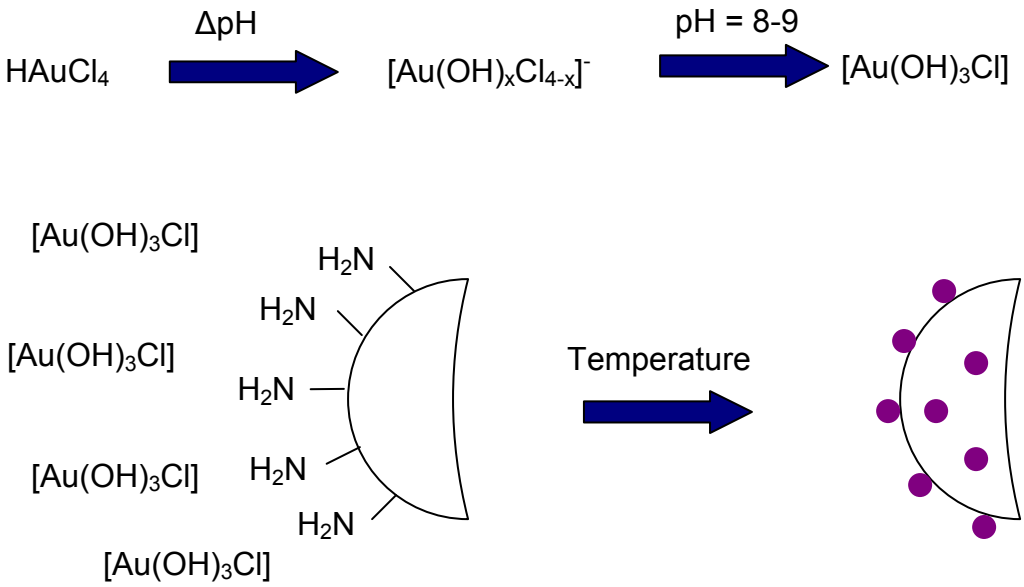

Figure G-1: Schematisation of the influence of pH over the deposition-precipitation process and the formation of gold seeds onto amine-modified silica nanoparticles.

Nevertheless, the method does not function for all metal oxide surfaces: in the case of gold deposition, the isoelectric point of the substrate must be above 5. For example, Phonthammachai et *al*. found that gold seeds do not precipitate on bare silica particles because its isoelectric point is equal to 2 [*Phonthammachai, 2007*]. For this reason, the silica surface is negatively charge for all pH above 2 and consequently repel the likewise negatively charged $[Au(OH)_xCl_{4-x}]^-$. Surface functionalisation - in the silica case with amine groups - overcome this issue as the amine-modified particles have an isoelectric point of 9. In consequence, the particles are slightly positively charged below a pH of 9 whereas $[Au(OH)_xCl_{4-x}]^-$ species are predominantly formed at pH comprised between 7 and 9. Hence this pH condition is optimal for the precipitation of gold seed onto silica.

Appendix I Supplementary materials for the coating of magnetite nanoparticles with silica and hybrid silica

I.1 TEOS-coated nanoparticles

Table I-1: Parameters for the preparation of silica-coated magnetite nanoparticles.

Sample	V (Fe_3O_4)	V (arginine)	V (TEOS)	V (dye)	V (APTES)	V (THPMP)
1	700 µL	50 mL	350 µL	100 µL (MB)	X	X
2	700 µL	50 mL	175 µL	75 µL (MB)	X	X
3	1 mL	25 mL	250 µL	40 µL (MB)	20 µL	40 µL
4	1 mL	25 mL	500 µL	40 µL (MB)	20 µL	40 µL
5	1 mL	25 mL	1 mL	40 µL (MB)	20 µL	40 µL
6	1 mL	25 mL	250 µL	30 µL (R6G)	30 µL	60 µL
7	1 mL	25 mL	500 µL	30 µL (R6G)	30 µL	60 µL

I.2 Deposition of a hybrid layer

Table I-2: Parameters for the preparation of silica-coated magnetite nanoparticles.

Sample	V (Fe_3O_4)	V (arginine)	V (TEOS)	V (VTEOS)	V (dye)	V (APTES)	V (THPMP)
8	1 mL	25 mL	200 µL	100 µL	30 µL (R6G)	20 µL	40 µL
9	1 mL	25 mL	150 µL	150 µL	40 µL (MB)	20 µL	40 µL
10	1 mL	25 mL	250 µL	50 µL	40 µL (MB)	20 µL	40 µL
11	750 µL	30 mL	95 µL	65 µL	50 µL (R6G)	15 µL	15 µL
12	750 µL	30 mL	190 µL	130 µL	40 µL (R6G)	30 µL	30 µL
13	375 µL	15 mL	180 µL	130 µL	50 µL (MB)	20 µL	20 µL
14	375 µL	15 mL	95/90 µL	65/X µL	50 µL (MB)	20 µL	20 µL
15	375 µL	15 mL	130/90	X	50 µL (MB)	20 µL	20 µL
16	1 mL	25 mL	200 µL	X	40 µL (MB)	X	50 µL
17	1 mL	25 mL	230 µL	X	5 µL (FI)	20 µL	X

I.3 Deposition of a second layer onto nanocomposites

Table I-3: Parameters for the deposition of silica and hybrid layers onto magnetite-silica nanoparticles.

Experiment	V (batch)	V (TEOS)	V (VTEOS)	V(APTES)	V (dye)
Batch 2-1	5 mL	5 µL	X	X	10 µL (AO)
Batch 2-2	5 mL	10 µL	X	X	10 µL (AO)
Batch 2-3	5 mL	10 µL	5 µL	X	15 µL (AO)
Batch 2-4	5 mL	10 µL	10 µL	X	15 µL (AO)

I.4 TEOS-coated nanoparticles

Table I-4: Parameters for the deposition of hybrid layers onto magnetite-nanoparticles.

Sample	V (arginine)	V (TEOS)	V (VTEOS)	V (THPMP)	V (APTES)	V (dye)
18 - Layer 1	30 mL	95 µL	65 µL	X	X	20 µL (R6G)
18 - Layer 2	X	95 µL	65 µL	30 µL	30 µL	25 µL (MB)
19 - Layer 1	30 mL	95 µL	65 µL	X	X	30 µL (MB)
19 - Layer 2	X	95 µL	65 µL	15 µL	15 µL	25 µL (R6G)
20 - Layer 1	30 mL	95 µL	65 µL	20 µL	X	30 µL (MB)
20 - Layer 2	X	95 µL	65 µL	15 µL	15 µL	40 µL (AO)
21 – Layer 1	10 mL	60 µL	60 µL	X	5 µL	15 µL (LY)
21 – Layer 2	5 mL	100 µL	X	X	X	20 µL (AO)
22 – Layer 1	10 mL	60 µL	60 µL	X	10 µL	15 µL (LY)
22 – Layer 2	5 mL	100 µL	X	X	X	20 µL (AO)
23 – Layer 1	10 mL	60 µL	60 µL	5 µL	X	40 µL (MB)
23 – Layer 2	5 mL	60 µL	X	X	X	20 µL (AO)
24 – Layer 1	10 mL	60 µL	60 µL	X	2.5 µL	15 µL (LY)
24 – Layer 2	5 mL	60 µL	X	X	X	20 µL (AO)
25 – Layer 1	10 mL	30 µL	30 µL	X	1.5 µL	15 µL (Fl)
25 – Layer 2	5 mL	30 µL	X	X	X	15 µL (R6G)
26 – Layer 1	10 mL	30 µL	30 µL	X	1.5 µL	15 µL (Fl)
26 – Layer 2	5 mL	30 µL	X	X	X	15 µL (RB)

Appendix J Supplementary materials for synthesis of multifunctional nanoparticles

J.1 Deposition-precipitation onto magnetite-silica

Table J-1: Volume of reagents for the decoration of nanocomposites with gold seeds.

Sample	V (Fe_3O_4)	V (TEOS)	V (APTES)	V (THPMP)	V (MB)
Mg-DP 1	700 µL	100 µL	10 µL*	5 µL*	50 µL
Mg-DP 2	500 µL	100 µL	10 µL	30 µL	50 µL
Mg-DP 3	500 µL	100 µL	20 µL	40 µL	50 µL
Mg-DP 4	500 µL	100 µL	10 µL	20 µL	50 µL
Mg-DP 5	500 µL	125 µL	20 µL	40 µL	50 µL
Mg-DP 6	500 µL	200 µL	20 µL (1h)	40 µL	50 µL
Mg-DP 7	500 µL	300 µL	7.5 µL (30')	25 µL	50 µL

J.2 Effect of reducer concentration on the growth of gold shell

Table J-2: Effect of sodium borohydride to grow a gold shell onto MgAu-1.

Sample	DP time	V (batch)	V (K-gold)	V ($NaBH_4$)
MgAu-1	4 h	200 µL	10 mL	1 mL
MgAu-1	4 h	200 µL	20 mL	2 mL
MgAu-1	4 h	200 µL	40 mL	4 mL
MgAu-1	4 h	200 µL	10 mL	100 µL
MgAu-1	4 h	200 µL	10 mL	200 µL
MgAu-1	4 h	200 µL	10 mL	500 µL
MgAu-1	4 h	200 µL	10 mL	1 mL

Table J-3: Effect of sodium borohydride and formaldehyde to grow a gold shell onto MgAu-2.

Sample	DP time	V (batch)	V (K-gold)	V ($NaBH_4$)	V (CH_2OH)
MgAu-2	1 h	200 µL	2 mL	50 µL	X
MgAu-2	1 h	200 µL	2 mL	100 µL	X
MgAu-2	1 h	200 µL	2 mL	200 µL	X
MgAu-2	2 h	100 µL	2 mL	50 µL	X
MgAu-2	2 h	100 µL	2 mL	200 µL	X
MgAu-2	2 h	100 µL	5 mL	50 µL	X
MgAu-2	2 h	100 µL	5 mL	100 µL	X
MgAu-2	2 h	100 µL	5 mL	200 µL	X
MgAu-2	2 h	100 µL	5 mL	500 µL	X
MgAu-2	3 h	100 µL	2 mL	X	200 µL
MgAu-2	3 h	100 µL	2 mL	X	500 µL
MgAu-2	3 h	100 µL	5 mL	X	500 µL
MgAu-2	3 h	100 µL	5 mL	X	1 mL
MgAu-2	3 h	100 µL	5 mL	X	3 mL

Table J-43: Effect of hydroxylamine to grow a gold shell onto MgAu-3.

Sample	DP time	V (batch)	V (K-gold)	V (NH_2OH)
MgAu-3	1 h 30	100 µL	2 mL	1 mL
MgAu-3	1 h 30	200 µL	2 mL	1 mL
MgAu-3	1 h 30	300 µL	2 mL	1 mL
MgAu-3	1 h 30	450 µL	2 mL	1 mL
MgAu-3	1 h 30	250 µL	2 mL	500 µL
MgAu-3	1 h 30	250 µL	2 mL	1 mL
MgAu-3	1 h 30	250 µL	2 mL	2.5 mL
MgAu-3	1 h 30	250 µL	2 mL	5 mL
MgAu-3	1 h 30	250 µL	5 mL	2.5 mL
MgAu-3	1 h 30	250 µL	10 mL	5 mL

J.3 Effect of gold platting solution

Table J-5: Volume of K-gold solution used to grow a gold layer.

Sample	DP time	V (batch)	V (K-gold)	pH	V (NH_2OH)
Batch 12	15’	250 µL	20 mL	9.9	1 mL
Batch 12	15’	250 µL	20 mL	10.1	1 mL
Batch 12	15’	250 µL	50 mL	9.9	2.5 mL
Batch 12	15’	250 µL	50 mL	10.1	2.5 mL
Batch 6	2 h	1 mL	10 mL		250 µL
Batch 6	2 h	1 mL	10 mL		500 µL
Batch 6	2 h	1 mL	10 mL		750 µL
Batch 6	2 h	1 mL	10 mL		1 mL

J.4 Effect of deposition-precipitation on the final gold coating

TableJ-6: Deposition-precipitation duration before gold ion nucleation.

Sample	DP time	V (batch)	V (K-gold)	V (NH_2OH)
Batch 18	45 min	250 µL	10 mL	500 µL
Batch 18	45 min	250 µL	15 mL	500 µL
Batch 18	60 min	250 µL	10 mL	500 µL
Batch 18	60 min	250 µL	15 mL	500 µL
Batch 19	X	500 µL	15 mL	500 µL
Batch 19	X	500 µL	15 mL	1 mL
Batch 19	45 min	500 µL	15 mL	500 µL
Batch 19	45 min	500 µL	15 mL	1 mL
Batch 19	60 min	500 µL	15 mL	500 µL
Batch 19	60 min	500 µL	15 mL	1 mL
Batch 3	15 min	500 µL	15 mL	1 mL
Batch 3	30 min	500 µL	15 mL	1 mL
Batch 3	45 min	500 µL	15 mL	1 mL
Batch 3	60 min	500 µL	15 mL	1 mL
Batch 4	15 min	500 µL	10 mL	1 mL
Batch 4	30 min	500 µL	10 mL	1 mL
Batch 4	45 min	500 µL	10 mL	1 mL
Batch 4	60 min	500 µL	10 mL	1 mL
Batch 5	15 min	500 µL	5 mL	500 µL
Batch 5	30 min	500 µL	5 mL	500 µL
Batch 5	45 min	500 µL	5 mL	500 µL
Batch 5	60 min	500 µL	5 mL	500 µL
Batch 6	30 min	500 µL	10 mL	1 mL
Batch 6	1 h	500 µL	10 mL	1 mL
Batch 6	2 h	500 µL	10 mL	1 mL
Batch 6	3 h	500 µL	10 mL	1 mL

J.5 Iterative hydroxylamine seeding technique

Table J-74: Procedure for the regrowth of the gold layer in batches 8 and 11

Sample	Regrowth step	DP time	V (batch)	V (K-gold)	V (NH_2OH)
Batch 11	X1	50 min	25 mL	25 mL	2.5 mL
Batch 11	X2	X	X	20 mL	2 mL
Batch 11	X3	X	X	15 mL	1.5 mL
Batch 11	X4	X	X	10 mL	1 mL
Batch 11	X5	X	X	5 mL	0.5 mL
Batch 8	X1	2h	20 mL	20 mL	2 mL
Batch 8	X3	X	X	15 mL	1.5 mL
Batch 8	X5	X	X	10 mL	1 mL
Batch 8	X7	X	X	5 mL	0.5 mL